Structural analysis of prestressed Saint Venant-Kirchhoff hyperelastic membranes.

Ruiz, Antonio Javier Gil

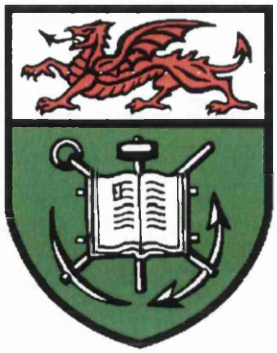

Structural Analysis of Prestressed Saint Venant-Kirchhoff Hyperelastic Membranes

by

Antonio Javier Gil Ruiz

Ingeniero de Caminos, Canales y Puertos

Thesis submitted to the University of Wales
in candidature for the degree of Doctor of Philosophy

October 2004

Civil and Computational Engineering Center

School of Engineering

University of Wales Swansea

ProQuest LLC.
789 East Eisenhower Parkway
P.O. Box 1346
Ann Arbor, MI 48106 – 1346

DECLARATION

This work has not previously been accepted in substance for any degree and is not being currently submitted in candidature for any degree.

Signed.....(candidate)
Date.....20 - 10 - 2004.....

STATEMENT 1

This thesis is the result of my own investigation, except where otherwise stated.

Other sources are acknowledged by footnotes giving explicit references. A bibliography is appended.

Signed.....(candidate)
Date.....20 - 10 - 2004.....

STATEMENT 2

I hereby give consent for my thesis, if accepted, to be available for photocopying and for inter-library loan, and for the title and summary to be made available to outside organizations.

Signed.....(candidate)
Date.....20 - 10 - 2004.....

Acknowledgements

I would like to express my profound gratitude to Professor Javier Bonet, my supervisor. I must confess without any hesitation that to have met him has been the greatest success throughout my entire professional career. Over his talented personality and outstanding research experience, I would point out his honesty, sincerity and friendship as remarkable features. He has ended up becoming a solid reference for my future.

I would also like to thank Dr. Richard Wood, firstly a research colleague, now an unforgettable friend. The numerous coffee breaks I spent in his office enabled me to embrace the computational mechanics and, the life itself, from another perspective.

I gratefully acknowledge the financial support received from the Spanish Ministry of Education, Culture and Sport, which allowed me to focus all my energy towards the completion of this research.

Many thanks go to my friends back in Linares, among whom I would like to emphasize Carlos, Fran, Manolo, José Manuel, Miki and David. Moreover, thanks to my people in Granada, specially, Luis, Rocío, David and Antonio. Thanks also to all my mates in Swansea, too numerous to mention, specially to John, Clare, Javier, Jose Luis Curiel, Jose Luis Padilla, George, Dhemi and, above all, Arturo and his inseparable friend Peter.

I would like to give a special thank you to all my brothers and sisters. It is worthwhile to mention them one by one. To Coral for their continuous support and encouragement during my time in Granada. To Rocío for the never ending study evenings that we passed together around the dining room's table. To Fany for the endless conversations to make me believe in my success as well as for her advice to come to Swansea, a decision that changed my life forever. I will never be able to pay you back as much as you did for me. To Maite and Inmaculada, for having faith in me and my future projects. To Ignacio for that time he travelled from Jaén to Granada to give me the necessary strength to adopt difficult decisions.

Finally, I would like to thank my parents for their support, patience, continuous help but most of all, for their love. They always phoned me when I most needed it. They are truly my guardian angels. This work is completely dedicated to them.

"It is not knowledge, but the act of learning, not possession but the act of getting there, which grants the greatest enjoyment. When I have clarified and exhausted a subject, then I turn away from it, in order to go into darkness again... I imagine the world conqueror must feel thus, who, after one kingdom is scarcely conquered, stretches out his arms for others".

Karl Friedrich Gauss (1777-1855)

To Maite, Fany, Inmaculada, Ignacio, Coral, Rocío and my parents

Outline

A Total Lagrangian formulation for prestressed structural membranes is described. The kinematics of prestressed membranes is displayed as a series of three successive configurations, namely, a nominally stressed initial equilibrium state $\Re_0$, a prestressed state $\Re_{pret}$ and a final in-service state $\Re$, for the time instants t^0, t^{pret} and t, respectively. Kinematic entities are fully derived, i.e., deformations gradient tensor, displacement gradient tensor, right Cauchy-Green tensor or Green-Lagrange strain tensor.

Among the wide group of available hyperelastic materials to describe moderate strain behavior, the Saint Venant-Kirchhoff model is chosen as the most adequate. By following its definition, the Helmholtz's free energy functional or strain energy functional w_{int} is used as a potential in order to obtain the second Piola-Kirchhoff stress tensor. Alternative stress tensors such as the Cauchy stress tensor or the first Piola-Kirchhoff stress tensor are derived as well.

Another physical feature that is taken into account is the likelihood of developing wrinkles. The proposed technique in order to capture wrinkles attempts to develop a set of conditions in terms of the Euler-Lagrange strain tensor along its principal directions. Subsequently, a modified Helmholtz's free energy functional will be introduced with the purpose of describing in an alternative manner the constitutive behaviour of the continuum medium after the moment of wrinkling.

The Force Density Method is reviewed in order to determinate initial shapes for tension structures. These equilibrium shapes are employed as initial guesses for the subsequent highly nonlinear problem that entails the structural analysis of the membrane under the actual presence of prestressing loading and external loading. It is shown that the Force Density Method can be regarded as an instrument for the transformation of a topological structure into a real spatial structure. A series of algorithms to obtain connectivity patterns are then presented.

A Total Lagrangian format set up along with a displacement-based isoparametric finite element formulation and a Newton-Raphson numerical scheme is adopted for the solution of the overall structural problem. Two-noded and three-noded linear finite elements will be employed to describe appropriately cable and membrane elements, respectively. The implementation of the discrete nonlinear system of equilibrium equations will be carried out by means of a very elegant procedure termed Direct Core Congruential Formulation (DCCF).

Apart from the well known second order Newton-Raphson method, other first order procedures such as the steepest descent method, the Polak-Ribiere method or the Fletcher-Reeves method are employed, along with parametric line searches, as valid alternatives when convergence is not accomplished in the former case. This results in a very flexible numerical solver.

Contents

I Preliminars xxv

1 Introduction 1
1.1 Characterization of tension structures. 3
1.2 State of the art. 5
1.3 Scope of the thesis. 10
1.4 Layout of the thesis. 12

II General Formulation of the problem 15

2 Strong Formulation 17
2.1 Introduction. 19
2.2 Eulerian formulation of the balance laws. 19
2.3 Lagrangian formulation of the balance laws. 21
2.4 Constitutive model. 22
2.5 Finite Hyperelasticity theory in initially prestressed bodies. 24
2.5.1 First load step and preliminary results 24
2.5.2 Second load step: strong formulation 26
2.5.3 Conclusions. 31

3 Weak Formulation 33
3.1 Introduction. 35
3.2 Total Lagrangian Formulation (TLF). 35
3.3 Updated Lagrangian Formulation (ULF). 38
3.4 Final considerations. 38

4 FEM Discretization 41
4.1 Introduction. 43
4.2 FEM standard formulation. 43
4.2.1 Displacements and deformations fields. 43
4.2.2 Equivalent internal nodal forces. 44
4.2.3 Equivalent external nodal forces. 45
4.2.4 Semidiscretization equations. 47
4.2.5 Linearization of the equivalent internal nodal forces. 48

4.2.6 Some considerations about the Updated Lagrangian Formulation. 50
4.3 Direct Core Congruential Formulation (DCCF). 50
4.3.1 Displacements and strains field. 51
4.3.2 Equivalent internal nodal forces vector. 53
4.3.3 Equivalent external nodal forces vector. 54
4.3.4 Linearization of the equivalent internal nodal forces vector. . . 54
4.4 Energy principles. 56
4.5 Concluding remarks 58

5 Total Lagrangian Formulation: cable and membrane elements 59
5.1 Introduction. 61
5.2 Cable elements. 62
5.3 Membrane elements 65

6 Nonconservative loading 71
6.1 Introduction. 73
6.2 Equivalent external nodal forces vector. 73
6.3 Linearization of the equivalent external nodal forces vector. 75

7 Wrinkling Analysis 77
7.1 Introduction. 79
7.2 Hyperelastic finite deformation theory along principal directions. . . . 80
7.3 Basic equations of wrinkling analysis. 83
7.3.1 Second Piola-Kirchhoff stress tensor. 86
7.3.2 Constitutive tensor. 87

8 Topological meshing algorithms 89
8.1 Introduction. 91
8.1.1 Generalities about the Force Density Method (FDM). 91
8.2 Topological meshing algorithms. 94
8.2.1 From the graph to the spatial mesh. 94
8.2.2 Remarks about the topological discretization criterion. 95
8.2.3 Shape finding flowchart. 96
8.3 Concluding remarks. 104

III Numerical methods 105

9 Unconstrained optimization: numerical methods 107
9.1 Introduction. 109
9.2 Local minimum point characterization. 110
9.3 Convex and concave functions. 111
9.4 Minimization and maximization of convex functions. 112

9.5 Numerical methods. . . . 112
9.6 The method of steepest descent. . . . 113
9.7 Newton's method. . . . 115
9.8 Parametric line search. . . . 116
9.8.1 Numerical parametric line search. . . . 117
9.9 Quasi-Newton's methods. . . . 119
9.9.1 Scaling. . . . 120
9.10 Conjugate direction methods. . . . 121
9.11 The conjugate gradient method. . . . 123
9.12 Computational improvements to the conjugate gradient method. . . . 125

10 Computational implementation **127**
10.1 Introduction. . . . 129
10.2 Shape finding. . . . 130
10.2.1 Sub-program MESHER.EXE architecture. . . . 131
10.3 Geometrically non-linear structural analysis. . . . 131
10.4 Sub-program NLTE.EXE architecture. . . . 132
10.4.1 Numerical schemes. . . . 137
10.4.2 Incremental strategy. . . . 138
10.4.3 Unconstrained optimization methods. . . . 139
10.4.4 Parametric line search. . . . 139
10.4.5 Convergence criteria. . . . 140

IV Numerical examples **141**

11 Robustness **143**
11.1 Introduction. . . . 145
11.2 Cable networks. . . . 145
11.2.1 Numerical example 1. . . . 145
11.2.2 Numerical example 2. . . . 147
11.3 Structural membranes. . . . 151
11.3.1 Numerical example 3. . . . 151
11.3.2 Numerical example 4. . . . 152
11.4 Follower loads and wrinkling analysis. . . . 156
11.4.1 Numerical example 5. . . . 156
11.4.2 Numerical example 6. . . . 162
11.4.3 Numerical example 7. . . . 169
11.5 Cable reinforced prestressed membranes. . . . 172
11.5.1 Numerical example 8. . . . 172
11.5.2 Numerical example 9. . . . 175

12 Structural applications **179**
12.1 Introduction. . . . 181
12.2 Structure 1: E1. . . . 181
12.2.1 Prestress loading 182
12.2.2 In-service loading 183
12.3 Structure 2: E2. . . . 197
12.3.1 Prestressing loading. . . . 197
12.3.2 In-service loading. . . . 199
12.4 Conclusions. . . . 213

V Conclusions **215**

13 Concluding remarks **217**
13.1 General considerations. . . . 219
13.2 Conclusions. . . . 220
13.2.1 About the proposal of the method. . . . 220
13.2.2 About the convergence of the numerical algorithms. . . . 221
13.3 Recommendations for further research. . . . 222

VI Apendices **225**

A Vector and tensor Algebra **227**
A.1 Introduction. . . . 229
A.2 Introduction to matrices. . . . 229
A.3 Vector and matrix norms. . . . 230
A.4 Iterative methods for the solution of linear system of equations. . . . 233
A.4.1 Jacobi method. . . . 233
A.4.2 Gauss-Seidel method. . . . 234
A.4.3 On the convergence of the method. . . . 235

B Nonlinear programming **239**
B.1 Introduction. . . . 241

C Graphs theory: fundamentals **243**
C.1 Introduction. . . . 245
C.2 Fundamentals of Graphs theory. . . . 245

D Nonlinear continuum mechanics: fundamentals **249**
D.1 Introduction. . . . 251
D.2 An introduction to kinematics. . . . 251
D.3 Strain numerical measures. . . . 253
D.4 Stress numerical measures. . . . 255

E Derivatives for the Saint Venant-Kirchhoff hyperelastic model 257
E.1 Introduction. 259
E.2 First derivatives. 259
E.2.1 Second derivatives. 260

VII References 261

List of Figures

1.1 Cable reinforced prestressed membrane 1. 4
1.2 Cable reinforced prestressed membrane 2. 5
1.3 Cable reinforced prestressed membrane 3. 7

2.1 Motion of a body. 25
2.2 Motion of a prestressed body. 27

3.1 Motion of a prestressed body. 36

4.1 Semidiscretized equilibrium equations in a Total Lagrangian Formulation. 47
4.2 DCCF scheme. 51
4.3 DCCF non-linear equilibrium equations. 55
4.4 Variational formulation of the structural problem. 58

5.1 Cable element description. 62
5.2 Membrane element description. 66

8.1 Shape finding flowchart. 97
8.2 Shape finding preprocessor flowchart. 97
8.3 Roof with radial meshing. 98
8.4 Meshing for a radial plane graph. 99
8.5 Roof with n-polygonal meshing. 99
8.6 Meshing for an n-polygonal plane graph. 100
8.7 Meshing for a rectangular planar graph. 100
8.8 Meshing for a rectangular-diagonal planar graph. 101
8.9 Roof with rectangular meshing. 102
8.10 Roof with rectangular-diagonal meshing. 102
8.11 Roof with triangular meshing. 103
8.12 Meshing for a triangular planar graph. 103
8.13 Roof with quadrangular meshing. 104
8.14 Meshing for a quadrangular planar graph. 104

10.1 Structural analysis strategy 129
10.2 Flowchart of the sub-program **FDMC.EXE** 130

10.3 Flowchart of the program **NLTE.EXE** 133
10.4 Flowchart of the iterative numerical scheme 134
10.5 Flowchart of the subroutine ***elementprop*** 135
10.6 Flowchart of the subroutine ***tension*** 136
10.7 Flowchart of the subroutine ***nonlinmethod.*** 137

11.1 Leonard: discretization. 145
11.2 Leonard: prestressed and in-service configurations. 146
11.3 Convergence curves. 146
11.4 Broughton: cable discretization. 147
11.5 Structural model: cable isometric view. 148
11.6 Structural model: cable lateral view. 148
11.7 Convergence curves. 149
11.8 Axial forces(Kip). 150
11.9 Levy & Spillers, 111: Discretization and Cauchy stress σ_{xx}. 151
11.10Numerical example 4: Discretization. 152
11.11Numerical example 4: Convergence curves. 153
11.12Numerical example 4: Displacements OX & OZ. 154
11.13Numerical example 4: Cauchy stresses σ_I & σ_{II}. 155
11.14Convergence curves. 157
11.15Kang & Im (1999). Initial and deformed airbag. Plan view. 157
11.16Kang & Im (1999). Initial and deformed airbag. Isometric view. 158
11.17Kang & Im (1999). Principal Cauchy stresses: σ_I and σ_{II}. 159
11.18Kang & Im (1999). Evolution of the minimum principal Cauchy stress (I). 160
11.19Kang & Im (1999). Evolution of the minimum principal Cauchy stress (II). 161
11.20Kang & Im (1997). Initial airbag: plan and isometric views. 162
11.21Kang & Im (1997). Deformed airbag: plan and isometric views. 163
11.22Convergence curves: membrane theory. 163
11.23Convergence curves: wrinkling theory. 164
11.24Kang & Im (1997). Principal Cauchy stresses: σ_I and σ_{II}. 165
11.25Kang & Im (1999). Deformed airbag 166
11.26Kang & Im (1997). Vertical displacement and radial contraction. 166
11.27Kang & Im (1997). Evolution of the principal Cauchy stress σ_{II} (I). . . . 167
11.28Kang & Im (1997). Evolution of the principal Cauchy stress σ_{II} (II). . . . 168
11.29Discretization 170
11.30Cauchy stress component σ_{xx} for $\frac{2M}{Ph} = 0.5$ 171
11.31Bending moment vs curvature. 171
11.32Cauchy stress σ_{xx} vs depth. 172
11.33Numerical example 8: isometric and plan views. 173
11.34Numerical example 8: equilibrium profile curves. 174
11.35Numerical example 8: Displacement and stress vs loading. 175
11.36Numerical example 9: isometric and plan views. 176
11.37Numerical example 9: equilibrium profile curves. 177

11.38Numerical example 9: Displacement and stress vs loading. 178

12.1 E1: initial configuration. 182
12.2 E1: initial configuration: plan view. 183
12.3 E1: initial configuration: isometric view. 184
12.4 E1: initial configuration. 185
12.5 E1: OX displacements. (a) Prestress load. (b) Snow load. 186
12.6 E1: OX displacements. (a) Wind load, hyp. I. (b) Wind load, hyp. II. . . 187
12.7 E1: OY displacements. (a) Prestress load. (b) Snow load. 188
12.8 E1: OY displacements. (a) Wind load, hyp. I. (b) Wind load, hyp. II. . . 189
12.9 E1: OZ displacements. (a) Prestress load. (b) Snow load. 190
12.10E1: OZ displacements. (a) Wind load, hyp. I. (b) Wind load, hyp. II. . . 191
12.11E1: Shape. (a) Prestressed load. (b) Wind load, hyp II. 192
12.12E1: Cauchy stress σ_I. (a) Prestress load. (b) Snow load. 193
12.13E1: Cauchy stress σ_I. (a) Wind load, hyp. I. (b) Wind load, hyp. II. . . . 194
12.14E1: Cauchy stress σ_{II}. (a) Prestress load. (b) Snow load. 195
12.15E1: Cauchy stress σ_{II}. (a) Wind load, hyp. I. (b) Wind load, hyp. II. . . 196
12.16E2: initial configuration, isometric view. 197
12.17E2: initial configuration, plan view. 198
12.18E2: initial configuration, plan view. 199
12.19E2: initial configuration, isometric view. 200
12.20E1: Reinforced cables and masts configuration. 201
12.21E2: OX displacements. (a) Prestress load. (b) Snow load. 202
12.22E2: OX displacements. (a) Wind load, hyp. I. (b) Wind load, hyp. II. . . 203
12.23E2: OY displacements. (a) Prestress load. (b) Snow load. 204
12.24E2: OY displacements. (a) Wind load, hyp. I. (b) Wind load, hyp. II. . . 205
12.25E2: OZ displacements. (a) Prestress load. (b) Snow load. 206
12.26E2: OZ displacements. (a) Wind load, hyp. I. (b) Wind load, hyp. II. . . 207
12.27E2: Shape. (a) Prestressed load. (b) Wind load, hyp II. 208
12.28E2: Cauchy stress σ_I. (a) Prestress load. (b) Snow load. 209
12.29E2: Cauchy stress σ_I. (a) Wind load, hyp. I. (b) Wind load, hyp. II. . . . 210
12.30E2: Cauchy stress σ_{II}. (a) Prestress load. (b) Snow load. 211
12.31E2: Cauchy stress σ_{II}. (a) Wind load, hyp. I. (b) Wind load, hyp. II. . . 212
12.32E2: convergence curves. (a) Prestress load. (b) Snow load. (c) Wind load, hyp. I. (c) Wind load, hyp. II. 213

List of Tables

11.1 Leonard: Displacements (in). 146
11.2 Leonard: Cauchy stresses (Ksi). 146
11.3 Displacements (in). 149
11.4 Levy & Spillers, 111: Displacements(in). 152
11.5 Numerical example 4: Displacements (in). 153
11.6 Numerical example 4: Cauchy stresses (Psi). 153
11.7 Kang & Im (1999). Displacements(cm). 158
11.8 Kang & Im (1999). Evolution of displacements (cm). 158
11.9 Kang & Im (1997). Evolution of displacements (cm). 164

12.1 E1: Boundary conditions (m). 181
12.2 E1: Boundary conditions (cm). 183
12.3 E2: Boundary conditions (m). 198
12.4 E2: Spatial coordinates (m). 199
12.5 E2: Boundary conditions (cm). 200

Nomenclature

A^{pret}	prestressed cable section area
b	force field per unit mass
$\mathbf{D}$	strain rate tensor
$\mathbf{e}$	Green-Lagrange strain vector
$\mathbf{E}$	Green-Lagrange strain tensor
E	Young modulus
$\mathbf{F}$	deformation gradient tensor
$\mathbf{f}_{ext}$	equivalent external forces
$\mathbf{f}_{int}$	equivalent internal forces
$\mathbf{g}$	displacement gradient vector
$\mathbf{G}$	displacement gradient tensor
$\mathbf{H_i}$	coefficient matrix
$\mathbf{h_i}$	coefficient vector
I	first invariant
II	second invariant
III	third invariant
J	jacobian
$\mathbf{K}^{geo}$	geometric stiffness matrix
$\mathbf{K}^{mat}$	material stiffness matrix
L^{pret}	prestressed cable length
$\mathbf{M}^{geo}$	core geometric stiffness matrix
$\mathbf{M}^{mat}$	core material stiffness matrix
N^I	standard shape function
$\mathbf{P}$	nominal stress tensor
$\mathbf{R}$	rotation tensor
$\mathbf{s}$	second Piola-Kirchhoff stress vector
$\mathbf{S}$	second Piola-Kirchhoff stress tensor
t	membrane thickness
$\mathbf{u}$	nodal displacements
$\mathbf{U}$	stretch tensor
V	current volume
V^{pret}	prestressed volume
$\mathbf{x}$	current coordinates
$\mathbf{X}^{pret}$	prestressed coordinates
w_{int}	taut Helmholtz's free energy
$\widehat{w}_{int}$	wrinkled Helmholtz's free energy
$\widetilde{w}_{int}$	slack Helmholtz's free energy
$\boldsymbol{\mathcal{C}}$	constitutive tangent modulus tensor
$\boldsymbol{\sigma}^{pret}$	prestressed Cauchy stress tensor
$\{\boldsymbol{\sigma}^{pret}\}$	prestressed Cauchy stress vector
$\boldsymbol{\sigma}$	Cauchy stress tensor
ν	Poisson ratio
Γ^{pret}	prestressed membrane area
Π	total potential energy
U	internal potential energy
Π_{ext}	external potential energy
$\delta\mathbf{u}$	virtual displacements
U	internal potential energy
ξ_α	principal strains
λ_α	principal stretches
ρ^{pret}	prestressed density
ρ	current density

Part I

Preliminars

Chapter 1

Introduction

1.1 Characterization of tension structures.

Tension structures are those in which the main load-carrying members transmit loads to the foundation or support system by tensile stresses with no compression or flexure allowed. Their cross-sectional dimensions and method of fabrication are such that their out-of-plane shear and flexural rigidities, as well as their buckling resistance, are negligible. They are load-adaptive in that members change geometry to accommodate changes in load rather than increase stress levels.

Tension structures can be comprised of membranes, cables or both. They include air-supported structures, pneumatic shells, prestressed membranes, cable networks, suspension cables, guyed towers and temporary shelters, among others.

There are two wide classes of tension structures: *cable structures*, comprising uniaxially stressed members, and *membrane structures*, comprising biaxially stressed members. According to Leonard (1988), these two general categories can be split into many more. Nevertheless, in this research we will focus on:

- **Cable networks**, in which prestressed segments are connected in a curved surface and loaded predominantly normal to that surface, i.e., suspended nets.
- **Prestressed membranes** in which fabric or rubber-like sheets are stretched over rigid members and/or perimeter cables, i.e., tents.

Because of the inherent nonlinear nature of tension structures, conventional linear analysis, which assumes small elastic deformations and displacements, is not applicable. Over the last few decades, considerable mathematical and computational development of suitable analysis techniques has been undertaken.

Among the enormous amount of advantages -see Leonard (1988), Berger (1996), Shaeffer (1996), Ishii (1995), and Wakefield (1999)- that the use of this kind of structures entail, it is important to point out the following ones:

1. They are lightweight and easy to erect, transport and dismantle.
2. They can be fabricated in a factory, which provides low installation costs.
3. The environmental loads are efficiently undergone by tensile stresses without the appearance of neither bending nor twisting.
4. They are load-adaptive, in such a way that they will modify its geometry to adapt properly to the applicable loads.
5. They contribute environmentally to a better and sustainable development.

These tension structures are achieving an increasing acceptance level in our society, for example, because of their aesthetic qualities and speed of erection. A large number of tensioned membranes are reinforced by means of interior and perimeter

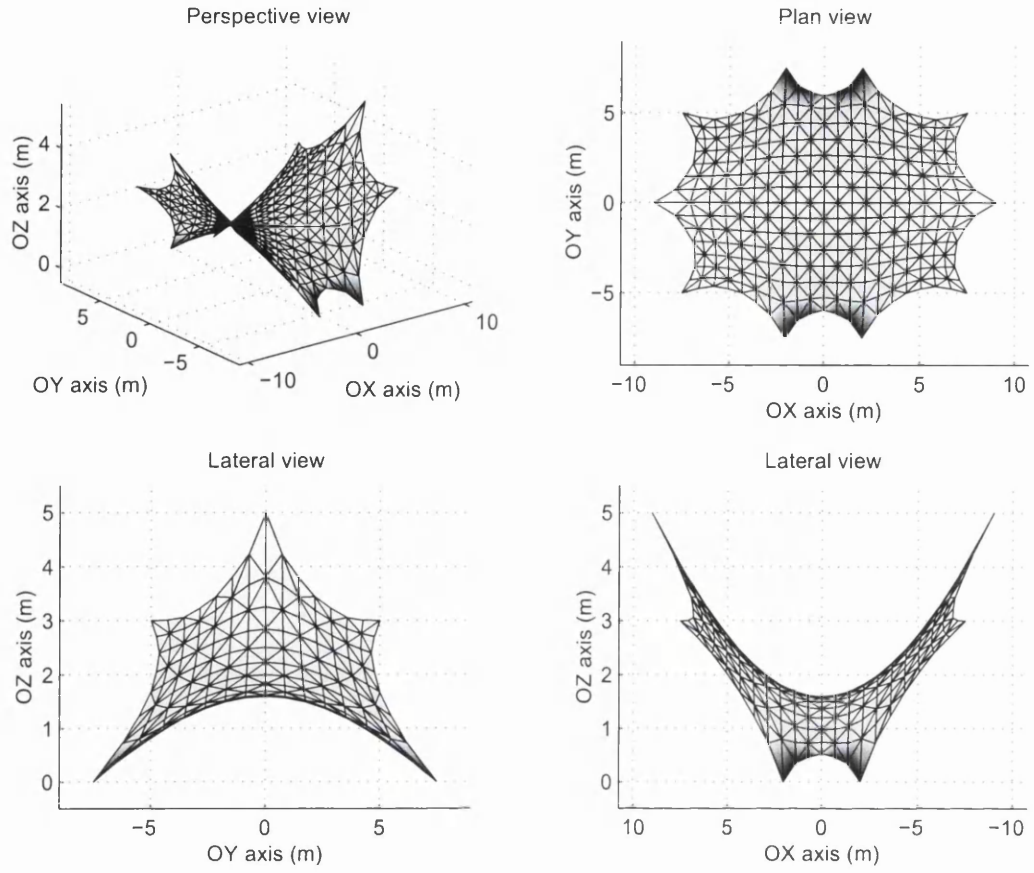

Figure 1.1: Cable reinforced prestressed membrane 1.

cables. At the same time, compressive rigid members such as masts, are assembled with the global structure in order to provide the adequate stability.

The design of cable reinforced prestressed membranes follows a three-stage procedure, involving:

- form-finding
- patterning
- static analysis

In this thesis, we will deal with the first and third of the above issues, specially focusing on the latter. The static analysis is a continuation of the form finding process, in which stresses and strains are calculated under imposed external loads. The problem is geometrically non-linear. The procedure begins with the form-found shape of the structure, which is initially in equilibrium. Static loads are subsequentially applied, and a new state of equilibrium is encountered. The procedure has to follow an incremental-iterative scheme, in which displacements and stresses are calculated from the acting loads.

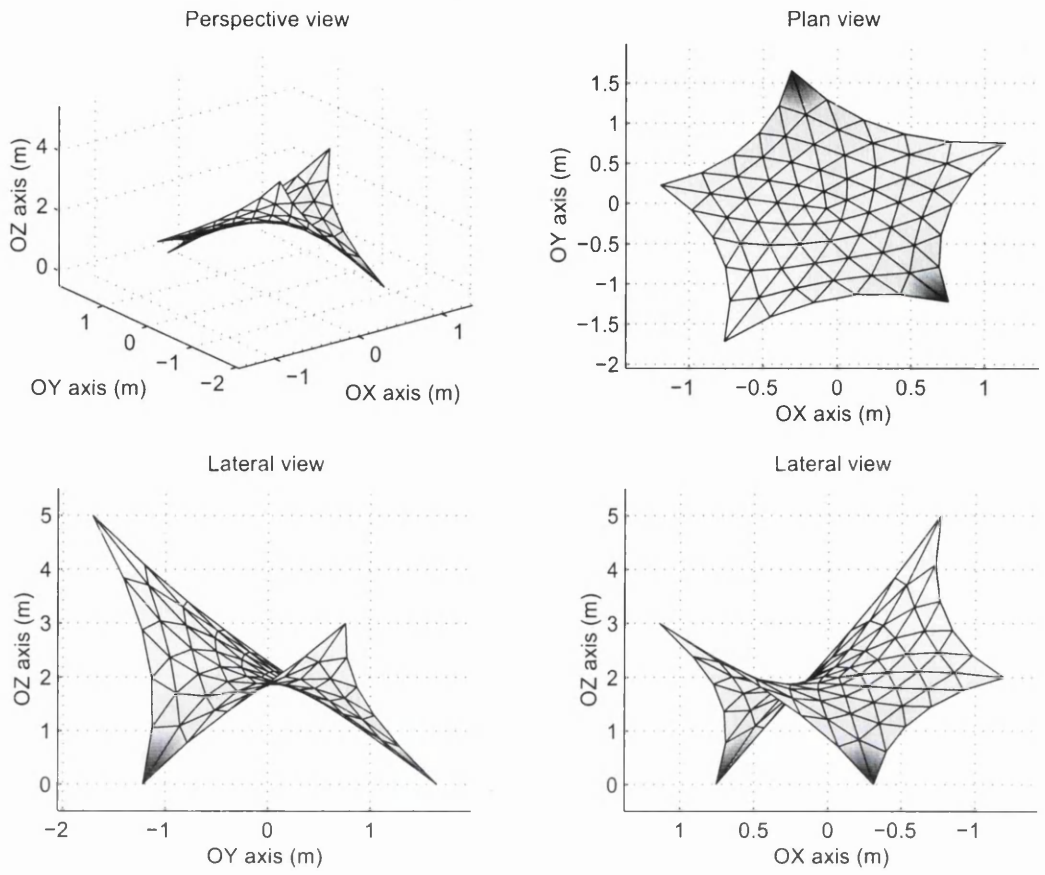

Figure 1.2: Cable reinforced prestressed membrane 2.

Among the wide variety of loads that can be applied on a cable reinforced prestressed membrane, two main categories can be underlined:

- Prestressed loading, which is applied with the purpose of serving the role of maintaining an equilibrium geometry for further calculations.
- In-service loading, where a diverse group of loads can be framed, namely, snow loading, wind loading, live loading, dead loading and so on.

1.2 State of the art.

Tension structures -cable networks and prestressed membranes, form part of a newly and increasing structural technology, which is enabling architects and civil engineers to develop new structural models. These designs are often characterized by their elegance and austerity. These structures, whose main trait is its small thickness, can adopt varied spatial geometries. Indeed, beautiful designs can be observed in Otto (1962), Otto (1967), Ishii (1995), Berger (1996), Majowiecki (1998), Berger (1999), Engel (2001) and Iványi (2002). In Hildebrandt and Tromba (1990), an interesting dissertation about living organisms with membrane morphology can be found.

Fabrics for tension membranes are usually constructed from natural fibers such as cotton (canvas fabric), ceramics (glass fibre) and synthetic organic fibers such as polyester. In order to improve waterproofing and durability, a range of plastic coatings has been developed:

- PVC (polyvinyl chloride) coated polyester.
- PTFE (polytetrafluorethylene) coated glass fibre.
- Silicone-coated glass.

A survey of tension membrane materials can be encountered in References such as Murcia (1990), Monjo (1991), Shaeffer (1996) and Lewis (1998). The small thickness of these structures combined with the use of low specific weight materials for their construction, entail a considerable decrease of the acting dead loads. This results in structures with a great performance to cover large unobstructed areas. Some authors, interested in their optimization, have reported some upshots, such as Sindel et al. (2001). To manifest neatly this issue, the literature -see Magara and Okamura (1986), Schlaich et al. (1990), Ando et al. (1999), Hangai and Wu (1999), Saitoh and Okada (1999), Ando et al. (2000), Saitoh and Okada (2001) and Schlaich (2002)- is replete of numerous structural applications showing tension membranes either isolated or combined with some other structural models, such as rigid frames or cable networks, among others. On the other hand, pneumatic structures are described in Herzog (1977).

The term membrane is quite generic and used to describe compositions of extremely thin sheets to form into flat or curved surfaces. They transmit loads to the supporting medium by means of planar direct and shear stresses. Their bending and transverse shear rigidities are negligible. Even though reinforced and prestressed concrete membranes, subjected to compression stresses, can be included into this category, their study exceeds the scope of this thesis.

Nevertheless, as an initial approach to the phenomenon and to gain progressive insight on the knowledge of these structures, it is worthwhile to point out References Tonda (1973), Courbon (1981), Jiménez Montoya et al. (1994) and Quintas Ripoll (1996). All these authors employ the small displacements linear elasticity theory, namely, a linear relationship between the Cauchy stress tensor $\boldsymbol{\sigma}$ and the linearized strain tensor $\boldsymbol{\epsilon}$[1]. Some other bibliographic sources are Torroja (1991), Candela (1994), M.O.P.T.M.A. (1994) or Sanz (1999), devoted to the study of anticlastic surfaces -those with negative Gaussian curvature-, specially hyperbolic paraboloids. In all of these cases, the analyzed membranes must behave rigidly, in such a way that displacements can be regarded as negligible. In so doing, initial and final membrane shapes can be identified as identical.

[1]This relationship is commonly formulated in index notation as $\sigma_{ij} = \mathcal{C}_{ijkl}\epsilon_{kl}$, where $\epsilon_{kl} = \frac{1}{2}(u_{k,l} + u_{l,k})$. The fourth order tensor $\mathcal{C}_{ijkl}$ gathers the constitutive elastic moduli.

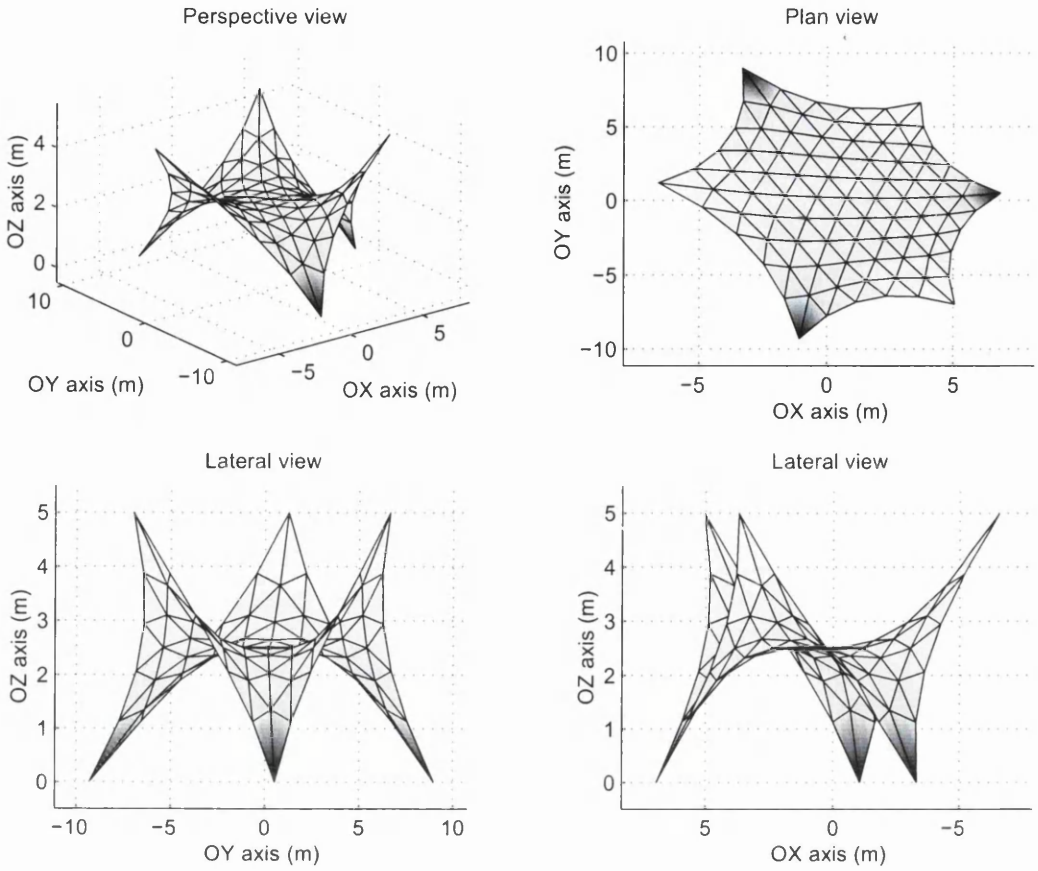

Figure 1.3: Cable reinforced prestressed membrane 3.

As a second approximation, the moderate displacements-small strain linear elasticity theory was used by authors such as Timoshenko and Woinowsky-Krieger (1959), Ramaswamy (1982) and Farshad (1992). The equilibrium equations are established on the final, yet unknown, displaced configuration which does not coincide with the initial unstressed configuration. This ends up in the inclusion of a geometrical nonlinearity within the problem.

Finally, and as a third approach, the theory of hyperelastic membranes, as for example, propounded by Otto (1967), Green and Zerna (1968) or Leonard (1988) treats the problem from an exact analytical viewpoint[2], arriving after complex algebraic manipulations to final formulae of difficult application. Some simplicity, although not much, may be accomplished if the Von Karman compatibility equations[3] are used -see Timoshenko and Woinowsky-Krieger (1959) and Crisfield (1991a). Regardless of the important implications of this approach into the theoretical understanding

[2]Covariant and contravariant coordinates are employed to describe the kinetics and kinematics of the process over curved surfaces.

[3]For comparison purposes, under a cartesian framework, the component 11 of the finite strain tensor might be formulated as $E_{11} = \frac{\partial u}{\partial X} + \frac{1}{2}((\frac{\partial u}{\partial X})^2 + (\frac{\partial v}{\partial X})^2 + (\frac{\partial w}{\partial X})^2)$; whereas, according to Von Karman, this expression can reduced to simply: $E_{11} = \frac{\partial u}{\partial X} + \frac{1}{2}(\frac{\partial w}{\partial X})^2$. As seen, transverse displacements w play a predominant role on the strain.

of these structures, a main disadvantage is that it results in a nonlinear partial differential equations of impossible analytical solution.

Because of this lack of numerical results, variational approaches ought to be taken into consideration as the best route to provide feasible solutions from a practical standpoint. The Galerkin approach, semidiscretized by means of the Finite Element Method (FEM), seemingly provides the best results[4]. Since its practical introduction in the papers by Turner et al. (1956) and Turner et al. (1960), a large amount of research has been devoted to this technique -see Felippa (2000) for a historical revision of the method-. Important non-linear applications of the method were initially those carried out by Oden (1967), Mallett and Marcal (1968), Oden and Key (1973) or Rajasekaran and Murray (1973).

The structural analysis of tension membranes is usually divided into two different stages, according to the loads acting on the membrane, namely, prestressed loading or live loading. The first of the former stages, commonly known as *form finding problem*, addresses the question of the surface geometry of a fabric tensioned between given boundaries -see Ramm (1992). According to Levy and Spillers (1995), different computational methods can be regarded in this category:

1. *"Force density method"*, where Linkwitz (1999) reviews the method proposed by himself in 1971.

2. *"Grid method"*, which is a slight modification of the above method, initiated by Siev and Eidelman in 1964 and formally presented by Levy and Spillers (1998).

3. *"Smoothing method"*, initiated by Haber and Abel (1982a) and Haber and Abel (1982b); it has been studied by different authors: Barnes (1988), Motro et al. (1994), Lewis and Lewis (1996) and Canner and Hsu (1999).

The first two of the above methods result in a spatial discretized system of algebraic linear equations, whereas the latter corresponds to a final nonlinear system of equations. All of the mentioned techniques were developed for cable networks. Nonlinear extrapolations in case of dealing with prestressed membranes were tackled in Kwun et al. (1994), Maurin and Motro (1998) and Nouri-Baranger (2002). A novel approach is the one due to Bletzinger (1997), termed the *Updated Reference Strategy (URS)*, improved in Bletzinger and Ramm (2001) and Bonet and Mahaney (2001).

This shape finding problem has been usually related to the search for optimum or minimal surfaces, whose basics are detailed in Hildebrandt and Tromba (1990), Castellano (1995), Do Carmo (1995) or Quesada (1996). Numerical applications are reported in Maurin and Motro (1997), Maurin and Motro (1997) and Zhang and Tabarrok (1999).

[4]This is due to the elliptic pattern of the involved structural problem -see Bathe (1996).

Once an initial equilibrium shape is obtained, the analysis of the membrane under external loads must be carried out. Numerous results have been published so far in the scientific literature, embodying different topics of the matter. Traditionally, cables were adopted as the initial structural, starting from which the overall prestressed membrane could be deployed. The analytical study of cables themselves is reviewed in Irvine (1981), Buchholdt (1985), Broughton and Ndumbaro (1994), Kadlcak (1994) and Gil (2001). Combination of cables to result in complex cable networks designs were studied by Argyris and Scharpf (1972), Peyrot and Goulois (1979), Monforton and El Hakim (1980), Jayaraman and Knudson (1981), Gründig and Bahndorf (1988), Swaddiwudhipong et al. (1989), Stefanou et al. (1994), Recuero (1994), Kwan (1998), Kebiche et al. (1999), Talvik (2001) and Arcaro (2001a). The Finite Element Method or a simple matrix analysis were the numerical schemes followed to achieve numerical outcomes. In all of theses approaches, a geometrically non-linear analysis, yet not complete, was undertaken. Indeed, the nonlinearity source is reproduced by means of a pseudo-geometric stiffness matrix which treats to incorporate some of the nonlinear effects of the analysis.

Some References -see Coyette and Guisset (1988) and Ashmawy et al. (1997)-, although presenting the problem in a finite element discretization basis, prefer to use first order iterative methods -conjugate gradient method- to find displacements and stresses in cable networks designs. An energetic approach is carried out by Gosling (1998) and a very technical exposition of nonlinear effects is gathered in Leu and Yang (1990). Nevertheless, the dynamic relaxation approach can be considered as the one mostly used by the scientist community: Brew and Brotton (1971), Lewis and Jones (1984), Barnes (1988) and Ramesh and Krishnamoorthy (1995).

A more sophisticated approach has treated the problem of finite hyperelasticity set on rubberlike membrane materials by means of the Finite Element Method. By following this path, interesting papers are those due to Oden and Sato (1967), Grutmann and Taylor (1992), Souza et al. (1995), Wu et al. (1996) and Taylor (2001), where initially unstressed membranes are analyzed when undergoing large strains take place. For these cases, the Updated Lagrangian Formulation (ULF) is considered to be the most suitable for the derivation of the tangent stiffness matrix. The three-noded isoparametric finite element is the most commonly employed to run the analyses. However, an alternative quadratic rectangular isoparametric element is developed in Gosling and Lewis (1996a) and Gosling and Lewis (1996b).

A local cartesian coordinate system was used as the basis to describe the kinematic of the deformation process. Nevertheless, some other concepts, such as natural coordinates -see Arcaro (2001b)- or convective coordinates -see Bonet and Mahaney (2001)- have been reported.

All these analyses were built up on the basis of membranes undergoing large strains, due to which hyperelastic models such as *Mooney-Rivlin* or *Neo-Hookean* were regarded. In Crisfield (1991b), Bonet and Wood (1997) and Holzapfel (2000) a survey of these materials is discussed. Despite of being of great concern in Biomechanics -see Humphrey (1998), this sort of membranes lack of application in Ar-

chitecture or Civil Engineering. In these situations, moderate strains are expected at most. Some authors have reported some results, namely, Sastre (1986), Tabarrok and Qin (1992), Levy and Spillers (1995), Jufen and Wanji (1997), Wakefield (1999) and Levy and Gal (2001). Nonetheless, all these References present two common features: the analysis is started from an initial unstressed configuration and a possible combination of cables and textile fabric is not conceived in advance.

Another topic of major concern in the actual design of this sort of structures is the correct treatment of the wrinkling phenomenon. Numerous authors have worked intensively in this field, some examples are: Miller et al. (1985), Roddeman et al. (1987a), Roddeman et al. (1987b), Steigmann and Pipkin (1989), Tabarrok and Qin (1992), Kang and Im (1997), Kang and Im (1999), Lu et al. (2001) and Stanuszek (2003). However, by following previous work by Mahaney (2002), a simple and efficient technique can be introduced.

1.3 Scope of the thesis.

The main aim of this thesis is the development of a complete analytical, numerical and computational methodology to deal with cable reinforced prestressed membranes. The simplicity acquired as a consequence of the reduced thickness as well as the spectacular spatial designs, enrich the beauty of the overall structure and, moreover, the calculation's difficulty.

A large number of tensioned membranes are reinforced by means of interior and perimeter cables. At the same time, compressive rigid members such as masts, are assembled with the global structure in order to provide the adequate stability. Conventional analysis and design is usually separated into two stages; initially by fixing the supports and determining the equilibrium shape of the cable-membrane and then, by checking the compressive members' resistance with respect to the reactions.

A proper approach adopted in this research is to consider membrane fabric, cables and compressive members in a single unified interactive manner. Consequently, the prestressed configuration is determined computationally exactly as in reality by stretching the cables or moving the supports. In the same way, realistic boundary conditions such as elastic foundations, or admissible loading conditions such as thermal effects or nonconservative forces, must be added to the analysis. The analysis will focus on those structural membranes undergoing large deformations though moderate strains, which is suitable for Civil Engineering applications. In addition, the formulation considers wrinkling. Finally, it remains necessary to compute a nominally stressed initial configuration, conventionally determined by form finding relying on classical methods such as the Force Density Method -see Linkwitz (1999)- or the Updated Reference Strategy -see Bletzinger and Ramm (2001).

Essentially, the motion of a prestressed membrane is governed by two physical laws, namely, the continuum equilibrium equations and the material constitutive

equation. Since static analysis will be just of main concern in this research, inertia effects can be ignored. The resulting equilibrium equations describe the balance at each point of the membrane between the internal stresses and the applied external forces. The constitutive equations, on the other hand, provides a relationship between the stresses and the strains of the membrane. Unfortunately, due to the complex and non-linear nature of the process, finding the motion of the membrane that satisfies both governing laws is practically impossible from an analytical standpoint.

In order to overcome theses drawbacks, the Finite Element Method can be used to approximate the motion of the membrane. In this case, a variational formulation will enable the equilibrium equations to be discretized at each node, according to a Lagrangian mesh, as the balance between equivalent external and internal nodal forces. To describe appropriately the non-linear nature of the phenomenon, kinetic and kinematic tensorial entities will be introduced for the sake of a better physical description of the problem.

Although membrane analysis for rubber-like materials based on Updated Lagrangian formulations have been fully studied in diverse References such as Bonet et al. (2000), a more suitable Total Lagrangian Formulation (TLF) for prestressed structural membranes has not been reported so far. The kinematics of prestressed membranes can be described by means of three successive configurations, namely, a nominally stressed initial equilibrium state $\Re_0$, a prestressed state $\Re_{pret}$ and a final in-service state $\Re$, for the time instants t^0, t^{pret} and t, respectively.

Among the wide group of available hyperelastic materials, the most adequate constitutive model to describe moderate strain behavior, is the *Saint Venant-Kirchhoff model*. By following its definition, the Helmholtz's free energy functional or strain energy functional w_{int} is a potential for the second Piola-Kirchhoff stress tensor $\mathbf{S}$. Therefore, a Taylor expansion of the former in terms of the Green-Lagrange strain tensor $\mathbf{E}$, combined with the assumption that the strain range can be assumed as moderate, enables the constitutive law for a prestressed hyperelastic Saint Venant-Kirchhoff material to be written in a simple manner[5].

Another physical feature that has to be taken into account when analyzing tension membrane structures, is the likelihood of developing wrinkles. These are manifestations of localized buckling regions which can appear across the membrane's spatial domain on account of an unexpected combination of the prestressing load with a certain in-service load situation. When any of the eigenvalues of the Cauchy stress tensor becomes null, the membrane -or cable- does not offer any resistance to be deformed any further along the corresponding principal direction. As a consequence, it can be argued that the energy functional acts as an adequate potential for the stress tensor in case of a pure tension material, otherwise it cannot be accepted as valid. The reason for this is based upon the fact of its lack of capacity to represent efficiently wrinkling conditions whatsoever.

[5]Appendix D reviews the fundamentals of continuum mechanics.

By following previous work by Mahaney (2002) and Gil (2003b), wrinkling conditions in terms of the Euler-Lagrange finite deformation tensor along principal directions will be obtained -see Gil and Bonet (2004). This will provide a framework to describe properly the initial instant when wrinkles start to be encountered. Subsequently, a modified Helmholtz's free energy functional will be introduced with the purpose of describing in an alternative manner the constitutive behaviour of the continuum medium after the moment of wrinkling.

The final set up problem may be understood as a classical unconstrained optimization problem for an objective functional which results to be the Total Potential Energy (TPE). As a consequence, any appropriate technique may be used to carry out this mathematical optimization, i.e., see Luenberger (1989). Apart from the well known second order Newton-Raphson method, other first order procedures such as the steepest descent method, the Polak-Ribiere method or the Fletcher-Reeves method can be employed, along with parametric line searches, as valid alternatives when convergence is not accomplished in the former case. This results in a very flexible numerical solver.

1.4 Layout of the thesis.

To achieve the scientific objectives detailed in the previous section, this thesis will be divided into different chapters which are outlined as follows:

- ***Chapter II*** reviews firstly the strong formulation of a structural problem starting from an initial unstressed configuration. Then, the same formulae will be presented when considering a prestressed configuration as the initial state. Concepts such as Green-Lagrange strain tensor, Piola-Kirchhoff or Cauchy stress tensors are introduced as basic tensorial tools to carry out the forthcoming numerical approach. Analogously, the Helmholtz's free energy functional or strain energy functional is defined for later calculations. The consideration of the Saint Venant-Kirchhoff hyperelastic material as the adopted model will be of great effect to end up with a linear constitutive relationship of easy implementation. The constitutive equations for hyperelastic materials can be found in Bonet and Wood (1997) or Holzapfel (2000).

- In ***Chapter III***, the weak formulation of the problem is developed by means of a Galerkin approach or, equivalently, by the Principle of Virtual Work. Some interesting References are Crisfield (1991a), Zienkiewicz and Taylor (1995), Bathe (1996) and Belytschko et al. (2000).

- The ***Chapter IV*** entails a comprehensive explanation of the Finite Element semidiscretization of the previously obtained weak form. After this weak form is derived in a straightforward manner, the displacement field is interpolated by means of shape functions based on a Lagrangian mesh geometry -see

Zienkiewicz (1982), Cook et al. (1989), Oñate (1995) and Smith and Griffiths (1998)-. A non-linear formulation is presented in Wood and Schrefler (1978) and Schrefler et al. (1983). The resulting formulation will be the so called Total Lagrangian Formulation (TLF). Afterwards, the exact linearization of the Total Lagrangian weak form of the momentum balance is carried out in detail. For the sake of further computing implementation reasons, the Direct Core Congruential Formulation (DCCF) is reviewed as the most appropriate one -see Felippa (2001).

- The ***Chapter V*** summarizes the DCCF for cable elements and membrane elements -isoparametric two-noded and three-noded finite elements. Numerical entities such as equivalent internal or external nodal forces vector, equivalent residual nodal forces vector, material stiffness matrix, geometric stiffness matrix, total tangent stiffness matrix or strain energy functional will be derived.

- ***Chapter VI*** discusses the concept of non-conservative forces or follower loads, specially useful when incorporating wind loads into the analysis in a pseudo-static manner. References such as Simo et al. (1991) and Belytschko et al. (2000) review this concept.

- ***Chapter VII*** will present an efficient numerical technique for the computational simulation of wrinkles in a prestressed membrane. Wrinkling conditions in terms of the Euler-Lagrange finite deformation tensor along principal directions will be obtained. This will provide a framework to describe properly the initial instant when wrinkles start to be encountered in a prestressed Saint Venant-Kirchhoff hyperelastic membrane. Subsequently, a modified Helmholtz's free energy functional will be introduced with the purpose of describing the modified constitutive behaviour of the continuum after the onset of wrinkling. Consistent derivations of the stress tensor as well as the constitutive tensor will de depicted. We should point out References such as Pipkin (1986), Liu et al. (2001) or Contri and Schrefler (1988).

- ***Chapter VIII*** studies the fundamentals and main algorithms pertaining to nonlinear optimization, implemented to solve the geometrically nonlinear problems which appear in this research. Authors such as Bergan (1980), Luenberger (1989), Haftka and Gürdal (1992), Samartín (1993), Kelley (1995), Dennis Jr. and Schnabel (1996) and Castillo and et al. (2002) have presented some results about them. With the objective of giving a complete and robust formulation to analyze the whole structural problem, a variational approach in terms of the Total Potential Energy functional (TPE) is introduced. Thus, the chapter introduces the different numerical algorithms that based upon incremental-iterative schemes are used in the present research. Some mathematical techniques are taken from Dahlquist et al. (1969), Burden and Douglas (1998), Krasnov et al. (1994) and Rade and Westergren (1999).

- ***Chapter VIII*** examines the developed computational implementation, according to a modular Architecture, by following the advice in Gaylord and Gaylord (1990). The computational languages which have been used to perform the computer code are: Fortran 90-95 and Matlab. See Smith (1995), MathWorks (1996), Nyhoff and Leestma (1997), Chapman (1998) and Pérez (1999) for further details.

- ***Chapter IX*** validates the methods presented in the previous chapters by comparing the numerical predictions with the ones shown in the existing literature. Different examples of cable networks as well as prestressed membranes will be analyzed.

- ***Chapter IX*** reveals the flexibility and robustness of the procedure, by means of a complete assemblage of fabric textile, reinforcing cables and rigid members which will be analyzed from its initial design stage to its final loaded configurations. Pseudo-static analysis will be run for snow and wind conditions according to Spanish standards.

- ***Chapter X*** concludes the thesis by summarizing the main points and indicating areas of further research.

- Finally, some ***appendices*** will be added with the purpose of reviewing some interesting concepts such as: tensor analysis, nonlinear continuum mechanics, graphs theory, nonlinear programming fundamentals and some key derivatives when dealing with wrinkling analysis. Some References of interest are Lichnerowicz (1962), Timoshenko and Goodier (1968), Malvern (1969), Santaló (1969), González de Posada (1983), Sokolnikoff (1987), Díaz del Valle (1989), Truesdell and Noll (1992), París (1996), Bonet and Wood (1997) or Chadwick (1999).

Part II

General Formulation of the problem

Chapter 2

Strong Formulation

2.1 Introduction.

The numerical resolution of any structural problem by means of a computational technique is comprised of four successive stages:

1. Posing the boundary value problem (BVP), which consists of the system of partial differential equations along with the boundary conditions. This stage is named **Strong Formulation**.

2. Posing the *Principle of Virtual Work* or *Principle of Virtual Power* to obtain the **Weak Formulation** of the problem.

3. Posing the space-time numerical scheme in order to transform the continuum problem into a discrete problem.

4. Computational implementation, whereby the mathematical formulation of the discretized problem is converted into a computer code by means of an algorithmic language.

This chapter is organized as follows. Sections 2 and 3 will summarize the conservation equations or balance laws of a continuum in terms of Eulerian and Lagrangian formulations, respectively. No attention will be devoted at this moment, towards the required continuity and boundary conditions, either Dirichlet, Neumann or mixed conditions. The following section will present in detail the strong formulation of the structural problem: prestressed membranes with immediate applications in Civil Engineering. The membranes will be considered to undergo large displacements but moderate strains. Therefore, nonlinear continuum mechanics principles dealing with large deformations on prestressed bodies will be accounted for. The constitutive model adopted for the material will be a prestressed Saint Venant-Kirchhoff hyperelastic one.

For a better understanding of this chapter, the inclusion of the appendix D has been considered very convenient, where the basics of nonlinear continuum mechanics are displayed in a brief manner.

2.2 Eulerian formulation of the balance laws.

The conservation equations of a continuum can be formulated in an Eulerian manner and in a local level as follows[1]:

1. Mass conservation.

$$\frac{D\rho}{Dt} + \rho div(\mathbf{v}) = 0 \qquad \dot{\rho} + \rho \frac{\partial v_i}{\partial x_i} = 0 \tag{2.1}$$

[1]To pose the forthcoming equations, the chain rule, Reynolds's transport theorem as well as Gauss-Ostrogowdski theorem have to be employed in a systematic manner -see Timoshenko and Goodier (1968), Green and Zerna (1968), Malvern (1969), Díaz del Valle (1989), Truesdell and Noll (1992), Chadwick (1999) and Holzapfel (2000).

2. Linear momentum conservation.

$$\rho \frac{Dv_i}{Dt} = \frac{\partial \sigma_{ji}}{\partial x_j} + \rho b_i \qquad \rho \frac{D\mathbf{v}}{Dt} = div(\boldsymbol{\sigma}) + \rho \mathbf{b} \tag{2.2}$$

3. Angular momentum conservation.

$$\sigma_{ij} = \sigma_{ji} \qquad \boldsymbol{\sigma} = \boldsymbol{\sigma}^T \tag{2.3}$$

4. Energy conservation (First law of Thermodynamics).

$$\rho \frac{Du_{int}}{Dt} = D_{ij}\sigma_{ij} \qquad \rho \dot{u}_{int} = \mathbf{D} : \boldsymbol{\sigma} \tag{2.4}$$

where:

ρ represents the continuum's density at time t.

$\frac{D(.)}{Dt}$ is the total or material derivative operator.

$\mathbf{v}$ symbolizes the velocity field.

$\mathbf{b}$ stands for the body force field acting per unit of mass.

$\boldsymbol{\sigma}$ represents the real or Cauchy stress tensor.

$\mathbf{D}$ represents the strain rate tensor or the symmetric part of the velocity gradient tensor.

u_{int} is the functional which represents the internal strain energy accumulated in the continuum per unit of mass.

Note that in the above equations and in what follows the Einstein's convention for the summation of repeated indices has been adopted. From the above equations, some considerations must be pointed out:

- The real or Cauchy stress tensor $\boldsymbol{\sigma}$ is a symmetric tensor, which is deduced for the angular momentum conservation law.
- The Cauchy stress tensor $\boldsymbol{\sigma}$ and the strain rate tensor $\mathbf{D}$ constitute a conjugate pair for the internal power, that is, their contracted product gives the rate of change of internal energy.
- The energy conservation law has been obtained neglecting possible thermal effects, that is, only mechanical processes were considered.

2.3 Lagrangian formulation of the balance laws.

For the prospective structural analysis carried out in this research, the formulation of the balance laws in a Lagrangian description results to be even more fundamental. These equations can be depicted as follows:

1. Mass conservation.

$$\rho(\mathbf{X},t)J = \rho_0(\mathbf{X}) \qquad \rho J = \rho_0 \tag{2.5}$$

2. Linear momentum conservation.

$$\rho_0 \frac{\partial v_i(\mathbf{X},t)}{\partial t} = \frac{\partial P_{ji}}{\partial X_j} + \rho_0 b_i \qquad \rho_0 \dot{\mathbf{v}} = \nabla_0 \cdot \mathbf{P} + \rho_0 \mathbf{b} \tag{2.6}$$

3. Angular momentum conservation.

$$F_{ik}P_{kj} = F_{jk}P_{ki}, \qquad S_{ij} = S_{ji}; \qquad \mathbf{F}\cdot\mathbf{P} = \mathbf{P}^T\cdot\mathbf{F}^T, \qquad \mathbf{S} = \mathbf{S}^T \tag{2.7}$$

4. Energy conservation (First law of Thermodynamics).

$$\rho_0 \frac{\partial u_{int}}{\partial t} = \frac{\partial F_{ji}}{\partial t} P_{ij} = \frac{\partial E_{ij}}{\partial t} S_{ij} \qquad \rho_0 \dot{u}_{int} = \dot{\mathbf{F}}^T : \mathbf{P} = \dot{\mathbf{E}} : \mathbf{S} \tag{2.8}$$

where, apart from the entities already defined in the previous section, new magnitudes arise which are known as follows:

ρ_0 represents the continuum's density at the initial configuration.

$\mathbf{F}$ represents the deformation gradient tensor.

J is the jacobian of the transformation or determinant of the deformation gradient tensor $\mathbf{F}$.

$\nabla_0 \cdot$ represents the divergence operator respect to the material coordinates $\mathbf{X}$.

$\mathbf{P}$ represents the nominal stress tensor, which is also known as the transpose of the First-Piola Kirchhoff stress tensor.

$\mathbf{S}$ stands for the second Piola-Kirchhoff stress tensor.

As in the former section, some keypoints must be remarked:

- The symmetrical feature of the second piola-Kirchhoff stress tensor $\mathbf{S}$. This is not the case of the nominal stress tensor $\mathbf{P}$.
- With respect to the internal power, two different conjugate pairs can be set up, namely, the nominal stress tensor $\mathbf{P}$ with the transpose of the ratio of the deformation gradient tensor $\dot{\mathbf{F}}^T$, and the second Piola-Kirchhoff stress tensor $\mathbf{S}$ with the ratio of the Euler-Lagrange strain tensor $\dot{\mathbf{E}}$.
- Once again, thermal effects were neglected when deriving the energy conservation equation.

2.4 Constitutive model.

Apart from the equilibrium and compatibility equations, in order to establish correctly the strong formulation of the problem, constitutive equations must be taken into consideration. This set of equations relates stresses and strains in a specific way according to the selected material's constitutive model. With the purpose of defining mathematically these equations, a multiaxial elastic model will be chosen.

The final constitutive relationship must satisfy independency with respect to rigid body motions, namely, translation and rotation. Equivalently, the mentioned relationship must be identical for two inertial observers. This principle is the so called *principle of material objectivity or frame indifference.* For a detailed and precise explanation of this principle, References Malvern (1969), Chadwick (1999), Belytschko et al. (2000) and Holzapfel (2000) are strongly recommended.

In particular, this research will be focused on those materials known as **hyperelastic**[2], a subset of the *Cauchy elastic materials*, or simply, *elastic materials.* This latter group is comprised of those materials in which the current stress state does not depend on the strain history, but only on the current strain state. On the other hand, the former group consists of those materials in which the Helmholtz's free energy functional[3], or simply, the strain energy functional, is independent on the strain or load history. On account of this fact, the Helmholtz's free energy functional can be expressed as a potential for the stress tensor as follows:

$$\mathbf{S} = \frac{\partial w_{int}(\mathbf{E})}{\partial \mathbf{E}}, \qquad S_{ij} = \frac{\partial w_{int}}{\partial E_{ij}} \tag{2.9}$$

where:

1. $\mathbf{S}$ stands for the second Piola-Kirchhoff stress tensor.

2. $\mathbf{E}$ represents the Green-Lagrange strain tensor.

3. w_{int} symbolizes the functional which stores the internal strain energy per unit initial volume, where $w_{int} = \rho_0 u_{int}$, according to equation (2.4).

This hyperelastic material is, roughly speaking, nothing more than a generalization for $\mathbf{R}^3$ of one-dimensional elasticity's principles. Therefore, the stress state depends exclusively on the current strain state. In addition to that, loading and unloading curves are identical, that is, no hysteretical processes are developed. Furthermore, the strains are reversible. The above mentioned characteristics have direct implications into the Helmholtz's free energy functional's features, namely, the latter is independent on the strain history, reversible and non-dissipative.

Moreover, according to the polar decomposition theorem, the deformation path of a material body, can be well known split into two successive deformation states,

[2]These materials are also known as *Green-elastic materials.*

[3]A complete definition and derivation of this energy functional can be found in Holzapfel (2000).

namely, a rigid body movement followed by a strain process or viceversa. This theorem is summarized in a formula which is given as:

$$\mathbf{F} = \mathbf{R} \cdot \mathbf{U} \quad \text{or} \quad \mathbf{F} = \mathbf{V} \cdot \mathbf{R} \tag{2.10}$$

where:

1. $\mathbf{F}$ is the deformation gradient tensor.
2. $\mathbf{R}$ stands for any rigid body rotation.
3. $\mathbf{U}, \mathbf{V}$ are tensors which represent the arisen internal strain, namely, stretches along principal directions.

Numerous engineering applications and, in particular, the one which is of concern throughout this research, namely, prestressed membranes, undergo moderate strains in spite of being subjected to large deformations. This means that the major contribution to the deformation gradient tensor comes from its rotating component. The behaviour of these specific materials is completely gathered by means of a mere extension of the small deformations linear-elastic law[4]. As a result of this, the constitutive equations of this sort of hyperelastic materials, known as *Saint Venant-Kirchhoff* materials, or simply, *Kirchhoff* materials, turn out to be:

$$S_{ij} = \mathcal{C}_{ijkl} E_{kl} \qquad \mathbf{S} = \boldsymbol{\mathcal{C}} : \mathbf{E} \tag{2.11}$$

As can be noted from comparing equation (2.11) with the classical small deformations linear-elastic constitutive equation, the second Piola-Kirchhoff stress tensor $\mathbf{S}$ and the Green-Lagrange strain tensor $\mathbf{E}$ have been substituted for the Cauchy stress tensor $\boldsymbol{\sigma}$ and the small strain tensor $\boldsymbol{\epsilon}$, respectively.

Furthermore, the Helmholtz's free energy functional for this particular constitutive model yields:

$$w_{int} = \frac{1}{2} S_{ij} E_{ij} = \frac{1}{2} \mathcal{C}_{ijkl} E_{kl} E_{ij} \qquad w_{int} = \frac{1}{2} \mathbf{S} : \mathbf{E} = \frac{1}{2} \mathbf{E} : \boldsymbol{\mathcal{C}} : \mathbf{E} \tag{2.12}$$

Within the Saint Venant-Kirchhoff hyperelastic materials, this investigation will deal with those associated with an isotropic response. Hence, equation (2.11) can be rewritten in terms of the Lamé constants λ and μ in the following manner:

$$S_{ij} = \lambda E_{kk} \delta_{ij} + 2\mu E_{ij} \qquad \mathbf{S} = \lambda \mathrm{tr}(\mathbf{E}) \mathbf{I} + 2\mu \mathbf{E} \tag{2.13}$$

Analogously, the above formula can be expressed as a function of the classical engineering constants, namely, Young modulus E and Poisson ratio ν, which can be related to the aforementioned parameters λ and μ as follows:

[4] In the case of the small deformations theory, the Cauchy stress tensor $\boldsymbol{\sigma}$ is obtained through a linear transformation of the small strain tensor $\boldsymbol{\epsilon}$ as follows: $\sigma_{ij} = \mathcal{C}_{ijkl} \epsilon_{kl} = \mathcal{C}_{ijkl} \frac{1}{2} \left(\frac{\partial u_k}{\partial x_l} + \frac{\partial u_l}{\partial x_k} \right)$.

$$\lambda = \frac{\nu E}{(1+\nu)(1-2\nu)} \qquad \mu = \frac{E}{2(1+\nu)} \tag{2.14}$$

Among the wide variety of membrane structures, other interesting applications can be found specially within the field of Biomechanics. In this case, the membranes undergo large strains allocated in the tensors $\mathbf{U}$ and $\mathbf{V}$. To describe properly this sort of behaviours, within the group of hyperelastic materials, alternative constitutive models arise as more suitable, either *Ogden*, *Money-Rivlin* or *Neo-Hookean* materials. In References Crisfield (1991b), Bonet and Wood (1997) and Holzapfel (2000), their basics are explained in a comprehensible fashion. In addition to that, several numerical applications can be encountered in Oden and Sato (1967), Grutmann and Taylor (1992), Souza et al. (1995), Wu et al. (1996), Bonet et al. (2000) and Mahaney (2002).

2.5 Finite Hyperelasticity theory in initially prestressed bodies.

The subject of this section is the geometrically nonlinear analysis of prestressed membrane structures with arbitrary geometry undergoing moderate strains. An increasing application of these structural models is reaching extremely different knowledge fields, which move from the well known Architectural field to the recently discovered Biomechanical field. In all these cases, it is feasible to find membranes undergoing large deformations and subjected to a previous state of prestressing. In particular, we will focus on those membranes where strains can be modeled as moderate, despite having large deformations. Two different and successive loading cases may be distinguished according to their effects on the stabilization of the prestressed membrane. The first one or prestressed loading is developed to provide the necessary in-surface rigidity to the membrane to overcome successfully the second loading step. This one, also named as in-service loading conditions is comprised of a wide group of loads: snow, wind or live loads among others.

The aim is to pose separately each one of these two loading stages, not just to simplify the whole formulation but to enable observing the effect of the prestressing into the overall structural response of the membrane. With the purpose of developing the strong formulation of the problem in a neat and explicit manner, the same notation as Iésan (1989) will be followed throughout the remainder of the chapter.

2.5.1 First load step and preliminary results

Let's consider a material body $\mathcal{B}$ in an initial undeformed configuration $\mathbf{B}_0$ with domain Ω_0 frontier $\partial\Omega_0$, defined within the 3D-Euclidean space. The material coordinates of a body's particle at a time $t = 0$ will be described according to $\mathbf{X} = (X_1, X_2, X_3)$. As a result of the application of a displacement field, the current

or spatial position of the body's particle at a time t may be obtained as a function of its material coordinates as[5] $x_i = x_i(X_A, t)$. Therefore, the body will move to a new configuration $\mathbf{B}_t$ with domain Ω_t and frontier $\partial\Omega_t$. See figure 2.1.

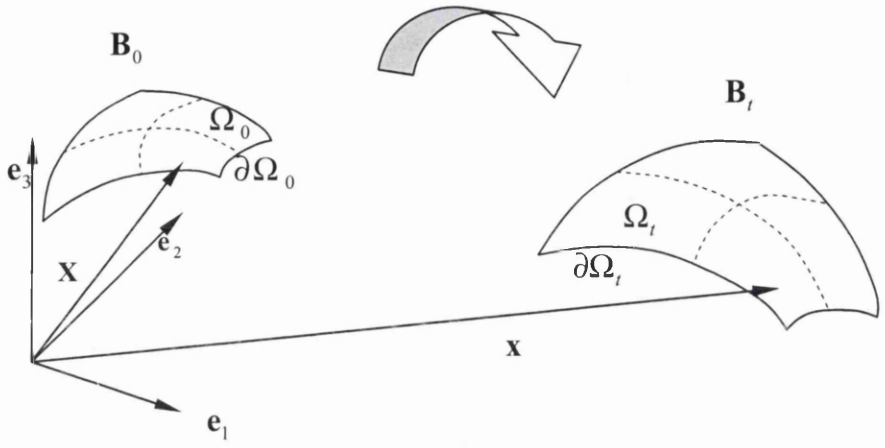

Figure 2.1: Motion of a body.

For convenience here and in what follows the standard summation for repeated indices is adopted, as well as the classical indices' convention to express spatial derivatives: $(\cdot)_{,k} = \frac{\partial(\cdot)}{\partial x_k}$. The balance of linear momentum at a local level, in the absence of inertial effects, may be expressed in Eulerian description as follows:

$$\sigma_{ji,j} + \rho b_i = 0 \ \ in\ \Omega_t, \qquad f_i = t_i d\Gamma = \sigma_{ji} n_j d\Gamma \ \ on\ \partial\Omega_t \tag{2.15}$$

The conservation of linear momentum is set up in the current configuration $\mathbf{B}_t$ of domain Ω_t, and the traction vector $\mathbf{t}$ may be deduced from the Cauchy stress tensor $\boldsymbol{\sigma}$ and the unit normal $\mathbf{n}$ on the frontier $\partial\Omega_t$. Analogously, the equation (2.15) may be obtained in Lagrangian description:

$$P_{Ai,A} + \rho_0 b_i = 0, \ \ in\ \Omega_0, \qquad f_i^0 = t_i^0 d\Gamma_0 = P_{Ai} n_A d\Gamma_0 \ \ on\ \partial\Omega_0 \tag{2.16}$$

In this case, the conservation of linear momentum is formulated at a local level in the initial undeformed configuration $\mathbf{B}_0$ of domain Ω_0, and the traction vector is implied from the nominal stress tensor $\mathbf{P}$ and the unit normal $\mathbf{n}$ on the frontier $\partial\Omega_0$. The upper and lower case indices stand for the initial and current configurations, respectively. This makes this stress tensor to be considered as a two-point tensor -see Belytschko et al. (2000), as a difference of the Eulerian consideration of the Cauchy stress tensor. It should be recalled that the nominal stress tensor is the transpose of the so called first Piola-Kirchhoff stress tensor -see Malvern (1969).

Another stress entity must be introduced for the sake of convenience: the second Piola-Kirchhoff stress tensor S_{AB}, which can be framed as a Lagrangian stress tensor. The mathematical relationships among the different enumerated stress tensors,

[5]Capital (A,B...) as opposed to (i,j...) indices have been used in order to clearly distinguish the initial configuration $\mathbf{B}_0$ from any other.

that is, Cauchy, nominal and second Piola-Kirchhoff stress tensors, are shown right below by means of the well known deformation gradient tensor $F_{iA} = x_{i,A}$ and its determinant or jacobian J:

$$J\sigma_{ij} = x_{i,A}P_{Aj} = x_{i,A}x_{j,B}S_{AB} \tag{2.17}$$

where:

$$x_{i,A} = \frac{\partial x_i}{\partial X_A} \tag{2.18}$$

Once the balance of linear momentum equations have been established in the two descriptions par excellence, this is, Eulerian and Lagrangian -formulae (2.15) and (2.16), respectively, another required equation is the one which gives the concept for the Green-Lagrange strain tensor E_{AB} and the right Cauchy-Green strain tensor C_{AB}:

$$E_{AB} = \frac{1}{2}(C_{AB} - \delta_{AB}); \qquad C_{AB} = x_{i,A}x_{i,B} \tag{2.19}$$

In the mathematical description of the material behaviour, the response of the material is characterized by a constitutive equation which gives the stress as a function of the deformation history of the body. For the structures presented in this research, the Saint Venant-Kirchhoff constitutive model can be concluded as the most appropriate for our purpose. Eventually, the formal mathematical formulae for this model may be summarized by using the Helmholtz's free energy functional or internal strain energy functional w_{int} as follows:

$$S_{AB} = \frac{\partial w_{int}}{\partial E_{AB}} = 2\frac{\partial w_{int}}{\partial C_{AB}} \tag{2.20}$$

$$S_{AB} = \mathcal{C}_{ABCD}E_{CD} \tag{2.21}$$

The equations gathered at (2.20) and (2.21) relate the second Piola-Kirchhoff stress tensor with the Green-Lagrange strain tensor by means of a fourth order tensor, known as the material elasticity tensor, which contains all the elastic moduli of the material. Therefore, the classical explicit expression for the strain energy functional per unit of volume would be:

$$w_{int} = \frac{1}{2}\mathcal{C}_{ABCD}E_{AB}E_{CD} \tag{2.22}$$

2.5.2 Second load step: strong formulation

Let's consider now three possible configurations of the material body: in one hand, an initial undeformed state $\mathbf{B}_0$ and, in the other hand, a primary state $\mathbf{B}_t$ and a secondary state $\mathbf{B}_{t^*}$, for the time instants t and t^*, respectively. Among these two stages, a displacement field $\mathbf{u} = (u_1, u_2, u_3)$ may be defined in $\mathbf{R}^3$. From now on,

quantities which proceed from the movement from the primary to the secondary state will be considered as incremental -see figure 2.2. It is thus feasible to obtain the spatial coordinates for the time t^* of a particle as a function of its material coordinates in the initial unstressed configuration B_0 according to $y_i = y_i(X_A, t^*)$.

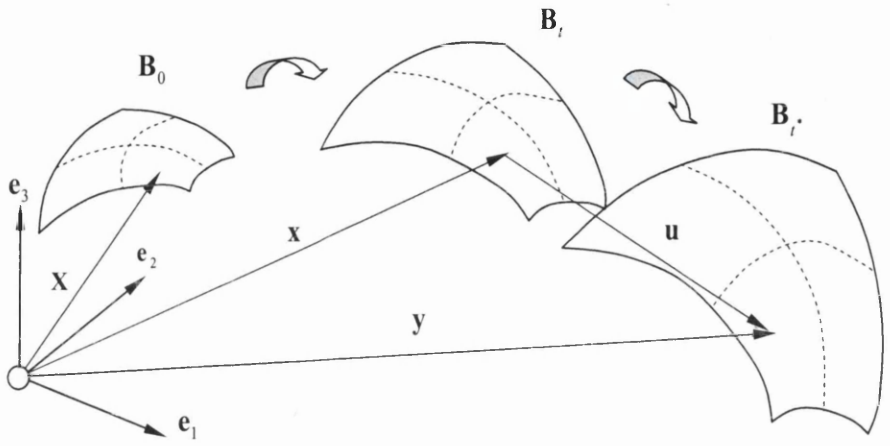

Figure 2.2: Motion of a prestressed body.

As a consequence, the complete deformation path is built up from the composition of two successive steps: the first one, from the initial configuration to the primary state and a second one, which can be traced from the primary state to a secondary state. By recalling the chain rule, relations among deformation gradient tensors can be displayed as follows:

$$\frac{\partial y_i}{\partial X_A} = \frac{\partial y_i}{\partial x_j}\frac{\partial x_j}{\partial X_A} \tag{2.23}$$

Formula (2.23) can be rewritten in index notation as follows:

$$y_{i,A} = y_{i,j}x_{j,A} \tag{2.24}$$

Analogously, the relation between jacobians is given as:

$$J^* = J'J \tag{2.25}$$

where J represents the jacobian at the primary state, J^* stands for the jacobian at the end of the secondary state and J' symbolizes the jacobian as a consequence of the incremental deformation. The scope of the next sections will be to set up the equations presented in the former section for the secondary state by adopting the primary one as the reference configuration -subjected to a previous stress field-.

Green-Lagrange strain tensor

A material particle's position in the primary and secondary states may be expressed in terms of the incremental displacement field as follows:

$$y_i = x_i + u_i \quad \Rightarrow \quad y_{i,A} = x_{i,A} + u_{i,A} = x_{i,A} + u_{i,j}x_{j,A} \tag{2.26}$$

The Green-Lagrange strain tensor for the secondary state is:

$$E^*_{AB} = \frac{1}{2}(y_{i,A}y_{i,B} - \delta_{AB}) \tag{2.27}$$

From (2.26) and (2.27), the Green-Lagrange strain tensor can be rewritten as:

$$E^*_{AB} = \frac{1}{2}(x_{i,A}x_{i,B} - \delta_{AB}) + \frac{1}{2}(2x_{i,A}x_{j,B}e_{ij} + u_{i,A}u_{i,B}) \tag{2.28}$$

where:

$$e_{ij} = \frac{1}{2}(u_{i,j} + u_{j,i}) \tag{2.29}$$

The difference between the Green-Lagrange strain tensor for the primary and secondary states can be obtained as:

$$E^*_{AB} - E_{AB} = x_{i,A}x_{j,B}e_{ij} + \frac{1}{2}u_{i,A}u_{i,B} = x_{i,A}x_{j,B}E'_{ij} \tag{2.30}$$

where:

$$E'_{ij} = e_{ij} + \frac{1}{2}u_{k,i}u_{k,j} \tag{2.31}$$

where the incremental Green-Lagrange strain tensor E'_{ij} has been introduced for the sake of convenience and it represents a relative measure of the strain at the secondary state by taking the primary one as an adequate reference. It should be remarked that this later one is not an unstressed state.

Nominal and second Piola-Kirchhoff stress tensors

As it was introduced formerly, the Eulerian Cauchy stress tensor may be transformed to a Lagrangian and a two-point stress tensor by considering an initial and a current stressed configurations. This two new tensorial entities were referred to as the second Piola-Kirchhoff and nominal stress tensors respectively. By considering as initial configurations the initial undeformed configuration and the primary state configuration, the following formulae can be obtained respectively:

$$J^*\sigma^*_{ij} = y_{i,A}P^*_{Aj} = y_{i,A}y_{j,B}S^*_{AB} \tag{2.32}$$

$$J'\sigma^*_{ij} = y_{i,k}P'_{kj} = y_{i,k}y_{j,l}S'_{kl} \tag{2.33}$$

By considering relation (2.25), equations (2.32) and (2.33) can be modified to obtain:

$$P'_{ij} = J^{-1}x_{i,A}x_{k,B}y_{j,k}S^*_{AB} \tag{2.34}$$

$$S'_{ij} = J^{-1} x_{i,A} x_{j,B} S^*_{AB} \tag{2.35}$$

The expressions gathered at (2.34) and (2.35) summarize the existing relationship between the nominal stress tensor P'_{ij} and the second Piola-Kirchhoff stress tensor S'_{ij} expressed in the prestressed configuration $\mathbf{B}_t$, with respect to the second Piola-Kirchhoff stress tensor S^*_{AB} represented at the initial undeformed state $\mathbf{B}_0$.

Linear momentum balance law

The conservation of linear momentum of the material body in the secondary state may be depicted with respect to three possible descriptions: $\mathbf{B}_0$, $\mathbf{B}_t$ and $\mathbf{B}_{t^*}$, according to a Lagrangian formulation for the first two ones or an Eulerian formulation for the later one. Thus:

$$\sigma^*_{ji,j} + \rho^* b_i = 0 \ \ in \ \ \Omega^*_t, \qquad f^*_i = t^*_i d\Gamma^* = \sigma^*_{ji} n^*_j d\Gamma^* \ \ on \ \partial\Omega^*_t \tag{2.36}$$

$$P^*_{Ai,A} + \rho_0 b_i = 0 \ \ in \ \ \Omega_0, \qquad f^*_i = t^{*0}_i d\Gamma_0 = P^*_{Ai} n_A d\Gamma_0 \ \ on \ \partial\Omega_0 \tag{2.37}$$

$$P'_{ji,j} + \rho b_i = 0 \ \ in \ \ \Omega_t, \qquad f^*_i = t'_i d\Gamma = P'_{ji} n_j d\Gamma \ \ on \ \partial\Omega_t \tag{2.38}$$

where:

$$\sigma^*_{ji,j} = \frac{\partial \sigma^*_{ji}}{\partial y_j} \tag{2.39}$$

$$P^*_{Ai,A} = \frac{\partial P^*_{Ai}}{\partial X_A} \tag{2.40}$$

$$P'_{ji,j} = \frac{\partial P'_{ji}}{\partial x_j} \tag{2.41}$$

The formula (2.38) along with the boundary and continuity conditions, synthesizes the strong formulation of the structural problem according to a Lagrangian description with respect to a reference stressed configuration. This equation will be used throughout the remainder of this paper.

Constitutive law

By accounting for the Saint Venant-Kirchhoff constitutive model adopted for the material behaviour, the expression (2.20) can be reformulated by means of a Taylor series expansion truncated after the first order as follows:

$$S^*_{AB} = \frac{\partial w_{int}}{\partial E^*_{AB}} = \frac{\partial w_{int}}{\partial E_{AB}} + \frac{\partial^2 w_{int}}{\partial E_{AB} \partial E_{CD}} (E^*_{CD} - E_{CD}) \tag{2.42}$$

The accuracy of this Taylor series depends directly on the smallness of the step $E^*_{CD} - E_{CD}$. For tension membrane structures in Civil Engineering applications, as it was aforementioned, this is a valid assumption. Thus, from (2.30) and (2.42), the following expression can be written down:

$$S^*_{AB} = S_{AB} + \mathcal{C}_{ABCD} x_{i,C} x_{j,D} E'_{ij} \tag{2.43}$$

By recalling (2.35) and (2.43):

$$S'_{ij} = J^{-1} x_{i,A} x_{j,B} S_{AB} + J^{-1} x_{i,A} x_{j,B} \mathcal{C}_{ABCD} x_{k,C} x_{l,D} E'_{kl} \tag{2.44}$$

The fourth order tensor of elastic moduli can be referred to the prestressed configuration as follows:

$$\mathcal{C}_{ijkl} = J^{-1} x_{i,A} x_{j,B} \mathcal{C}_{ABCD} x_{k,C} x_{l,D} \tag{2.45}$$

Eventually, equation (2.44) may be reformulated to give the final expression:

$$S'_{ij} = \sigma_{ij} + \mathcal{C}_{ijkl} E'_{kl} \tag{2.46}$$

This final formula is set up to show the constitutive law for a prestressed Saint Venant-Kirchhoff hyperelastic material. The second Piola-Kirchhoff stress tensor is expressed in terms of an easy linear relationship which depends on three tensorial entities: Cauchy stress tensor in the primary state, fourth order tensor of elastic moduli and the incremental Green-Lagrange strain tensor of the secondary state referred to the primary one.

Internal strain energy balance

Another important feature which needs to be obtained is the incremental strain energy accumulated into the structure along the deformation path from the primary to the secondary states. By performing again a Taylor series expansion truncated after the second order, the internal strain energy functional per unit of undeformed volume may be developed as:

$$w^*_{int} = w_{int} + \Omega + \Upsilon \tag{2.47}$$

where:

$$\Omega = \frac{\partial w_{int}}{\partial E_{AB}} (E^*_{AB} - E_{AB}) \tag{2.48}$$

$$\Upsilon = \frac{1}{2} \frac{\partial^2 w_{int}}{\partial E_{AB} \partial E_{CD}} (E^*_{AB} - E_{AB})(E^*_{CD} - E_{CD}) \tag{2.49}$$

The terms Ω and Υ can be expanded as:

$$\Omega = S_{AB} x_{i,A} x_{j,B} E'_{ij} = J \sigma_{ij} E'_{ij} \tag{2.50}$$

$$\Upsilon = \frac{1}{2}\mathcal{C}_{ABCD}x_{i,A}x_{j,B}E'_{ij}x_{k,C}x_{l,D}E'_{kl} = \frac{1}{2}J\mathcal{C}_{ijkl}E'_{ij}E'_{kl} \tag{2.51}$$

By substituting (2.50) and (2.51) back into (2.47), the incremental internal energy per unit volume is obtained as:

$$w^*_{int} - w_{int} = J[\sigma_{ij}E'_{ij} + \frac{1}{2}\mathcal{C}_{ijkl}E'_{ij}E'_{kl}] = Jw'_{int} \tag{2.52}$$

where w'_{int} represents the incremental energy per unit volume measured in the prestressed configuration. By integrating over the initial undeformed volume $\mathbf{\Omega}_0$ and by applying the mass conservation principle from this volume $\mathbf{\Omega}_0$ to the prestressed one $\mathbf{\Omega}_t$, the total incremental energy is given as:

$$\Delta W_{int} = \int_{\Omega_0}(w^*_{int} - w_{int})d\Omega_0 = \int_{\Omega_0} Jw'_{int}d\Omega_0 = \int_{\Omega_t} w'_{int}dV \tag{2.53}$$

Therefore, the internal strain energy functional per unit of volume of the primary state takes the final form:

$$w'_{int} = \sigma_{ij}E'_{ij} + \frac{1}{2}\mathcal{C}_{ijkl}E'_{ij}E'_{kl} \tag{2.54}$$

2.5.3 Conclusions.

In this last section and for the sake of convenience, the fundamental equations comprising the strong form of the structural problem are summarized as follows:

1. Balance of linear momentum in an Eulerian description.

$$\sigma^*_{ji,j} + \rho^* b_i = 0 \ \ in \ \ \mathbf{\Omega}^*_t, \qquad f^*_i = t^*_i d\Gamma^* = \sigma^*_{ji}n^*_j d\Gamma^* \ \ on \ \partial\mathbf{\Omega}^*_t \tag{2.55}$$

2. Balance of linear momentum in a Lagrangian description with respect to the prestressed configuration.

$$P'_{ji,j} + \rho b_i = 0 \ \ in \ \ \mathbf{\Omega}_t, \qquad f^*_i = t'_i d\Gamma = P'_{ji}n_j d\Gamma \ \ on \ \partial\mathbf{\Omega}_t \tag{2.56}$$

3. Relationship among the stress tensors.

$$J'\sigma^*_{ij} = y_{i,k}P'_{kj} = y_{i,k}y_{j,l}S'_{kl} \tag{2.57}$$

4. Relationship among the strain tensors.

$$E^*_{AB} - E_{AB} = x_{i,A}x_{j,B}E'_{ij}, \qquad E'_{ij} = \frac{1}{2}(u_{i,j} + u_{j,i}) + \frac{1}{2}u_{k,i}u_{k,j} \tag{2.58}$$

5. Constitutive equation for a prestressed Saint Venant-Kirchhoff hyperelastic material.

$$S'_{ij} = \sigma_{ij} + \mathcal{C}_{ijkl}E'_{kl} \tag{2.59}$$

6. Helmholtz's free energy functional per unit of volume in the prestressed configuration.

$$w'_{int} = \sigma_{ij}E'_{ij} + \frac{1}{2}\mathcal{C}_{ijkl}E'_{ij}E'_{kl} \tag{2.60}$$

Chapter 3

Weak Formulation

3.1 Introduction.

To set up the weak formulation of the structural problem, a Lagrangian mesh will be employed throughout the whole analysis[1]. By selecting this sort of mesh, elements and nodes move accompanying the continuum's deformation. Another attribute of Lagrangian meshes is that boundaries and interfaces coincide with the finite elements' edges or facets developed for the analysis of the structural problem.

The use of a Lagrangian mesh as well as a referential or Lagrangian formulation[2], are the common denominators of a weak Lagrangian formulation, which will be the one selected in this research. However, among this generic description, two specific formulations may be pointed out: Total Lagrangian Formulation and Updated Lagrangian Formulation.

- In the **Total Lagrangian Formulation (TLF)**, all variables are referred back to the referential description and the existing integrals and derivatives are performed with respect to the referential domain and coordinates, respectively.
- In the **Updated Lagrangian Formulation (ULF)**, all variables are referred back to the referential description whereas the existing integrals and derivatives are performed with respect to the current or spatial domain and coordinates, respectively.

In the next sections, special interest will be focused on the first of the above because of its usefulness to describe the behaviour of the structures analyzed in this research. Nonetheless, both formulations will be presented up to a certain extension to gain insight on both of them.

3.2 Total Lagrangian Formulation (TLF).

The above mentioned primary and secondary states can be understood as an initial prestressed state $\Re_{pret}$ and a final in service loading state $\Re$ due to the consideration of live and dead load. Henceforth, the coordinates of any body's particle, in both prestressed and final loaded states, are related by means of the incremental displacement field $\mathbf{u}$ as follows:

$$\mathbf{x} = \mathbf{X}^{pret} + \mathbf{u}, \quad x_i = X_i^{pret} + u_i \tag{3.1}$$

According to this nomenclature, the strong formulation of the problem in a Lagrangian description with respect to the prestressed configuration is summarized in figure 3.1. The configurations $\Re_{pret}$ represents a material body of domain V^{pret} with frontier Γ^{pret}. As can be observed, the super index $(')$ has been suppressed for the sake of simplicity.

[1]This sort of mesh is the most suitable for structural mechanics problems whereas Eulerian meshes are more useful in computational fluid dynamics problems.

[2]See appendix at the end to review some fundamentals about nonlinear structural mechanics.

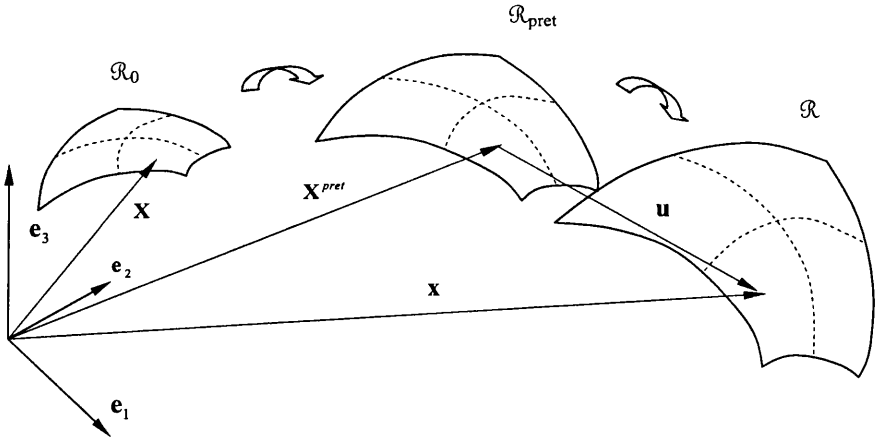

Figure 3.1: Motion of a prestressed body.

1. Balance of linear momentum.

$$\frac{\partial P_{ji}}{\partial X_j^{pret}} + \rho^{pret} b_i = 0 \ \ in \ \ V^{pret} \tag{3.2}$$

2. Transformation of stress tensors.

$$J\sigma_{ij} = \frac{\partial x_i}{\partial X_k^{pret}} P_{kj} = \frac{\partial x_i}{\partial X_k^{pret}} \frac{\partial x_j}{\partial X_l^{pret}} S_{kl}; \quad J = \det\left(\frac{\partial x_i}{\partial X_j^{pret}}\right) \tag{3.3}$$

3. Green-Lagrange strain tensor.

$$E_{ij} = \frac{1}{2}\left(\frac{\partial x_k}{\partial X_i^{pret}} \frac{\partial x_k}{\partial X_j^{pret}} - \delta_{ij}\right) \tag{3.4}$$

4. Constitutive law.

$$S_{ij} = \sigma_{ij}^{pret} + \mathcal{C}_{ijkl} E_{kl} \tag{3.5}$$

5. Internal strain energy functional per unit volume of prestressed configuration.

$$w_{int} = \sigma_{ij}^{pret} E_{ij} + \frac{1}{2} \mathcal{C}_{ijkl} E_{ij} E_{kl} \tag{3.6}$$

6. Boundary conditions.

$$t_i = P_{ji} n_j^{pret} = \bar{t}_i \ \ on \ \ \Gamma_{t_i}^{pret} \qquad u_i = \bar{u}_i \ \ on \ \ \Gamma_{u_i}^{pret} \tag{3.7}$$

To obtain the Total Lagrangian Formulation of the problem, the balance of linear momentum equation is multiplied by a test function $\delta\mathbf{u}$ and then integrated over the volume of the prestressed configuration:

$$\int_{V^{pret}} \delta u_i \left(\frac{\partial P_{ji}}{\partial X_j^{pret}} + \rho^{pret} b_i\right) dV = 0 \tag{3.8}$$

This integral equation represents a *weighted residual method.* As can be noted, a good approximation to the exact solution would imply that the conservation of linear momentum is nearly satisfied at all points of the domain V^{pret}. Amid the different weighted residual methods, the *Galerkin* approach will be the selected one, whose complete development may be encountered in: Cook et al. (1989), Crisfield (1991a), Oñate (1995), Zienkiewicz and Taylor (1995), Bathe (1996) and Belytschko et al. (2000). By applying, thus, the Gauss or divergence theorem[3] along with the well known chain rule, the weak form may be developed in a Total Lagrangian Format (TLF). Neglecting inertia forces, this gives:

$$\delta W_{int}(\delta u_i, u_i) = \delta W_{ext}(\delta u_i, u_i) \tag{3.9}$$

$$\delta W_{int} = \int_{V^{pret}} \delta F_{ij} P_{ji}\, dV = \int_{V^{pret}} \delta \mathbf{F}^T : \mathbf{P} dV \tag{3.10}$$

$$\delta W_{ext} = \int_{V^{pret}} \delta u_i \rho^{pret} b_i\, dV + \int_{\Gamma^{pret}} \delta u_i \bar{t}_i\, d\Gamma = \\ = \int_{V^{pret}} \delta \mathbf{u}^T \cdot \rho^{pret} \mathbf{b}\, dV + \int_{\Gamma^{pret}} \delta \mathbf{u}^T \cdot \bar{\mathbf{t}}\, d\Gamma \tag{3.11}$$

Equation (3.10) may be rewritten as a function of the second Piola-Kirchhoff stress tensor as well as the Euler-Lagrange strain tensor, as it can be noted from the following derivation:

$$\delta \mathbf{F}^T : \mathbf{P} = \delta F_{ij} P_{ji} = \delta F_{ij} F_{ik} S_{jk} = \frac{1}{2}(\delta F_{ij} F_{ik} + \delta F_{ik} F_{ij}) S_{jk} = \\ = \delta E_{jk} S_{jk} = \delta \mathbf{E} : \mathbf{S} \tag{3.12}$$

where in order to obtain the above formula, we have made use of the fact that the inner product of a symmetric and a skew-symmetric tensor is null. As can be detected, the work conjugacy property of the tensors $\mathbf{S}$ and $\mathbf{P}$ with $\mathbf{E}$ and $\mathbf{F}^T$, respectively, has been deduced.

From a structural standpoint, equation (3.9) is known as **Principle of Virtual Work** and physically it represents a set of equilibrium equations in a global level -for the whole domain V^{pret}, unlike the strong form (3.2) where the equilibrium is guaranteed in a local level.

From equations (3.9) to (3.12), we can observe that the Total Lagrangian Formulation requires to know the referential or material coordinates of the continuum configuration $\Re_{pret}$ and to refer all the scalar, vector and tensor magnitudes with respect to it. Finally, the numerical integration will be carried out over the volume V^{pret} and its contour Γ^{pret}.

[3] As it was pinpointed at the beginning of this chapter, the derivatives required in this derivation will be evaluated with respect to the material coordinates.

3.3 Updated Lagrangian Formulation (ULF).

This formulation is obtained through the Eulerian description of the equations of motion. Once established the balance of linear momentum equation, that is:

$$\frac{\partial \sigma_{ji}}{\partial x_j} + \rho b_i = 0 \ \ in \ \ V \tag{3.13}$$

the integral equation to describe the weak formulation of the problem is, in this case, set up by means of a test function δv_i. As a consequence of this selection, the Galerkin method is known, from a structural point of view, as **Principle of Virtual Power**. Therefore:

$$\delta \dot{W}_{int}(\delta v_i, v_i) = \delta \dot{W}_{ext}(\delta v_i, v_i) \tag{3.14}$$

$$\delta \dot{W}_{int} = \int_V \delta D_{ij} \sigma_{ji} \, dV = \int_V \delta \mathbf{D} : \boldsymbol{\sigma} dV \tag{3.15}$$

$$\delta \dot{W}_{ext} = \int_V \delta v_i \rho b_i \ dV + \int_\Gamma \delta v_i \bar{t}_i \ d\Gamma = \int_V \delta \mathbf{v}^T \cdot \rho \mathbf{b} \ dV + \int_\Gamma \delta \mathbf{v}^T \cdot \bar{\mathbf{t}} \ d\Gamma \tag{3.16}$$

In the above equation (3.15), $\mathbf{D}$ is the so called strain rate tensor or rate of deformation tensor[4]. As can be noted, in the **ULF** the different magnitudes though expressed with respect to the Lagrangian coordinates, are integrated with respect to the current domain V and its boundary Γ.

3.4 Final considerations.

As it has been observed in the former sections, the main difference between the **ULF** and the **TLF** lie in the configurations which are used to carry out the derivatives and the integrals that arise in the equations. For the former, spatial coordinates $\mathbf{x}$ and spatial domain V are used, whereas for the latter, material coordinates $\mathbf{X}^{pret}$ and referential domain V^{pret} are employed. Therefore, while the integral domain for the **TLF** remains fixed throughout the complete structural analysis, in the **ULF** the material domain must be updated continuously

This updated procedure in the geometric and mechanical properties entails a considerable increase in the computational time for each iteration or time step. However, in those problems where large strains are foreseen, the **ULF** is preferable to the detriment of the **TLF** -which is not our particular case.

In accordance with Crisfield (1991a) and Belytschko et al. (2000), the **TLF** is the most suitable when dealing with structural problems undergoing large rotations

[4]See appendix D for further details.

but small or moderate strains. This behaviour is characteristic of Saint Venant-Kirchhoff hyperelastic materials. In this situation, the computational time can be safely reduced for the sake of keeping the integration domain fixed throughout the nonlinear algorithm. As a consequence, this formulation will be the selected one for the successive chapters of this research.

Another important issue that is convenient to point out, is the fact that the transition from the **TLF** to the **ULF** and viceversa, may be easily obtained by simply applying classical push forward and pull back operations, as depicted in Bonet and Wood (1997) and Holzapfel (2000).

Chapter 4

FEM Discretization

4.1 Introduction.

The numerical procedure which will be employed for the computational resolution of the structural problem is the well known **Finite Element Method (FEM)**. This technique, widely and extensively described in References such as Zienkiewicz (1982), Oñate (1995), Bathe (1996) or Smith and Griffiths (1998), enables the discretization of the problem's weak formulation. This discretization allows to transform the continuous problem into a n-dimensional algebraic system of non-linear equations.

The numerical strategy will be built upon the **Direct Stiffness Method (DSM)**, that is, the formulation will be established based on the displacements field and the resolution will be accomplished through the so called stiffness matrix. Hence, the displacements field as well as the domain's geometry will be both discretized in terms of the Lagrangian nodes' displacements and the spatial Lagrangian nodes' geometry, respectively. Furthermore, the interpolation technique will require the definition of the so called shape functions. The reading of appealing References such as Turner et al. (1956), Turner et al. (1960) and Felippa (2000) is encouraged for the sake of historical reasons in the development of this numerical technique over the last decades.

In this chapter, equivalent internal and external nodal forces vectors are derived, starting from the virtual work balance $\delta W_{int}(\delta u_i, u_i) = \delta W_{ext}(\delta u_i, u_i)$ presented in the previous chapter. At first, a standard formulation based on tensor and matrix notations will be depicted. Finally, and in the wake of setting up some basic notation criteria, namely, the kinetic and kinematic Voigt rules along with the rule for vectorization of a matrix, a more sophisticated formulation will be detailed, named **Diret Core Congruential Formulation (DCCF)**. The FEM spatial discretization will be undertaken according to a TLF.

Thus, our main objective is to present the formulation for an isoparametric finite element and describe an effective implementation. The principal idea of the isoparametric finite element formulation is to achieve the relationship between the element displacements at any point and the element nodal point displacements directly through the use of interpolation functions.

Finally, with the objective of giving a complete and robust formulation to analyze the whole structural problem, another variational approach in terms of the minimization of the **Total Potential Energy (TPE)** functional is introduced. As a consequence, any numerical strategy to solve an unconstrained optimization problem could be employed to accomplish the solution.

4.2 FEM standard formulation.

4.2.1 Displacements and deformations fields.

In an isoparametric finite element, the displacements field as well as the spatial coordinates of any material point, are discretized by means of the same shape functions,

according to the following formula:

$$x_i = x_i{}^I N^I \qquad u_i = u_i{}^I N^I \quad i = 1,2,3 \;\; I = 1 \ldots Nnodes \tag{4.1}$$

where $Nnodes$ represents the total number of Lagrangian nodes in the mesh and N^I stands for the shape function[1] corresponding to node I.

The second above equality can be expanded in a matrix form as follows:

$$\mathbf{u} = \begin{bmatrix} u_1 \\ u_2 \\ u_3 \end{bmatrix} = \begin{bmatrix} u_1^1 & u_1^2 & \ldots & u_1^{Nnodes-1} & u_1^{Nnodes} \\ u_2^1 & u_2^2 & \ldots & u_2^{Nnodes-1} & u_2^{Nnodes} \\ u_3^1 & u_3^2 & \ldots & u_3^{Nnodes-1} & u_3^{Nnodes} \end{bmatrix} \cdot \begin{bmatrix} N^1 \\ N^2 \\ \vdots \\ N^{Nnodes-1} \\ N^{Nnodes} \end{bmatrix} = \mathbf{u}_{dis} \cdot \{\mathbf{N}\} \tag{4.2}$$

where we have defined the matrix which gathers the displacements of each one of the nodes of the mesh and the vector which allocates the nodal shape functions, namely, $\mathbf{u}_{dis}$ and $\{\mathbf{N}\}$, respectively.

The deformation gradient tensor and its variational perturbation may be discretized straightforwardly as:

$$F_{ij} = \frac{\partial x_i}{\partial X_j^{pret}} = x_i{}^I \frac{\partial N^I}{\partial X_j^{pret}} = x_i{}^I B_j{}^I \;\; \Rightarrow \;\; \delta F_{ij} = \delta x_i{}^I B_j{}^I = \delta u_i{}^I B_j{}^I \tag{4.3}$$

where we have made use of the fact that $\delta \mathbf{x} = \delta \mathbf{X}^{pret} + \delta \mathbf{u} = \delta \mathbf{u}$. Therefore, by introducing the discretization matrices $\mathbf{x}_{dis}$ and $\delta \mathbf{u}_{dis}$, it is feasible to formulate:

$$\mathbf{F} = \mathbf{x}_{dis} \cdot \mathbf{B}^T \;\; \Rightarrow \;\; \delta \mathbf{F} = \delta \mathbf{u}_{dis} \cdot \mathbf{B}^T \tag{4.4}$$

where:

$$\mathbf{B} = \left[B_i{}^I\right] = \begin{bmatrix} \frac{\partial N^1}{\partial X_1^{pret}} & \frac{\partial N^2}{\partial X_1^{pret}} & \cdots & \frac{\partial N^{Nnodes}}{\partial X_1^{pret}} \\ \frac{\partial N^1}{\partial X_2^{pret}} & \frac{\partial N^2}{\partial X_2^{pret}} & \cdots & \frac{\partial N^{Nnodes}}{\partial X_2^{pret}} \\ \frac{\partial N^1}{\partial X_3^{pret}} & \frac{\partial N^2}{\partial X_3^{pret}} & \cdots & \frac{\partial N^{Nnodes}}{\partial X_3^{pret}} \end{bmatrix} \tag{4.5}$$

4.2.2 Equivalent internal nodal forces.

By recalling the weak formulation of the problem, the internal virtual work δW_{int} written in a Total Lagrangian Format can be developed as follows:

$$\delta W_{int} = \int_{V^{pret}} \delta F_{ij} P_{ji} \, dV = \int_{V^{pret}} \delta \mathbf{F}^T : \mathbf{P} dV \tag{4.6}$$

[1] Recall that $N^I(\mathbf{x}^J) = \delta^{IJ}$, $\forall \, I, J$ of the Lagrangian mesh.

By substituting equation (4.4) into (4.6), applying the relationship between the nominal stress tensor $\mathbf{P}$ and the second Piola Kirchhoff stress tensor $\mathbf{S}$ and, by extracting the test function out of the integral for the sake of its constancy, it turns out to be:

$$\delta W_{int} = \int_{V^{pret}} \delta u_i{}^I B_j{}^I P_{ji}\, dV = \int_{V^{pret}} \delta u_i{}^I B_j{}^I S_{jk} F_{ik}\, dV =$$
$$= \int_{V^{pret}} \delta u_i{}^I B_j{}^I S_{jk} x_i{}^J B_k{}^J\, dV = \delta u_i{}^I \int_{V^{pret}} B_j{}^I S_{jk} x_i{}^J B_k{}^J\, dV =$$
$$= \delta u_i{}^I f_{i_{int}}^I = \delta \mathbf{u}_{dis} : \mathbf{f}_{int} \quad (4.7)$$

The former expression enables to come out with the internal virtual work starting from the scalar product (:) of two matrices, namely, the matrix $\delta \mathbf{u}_{dis}$ which gathers the nodal virtual displacements and the matrix $\mathbf{f}_{int}$ of the equivalent internal nodal forces. The latter can be expanded to yield:

$$\mathbf{f}_{int} = \begin{bmatrix} f_{1_{int}}^1 & f_{1_{int}}^2 & \cdots & f_{1_{int}}^{Nnodes-1} & f_{1_{int}}^{Nnodes} \\ f_{2_{int}}^1 & f_{2_{int}}^2 & \cdots & f_{2_{int}}^{Nnodes-1} & f_{2_{int}}^{Nnodes} \\ f_{3_{int}}^1 & f_{3_{int}}^2 & \cdots & f_{3_{int}}^{Nnodes-1} & f_{3_{int}}^{Nnodes} \end{bmatrix} \quad (4.8)$$

the above expression (4.7) can be rewritten in a more compact manner as:

$$\mathbf{f}_{int} = \int_{V^{pret}} \mathbf{P}^T \cdot \mathbf{B}\, dV = \int_{V^{pret}} \mathbf{F} \cdot \mathbf{S} \cdot \mathbf{B}\, dV = \int_{V^{pret}} \mathbf{x}_{dis} \cdot \mathbf{B}^T \cdot \mathbf{S} \cdot \mathbf{B}\, dV =$$
$$= \int_{V^{pret}} (\mathbf{X}_{dis}^{pret} + \mathbf{u}_{dis}) \cdot \mathbf{B}^T \cdot \mathbf{S} \cdot \mathbf{B}\, dV \quad (4.9)$$

4.2.3 Equivalent external nodal forces.

On the other hand, an analogous discretization technique can be used for the counterpart external virtual work δW_{ext}, that is:

$$\delta W_{ext} = \int_{V^{pret}} \delta u_i \rho^{pret} b_i\, dV + \int_{\Gamma^{pret}} \delta u_i \bar{t}_i\, d\Gamma =$$
$$= \int_{V^{pret}} \delta \mathbf{u}^T \cdot \rho^{pret} \mathbf{b}\, dV + \int_{\Gamma^{pret}} \delta \mathbf{u}^T \cdot \bar{\mathbf{t}}\, d\Gamma \quad (4.10)$$

By substituting (4.4) into (4.10):

$$\delta W_{ext} = \int_{V^{pret}} \delta u_i{}^I N^I \rho^{pret} b_i \, dV + \int_{\Gamma^{pret}} \delta u_i{}^I N^I \bar{t}_i \, d\Gamma =$$

$$= \delta u_i{}^I \left[\int_{V^{pret}} N^I \rho^{pret} b_i \, dV + \int_{\Gamma^{pret}} N^I \bar{t}_i \, d\Gamma \right] = \delta u_i{}^I f_{i_{ext}}{}^I = \delta \mathbf{u}_{dis} : \mathbf{f}_{ext} \quad (4.11)$$

As before, the external virtual work has been obtained as the scalar product of the nodal virtual displacements matrix $\delta \mathbf{u}_{dis}$ and the equivalent external nodal forces matrix $\mathbf{f}_{ext}$. The latter can be expanded easily as:

$$\mathbf{f}_{ext} = \begin{bmatrix} f_{1_{ext}}^1 & f_{1_{ext}}^2 & \cdots & f_{1_{ext}}^{Nnodes-1} & f_{1_{ext}}^{Nnodes} \\ f_{2_{ext}}^1 & f_{2_{ext}}^2 & \cdots & f_{2_{ext}}^{Nnodes-1} & f_{2_{ext}}^{Nnodes} \\ f_{3_{ext}}^1 & f_{3_{ext}}^2 & \cdots & f_{3_{ext}}^{Nnodes-1} & f_{3_{ext}}^{Nnodes} \end{bmatrix} \quad (4.12)$$

In matrix notation, $\mathbf{f}_{ext}$, in its turn, may be rewritten in the following way:

$$\mathbf{f}_{ext} = \int_{V^{pret}} \rho^{pret} \mathbf{b} \cdot \{\mathbf{N}\}^T \, dV + \int_{\Gamma^{pret}} \bar{\mathbf{t}} \cdot \{\mathbf{N}\}^T \, d\Gamma \quad (4.13)$$

where $\rho^{pret}\mathbf{b}$ and $\bar{\mathbf{t}}$ represent the body force field acting per unit of prestressed volume and the surface tension field acting on the boundary of the domain, respectively:

$$\mathbf{b}^T = \begin{bmatrix} b_1 & b_2 & b_3 \end{bmatrix} \qquad \bar{\mathbf{t}}^T = \begin{bmatrix} \bar{t}_1 & \bar{t}_2 & \bar{t}_3 \end{bmatrix} \quad (4.14)$$

Another contribution to the equivalent external nodal forces vector is coming from initial non-mechanical deformations of the structure[2]. As a matter of fact, equation (4.9) may be rewritten to account for these initial non-mechanical deformations, that is:

$$S_{ij} = \sigma_{ij}^{pret} + \mathcal{C}_{ijkl}(E_{kl} - E_{kl}^0) \qquad \mathbf{S} = \boldsymbol{\sigma}^{pret} + \boldsymbol{\mathcal{C}} \cdot (\mathbf{E} - \mathbf{E}^0) \quad (4.15)$$

By substituting (4.15) back into (4.9), it yields:

$$\mathbf{f}_{int} = \int_{V^{pret}} \mathbf{x}_{dis} \cdot \mathbf{B}^T \cdot \mathbf{S} \cdot \mathbf{B} \, dV = \int_{V^{pret}} \mathbf{x}_{dis} \cdot \mathbf{B}^T \cdot (\boldsymbol{\sigma}^{pret} + \boldsymbol{\mathcal{C}} \cdot (\mathbf{E} - \mathbf{E}^0)) \cdot \mathbf{B} \, dV =$$

$$= \int_{V^{pret}} \mathbf{x}_{dis} \cdot \mathbf{B}^T \cdot (\boldsymbol{\sigma} + \boldsymbol{\mathcal{C}} \cdot \mathbf{E}) \cdot \mathbf{B} \, dV - \int_{V^{pret}} \mathbf{x}_{dis} \cdot \mathbf{B}^T \cdot \boldsymbol{\mathcal{C}} \cdot \mathbf{E}^0 \cdot \mathbf{B} \, dV \quad (4.16)$$

The last term in the right hand side of (4.16), can be regarded as an equivalent external nodal forces source. Henceforth, this term will be treated as so. Finally, the whole equivalent external nodal forces vector may be written down as follows:

[2]These initial deformations can stem from thermal effects acting on the structure, i.e., sudden change in temperature conditions.

$$\mathbf{f}_{ext} = \int_{V^{pret}} \rho^{pret}\mathbf{b}\cdot\{\mathbf{N}\}^T\, dV + \int_{\Gamma^{pret}} \bar{\mathbf{t}}\cdot\{\mathbf{N}\}^T\, d\Gamma + \int_{V^{pret}} \mathbf{x}_{dis}\cdot\mathbf{B}^T\cdot\boldsymbol{\mathcal{C}}\cdot\mathbf{E}^0\cdot\mathbf{B}\, dV \quad (4.17)$$

By only knowing the initial Green-Lagrange strain tensor $\mathbf{E}^0$, equation (4.17) may be calculated by means of the fourth order tangent moduli tensor $\boldsymbol{\mathcal{C}}$. As a consequence, thermal effects can be computationally assimilated to mechanical processes.

4.2.4 Semidiscretization equations.

The semidiscretized[3] weak formulation is highlighted in figure (4.1). Equivalent external and internal nodal forces matrices are detailed along with its particularization for each one of the nodes of the Lagrangian mesh, namely, $\mathbf{f}^I_{int}$ and $\mathbf{f}^I_{ext}$.

* **Semidiscretized equilibrium equations**

$$\mathbf{f}_{int} = \mathbf{f}_{ext} \qquad \mathbf{f}^I_{int_{3\times1}} = \mathbf{f}^I_{ext_{3\times1}} \qquad I = 1\ldots Nnodes$$

* **Equivalent internal nodal forces**

$$\mathbf{f}_{int} = \int_{V^{pret}} \mathbf{P}^T\cdot\mathbf{B}\, dV = \int_{V^{pret}} \mathbf{x}_{dis}\cdot\mathbf{B}^T\cdot\mathbf{S}\cdot\mathbf{B}\, dV$$
$$\mathbf{f}^I_{int_{3\times1}} = \int_{V^{pret}} \mathbf{P}^T_{3\times3}\cdot\mathbf{B}^I_{3\times1}\, dV = \int_{V^{pret}} \mathbf{x}^I_{dis_{3\times1}}\cdot\mathbf{B}^{I^T}_{1\times3}\cdot\mathbf{S}_{3\times3}\cdot\mathbf{B}^I_{3\times1}\, dV$$

* **Equivalent external nodal forces**

$$\mathbf{f}_{ext} = \int_{V^{pret}} \rho\mathbf{b}\cdot\{\mathbf{N}\}^T\, dV + \int_{\Gamma^{pret}} \bar{\mathbf{t}}\cdot\{\mathbf{N}\}^T\, d\Gamma$$
$$\mathbf{f}^I_{ext_{3\times1}} = \int_{V^{pret}} \rho_{1\times1}\mathbf{b}_{3\times1}N^I_{1\times1}\, dV + \int_{\Gamma^{pret}} \bar{\mathbf{t}}_{3\times1}N^I_{1\times1}\, d\Gamma$$

Figure 4.1: Semidiscretized equilibrium equations in a Total Lagrangian Formulation.

As it has been already established, in the finite element analysis we approximate the body as an assemblage of discrete finite elements interconnected at nodal points on the element boundaries. The displacements of every single node, measured in a *local coordinate system* -to be chosen conveniently- within each finite element must be transformed to a *global coordinate system* through the corresponding rotation matrix. This transformation, which will affect the resulting equivalent external and internal nodal forces, may be mathematically formulated as follows:

[3]The *semidiscretization* term is used to refer just to spatial discretization whereas the term *discretization* is employed when both spatial and time discretization are developed as a whole -see Belytschko et al. (2000)-.

$$\mathbf{f}_{int}^{e^G} = \mathbf{T}^e \cdot \mathbf{f}_{int}^e \quad \mathbf{f}_{ext}^{e^G} = \mathbf{T}^e \cdot \mathbf{f}_{ext}^e \quad e = 1 \dots Nelem \tag{4.18}$$

where:

$\mathbf{f}_{ext}^e$, $\mathbf{f}_{int}^e$ stand for the local equivalent external and internal nodal forces matrices for a single finite element e.

$\mathbf{f}_{ext}^{e^G}$, $\mathbf{f}_{int}^{e^G}$ stand for the global equivalent external and internal nodal forces matrices for a single finite element e.

$\mathbf{T}^e$ is the rotation matrix at the finite element e.

$Nelem$ is the total number of discrete finite elements.

4.2.5 Linearization of the equivalent internal nodal forces.

The semidiscretized system of equilibrium equations -see figure 4.1- may be identified mathematically with an algebraic system of non-linear integral equations. Analytical solutions for this system are impossible to achieve, so alternative numerical methods must be taken into consideration.

One of the most classical and accurate of these methods is based on a perturbation or linearization technique. In this case, the equivalent internal nodal forces matrix is expanded around a known value by means of a Taylor series truncated after the first order. Indeed, the total differential[4] of this matrix with respect to the displacement field, can be calculated as:

$$d\mathbf{f}_{int} = d \int_{V^{pret}} \frac{\partial N^I}{\partial X_j^{pret}} P_{ji}\, dV = \int_{V^{pret}} \frac{\partial N^I}{\partial X_j^{pret}} dP_{ji}\, dV =$$
$$= \int_{V^{pret}} \frac{\partial N^I}{\partial X_j^{pret}} d(S_{jk}F_{ik})\, dV = \int_{V^{pret}} \frac{\partial N^I}{\partial X_j^{pret}} dS_{jk}F_{ik}\, dV + \int_{V^{pret}} \frac{\partial N^I}{\partial X_j^{pret}} S_{jk} dF_{ik}\, dV \tag{4.19}$$

In the above derivation, the differential operator has been introduced within the integrand. At the same time, due to the consideration of a Total Lagrangian Formulation, the partial derivatives of the shape functions do not depend on the displacements. As a result of this fact, the differential operator is conveyed only to the second part of the integrand. The relationship between the nominal stress tensor $\mathbf{P}$ and the second Piola-Kirchhoff stress tensor $\mathbf{S}$ has been also accounted for.

Right hand side of equation (4.19) is comprised of two terms. The second one can be expanded as follows:

[4]This operator represents the so called *total directional derivative* according to Bonet and Wood (1997), namely: $d\Phi = D\Phi(x)[u] = \lim_{\epsilon \to 0} \frac{d\Phi(x+\epsilon u)}{du}$. In this case, the scalar function which depends on the variable x is derivated with respect to an incremental direction u.

$$\int_{V^{pret}} \frac{\partial N^I}{\partial X_j^{pret}} S_{jk} dF_{ik}\, dV = \int_{V^{pret}} \frac{\partial N^I}{\partial X_j^{pret}} S_{jk} du_i{}^J \frac{\partial N^J}{\partial X_k^{pret}}\, dV =$$

$$= \int_{V^{pret}} \frac{\partial N^I}{\partial X_j^{pret}} S_{jk} \frac{\partial N^J}{\partial X_k^{pret}}\, dV du_i{}^J = \int_{V^{pret}} \frac{\partial N^I}{\partial X_j^{pret}} S_{jk} \frac{\partial N^J}{\partial X_k^{pret}}\, dV \delta_{il} du_l{}^J \quad (4.20)$$

where the Kronecker delta second order tensor δ_{il} has been introduced for the sake of completeness. As regards the first term of the right hand side of equation (4.19), a similar derivation yields:

$$\int_{V^{pret}} \frac{\partial N^I}{\partial X_j^{pret}} dS_{jk} F_{ik}\, dV = \int_{V^{pret}} \frac{\partial N^I}{\partial X_j^{pret}} \mathcal{C}_{jklm} dE_{lm} F_{ik}\, dV \quad (4.21)$$

The total differential for the Green-Lagrange strain tensor is achieved as follows:

$$dE_{lm} = \frac{1}{2}(F_{pl} dF_{pm} + dF_{pl} F_{pm}) = \frac{1}{2}\left(F_{pl} du_p{}^M \frac{\partial N^M}{\partial X_m^{pret}} + du_p{}^L \frac{\partial N^L}{\partial X_l^{pret}} F_{pm} \right) \quad (4.22)$$

By taking into account the symmetry of the tensor $\boldsymbol{\mathcal{C}}$, substitution of equation (4.22) back into (4.21), gives:

$$\int_{V^{pret}} \frac{\partial N^I}{\partial X_j^{pret}} \mathcal{C}_{jklm} dE_{lm} F_{ik}\, dV = \int_{V^{pret}} F_{ik} \frac{\partial N^I}{\partial X_j^{pret}} \mathcal{C}_{jklm} F_{pl} \frac{\partial N^M}{\partial X_m^{pret}}\, dV du_p{}^M \quad (4.23)$$

Finally, expression (4.19) may be rewritten per every single node of the Lagrangian mesh a follows:

$$d\mathbf{f}_{int}^I = d\mathbf{f}_{int}^{mat^I} + d\mathbf{f}_{int}^{geo^I} = (\mathbf{K}^{mat^{IJ}} + \mathbf{K}^{geo^{IJ}}) d\mathbf{u}^J \quad (4.24)$$

where after renaming some indices:

$$K_{ij}^{mat^{IJ}} = \int_{V^{pret}} F_{ik} \frac{\partial N^I}{\partial X_p^{pret}} \mathcal{C}_{pklm} F_{jl} \frac{\partial N^J}{\partial X_m^{pret}}\, dV \quad (4.25)$$

$$K_{ij}^{geo^{IJ}} = \delta_{ij} \int_{V^{pret}} \frac{\partial N^I}{\partial X_l^{pret}} S_{lk} \frac{\partial N^J}{\partial X_k^{pret}}\, dV \quad (4.26)$$

Formulas (4.25) and (4.26) represent two different components of the equivalent internal nodal forces vector differential $d\mathbf{f}_{int}^I$, which may be described as:

1. Equation (4.25) stands for the variation of the second Piol-Kirchhoff stress tensor with respect to the displacements field of the mesh, resulting in the well known symmetric **material stiffness matrix**.

2. Equation (4.26) accounts for the fact that the equilibrium was set up on the deformed configuration and not on the initial one[5], resulting in the **geometric stiffness matrix** or **initial stress matrix**, which is a diagonal matrix.

Those matrices are added up to yield the referred to as **total tangent stiffness matrix**, that is:

$$\mathbf{K}^{tan^{IJ}} = \mathbf{K}^{mat^{IJ}} + \mathbf{K}^{geo^{IJ}} \tag{4.27}$$

4.2.6 Some considerations about the Updated Lagrangian Formulation.

Semidiscretized non-linear equilibrium equations in a **TLF** can be straightforwardly conveyed into a **ULF** -if required- by taken into account the following mathematical relationships:

$$\rho J = \rho^{pret} \tag{4.28}$$

$$J\sigma_{ij} = F_{ik}P_{kj} = \frac{\partial x_i}{\partial X_k^{pret}} P_{kj} \tag{4.29}$$

$$\frac{\partial N^I}{\partial X_k^{pret}} = \frac{\partial N^I}{\partial x_j} \frac{\partial x_j}{\partial X_k^{pret}} \tag{4.30}$$

By substituting formulae (4.28) to (4.30) back into (4.7) and (4.13), it yields:

$$f_{i_{int}}^{\ I} = \int_V \sigma_{ij} \frac{\partial N^I}{\partial x_j}\, dV \tag{4.31}$$

$$f_{i_{ext}}^{\ I} = \int_V \rho b_i N^I\, dV + \int_\Gamma \bar{t}_i N^I\, d\Gamma \tag{4.32}$$

Once again, we see that the domain as well as the coordinates of the Lagrangian nodes must be updated after each increment. Then, the rest of geometrical and mechanical properties must be updated analogously.

4.3 Direct Core Congruential Formulation (DCCF).

From the computational viewpoint, a very elegant procedure termed **Direct Core Congruential Formulation (DCCF)** may be applied to perform the implementation stage of the formulation developed above. This methodology, hardly used in the existing literature, presents as pioneer studies the ones due to Mallett and

[5]This is a main difference with respect to the classical linear elasticity.

Marcal (1968) and Rajasekaran and Murray (1973). The main ideas behind this formulation can be discovered in the notable paper due to Crivelli and Felippa (1993). A more recent paper about the topic is Felippa et al. (1994).

The scope of the DCCF is establishing the set of global equilibrium equations (internal forces and stiffness matrix) in a *core space* in terms of the components of the displacement gradient tensor $\mathbf{G}$ at each material point, which is given as:

$$G_{ij} = \frac{\partial u_i}{\partial X_j^{pret}} \tag{4.33}$$

Therefore, this new set of equations is completely independent of the geometry of the structure and of the adopted discretization properties[6]. Afterwards, every single component of the displacement gradient tensor may be easily expressed in terms of the nodal displacements of the Lagrangian mesh. Naturally, it is at this stage when properties concerning geometry and discretization are brought to light[7]. The consideration of only traslational degrees of freedom for the nodes of the Lagrangian mesh makes the DCCF specially simple and easy to implement. The figure 4.2 shows a summary of this formulation:

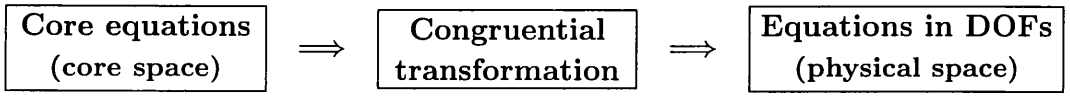

Figure 4.2: DCCF scheme.

For the development of this formulation, kinetic and kinematic Voigt rules, as well as the criterion to vectorize matrices will be used extensively -see Belytschko et al. (2000).

The key goal and the reason to choose such an implementation technique, is to attempt to make the core equations as independent as possible with respect to finite element mesh criteria, such as the element geometry, the selected shape functions and the selection of nodal degrees of freedom. Complete independence may be accomplished if the displacement gradient tensor is linear, that is, only translational degrees of freedom are regarded, which is our case. At the same time, this approach enables to clearly distinguish the different sources of nonlinearity that arise in the analysis of geometrically nonlinear structures.

4.3.1 Displacements and strains field.

As it was already explained, the displacements field can be discretized by means of the shape functions according to the following expression:

[6]The term *core* emphasizes the independence of these equations with respect to the discretization decisions, i.e. geometry, shape functions and choice of nodal degrees of freedom.

[7]By following this technique, a general set of equilibrium equations (internal nodal forces and stiffness matrix) will be derived in a core space. Afterwards, these equations will be particularized for every different finite element, i.e. cable or membrane element.

$$u_i = u_i{}^I N^I \quad i = 1,2,3 \quad I = 1 \ldots Nnodes \tag{4.34}$$

where $Nnodes$ represents the total number of Lagrangian nodes and N^I is the shape function pertaining to node I. By employing the vectorization of the nodal displacements matrix, we obtain:

$$\mathbf{u} = \begin{bmatrix} N^1 & 0 & 0 & \ldots & N^{Nnodes} & 0 & 0 \\ 0 & N^1 & 0 & \ldots & 0 & N^{Nnodes} & 0 \\ 0 & 0 & N^1 & \ldots & 0 & 0 & N^{Nnodes} \end{bmatrix} \cdot \begin{bmatrix} u_1^1 \\ u_2^1 \\ u_3^1 \\ \vdots \\ u_1^{Nnodes} \\ u_2^{Nnodes} \\ u_3^{Nnodes} \end{bmatrix} = \mathbf{N} \cdot \{\mathbf{u}_{dis}\} \tag{4.35}$$

The displacement gradient tensor $\mathbf{G}$ can be turned into the vector $\mathbf{g}$ as:

$$\begin{aligned} \mathbf{g}^T &= \begin{bmatrix} g_1 & g_2 & g_3 & g_4 & g_5 & g_6 & g_7 & g_8 & g_9 \end{bmatrix} = \\ &= \begin{bmatrix} \frac{\partial u_1}{\partial X_1^{pret}} & \frac{\partial u_2}{\partial X_1^{pret}} & \frac{\partial u_3}{\partial X_1^{pret}} & \frac{\partial u_1}{\partial X_2^{pret}} & \frac{\partial u_2}{\partial X_2^{pret}} & \frac{\partial u_3}{\partial X_2^{pret}} & \frac{\partial u_1}{\partial X_3^{pret}} & \frac{\partial u_2}{\partial X_3^{pret}} & \frac{\partial u_3}{\partial X_3^{pret}} \end{bmatrix} \end{aligned} \tag{4.36}$$

This vector $\mathbf{g}$ can be also obtained starting from the discretization (4.35), by means of the definition of a new matrix $\mathbf{B}$ as follows:

$$\mathbf{g} = \mathbf{B} \cdot \{\mathbf{u}_{dis}\} \tag{4.37}$$

where:

$$\mathbf{B} = \begin{bmatrix} \frac{\partial N^1}{\partial X_1^{pret}} & 0 & 0 & \ldots & \frac{\partial N^{Nnodes}}{\partial X_1^{pret}} & 0 & 0 \\ 0 & \frac{\partial N^1}{\partial X_1^{pret}} & 0 & \ldots & 0 & \frac{\partial N^{Nnodes}}{\partial X_1^{pret}} & 0 \\ 0 & 0 & \frac{\partial N^1}{\partial X_1^{pret}} & \ldots & 0 & 0 & \frac{\partial N^{Nnodes}}{\partial X_1^{pret}} \\ \frac{\partial N^1}{\partial X_2^{pret}} & 0 & 0 & \ldots & \frac{\partial N^{Nnodes}}{\partial X_2^{pret}} & 0 & 0 \\ 0 & \frac{\partial N^1}{\partial X_2^{pret}} & 0 & \ldots & 0 & \frac{\partial N^{Nnodes}}{\partial X_2^{pret}} & 0 \\ 0 & 0 & \frac{\partial N^1}{\partial X_2^{pret}} & \ldots & 0 & 0 & \frac{\partial N^{Nnodes}}{\partial X_2^{pret}} \\ \frac{\partial N^1}{\partial X_3^{pret}} & 0 & 0 & \ldots & \frac{\partial N^{Nnodes}}{\partial X_3^{pret}} & 0 & 0 \\ 0 & \frac{\partial N^1}{\partial X_3^{pret}} & 0 & \ldots & 0 & \frac{\partial N^{Nnodes}}{\partial X_3^{pret}} & 0 \\ 0 & 0 & \frac{\partial N^1}{\partial X_3^{pret}} & \ldots & 0 & 0 & \frac{\partial N^{Nnodes}}{\partial X_3^{pret}} \end{bmatrix} \tag{4.38}$$

The Green-Lagrange strain tensor $\mathbf{E}$ can be transformed into a vector $\mathbf{e}$ by means of the kinematic Voigt rule:

$$\mathbf{e}^T = [\ e_1 \quad e_2 \quad e_3 \quad e_4 \quad e_5 \quad e_6\ ] = [\ E_{11} \quad E_{22} \quad E_{33} \quad 2E_{23} \quad 2E_{13} \quad 2E_{12}\ ] \tag{4.39}$$

According to appendix D, the Green-Lagrange strain tensor $\mathbf{E}$ can be expressed in terms of the displacement gradient tensor $\mathbf{G}$, namely: $\mathbf{E} = \frac{1}{2}(\mathbf{G}+\mathbf{G}^T)+\frac{1}{2}\mathbf{G}^T\cdot\mathbf{G}$. This expression can be rewritten by means of the new vectors $\mathbf{e}$ and $\mathbf{g}$ as follows:

$$e_i = \mathbf{h_i}^T\cdot\mathbf{g}+\frac{1}{2}\mathbf{g}^T\cdot\mathbf{H_i}\cdot\mathbf{g} = \mathbf{h_i}^T\cdot\mathbf{B}\cdot\mathbf{u}_{dis}+\frac{1}{2}\mathbf{u}_{dis}^T\cdot\mathbf{B}^T\cdot\mathbf{H_i}\cdot\mathbf{B}\cdot\mathbf{u}_{dis} \tag{4.40}$$

where $\mathbf{h_i}$ and $\mathbf{H_i}$ are a vector of order n_g and a symmetric matrix of order $n_g\times n_g$, where n_g represents the dimension of the vector $\mathbf{g}$. Both of them are constituted of numerical values comprising $(1,0)$. Examples of $\mathbf{h_i}$ and $\mathbf{H_i}$ will be given in the next chapter for particular finite elements.

4.3.2 Equivalent internal nodal forces vector.

As it was already described, the internal virtual work can be obtained by means of the inner product of the virtual Green-Lagrange strain tensor $\delta\mathbf{E}$ and the second Piola-Kirchhoff stress tensor $\mathbf{S}$. The latter is detailed as follows:

$$\mathbf{s}^T = [\ s_1 \quad s_2 \quad s_3 \quad s_4 \quad s_5 \quad s_6\ ] = [\ S_{11} \quad S_{22} \quad S_{33} \quad S_{23} \quad S_{13} \quad S_{12}\ ] \tag{4.41}$$

Thus:

$$\delta W_{int} = \int_{V^{pret}} \delta\mathbf{E}:\mathbf{S}\ dV = \int_{V^{pret}} \delta\mathbf{e}^T\cdot\mathbf{s}\ dV = \int_{V^{pret}} \delta e_i s_i\ dV \tag{4.42}$$

Therefore, the virtual variation of formula (4.40), turns out to be:

$$\begin{aligned}\delta e_i &= \mathbf{h_i}^T\cdot\delta\mathbf{g}+\frac{1}{2}(\delta\mathbf{g}^T\cdot\mathbf{H_i}^T\cdot\mathbf{g}+\mathbf{g}^T\cdot\mathbf{H_i}^T\cdot\delta\mathbf{g}) = \\ &= \mathbf{h_i}^T\cdot\mathbf{B}\cdot\delta\mathbf{u}_{dis}+\frac{1}{2}(\delta\mathbf{u}_{dis}^T\cdot\mathbf{B}^T\cdot\mathbf{H_i}^T\cdot\mathbf{B}\cdot\mathbf{u}_{dis}+\mathbf{u}_{dis}\cdot\mathbf{B}^T\cdot\mathbf{H_i}^T\cdot\mathbf{B}\cdot\delta\mathbf{u}_{dis}) = \\ &= \delta\mathbf{u}_{dis}^T\cdot\mathbf{B}^T\cdot[\mathbf{h_i}+\frac{1}{2}(\mathbf{H_i}+\mathbf{H_i}^T)\cdot\mathbf{B}\cdot\mathbf{u}_{dis}] = \delta\mathbf{u}_{dis}^T\cdot\mathbf{B}^T\cdot[\mathbf{h_i}+\frac{1}{2}(\mathbf{H_i}+\mathbf{H_i}^T)\cdot\mathbf{g}]\end{aligned} \tag{4.43}$$

By substituting (4.43) back into (4.42) and by attending to the symmetry of the matrix $\mathbf{H_i}$:

$$\begin{aligned}\delta W_{int} &= \int_{V^{pret}} \delta\mathbf{u}_{dis}^T\cdot\mathbf{B}^T\cdot[\mathbf{h_i}+\mathbf{H_i}\cdot\mathbf{g}]s_i\ dV = \\ &= \delta\mathbf{u}_{dis}^T\cdot\int_{V^{pret}}\mathbf{B}^T\cdot[\mathbf{h_i}+\mathbf{H_i}\cdot\mathbf{g}]s_i\ dV = \delta\mathbf{u}_{dis}^T\cdot\mathbf{f}^{int}\end{aligned} \tag{4.44}$$

where the equivalent internal nodal force vector is written as:

$$\mathbf{f}_{int} = \int_{V^{pret}} \mathbf{B}^T \cdot [\mathbf{h_i} + \mathbf{H_i} \cdot \mathbf{g}] s_i \, dV = \int_{V^{pret}} \mathbf{B}^T \cdot \boldsymbol{\phi}_{int} \, dV \tag{4.45}$$

where:

$$\boldsymbol{\phi}_{int} = s_i[\mathbf{h_i} + \mathbf{H_i} \cdot \mathbf{g}] = s_1[\mathbf{h_1} + \mathbf{H_1} \cdot \mathbf{g}] + \ldots + s_6[\mathbf{h_6} + \mathbf{H_6} \cdot \mathbf{g}] \tag{4.46}$$

Equation (4.45) constitutes the so called congruential transformation from the core space to the real space of variables.

4.3.3 Equivalent external nodal forces vector.

Analogously, the equivalent external nodal forces vector can be deduced to give:

$$\begin{aligned} \delta W_{ext} &= \int_{V^{pret}} \delta \mathbf{u}^T \cdot \rho \mathbf{b} \, dV + \int_{\Gamma^{pret}} \delta \mathbf{u}^T \cdot \bar{\mathbf{t}} \, d\Gamma = \\ &= \int_{V^{pret}} \delta \mathbf{u}_{dis}^T \cdot \mathbf{N}^T \cdot \rho \mathbf{b} \, dV + \int_{\Gamma^{pret}} \delta \mathbf{u}_{dis}^T \cdot \mathbf{N}^T \cdot \bar{\mathbf{t}} \, d\Gamma = \\ &= \delta \mathbf{u}_{dis}^T \cdot [\int_{V^{pret}} \mathbf{N}^T \cdot \rho \mathbf{b} \, dV + \int_{\Gamma^{pret}} \mathbf{N}^T \cdot \bar{\mathbf{t}} \, d\Gamma] = \delta \mathbf{u}_{dis}^T \cdot \mathbf{f}_{ext} \end{aligned} \tag{4.47}$$

Thus:

$$\mathbf{f}_{ext} = \int_{V^{pret}} \mathbf{N}^T \cdot \rho \mathbf{b} \, dV + \int_{\Gamma^{pret}} \mathbf{N}^T \cdot \bar{\mathbf{t}} \, d\Gamma \tag{4.48}$$

Thermal effects or initial deformations can be handled and considered as external applied forces. Their contribution is mathematically represented as:

$$\mathbf{f}_{ext} = \int_{V^{pret}} \mathbf{B}^T \cdot \boldsymbol{\phi}_{int}^0 \, d\Gamma \tag{4.49}$$

where:

$$\boldsymbol{\phi}_{int}^0 = (\mathcal{C}_{ij} e_j^0)[\mathbf{h_i} + \mathbf{H_i} \cdot \mathbf{g}] \tag{4.50}$$

4.3.4 Linearization of the equivalent internal nodal forces vector.

Because of the nonlinearity of the equilibrium equations -see figure 4.3-, and by proceeding identically as above, the linearization of the equivalent internal nodal forces vector can be accomplished as:

* **Equilibrium equations**

$$\mathbf{f}_{int} = \mathbf{f}_{ext}$$

* **Equivalent internal nodal forces**

$$\mathbf{g} = \mathbf{B} \cdot \mathbf{u}_{dis}$$

$$e_i = \mathbf{h_i}^T \cdot \mathbf{g} + \tfrac{1}{2}\mathbf{g}^T \cdot \mathbf{H_i} \cdot \mathbf{g}$$

$$\phi_{int} = s_i[\mathbf{h_i} + \mathbf{H_i} \cdot \mathbf{g}]$$

$$\mathbf{f}_{int} = \int_{V^{pret}} \mathbf{B}^T \cdot \phi_{int}\, dV$$

* **Equivalent external nodal forces**

$$\mathbf{f}_{ext} = \int_{V^{pret}} \mathbf{N}^T \cdot \rho\mathbf{b}\, dV + \int_{\Gamma^{pret}} \mathbf{N}^T \cdot \bar{\mathbf{t}}\, d\Gamma$$

Figure 4.3: DCCF non-linear equilibrium equations.

$$d\mathbf{f}_{int} = d\int_{V^{pret}} \mathbf{B}^T \cdot \phi_{int}\, dV = \int_{V^{pret}} \mathbf{B}^T \cdot d\phi_{int}\, dV \tag{4.51}$$

$$d\phi_{int} = d[s_i(\mathbf{h_i} + \mathbf{H_i} \cdot \mathbf{g})] = ds_i(\mathbf{h_i} + \mathbf{H_i} \cdot \mathbf{g}) + s_i\mathbf{H_i} \cdot d\mathbf{g} \tag{4.52}$$

If the constitutive equations are reformulated in Voigt notation as follows:

$$s_i = \sigma_i^{pret} + \mathcal{C}_{ij}e_j \tag{4.53}$$

Then:

$$ds_i = \mathcal{C}_{ij}de_j = \mathcal{C}_{ij}d\mathbf{g}^T \cdot [\mathbf{h_j} + \mathbf{H_j} \cdot \mathbf{g}] = \mathcal{C}_{ij}[\mathbf{h_j}^T + \mathbf{g}^T \cdot \mathbf{H_j}] \cdot \mathbf{g} \tag{4.54}$$

By substituting (4.54) back into (4.52):

$$d\phi_{int} = [\mathbf{h_i} + \mathbf{H_i} \cdot \mathbf{g}]\mathcal{C}_{ij}[\mathbf{h_j}^T + \mathbf{g}^T \cdot \mathbf{H_j}] \cdot d\mathbf{g} + s_i\mathbf{H_i} \cdot d\mathbf{g} \tag{4.55}$$

By including (4.55) in (4.51), it yields:

$$d\mathbf{f}_{int} = \int_{V^{pret}} \mathbf{B}^T \cdot \mathbf{M}^{tan} \cdot \mathbf{B}\, dV \cdot d\mathbf{u}_{dis} = \mathbf{K}^{tan} \cdot d\mathbf{u}_{dis} \tag{4.56}$$

where:

$$\mathbf{M}^{tan} = [\mathbf{h_i} + \mathbf{H_i} \cdot \mathbf{g}]\mathcal{C}_{ij}[\mathbf{h_j}^T + \mathbf{g}^T \cdot \mathbf{H_j}] + s_i\mathbf{H_i} = \mathbf{M}^{mat} + \mathbf{M}^{geo} \tag{4.57}$$

Equation (4.56) defines the total tangent stiffness matrix $\mathbf{K}^{tan}$ in terms of an integral equation as a function of a matrix $\mathbf{M}^{tan}$, which is named *core total tangent stiffness matrix*. This integral equation constitutes the so called congruential transformation from the core space to the real space of variables. Furthermore, equation (4.57) represents the core total tangent stiffness matrix as the summation of two components, that is, the core material one $\mathbf{M}^{mat}$ and the core geometric one $\mathbf{M}^{geo}$.

$$\begin{aligned}\mathbf{M}^{mat} &= [\mathbf{h_i} + \mathbf{H_i} \cdot \mathbf{g}]\mathcal{C}_{ij}[\mathbf{h_j}^T + \mathbf{g}^T \cdot \mathbf{H_j}] = \mathbf{M}_0 + \mathbf{M}_1 + \mathbf{M}_1^T + \mathbf{M}_2 = \\ &= \mathbf{h_i}\mathcal{C}_{ij}\mathbf{h_j}^T + \mathbf{h_i}\mathcal{C}_{ij}\mathbf{g}^T \cdot \mathbf{H_j} + \mathbf{H_i} \cdot \mathbf{g}\mathcal{C}_{ij}\mathbf{h_j}^T + \mathbf{H_i} \cdot \mathbf{g}\mathcal{C}_{ij}\mathbf{g}^T \cdot \mathbf{H_j} \quad (4.58)\end{aligned}$$

where:

$\mathbf{M}^{geo}$ represents the core geometric stiffness matrix, as a result of non-linear effects.

$\mathbf{M}^{mat}$ represents the core material stiffness matrix.

$\mathbf{M}_0$ accounts for the linear effects.

$\mathbf{M}_1 + \mathbf{M}_1^T + \mathbf{M}_2$ account for the non-linear effects.

Finally, the total tangent stiffness matrix in global coordinates can be represented as:

$$\mathbf{K}^{tan^{e^{IJ^G}}} = \mathbf{T}^e \cdot \mathbf{K}^{tan^{e^{IJ}}} \cdot \mathbf{T}^{e^T} = \mathbf{T}^e \cdot \int_{V^{pret}} \mathbf{B}^{I^T} \cdot \mathbf{M}^{tan^e} \cdot \mathbf{B}^J \, dV \cdot \mathbf{T}^{e^T} \quad (4.59)$$

where:

$\mathbf{T}^e$ represents the rotation matrix at the finite element e.

$\mathbf{K}^{tan^{e^{IJ^G}}}$ represents the global total stiffness matrix corresponding to the nodes I and J belonging to the finite element e.

$\mathbf{K}^{tan^{e^{IJ}}}$ symbolizes the local total stiffness matrix corresponding to the nodes I and J belonging to the finite element e.

4.4 Energy principles.

The mathematical formulation of the structural problem has been collected in figures 4.1 or 4.3, which summarize the global equilibrium of the membrane by means of a system of nonlinear equations imposed on the nodes of the Lagrangian mesh. The solution of this system of equations by means of a perturbation-like or Newton-Raphson-like scheme may result in an algorithm with bad convergence properties. For the sake of this reason and given the implicit characteristics of the structural

membrane to be analyzed, an alternative approach based upon energy principles may be taken into consideration -see Oden and Ripperger (1981) for a further explanation of this technique.

Let us consider once again the material body in an initial prestressed configuration $\Re_{pret}$ -primary state, which after the application of a displacement field, it maps into a configuration $\Re$ -secondary state. The consideration of the loading process undertaken over the material body, enables the definition of three classical mathematical functionals known as:

- External potential energy functional.

$$\Pi_{ext} = -\int_{V^{pret}} \int_{\Re_{pret}}^{\Re} \rho^{pret} b_i du_i \; dV - \int_{\Gamma^{pret}} \int_{\Re_{pret}}^{\Re} \bar{t}_i du_i \, d\Gamma \tag{4.60}$$

- Internal potential energy functional.

$$U = \int_{V^{pret}} \int_{\Re_{pret}}^{\Re} S_{ij} dE_{ij} \; dV \tag{4.61}$$

- Total potential energy functional.

$$\Pi = U + \Pi_{ext} \tag{4.62}$$

The former functionals gather the external, internal and total potential energy accumulated in the structural membrane along the loading path. The process is considered to be adiabatic and kinematically slow, so the generation of thermal and kinematic energies can be neglected.

The system of global equilibrium nonlinear equations represented in the equation (4.4) was obtained through the semidiscretization procedure starting from the weak form of the structural problem or, equivalently, by means of the well known Principle of Virtual Work (PVW). From a mathematical perspective, this means that both internal and external nodal forces are derived from potential functionals, known as $\mathbf{U}$ and $-\mathbf{\Pi}_{ext}$ respectively. This mathematical property makes the mechanical system to be named as conservative. This principle is nothing more than the variational formulation of the total potential energy, also known as the Minimum Potential Energy Principle.

$$\delta\Pi = \delta U + \delta\Pi_{ext} = \delta W_{int} - \delta W_{ext} = 0 \Longleftrightarrow \delta W_{int} = \delta W_{ext} \tag{4.63}$$

Equation 4.63 represents the minimization of the total potential energy functional with respect to the displacement field. This formula may be understood as a classical unconstrained optimization problem for an objective function which results to be the total potential energy $\prod$. As a consequence, any appropriate technique may be used to carry out this mathematical optimization.

This alternative approach of understanding the structural problem by means of minimization techniques can be found in many References, for instance, Oden (1967), Bergan (1980), Monforton and El Hakim (1980), Hildebrandt and Tromba (1990), Leu and Yang (1990) and Gosling (1998). Figure 4.4 summarizes the different steps to reach the equilibrium solution: the total potential energy functional (zero order methods), its gradient or unbalanced force vector (first order methods), or even its hessian or total tangent stiffness matrix (second order methods). A comprehensive[8] explanation of these procedures is developed in Haftka and Gürdal (1992) and Samartín (1993).

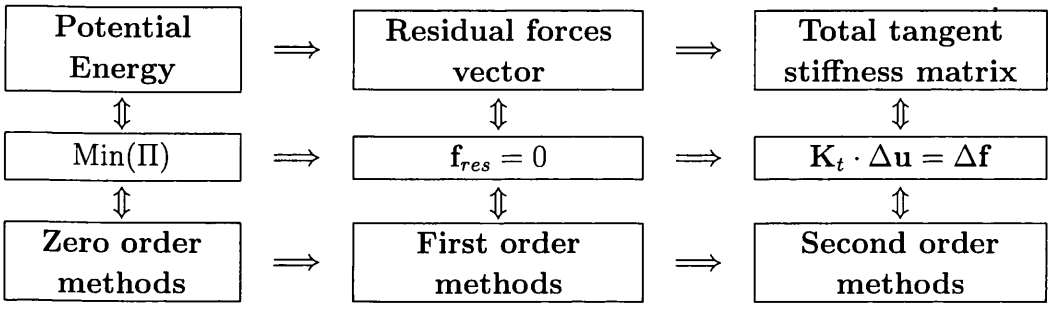

Figure 4.4: Variational formulation of the structural problem.

4.5 Concluding remarks

The complete structure is idealized as an assemblage of individual structural elements. The element stiffness matrices corresponding to global degrees of freedom of the structural idealization are calculated, and then the total stiffness matrix is formed by addition of the element stiffness matrices. The solution of the equilibrium equations of the assemblage of elements yields the element displacements, which are then used to calculate the element stresses.

Trial functions are used to approximate the actual displacements of the structure. The result of this is that the partial differential equilibrium equations are not satisfied in general, but this error is reduced as the finite element idealization of the structure or the continuum is refined.

The general formulation of the displacement-based finite element method is based on the use of virtual displacements, which is equivalent to the use of the Galerkin method, and also analogous to the use of the Ritz method to minimize the Total Potential Energy of the system -see Bathe (1996).

[8]According to Samartín (1993), first order methods are named *implicit methods* and second order methods are also known as *explicit methods*.

Chapter 5

Total Lagrangian Formulation: cable and membrane elements

5.1 Introduction.

Among the wide variety of tension structures in Architecture and Civil Engineering, both prestressed membranes and cable networks constitute a very remarkable group. These structures are achieving an increasing acceptance level in our society, for example, because of their aesthetic qualities and speed of erection. A large number of tensioned membranes are reinforced by means of interior and perimeter cables. Thus, the analysis of cable elements can be considered as a previous step for a further and comprehensive study of prestressed membranes. Extensive bibliography can be found related to the matter, although the most appealing References in accordance with the author's criterion are pointed out below. These References can be split into two distinct groups:

1. Those were analytical solutions are pursued by the author, namely, Otto (1962), Leonard (1988) and Kadlcak (1994).

2. Those were numerical solutions are attained by the author, that is, Peyrot and Goulois (1979), Jayaraman and Knudson (1981), Buchholdt (1985), Coyette and Guisset (1988), Swaddiwudhipong et al. (1989), Broughton and Ndumbaro (1994), Stefanou et al. (1994), Kwan (1998) and Arcaro (2001a).

Analogously, throughout the last decades, the state of the art of prestressed membranes shows a broad variety of publications, which might be allocated in three different categories:

1. Basic examples which are analyzed by means of analytical approaches; the strong formulation is solved in domains of simple geometry: see Timoshenko and Woinowsky-Krieger (1959), Otto (1967), Herzog (1977), Cortell (1984) and Leonard (1988).

2. Membranes which are assimilated to cable networks, whereby orthotropic hyperelastic membranes can be analyzed in a fairly accurate manner. Any of the References mentioned in previous paragraphs are valid examples.

3. The exact continuum approach for large strain non-prestressed membranes is studied in multiple References: Oden and Sato (1967), Grutmann and Taylor (1992), Souza et al. (1995), Wu et al. (1996) and Taylor (2001), Gosling and Lewis (1996a) and Gosling and Lewis (1996b). Recent developments are due to Bonet et al. (2000) and Bonet and Mahaney (2001). In all of them an ULF was employed.

The aim of this chapter is to summarize the Total Lagrangian Formulation (TLF) according to a Direct Core Congruential Format (DCCF) of both cable and membrane elements.

5.2 Cable elements.

Let us establish, according to figure 5.1, a fixed local coordinate system $OX_1^{pret}X_2^{pret}X_3^{pret}$. The direction OX_1^{pret} is adopted to move along the longitudinal axis of the cable. According to this criterion, the linear one-dimensional shape functions result to be:

$$N^1(X_1^{pret}) = 1 - \frac{X_1^{pret}}{L^{pret}} \qquad N^2(X_1^{pret}) = \frac{X_1^{pret}}{L^{pret}} \tag{5.1}$$

where L^{pret} stands for the initial prestressed length of the cable element. The displacement field and the final spatial coordinates may thus be interpolated in a standard manner as follows:

$$u_i = N^1 u_i^1 + N^2 u_i^2 \qquad x_i = N^1 x_i^1 + N^2 x_i^2 \qquad i = 1,2,3 \tag{5.2}$$

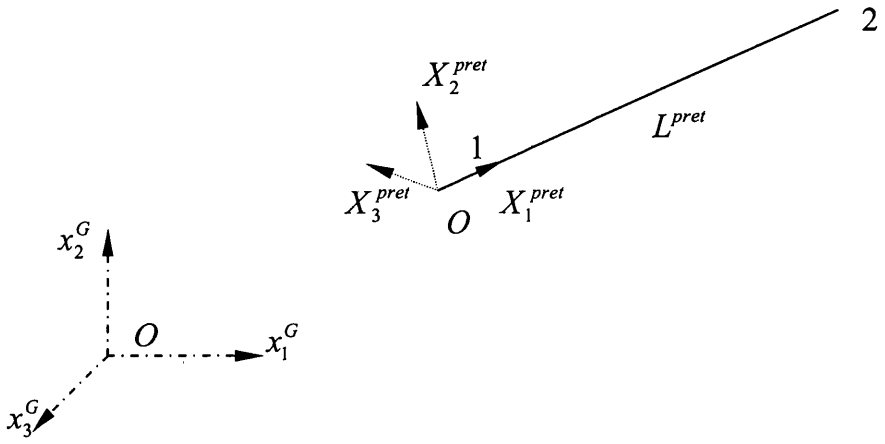

Figure 5.1: Cable element description.

The deformation gradient tensor F_{ij} may be composed as the sum of the displacement gradient tensor G_{ij} and the second order identity tensor δ_{ij} as:

$$F_{ij} = G_{ij} + \delta_{ij} \qquad G_{ij} = \frac{\partial u_i}{\partial X_j^{pret}} = (u_i^2 - u_i^1)\frac{\delta_{1j}}{L^{pret}} \qquad i,j = 1,2,3 \tag{5.3}$$

By employing the Direct Core Congruential Formulation (DCCF), the vectorized displacement gradient tensor is given in its transpose form as:

$$\mathbf{g}^T = \left[\frac{u_1^{21}}{L^{pret}} \quad \frac{u_2^{21}}{L^{pret}} \quad \frac{u_3^{21}}{L^{pret}} \quad 0 \quad 0 \quad 0 \quad 0 \quad 0 \quad 0 \right] \qquad u_i^{21} = u_i^2 - u_i^1 \tag{5.4}$$

By realizing that only the first three components of the former vector $\mathbf{g}$ are not null, let's define henceforth a particularized displacement gradient vector $\mathbf{g}_c$ for a cable finite element as: $\mathbf{g}_c^T = (\ g_1 \quad g_2 \quad g_3\ )$. This vector may be related with the nodal displacement vector as follows:

$$\mathbf{g}_c = \mathbf{B}_c \cdot \mathbf{u} = \begin{bmatrix} \frac{\partial N^1}{\partial X_1^{pret}} & 0 & 0 & \frac{\partial N^2}{\partial X_1^{pret}} & 0 & 0 \\ 0 & \frac{\partial N^1}{\partial X_1^{pret}} & 0 & 0 & \frac{\partial N^2}{\partial X_1^{pret}} & 0 \\ 0 & 0 & \frac{\partial N^1}{\partial X_1^{pret}} & 0 & 0 & \frac{\partial N^2}{\partial X_1^{pret}} \end{bmatrix} \cdot \begin{bmatrix} u_1^1 \\ u_2^1 \\ u_3^1 \\ u_1^2 \\ u_2^2 \\ u_3^2 \end{bmatrix} \tag{5.5}$$

where the new matrix $\mathbf{B}_c$ has been introduced for the sake of convenience. Because of dealing with a cable element and by neglecting the transversal effects of the deformation, just the component E_{11} of the Green-Lagrange strain tensor is of main concern. This term may be described in terms of the components of the vector $\mathbf{g}_c$ as:

$$E_{11} = g_1 + \frac{1}{2}(g_1^2 + g_2^2 + g_3^2) = \mathbf{h_1}^T \cdot \mathbf{B}_c \cdot \mathbf{u} + \frac{1}{2}\mathbf{u}^T \cdot \mathbf{B}_c^T \cdot \mathbf{H_1} \cdot \mathbf{B}_c \cdot \mathbf{u} \tag{5.6}$$

where $\mathbf{H_1}$ stands for the second order identity tensor and $\mathbf{h_1}$ represents the first column of the latter. By adopting s_1 to symbolize the component S_{11} of the second Piola-Kirchhoff stress tensor, the vector of local equivalent internal forces may be represented as well by means of the DCCF as follows:

$$\mathbf{f}_{int} = \int_{V^{pret}} \mathbf{B}_c^T \cdot \phi_{int} dV = A^{pret} L^{pret} \mathbf{B}_c^T \cdot \phi_{int} = A^{pret} \begin{bmatrix} -\mathbf{I}_3 \\ \mathbf{I}_3 \end{bmatrix} \cdot \phi_{int} \tag{5.7}$$

where A^{pret} stands for the cross sectional area of the cable in the prestressed configuration, $\mathbf{I}_3$ is the 3x3 identity matrix and ϕ_{int} is presented right below as :

$$\phi_{int} = s_1(\mathbf{h_1} + \mathbf{H_1} \cdot \mathbf{B}_c \cdot \mathbf{u}) = \begin{bmatrix} s_1(1+g_1) \\ s_1 g_2 \\ s_1 g_3 \end{bmatrix} \qquad \mathbf{g}_c = \frac{1}{L^{pret}} \begin{bmatrix} u_1^{21} \\ u_2^{21} \\ u_3^{21} \end{bmatrix} \tag{5.8}$$

By combining equations (5.7), (5.8) and by premultiplying by the correspondent rotation matrix, it is feasible to accomplish the global vector of internal forces with respect to a global cartesian reference system $OX_1^G X_2^G X_3^G$:

$$\mathbf{f}_{int}^{G^T} = \frac{S_{11} A^{pret}}{L^{pret}} \begin{bmatrix} -x_1^{21^G} & -x_2^{21^G} & -x_3^{21^G} & x_1^{21^G} & x_2^{21^G} & x_3^{21^G} \end{bmatrix} \tag{5.9}$$

where:

$$x_i^{21^G} = X_i^{21^G} + u_i^{21^G} = x^{2^G} - x^{1^G} = X^{2^G} - X^{1^G} + u^{2^G} - u^{1^G} \tag{5.10}$$

The constitutive equation according to the prestressed Saint Venant-Kirchhoff hyperelastic material may be represented as:

$$S_{11} = \sigma_{11}^{pret} + E(E_{11} - E_{11}^0) \tag{5.11}$$

where the initial Green-Lagrange strain component E_{11}^0 may be considered as a possible thermal effect which depends upon the dilatational coefficient, the initial and final temperatures as:

$$E_{11}^0 = \alpha \Delta T = \alpha(T^{end} - T^{ini}) \tag{5.12}$$

The linearization of the equivalent internal forces vector is fundamental to solve the geometrically nonlinear equilibrium problem. After carrying it out, the so called total tangent stiffness matrix appears to be the key feature of this technique. By means of the DCCF, an interesting relationship may be obtained whereby the latter matrix can be related to the one expressed in terms of the components of the displacement gradient tensor as follows:

$$\mathbf{K}^{tan} = \int_{V^{pret}} \mathbf{B}_c^T \cdot \mathbf{M}^{tan} \cdot \mathbf{B}_c dV \tag{5.13}$$

where the matrix in terms of the displacement gradient variables can be developed easily as:

$$\mathbf{M}^{tan} = [\mathbf{h}_1 + \mathbf{H}_1 \cdot \mathbf{g}_c] C_{11} [\mathbf{h}_1^T + \mathbf{g}_c^T \cdot \mathbf{H}_1] + s_1 \mathbf{H}_1 = \mathbf{M}^{mat} + \mathbf{M}^{geo} \tag{5.14}$$

By substituting equation (5.14) back into equation (5.13) and after performing the necessary algebraic operations, the geometrical and material submatrices corresponding to nodes I and J can be deduced as:

$$\mathbf{K}^{geo^{IJ}} = \int_{V^{pret}} \mathbf{B}_c^{I^T} \cdot \mathbf{M}^{geo} \cdot \mathbf{B}_c^J dV = (-1)^{I+J} \frac{A^{pret}(\sigma_{11}^{pret} + EE_{11})}{L^{pret}} \mathbf{I}_3 \tag{5.15}$$

$$\mathbf{K}^{mat^{IJ}} = \int_{V^{pret}} \mathbf{B}_c^{I^T} \cdot \mathbf{M}^{mat} \cdot \mathbf{B}_c^J dV = (-1)^{r+s} \frac{EA^{pret}}{L^{pret}} \begin{bmatrix} x_1^{21} \\ x_2^{21} \\ x_3^{21} \end{bmatrix} \cdot \begin{bmatrix} x_1^{21} & x_2^{21} & x_3^{21} \end{bmatrix} \tag{5.16}$$

where E stands for the Young modulus for a particular considered cable element and x_i^{21} represents the difference between the ith spatial current coordinate of the extreme nodes of the element. To obtain the final total tangent stiffness matrix, it is only required to add equations (5.15) and (5.16) and to perform the corresponding rotating transformation from the local to the global reference frame.

The total incremental internal strain energy of the structure can be formulated as:

$$W_{int} = \int_{V^{pret}} w_{int} dV = \sum_{i=1}^{Nelem} A^{pret} L^{pret} [E_{11} \sigma_{11}^{pret} + \frac{1}{2} E E_{11}^2] \tag{5.17}$$

Relationship between the second Piola-Kirchhoff stress tensor and the Cauchy stress tensor is accomplished by means of a push forward operation $\boldsymbol{\sigma} = J^{-1}\mathbf{F}\cdot\mathbf{S}\cdot\mathbf{F}^T$. Once obtained the deformation gradient tensor and its jacobian:

$$\mathbf{F} = \begin{bmatrix} 1 + \frac{u^{21}}{L^{pret}} & 0 & 0 \\ \frac{v^{21}}{L^{pret}} & 1 & 0 \\ \frac{w^{21}}{L^{pret}} & 0 & 1 \end{bmatrix} \Rightarrow J = \det(\mathbf{F}) = 1 + \frac{u^{21}}{L^{pret}} \tag{5.18}$$

Thus:

$$\sigma_{11} = (1 + \frac{u^{21}}{L^{pret}}) S_{11} \tag{5.19}$$

Or analogously:

$$\sigma_{11} = S_{11}[1 + \frac{1}{L^{pret^2}} \begin{bmatrix} X_1^{21^G} & X_2^{21^G} & X_3^{21^G} \end{bmatrix} \cdot \begin{bmatrix} u_1^{21^G} \\ u_2^{21^G} \\ u_3^{21^G} \end{bmatrix}] \tag{5.20}$$

5.3 Membrane elements

The textile membrane is approximated by a discrete model consisting of a finite number *elem* of flat three-node isoparametric elements with linear shape functions. The geometry of each element in the initial prestressed state is thus, according to figure 5.2, defined by a plane of uniform thickness t bounded by straight lines which intersects at three points called nodes.

Once again, apart from the global reference frame, a fixed local coordinate system $OX_1^{pret}X_2^{pret}X_3^{pret}$ is established for each element. For the sake of simplicity, it is assumed that each element lies in the $OX_1^{pret}X_2^{pret}$ plane of its local coordinate system. Thus, the displacement field and the current coordinates can be interpolated in terms of the shape functions as:

$$u_i = N^1 u_i^1 + N^2 u_i^2 + N^3 u_i^3 \qquad x_i = N^1 x_i^1 + N^2 x_i^2 + N^3 u_i^3 \qquad i = 1,2,3 \tag{5.21}$$

$$
\begin{aligned}
N^I(X_1^{pret}, X_2^{pret}) &= \tfrac{1}{2\Gamma^{pret}}(a^I + b^I X_1^{pret} + c^I X_2^{pret}) \\
a^I &= X_1^{pret^J} X_2^{pret^K} - X_1^{pret^K} X_2^{pret^J} \\
b^I &= X_2^{pret^J} - X_2^{pret^K} \\
c^I &= X_1^{pret^K} - X_1^{pret^J} \\
\Gamma^{pret} &= \tfrac{1}{2}(c^K b^J - c^J b^K) \qquad I, J, K = 1, 2, 3
\end{aligned}
\tag{5.22}
$$

where Γ^{pret} is the area of the initial prestressed triangle. Note that the quantities a^I, b^I and c^I -named Zienkiewicz's coefficients, see for instance Levy and Spillers (1995)- are independent of the deformation of the membrane and are computed directly from the geometry of the initially prestressed shape. According to the DCCF, the vectorized displacement gradient tensor is given in its transpose form as:

$$
\begin{aligned}
\mathbf{g}^T &= \begin{bmatrix} g_1 & g_2 & g_3 & g_4 & g_5 & g_6 & g_7 & g_8 & g_9 \end{bmatrix} \\
\mathbf{g}^T &= \begin{bmatrix} \frac{b^I u_1^I}{2\Gamma^{pret}} & \frac{b^I u_2^I}{2\Gamma^{pret}} & \frac{b^I u_3^I}{2\Gamma^{pret}} & \frac{c^I u_1^I}{2\Gamma^{pret}} & \frac{c^I u_2^I}{2\Gamma^{pret}} & \frac{c^I u_3^I}{2\Gamma^{pret}} & 0 & 0 & 0 \end{bmatrix}
\end{aligned}
\tag{5.23}
$$

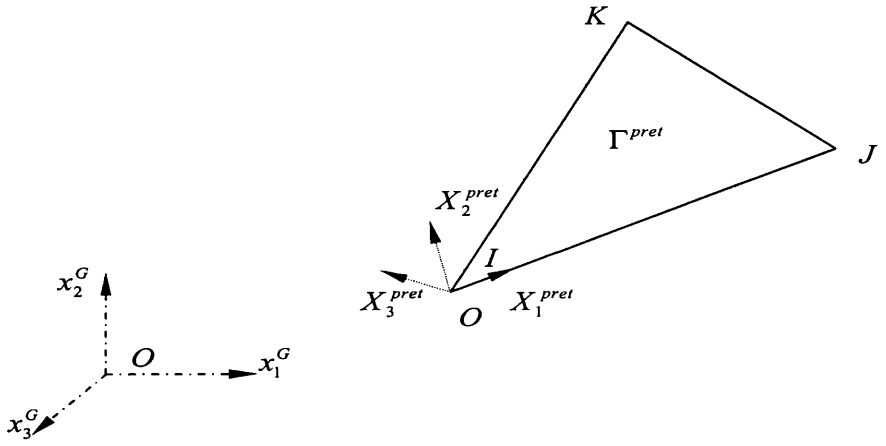

Figure 5.2: Membrane element description.

As it was recognized for the cable net approach, only the first six components of the vector $\mathbf{g}$ are distinct of zero. Therefore, it results convenient to consider a particular displacement gradient vector for the membrane case which will be named $\mathbf{g}_m$ as:

$$\mathbf{g}_m = \begin{bmatrix} g_1 \\ g_2 \\ g_3 \\ g_4 \\ g_5 \\ g_6 \end{bmatrix} = \mathbf{B}_m \cdot \mathbf{u} = \frac{1}{2\Gamma^{pret}} \begin{bmatrix} b^1\mathbf{I}_3 & b^2\mathbf{I}_3 & b^3\mathbf{I}_3 \\ c^1\mathbf{I}_3 & c^2\mathbf{I}_3 & c^3\mathbf{I}_3 \end{bmatrix} \cdot \begin{bmatrix} u_1^1 \\ u_2^1 \\ u_3^1 \\ u_1^2 \\ u_2^2 \\ u_3^2 \\ u_1^3 \\ u_2^3 \\ u_3^3 \end{bmatrix} \tag{5.24}$$

By neglecting the transversal deformations effects along the thickness of the membrane -an appropriate consideration for prestressed membranes developed into the architectural field, the Green-Lagrange strain tensor may be obtained according to the DCCF. In Voigt notation -see Belytschko et al. (2000) for further details, the first 2x2 minor may be depicted as:

$$\mathbf{e}^T = \begin{bmatrix} e_1 & e_2 & e_3 \end{bmatrix} = \begin{bmatrix} E_{11} & E_{22} & 2E_{12} \end{bmatrix} \tag{5.25}$$

$$e_i = \mathbf{h_i}^T \cdot \mathbf{g}_m + \frac{1}{2}\mathbf{g}_m^T \cdot \mathbf{H_i} \cdot \mathbf{g}_m = \mathbf{h_i}^T \cdot \mathbf{B}_m \cdot \mathbf{u} + \frac{1}{2}\mathbf{u}^T \cdot \mathbf{B}_m^T \cdot \mathbf{H_i} \cdot \mathbf{B}_m \cdot \mathbf{u} \tag{5.26}$$

$$\mathbf{H}_1 = \begin{bmatrix} \mathbf{I}_3 & \mathbf{0}_3 \\ \mathbf{0}_3 & \mathbf{0}_3 \end{bmatrix} \quad \mathbf{H}_2 = \begin{bmatrix} \mathbf{0}_3 & \mathbf{0}_3 \\ \mathbf{0}_3 & \mathbf{I}_3 \end{bmatrix} \quad \mathbf{H}_3 = \begin{bmatrix} \mathbf{0}_3 & \mathbf{I}_3 \\ \mathbf{I}_3 & \mathbf{0}_3 \end{bmatrix} \tag{5.27}$$

$$\begin{aligned} \mathbf{h}_1^T &= \begin{bmatrix} 1 & 0 & 0 & 0 & 0 & 0 \end{bmatrix} \\ \mathbf{h}_2^T &= \begin{bmatrix} 0 & 0 & 0 & 0 & 1 & 0 \end{bmatrix} \\ \mathbf{h}_3^T &= \begin{bmatrix} 0 & 1 & 0 & 1 & 0 & 0 \end{bmatrix} \end{aligned} \tag{5.28}$$

where again $\mathbf{I}_3$ stands for the 3×3 identity matrix and $\mathbf{0}_3$ represents the 3×3 null matrix. The vector of local equivalent internal forces is particularized for the triangular flat element by using the DCCF as:

$$\mathbf{f}_{int} = \int_{V^{pret}} \mathbf{B}_m^T \cdot \phi_{int}\, dV = t\, \Gamma^{pret} \mathbf{B}_m^T \phi_{int} = \frac{t}{2} \begin{bmatrix} b^1\mathbf{I}_3 & c^1\mathbf{I}_3 \\ b^2\mathbf{I}_3 & c^2\mathbf{I}_3 \\ b^3\mathbf{I}_3 & c^3\mathbf{I}_3 \end{bmatrix} \phi_{int} \tag{5.29}$$

where t stands for the membrane thickness, c^I, b^I have already been introduced above and ϕ_{int} is presented right below as:

$$\phi_{int} = s_i \mathbf{h_i} + s_i \mathbf{H_i g} = \begin{bmatrix} s_1(1+g_1) + s_3 g_4 \\ s_1 g_2 + s_3(1+g_5) \\ s_1 g_3 + s_3 g_6 \\ s_2 g_4 + s_3(1+g_1) \\ s_2(1+g_5) + s_3 g_2 \\ s_2 g_6 + s_3 g_3 \end{bmatrix} \tag{5.30}$$

By particularizing the constitutive equations for the prestressed isotropic Saint Venant-Kirchhoff textile in a taut state, they can be shown in Voigt form as:

$$\mathbf{s} = \{\boldsymbol{\sigma}^{pret}\} + \mathcal{C} \cdot \mathbf{e}$$

$$\begin{bmatrix} s_1 \\ s_2 \\ s_3 \end{bmatrix} = \begin{bmatrix} \sigma_{11}^{pret} \\ \sigma_{22}^{pret} \\ \sigma_{12}^{pret} \end{bmatrix} + \frac{1}{1-\nu^2} \begin{bmatrix} E & \nu E & 0 \\ \nu E & E & 0 \\ 0 & 0 & \frac{E(1-\nu)}{2} \end{bmatrix} \cdot \begin{bmatrix} e_1 \\ e_2 \\ e_3 \end{bmatrix} \tag{5.31}$$

Thermal effects may be included into the constitutive equations by means of the following modification to the above formula:

$$\mathbf{s} = \{\boldsymbol{\sigma}^{pret}\} + \mathcal{C} \cdot (\mathbf{e} - \mathbf{e}^0) \tag{5.32}$$

where the initial Lagrangian deformation tensor in Voigt notation may be expressed in terms of an isotropic thermal process, see (Oñate 1995):

$$\mathbf{e}^0 = \alpha \Delta T \begin{bmatrix} 1 \\ 1 \\ 0 \end{bmatrix} = \alpha (T^{end} - T^{ini}) \begin{bmatrix} 1 \\ 1 \\ 0 \end{bmatrix} \tag{5.33}$$

The total tangent stiffness matrix may be computed by means of the congruential transformation and thus the submatrix due to the contribution of the nodes I and J is depicted as:

$$\mathbf{K}^{IJ} = \frac{t}{4\Gamma^{pret}} (b^I b^J \mathbf{M}_{11} + c^I c^J \mathbf{M}_{22} + b^I c^J \mathbf{M}_{12} + c^I b^J \mathbf{M}_{21}) \qquad \mathbf{M}_{ij} = \mathbf{M}_{ij}^{geo} + \mathbf{M}_{ij}^{mat} \tag{5.34}$$

After some tedious but straightforward algebra, the geometrical and material components of the stiffness matrix $\mathbf{S}$ can be developed as follows:

$$\mathbf{M}^{geo} = \begin{bmatrix} \mathbf{M}_{11}^{geo} & \mathbf{M}_{12}^{geo} \\ \mathbf{M}_{21}^{geo} & \mathbf{M}_{22}^{geo} \end{bmatrix} \qquad \mathbf{M}^{mat} = \begin{bmatrix} \mathbf{M}_{11}^{mat} & \mathbf{M}_{12}^{mat} \\ \mathbf{M}_{21}^{mat} & \mathbf{M}_{22}^{mat} \end{bmatrix} \tag{5.35}$$

$$\mathbf{M}_{11}^{geo} = s_1 \mathbf{I}_3 \qquad \mathbf{M}_{11}^{mat} = \mathcal{C}_{11} \mathbf{f}_1 \mathbf{f}_1^T + \mathcal{C}_{33} \mathbf{f}_2 \mathbf{f}_2^T + \mathcal{C}_{13} \mathbf{f}_1 \mathbf{f}_2^T + \mathcal{C}_{31} \mathbf{f}_2 \mathbf{f}_1^T \tag{5.36}$$

$$\mathbf{M}_{12}^{geo} = s_3 \mathbf{I}_3 \qquad \mathbf{M}_{12}^{mat} = \mathcal{C}_{13} \mathbf{f}_1 \mathbf{f}_1^T + \mathcal{C}_{32} \mathbf{f}_2 \mathbf{f}_2^T + \mathcal{C}_{12} \mathbf{f}_1 \mathbf{f}_2^T + \mathcal{C}_{33} \mathbf{f}_2 \mathbf{f}_1^T \tag{5.37}$$

$$\mathbf{M}_{21}^{geo} = s_3\mathbf{I}_3 \qquad \mathbf{M}_{21}^{mat} = \mathcal{C}_{31}\mathbf{f}_1\mathbf{f}_1^T + \mathcal{C}_{23}\mathbf{f}_2\mathbf{f}_2^T + \mathcal{C}_{33}\mathbf{f}_1\mathbf{f}_2^T + \mathcal{C}_{21}\mathbf{f}_2\mathbf{f}_1^T \tag{5.38}$$

$$\mathbf{M}_{22}^{geo} = s_2\mathbf{I}_3 \qquad \mathbf{M}_{22}^{mat} = \mathcal{C}_{33}\mathbf{f}_1\mathbf{f}_1^T + \mathcal{C}_{22}\mathbf{f}_2\mathbf{f}_2^T + \mathcal{C}_{32}\mathbf{f}_1\mathbf{f}_2^T + \mathcal{C}_{23}\mathbf{f}_2\mathbf{f}_1^T \tag{5.39}$$

where s_i is the ith-component of the second Piola-Kirchfoff stress tensor in Voigt notation, $\mathbf{I}_3$ is the 3×3 identity matrix, $\mathcal{C}_{ij}$ is a component of the fourth order tensor of elastic moduli in Voigt notation and the vectors $\mathbf{f}_1$ and $\mathbf{f}_2$ constitute the first and second column of the deformation gradient tensor which can be expressed in their transpose forms as:

$$\mathbf{f}_1^T = \begin{bmatrix} 1+g_1 & g_2 & g_3 \end{bmatrix} \qquad \mathbf{f}_2^T = \begin{bmatrix} g_4 & 1+g_5 & g_6 \end{bmatrix} \tag{5.40}$$

The incremental internal strain energy is obtained as:

$$W_{int} = \int_{V^{pret}} w_{int}\, dV = \sum_{i=1}^{Nelem} t\, \Gamma^{pret}[\mathbf{e}^T \cdot \{\boldsymbol{\sigma}^{pret}\} + \frac{1}{2}\mathbf{e}^T \cdot \mathcal{C} \cdot \mathbf{e}] \tag{5.41}$$

Eventually, relationship between both Lagrangian and Eulerian stress tensors is accomplished through the use of a classical push forward operation, that is:

$$\mathbf{F} = \begin{bmatrix} 1+g_1 & g_4 & 0 \\ g_2 & 1+g_5 & 0 \\ g_3 & g_6 & 1 \end{bmatrix} \Rightarrow J = \det(\mathbf{F}) = (1+g_1)(1+g_5) - g_2g_4 \tag{5.42}$$

Therefore:

$$\{\boldsymbol{\sigma}\} = \frac{1}{J}\begin{bmatrix} (1+g_1)^2 & g_4^2 & 2(1+g_1)g_4 \\ g_2^2 & (1+g_5)^2 & 2(1+g_5)g_2 \\ (1+g_1)g_2 & (1+g_5)g_4 & (1+g_1)(1+g_5)+g_2g_4 \end{bmatrix} \cdot \mathbf{s} \tag{5.43}$$

Chapter 6

Nonconservative loading

6.1 Introduction.

A mechanical system is said to be **conservative** when both external and internal forces come from a potential functional. In other words, both types of forces can be derived as the gradient of the total potential energy. Mathematically:

$$\Pi = U + \Pi_{ext} \tag{6.1}$$

$$\mathbf{f}_{int} = \nabla U \quad \Longrightarrow \mathbf{f}_{int} \text{ are conservative} \tag{6.2}$$

$$\mathbf{f}_{ext} = -\nabla \Pi_{ext} \quad \Longrightarrow \mathbf{f}_{ext} \text{ are conservative} \tag{6.3}$$

When considering hyperelastic the constitutive behaviour of the material, it entails that the internal forces can be attained according to formula (6.2). This means that these forces constitute the gradient of the internal or strain energy functional. Therefore, the term *conservative* depends directly on the status of the external forces, that is, whether or not these forces come from a potential.

Non-conservative forces cannot be expressed by means of the formula (6.3). This fact prevents one to define a general Total Potential Energy **(TPE)** functional from which to derive both internal and external forces. Moreover, optimization numerical techniques cannot be applied at the energy level, unless the energy consumed by the non-conservative forces is stored incrementally[1].

Amongst the types of loading likely to act on prestressed membranes, there is one specific load which can be categorized as non-conservative. This is the so called wind loading. Usually, the wind is supposed to be applied pseudo-statically as an external distributed force normal to the exposed surface. Therefore, wind loading's direction changes continuously along with the membrane's deformation. This is the reason why theses forces are also known in the specific literature as *follower loads.*

The purpose of this chapter is to obtain in accordance with a **TLF**, the equivalent external nodal forces vector as well as its variation with respect to the displacements field of the prestressed membrane. Therefore, when using second order iterative schemes, a external load stiffness matrix will arise in order to be added to the already derived stiffness matrix.

6.2 Equivalent external nodal forces vector.

The external wind loading $\bar{\mathbf{t}}$ acting on the current surface of the membrane Γ, can be transformed into an equivalent external nodal forces vector by means of an **ULF** as follows:

[1] As was pointed out in a previous chapter, optimization methods working at the force level are named *first order methods*, whereas methods working at the stiffness level are known as *second order methods.*

$$\mathbf{f}^I_{ext} = \int_\Gamma N^I \bar{\mathbf{t}} d\Gamma \tag{6.4}$$

By regarding the wind load $\bar{\mathbf{t}}$ as continuously normal to the exposed surface, it can be rewritten in a more convenient manner by means of the unit normal vector $\mathbf{n}$ as:

$$\bar{\mathbf{t}} = -p\,\mathbf{n} \tag{6.5}$$

where p is the so called pressure parameter. By substituting equation (6.5) back into (6.4), and by taken into consideration Nanson's rule, see appendix D, the external force vector can be expressed in a TLF as:

$$\mathbf{n}\, d\Gamma = J\mathbf{F}^{-T} \cdot \mathbf{n}^{pret} d\Gamma^{pret} \tag{6.6}$$

$$\mathbf{f}^I_{ext} = \int_{\Gamma^{pret}} -p\, N^I J\mathbf{F}^{-T} \cdot \mathbf{n}^{pret} d\Gamma^{pret} = \int_{\Gamma^{pret}} -p\, N^I \mathrm{Adj}(\mathbf{F}) \cdot \mathbf{n}^{pret} d\Gamma^{pret} \tag{6.7}$$

where $\mathrm{Adj}(\mathbf{F})$ is the adjunct[2] matrix of $\mathbf{F}$. By particularizing for a three-noded isoparametric finite element, matrices $\mathbf{F}$ and $\mathrm{Adj}(\mathbf{F})$ can be rewritten in a DCCF as follows:

$$\mathbf{F} = \begin{bmatrix} 1+g_1 & g_4 & 0 \\ g_2 & 1+g_5 & 0 \\ g_3 & g_6 & 1 \end{bmatrix} \tag{6.8}$$

$$\mathrm{Adj}(\mathbf{F}) = \begin{bmatrix} 1+g_5 & -g_2 & g_2g_6 - (1+g_5)g_3 \\ -g_4 & 1+g_1 & g_3g_4 - (1+g_1)g_6 \\ 0 & 0 & (1+g_1)(1+g_5) - g_2g_4 \end{bmatrix} \tag{6.9}$$

As the unit normal vector in a local coordinate system can be expressed as $\mathbf{n}^{pret} = (0\ 0\ 1)^T$, then:

$$\mathrm{Adj}(\mathbf{F}) \cdot \mathbf{n}^{pret} = \begin{bmatrix} g_2g_6 - (1+g_5)g_3 \\ g_3g_4 - (1+g_1)g_6 \\ (1+g_1)(1+g_5) - g_2g_4 \end{bmatrix} \tag{6.10}$$

As for triangular finite elements the components of the displacement gradient tensor are constant within an element, thus, from equation (6.7):

$$\mathbf{f}^I_{ext} = -p\mathrm{Adj}(\mathbf{F}) \cdot \mathbf{n}^{pret} \int_{\Gamma^{pret}} N^I d\Gamma^{pret} = -p\frac{\Gamma^{pret}}{3}\mathrm{Adj}(\mathbf{F}) \cdot \mathbf{n}^{pret} \tag{6.11}$$

[2]Recall Cramer's Rule to calculate the inverse of a matrix $\mathbf{F}$ as: $\mathbf{F}^{-1} = \frac{1}{\det(\mathbf{F})}\mathrm{Adj}(\mathbf{F})^T$.

Eventually, in a global coordinate system, the above vector can be formulated by means of the rotation matrix $\mathbf{T}$ as follows:

$$\mathbf{f}_{ext}^{Ig} = \frac{-p\Gamma^{pret}}{3}\mathbf{T} \cdot \begin{bmatrix} g_2 g_6 - (1+g_5)g_3 \\ g_3 g_4 - (1+g_1)g_6 \\ (1+g_1)(1+g_5) - g_2 g_4 \end{bmatrix} \tag{6.12}$$

6.3 Linearization of the equivalent external nodal forces vector.

Applying a linearization or perturbation technique on the equivalent external nodal forces vector, a new stiffness matrix component is deduced, whose effect must be added up to the already calculated one. As it can be observed:

$$\mathbf{f}_{int} - \mathbf{f}_{ext} = \mathbf{0} \Longrightarrow (\mathbf{K}_{int} - \mathbf{K}_{ext}) \cdot \Delta\mathbf{u} = \mathbf{0} \tag{6.13}$$

Given the Lagrangian nodes I and J belonging to the same finite element, the component $\mathbf{K}_{ext}^{IJ}$ is obtained as:

$$\mathbf{K}_{ext}^{IJ} = \frac{\partial \mathbf{f}_{ext}^{I}}{\partial \mathbf{u}^{J}} \tag{6.14}$$

By employing the DCCF:

$$\mathbf{g}_m = \begin{bmatrix} g_1 \\ g_2 \\ g_3 \\ g_4 \\ g_5 \\ g_6 \end{bmatrix} = \mathbf{B}_m \cdot \mathbf{u} = \frac{1}{2\Gamma^{pret}} \begin{bmatrix} b^1\mathbf{I}_3 & b^2\mathbf{I}_3 & b^3\mathbf{I}_3 \\ c^1\mathbf{I}_3 & c^2\mathbf{I}_3 & c^3\mathbf{I}_3 \end{bmatrix} \cdot \begin{bmatrix} u_1^1 \\ u_2^1 \\ u_3^1 \\ u_1^2 \\ u_2^2 \\ u_3^2 \\ u_1^3 \\ u_2^3 \\ u_3^3 \end{bmatrix} \tag{6.15}$$

Thus, the components of the vector $Adj(\mathbf{F}) \cdot \mathbf{n}^{pret}$ can be reformulated as:

$$\Omega_1 = g_2 g_6 - (1+g_5)g_3 = \frac{1}{4\Gamma^{pret^2}} b^J c^K u_2^J u_3^K - (1 + \frac{1}{2\Gamma^{pret}} c^J u_2^J)\frac{1}{2\Gamma^{pret}} b^K u_3^K \tag{6.16}$$

$$\Omega_2 = g_3 g_4 - (1+g_1)g_6 = \frac{1}{4\Gamma^{pret^2}} b^J c^K u_3^J u_1^K - (1 + \frac{1}{2\Gamma^{pret}} b^J u_1^J)\frac{1}{2\Gamma^{pret}} c^K u_3^K \tag{6.17}$$

$$\Omega_3 = (1+g_1)(1+g_5) - g_2 g_4 = \\ = (1 + \frac{1}{2\Gamma^{pret}} b^J u_1^J)(1 + \frac{1}{2\Gamma^{pret}} c^K u_2^K) - \frac{1}{4\Gamma^{pret^2}} b^J c^K u_2^J u_1^K \tag{6.18}$$

Thus:

$$\mathbf{K}_{ext}^{IJ} = \frac{-p\Gamma^{pret}}{3} \begin{bmatrix} \frac{\partial \Omega_1}{\partial u_1^J} & \frac{\partial \Omega_1}{\partial u_2^J} & \frac{\partial \Omega_1}{\partial u_3^J} \\ \frac{\partial \Omega_2}{\partial u_1^J} & \frac{\partial \Omega_2}{\partial u_2^J} & \frac{\partial \Omega_2}{\partial u_3^J} \\ \frac{\partial \Omega_3}{\partial u_1^J} & \frac{\partial \Omega_3}{\partial u_2^J} & \frac{\partial \Omega_3}{\partial u_3^J} \end{bmatrix} \tag{6.19}$$

By carrying out some calculations, the above matrix can be simplified as follows:

$$\mathbf{K}_{ext}^{IJ} = \frac{-p}{6} \begin{bmatrix} 0 & g_6 b^J - g_3 c^J & g_2 c^J - (1+g_5) b^J \\ -g_6 b^J + g_3 c^J & 0 & g_4 b^J - (1+g_1) c^J \\ (1+g_5) b^J - g_2 c^J & (1+g_1) c^J - g_4 b^J & 0 \end{bmatrix} \tag{6.20}$$

This matrix is easily implemented into a computer code if defining the following parameters:

$$\zeta^J = g_6 b^J - g_3 c^J \tag{6.21}$$

$$\eta^J = g_2 c^J - (1+g_5) b^J \tag{6.22}$$

$$\mu^J = g_4 b^J - (1+g_1) c^J \tag{6.23}$$

The element stiffness may be assembled to come out with:

$$\mathbf{K}_{ext}^{IJ} = \mathbf{K}_{ext}^{I} = \frac{-p}{6} \begin{bmatrix} 0 & \zeta^I & \eta^I \\ -\zeta^I & 0 & \mu^I \\ -\eta^I & -\mu^I & 0 \end{bmatrix} \tag{6.24}$$

As can be straightforwardly seen, the matrix's elements do not depend on their rows but on their columns. Therefore, for nodes $1, 2, 3$ of a triangular finite element e, this matrix can be finally presented as:

$$\mathbf{K}_{ext}^{e} = \begin{bmatrix} \mathbf{K}_{ext}^1 & \mathbf{K}_{ext}^2 & \mathbf{K}_{ext}^3 \\ \mathbf{K}_{ext}^1 & \mathbf{K}_{ext}^2 & \mathbf{K}_{ext}^3 \\ \mathbf{K}_{ext}^1 & \mathbf{K}_{ext}^2 & \mathbf{K}_{ext}^3 \end{bmatrix} \tag{6.25}$$

Because of the lack of symmetry of this matrix, the final total tangent stiffness matrix will not be symmetric any more when dealing with non-conservative body forces. However, it can be shown that for a closed structure in a constant pressure field, the assembled external load stiffness is symmetric, see Bonet and Wood (1997) and Belytschko et al. (2000) for further details.

Chapter 7

Wrinkling Analysis

7.1 Introduction.

In the last decades, membranes have been widely used in many different Civil Engineering fields, see Wakefield (1999), Hangai and Wu (1999), Saitoh and Okada (1999) and Ando et al. (2000). Under certain loading conditions, a high likelihood exits for the development of wrinkled and slack regions within an otherwise taut membrane surface. The existence and severity of such wrinkled regions may have an important adverse effect on the overall stability of the structure. Therefore, a precise analysis of the wrinkling phenomenon is required. This undesiderable effect may be the result of an inadequate initial shape or of an inappropriate prestressed distribution or, may eventually be due to excessive loading in service conditions.

The proposed technique will move away from those other approaches where the modification of the kinematics of the problem is carried out in advance, see Roddeman et al. (1987a), Roddeman et al. (1987b), Steigmann and Pipkin (1989), Kang and Im (1997), Kang and Im (1999) and Lu et al. (2001), which tend to increase the difficulty of the involved formulation. Other authors such as Tabarrok and Qin (1992) and Stanuszek (2003), directly modify the expression for the second Piola-Kirchhof stress tensor, resulting in a modified Newton-Raphson algorithm. By following previous work by Gil (2003a), Gil (2003b) and Mahaney (2002), this chapter will present an efficient numerical technique for the computational simulation of wrinkles in a prestressed membrane, based upon the modification of the Helmholtz's free energy functional.

Once the fundamental equations for the analysis of prestressed membranes have been presented in previous chapters, an adequate methodology to study the occurrence of wrinkles can be developed. First of all, the basics of the hyperelastic finite deformation theory along principal directions is briefly introduced. The exposed framework is based upon the work of Bonet and Wood (1997), where an exhaustive treatment of the subject can be found. The next section is focused on the wrinkling phenomenon itself. A characterization in terms of the eigenvalues of the Cauchy stress tensor is presented to localize adequately each one of the possible membrane's states: slack, wrinkled or taut. A detailed derivation of these eigenvalues by taking as initial assumption the Helmholtz's free energy functional for prestressed hyperelastic Saint Venant-Kirchhoff membranes is performed. As a consequence, alternative and easy handling formulae will be encountered for the computational analysis of wrinkling. Specifically, a modified Helmholtz's free energy functional will be shown for wrinkled regions across the membrane's surface.

Next section focuses on the mathematical development of the stress and constitutive tensors after the appearance of wrinkling. A consistent derivation, see Malvern (1969), Chadwick (1999) and Holzapfel (2000), will be provided with the purpose of guaranteeing quadratic convergence under the use of a Newton-Raphson numerical scheme. The Voigt notation will be employed for the sake of notation purposes, see Belytschko et al. (2000).

7.2 Hyperelastic finite deformation theory along principal directions.

Let $\{\mathbf{N}_\alpha\}^{\alpha=1,2,3}$ be the unit orthogonal triad which defines the principal directions corresponding to the Green-Lagrange strain tensor $\mathbf{E}$. Likewise, this spatial triad aligns with the principal directions of the right Cauchy-Green deformation tensor $\mathbf{C}$. By considering ξ_α to be any of the eigenvalues of the tensor $\mathbf{E}$ (principal strains), it is feasible to develop the following expressions for the second order identity tensor $\mathbf{I}$, the tensor $\mathbf{E}$ and its inverse $\mathbf{E}^{-1}$, namely:

$$\mathbf{I} = \sum_{\alpha=1}^{3} \mathbf{N}_\alpha \otimes \mathbf{N}_\alpha \tag{7.1}$$

$$\mathbf{E} = \sum_{\alpha=1}^{3} \xi_\alpha \mathbf{N}_\alpha \otimes \mathbf{N}_\alpha \tag{7.2}$$

$$\mathbf{E}^{-1} = \sum_{\alpha=1}^{3} \frac{1}{\xi_\alpha} \mathbf{N}_\alpha \otimes \mathbf{N}_\alpha \tag{7.3}$$

Analogously, the right Cauchy-Green tensor can be expressed in terms of their eigenvalues, i.e. the stretches $\{\lambda_\alpha\}^{\alpha=1,2,3}$, as follows:

$$\mathbf{C} = \sum_{\alpha=1}^{3} \lambda_\alpha^2 \mathbf{N}_\alpha \otimes \mathbf{N}_\alpha \tag{7.4}$$

Hence, equations (7.2) and (7.4) can be combined in a straightforward manner to derive a relationship between the principal strains ξ_α and the stretches λ_α as:

$$\xi_\alpha = \frac{1}{2}(\lambda_\alpha^2 - 1) \tag{7.5}$$

By accounting for the polar decomposition theorem, i.e. $\mathbf{F} = \mathbf{R} \cdot \mathbf{U}$, the right Cauchy-Green tensor $\mathbf{C}$ can be rewritten in terms of the symmetric stretch tensor $\mathbf{U}$ as:

$$\mathbf{C} = \mathbf{F}^T \cdot \mathbf{F} = \mathbf{U} \cdot \mathbf{U} \tag{7.6}$$

Thus, relating equations (7.4) and (7.6), the material stretch tensor can be easily obtained as:

$$\mathbf{U} = \sum_{\alpha=1}^{3} \lambda_\alpha \mathbf{N}_\alpha \otimes \mathbf{N}_\alpha \tag{7.7}$$

The mapping of the unit triad $\mathbf{N}_\alpha{}^{\alpha=1,2,3}$ given by the tensor $\mathbf{F}$, after substituting the polar de composition theorem, enables to obtain a simple relationship with the unit triad $\mathbf{n}_\alpha{}^{\alpha=1,2,3}$, as follows:

$$\mathbf{F} \cdot \mathbf{N}_\alpha = \mathbf{R} \cdot \mathbf{U} \cdot \mathbf{N}_\alpha = \lambda_\alpha \mathbf{R} \cdot \mathbf{N}_\alpha = \lambda_\alpha \mathbf{n}_\alpha \tag{7.8}$$

By following the definition of a Saint Venant-Kirchhoff constitutive behaviour, the Helmholtz's free energy functional or strain energy functional w_{int} is a potential for the second Piola-Kirchhoff stress tensor, namely:

$$S_{ij} = \frac{\partial w_{int}}{\partial E_{ij}} = 2\frac{\partial w_{int}}{\partial C_{ij}} \tag{7.9}$$

For an isotropic behaviour, the aforementioned relation is independent on the adopted spatial coordinate system. Therefore, the Helmholzt's free energy functional can be expressed undoubtedly in terms of the three invariants of the Green-Lagrange strain tensor as follows:

$$w_{int} = w_{int}(I_{\mathbf{E}}, II_{\mathbf{E}}, III_{\mathbf{E}}) \tag{7.10}$$

By combining equations (7.9) and (7.10) and by carrying out the chain rule, the following formula can be displayed:

$$S_{ij} = \frac{\partial w_{int}}{\partial I_{\mathbf{E}}}\frac{\partial I_{\mathbf{E}}}{\partial E_{ij}} + \frac{\partial w_{int}}{\partial II_{\mathbf{E}}}\frac{\partial II_{\mathbf{E}}}{\partial E_{ij}} + \frac{\partial w_{int}}{\partial III_{\mathbf{E}}}\frac{\partial III_{\mathbf{E}}}{\partial E_{ij}} \tag{7.11}$$

The formal definition of the cited invariants of $\mathbf{E}$ allows to derive in tensorial notation:

$$I_{\mathbf{E}} = E_{ii} \quad \Longrightarrow \quad \frac{\partial I_{\mathbf{E}}}{\partial Eij} = \delta_{ij} \tag{7.12}$$

$$II_{\mathbf{E}} = E_{ij}E_{ij} \quad \Longrightarrow \quad \frac{\partial II_{\mathbf{E}}}{\partial Eij} = 2E_{ij} \tag{7.13}$$

$$III_{\mathbf{E}} = \det(\mathbf{E}) \quad \Longrightarrow \quad \frac{\partial III_{\mathbf{E}}}{\partial Eij} = \det(\mathbf{E})E_{ij}^{-1} \tag{7.14}$$

Formulae (7.12) to (7.14) can be substituted back into (7.11) to reflect:

$$S_{ij} = \frac{\partial w_{int}}{\partial I_{\mathbf{E}}}\delta_{ij} + 2\frac{\partial w_{int}}{\partial II_{\mathbf{E}}}E_{ij} + \det(\mathbf{E})\frac{\partial w_{int}}{\partial III_{\mathbf{E}}}E_{ij}^{-1} \tag{7.15}$$

Finally, expressions (7.1) to (7.3) can be combined with (7.15), namely:

$$\mathbf{S} = \sum_{\alpha=1}^{3}\left(\frac{\partial w_{int}}{\partial I_{\mathbf{E}}} + 2\frac{\partial w_{int}}{\partial II_{\mathbf{E}}}\xi_\alpha + \frac{\partial w_{int}}{\partial III_{\mathbf{E}}}\frac{\det(\mathbf{E})}{\xi_\alpha}\right)\mathbf{N}_\alpha \otimes \mathbf{N}_\alpha \tag{7.16}$$

An important remark to be pointed out from formula (7.16) is that the expression between parenthesis is a scalar. This implies that the principal directions pertaining to the tensors $\mathbf{C}$, $\mathbf{E}$ and $\mathbf{S}$ are coincident. The invariants of the tensor $\mathbf{E}$ and their derivatives can be displayed as follows:

$$I_{\mathbf{E}} = \xi_1 + \xi_2 + \xi_3 \tag{7.17}$$

$$II_{\mathbf{E}} = \xi_1^2 + \xi_2^2 + \xi_3^2 \tag{7.18}$$

$$III_{\mathbf{E}} = \xi_1 \xi_2 \xi_3 \tag{7.19}$$

$$\frac{\partial I_{\mathbf{E}}}{\partial \xi_\alpha} = 1 \tag{7.20}$$

$$\frac{\partial II_{\mathbf{E}}}{\partial \xi_\alpha} = 2\xi_\alpha \tag{7.21}$$

$$\frac{\partial III_{\mathbf{E}}}{\partial \xi_\alpha} = \frac{\det(\mathbf{E})}{\xi_\alpha} \tag{7.22}$$

These formulae along with the foregoing expression (7.16) for the second Piola-Kirchhoff stress tensor, allows to rewrite the latter in terms of the eigenvalues of the Green-Lagrange strain tensor $\mathbf{E}$, namely:

$$\mathbf{S} = \sum_{\alpha=1}^{3} \frac{\partial w_{int}}{\partial \xi_\alpha} \mathbf{N}_\alpha \otimes \mathbf{N}_\alpha = \sum_{\alpha=1}^{3} S_\alpha \mathbf{N}_\alpha \otimes \mathbf{N}_\alpha \tag{7.23}$$

With the purpose of obtaining an analogous expression for the Cauchy stress tensor $\boldsymbol{\sigma}$, the classical formula relating stress tensors $\mathbf{S}$ and $\boldsymbol{\sigma}$ is presented as follows:

$$\boldsymbol{\sigma} = J^{-1} \mathbf{F} \cdot \mathbf{S} \cdot \mathbf{F}^T \tag{7.24}$$

Substituting equation (7.23) into (7.24) results, after accounting for equations (7.5) and (7.8), in:

$$\boldsymbol{\sigma} = J^{-1}\mathbf{F} \cdot \left(\sum_{\alpha=1}^{3} \frac{\partial w_{int}}{\partial \xi_\alpha} \mathbf{N}_\alpha \otimes \mathbf{N}_\alpha \right) \cdot \mathbf{F}^T = \sum_{\alpha=1}^{3} J^{-1} \frac{\partial w_{int}}{\partial \xi_\alpha} (\mathbf{F} \cdot \mathbf{N}_\alpha) \otimes (\mathbf{F} \cdot \mathbf{N}_\alpha) =$$
$$= \sum_{\alpha=1}^{3} J^{-1}(1 + 2\xi_\alpha) \frac{\partial w_{int}}{\partial \xi_\alpha} \mathbf{n}_\alpha \otimes \mathbf{n}_\alpha \tag{7.25}$$

Eventually, formula (7.25) provides the relationship between the principal components of both stress tensor entities, $\boldsymbol{\sigma}$ and $\mathbf{S}$, which is given as:

$$\sigma_\alpha = \frac{(1 + 2\xi_\alpha)}{J} \frac{\partial w_{int}}{\partial \xi_\alpha} = \frac{(1 + 2\xi_\alpha)}{J} S_\alpha \tag{7.26}$$

7.3 Basic equations of wrinkling analysis.

Since membranes cannot undergo any compressive loading state, wrinkling phenomenon in a certain part of the membrane may be explained by a local buckling process. Among the wide variety of criteria to set whether wrinkling is being developed or not, the well known condition based upon the Cauchy stress tensor will be selected as the most preferable. Whenever any of the eigenvalues of this tensor $\boldsymbol{\sigma}$ becomes null, the membrane does not offer any resistance to be deformed any further. Roughly speaking, the Cauchy stress tensor does not admit negative eigenvalues or compression along the principal axes. Under this consideration, a set of equations will be obtained to be added to the classical kinetic, kinematic and constitutive equations presented in previous chapters.

Denoting the principal stresses by σ_1 and σ_2, with $\sigma_1 \geq \sigma_2$, the three states of a wrinkled membrane can be summarized as follows:

1. Taut state

$$\sigma_1 > 0, \quad \sigma_2 > 0 \tag{7.27}$$

2. Wrinkled state

$$\sigma_1 > 0, \quad \sigma_2 = 0 \tag{7.28}$$

3. Slack state

$$\sigma_1 = 0, \quad \sigma_2 = 0 \tag{7.29}$$

Let us recall the formula for the Helmholtz's free energy functional in the case of a prestressed Saint Venant-Kirchhoff hyperelastic membrane. For the sake of minimizing the number of indices displayed in forthcoming formulas, Voigt notation will be employed throughout the remaining of this section:

$$w_{int} = \sigma_i^{pret} e_i + \frac{1}{2} e_i \mathcal{C}_{ij} e_j \quad i,j = 1,2,3 \tag{7.30}$$

where:

w_{int} stands for the Helmholtz's free energy functional.

σ_i^{pret} represents the prestressed Cauchy stress tensor.

e_i stands for the Euler-Lagrange finite strain tensor.

$\mathcal{C}_{ij}$ represents the fourth order tangent moduli tensor.

Strain and stress tensors $\mathbf{E}$ and $\boldsymbol{\sigma}^{pret}$ can be rewritten in principal directions, which allows to reformulate the above equation (7.30) as:

$$w_{int} = \sigma_\alpha^{pret} \xi_\alpha + \frac{1}{2} \xi_\alpha \mathcal{C}_{\alpha\beta} \xi_\beta \quad \alpha,\beta = 1,2 \tag{7.31}$$

where:

σ_α^{pret} represents the prestressed Cauchy stress tensor in principal directions.

ξ_α stands for the Euler-Lagrange finite strain tensor in principal directions.

$\mathcal{C}_{\alpha\beta}$ represents the fourth order tangent moduli tensor.

The above tangent moduli tensor is defined for a Saint Venant-Kirchhoff material in Voigt notation as follows:

$$[\mathcal{C}_{\alpha\beta}] = \frac{1}{1-\nu^2}\begin{bmatrix} E & \nu E & 0 \\ \nu E & E & 0 \\ 0 & 0 & \frac{E(1-\nu)}{2} \end{bmatrix} \tag{7.32}$$

Equations (7.31) and (7.32), after being combined and expanded, can be rearranged in terms of the eigenvalues of the Green-Lagrange tensor $\mathbf{E}$, namely, ξ_1 and ξ_2, as:

$$w_{int}(\xi_1, \xi_2) = w_{int}^{pret}(\xi_1, \xi_2) + w_{int}^{0}(\xi_1, \xi_2) \tag{7.33}$$

$$w_{int}^{pret}(\xi_1, \xi_2) = \sigma_1^{pret}\xi_1 + \sigma_2^{pret}\xi_2 \tag{7.34}$$

$$w_{int}^{0}(\xi_1, \xi_2) = \frac{E\nu}{2(1-\nu^2)}(\xi_1 + \xi_2)^2 + \frac{E}{2(1+\nu)}(\xi_1^2 + \xi_2^2) \tag{7.35}$$

The principal strains ξ_1 and ξ_2 can be straightforwardly related to the principal invariants of the Green-Lagrange tensor, namely, $I_{\mathbf{E}}$ and $II_{\mathbf{E}}$, as:

$$I_{\mathbf{E}} = \xi_1 + \xi_2, \quad II_{\mathbf{E}} = \xi_1^2 + \xi_2^2 \tag{7.36}$$

Substitution of equation (7.36) back into formulae (7.33)-(7.35), would enable, if required, to re-define the energy functional w_{int} in terms of the invariants $I_{\mathbf{E}}$ and $II_{\mathbf{E}}$. Once the definition for the energy functional has been established, the onset of wrinkling can be characterized when the smallest of the σ_α values reaches the null value. Ordering the former ones in such a way that $\sigma_1 \geq \sigma_2$, it can be concluded:

$$\sigma_2 = 0 \tag{7.37}$$

By taking into account equation (7.26), the above condition can be re-expressed as follows:

$$S_2 = \frac{\partial w_{int}}{\partial \xi_2} = 0 \tag{7.38}$$

The above equation can be particularized for the energy functional (7.33)-(7.35), namely:

$$S_2 = \sigma_2^{pret} + \frac{E}{(1-\nu^2)}(\nu\xi_1 + \xi_2) = 0 \tag{7.39}$$

Therefore, the following relationship between principal strains ξ_1 and ξ_2 is deduced:

$$\xi_2 = f(\xi_1) := -\frac{E\nu\xi_1 + \sigma_2^{pret}(1-\nu^2)}{E} \tag{7.40}$$

Equations (7.33)-(7.35) and (7.40) can be combined to result in a modified Helmholtz's free energy functional which is given only in terms of the largest nonzero principal strain, namely:

$$\widehat{w}_{int} = \widehat{w}_{int}^{pret} + \widehat{w}_{int}^{0} \tag{7.41}$$

$$\widehat{w}_{int}^{pret} = \sigma_1^{pret}\xi_1 + \sigma_2^{pret} f(\xi_1) \tag{7.42}$$

$$\widehat{w}_{int}^{0} = \frac{E\nu}{2(1-\nu^2)}(\xi_1 + f(\xi_1))^2 + \frac{E}{2(1+\nu)}(\xi_1^2 + f(\xi_1)^2) \tag{7.43}$$

Analogously, the condition that must be fulfilled for wrinkling to occur in both principal directions, is that the principal Cauchy stresses σ_1 and σ_2 must be zero simultaneously. This can be obtained as follows:

$$\sigma_1 = 0 \tag{7.44}$$

Therefore, from formula (7.26) one obtains:

$$S_1 = \frac{\partial \widehat{w}_{int}}{\partial \xi_1} = 0 \implies \xi_1 = g := -\frac{\sigma_1^{pret} - \nu\sigma_2^{pret}}{E} \tag{7.45}$$

By substituting back this new condition into equations (7.41) to (7.43), a new expression for the modified Helmholtz's free energy functional is given as:

$$\widetilde{w}_{int} = -\frac{1}{2E}(\sigma_1^{pret^2} - 2\nu\sigma_1^{pret}\sigma_2^{pret} + \sigma_2^{pret^2}) \tag{7.46}$$

Therefore, as a consequence of the foregoing derivation, a set of conditions can be established to define uniquely the distinct wrinkling situations:

1. Taut state

$$\xi_1 > g, \quad \xi_2 > f(\xi_1) \tag{7.47}$$

2. Wrinkled state

$$\xi_1 > g, \quad \xi_2 \leq f(\xi_1) \tag{7.48}$$

3. Slack state

$$\xi_1 \leq g \tag{7.49}$$

where:

$$f(\xi_1) := -\frac{E\nu\xi_1 + \sigma_2^{pret}(1-\nu^2)}{E} \tag{7.50}$$

$$g := -\frac{\sigma_1^{pret} - \nu\sigma_2^{pret}}{E} \tag{7.51}$$

The Helmholtz's free energy functional for each one of the aforementioned situations is given as:

1. Taut state

$$w_{int} = w_{int}^{pret} + w_{int}^{0} \tag{7.52}$$

2. Wrinkled state

$$\widehat{w}_{int} = \widehat{w}_{int}^{pret} + \widehat{w}_{int}^{0} \tag{7.53}$$

3. Slack state

$$\widetilde{w}_{int} = -\frac{1}{2E}(\sigma_1^{pret^2} - 2\nu\sigma_1^{pret}\sigma_2^{pret} + \sigma_2^{pret^2}) \tag{7.54}$$

Once the modified Helmholtz's free energy functional has been properly defined for the different membrane states, consistent derivations for the second Piola-Kirchhoff and Cauchy stress tensors, as well as for the fourth order tangent moduli tensor can be formulated. For the taut state, derivations were presented in previous sections. For the wrinkled state, the corresponding formulae will be described subsequently. For the last case, the fact that the energy functional is no longer function of the strain ξ_α, leads to null values for each and every one of the above cited tensor entities.

7.3.1 Second Piola-Kirchhoff stress tensor.

As was previously pointed out, the energy functional can be redefined in terms of the invariants of the Green-Lagrange strain tensor $\mathbf{E}$, namely, $I_{\mathbf{E}}$ and $II_{\mathbf{E}}$. Thus, the second Piola-Kirchhoff stress tensor could be formulated as:

$$S_{ij} = \frac{\partial w_{int}}{\partial E_{ij}} = \frac{\partial w_{int}}{\partial I_{\mathbf{E}}}\delta_{ij} + 2\frac{\partial w_{int}}{\partial II_{\mathbf{E}}}E_{ij} \tag{7.55}$$

The former expression can be expanded in terms of the results for the first order partial derivatives of the Helmholtz's free energy functional, see appendix E for further details. Thus:

$$\frac{\partial w_{int}}{\partial I_{\mathbf{E}}} = \frac{\xi_2}{\xi_2 - \xi_1}\frac{\partial w_{int}}{\partial \xi_1} \tag{7.56}$$

$$\frac{\partial w_{int}}{\partial II_{\mathbf{E}}} = \frac{-1}{2(\xi_2 - \xi_1)}\frac{\partial w_{int}}{\partial \xi_1} \tag{7.57}$$

When the membrane achieves a wrinkled state, a new energy functional $\widehat{w}_{int}$ arises defined according to formulae (7.41) to (7.43). Hence, a new second Piola-Kirchhoff stress tensor can be defined in accordance with equation (7.55) as:

$$\widehat{S}_{ij} = \frac{\partial \widehat{w}_{int}}{\partial E_{ij}} = \frac{\partial \widehat{w}_{int}}{\partial I_{\mathbf{E}}}\delta_{ij} + 2\frac{\partial \widehat{w}_{int}}{\partial II_{\mathbf{E}}}E_{ij} \tag{7.58}$$

By accounting for formula (7.40), the first derivatives of the functional $\widehat{w}_{int}$ can be rewritten as:

$$\frac{\partial \widehat{w}_{int}}{\partial I_{\mathbf{E}}} = \frac{f(\xi_1)}{f(\xi_1) - \xi_1}\frac{d\widehat{w}_{int}}{d\xi_1} \tag{7.59}$$

$$\frac{\partial \widehat{w}_{int}}{\partial II_{\mathbf{E}}} = \frac{-1}{2(f(\xi_1) - \xi_1)}\frac{d\widehat{w}_{int}}{d\xi_1} \tag{7.60}$$

where:

$$\frac{d\widehat{w}_{int}}{d\xi_1} = \frac{d\widehat{w}_{int}^{pret}}{d\xi_1} + \frac{d\widehat{w}_{int}^{0}}{d\xi_1} \tag{7.61}$$

The first term on the right hand side of equation (7.61) is obtained by means of equations (7.40) and (7.42) as:

$$\frac{d\widehat{w}_{int}^{pret}}{d\xi_1} = \sigma_1^{pret} - \nu\sigma_2^{pret} \tag{7.62}$$

Analogously, the second term on the right hand side of equation (7.61) can be formulated from equations (7.40) and (7.43) after some algebra as:

$$\frac{d\widehat{w}_{int}^{0}}{d\xi_1} = E\xi_1 \tag{7.63}$$

By substituting expressions (7.59) to (7.63) back into formula (7.58) and by employing the Voigt notation to describe both second Piola-Kirchhoff stress tensor $\widehat{\mathbf{S}}$ ($\widehat{\mathbf{s}}$) and Green-Lagrange strain tensor $\mathbf{E}$ ($\mathbf{e}$), the following expression can be obtained:

$$\widehat{\mathbf{s}} = \frac{\sigma_1^{pret} - \nu\sigma_2^{pret} + E\xi_1}{f(\xi_1) - \xi_1}\begin{bmatrix} f(\xi_1) - e_1 \\ f(\xi_1) - e_2 \\ -e_3/2 \end{bmatrix} \tag{7.64}$$

7.3.2 Constitutive tensor.

By following the pattern of formula (7.58), the fourth order constitutive tensor is obtained in terms of the second order partial derivatives of $\widehat{w}_{int}$, see appendix E for further details, as follows, :

$$\widehat{C}_{ijkl} = \frac{\partial \widehat{S}_{ij}}{\partial E_{kl}} = \frac{\partial^2 \widehat{w}_{int}}{\partial I_{\mathbf{E}} \partial I_{\mathbf{E}}} \delta_{ij}\delta_{kl} + 2\frac{\partial^2 \widehat{w}_{int}}{\partial I_{\mathbf{E}} \partial II_{\mathbf{E}}} \delta_{ij} E_{kl} + 2\frac{\partial^2 \widehat{w}_{int}}{\partial II_{\mathbf{E}} \partial I_{\mathbf{E}}} E_{ij}\delta_{kl} + \\ + 4\frac{\partial^2 \widehat{w}_{int}}{\partial II_{\mathbf{E}} \partial II_{\mathbf{E}}} E_{ij}E_{kl} + 2\frac{\partial \widehat{w}_{int}}{\partial II_{\mathbf{E}}} \delta_{ij}\delta_{kl} \quad (7.65)$$

Each one of the above terms can be expanded in Voigt notation, namely:

$$\widehat{C} = \frac{\partial^2 \widehat{w}_{int}}{\partial I_{\mathbf{E}}^2} \begin{bmatrix} 1 & 1 & 0 \\ 1 & 1 & 0 \\ 0 & 0 & 0 \end{bmatrix} + 2\frac{\partial^2 \widehat{w}_{int}}{\partial I_{\mathbf{E}} \partial II_{\mathbf{E}}} \begin{bmatrix} e_1 & e_2 & \frac{e_3}{2} \\ e_1 & e_2 & \frac{e_3}{2} \\ 0 & 0 & 0 \end{bmatrix} + \\ + 2\frac{\partial^2 \widehat{w}_{int}}{\partial II_{\mathbf{E}} \partial I_{\mathbf{E}}} \begin{bmatrix} e_1 & e_1 & 0 \\ e_2 & e_2 & 0 \\ \frac{e_3}{2} & \frac{e_3}{2} & 0 \end{bmatrix} + 4\frac{\partial^2 \widehat{w}_{int}}{\partial II_{\mathbf{E}}^2} \begin{bmatrix} e_1^2 & e_1 e_2 & e_1\frac{e_3}{2} \\ e_2 e_1 & e_2^2 & e_2\frac{e_3}{2} \\ \frac{e_3}{2}e_1 & \frac{e_3}{2}e_2 & (\frac{e_3}{2})^2 \end{bmatrix} + \\ + 2\frac{\partial \widehat{w}_{int}}{\partial II_{\mathbf{E}}} \begin{bmatrix} 1 & 0 & 0 \\ 0 & 1 & 0 \\ 0 & 0 & \frac{1}{2} \end{bmatrix} \quad (7.66)$$

REMARK: In case of considering a cable element instead of a membrane element, the wrinkling condition is simply accomplished when the Cauchy stress component σ_{11} becomes zero. This requirement implies immediately the following value for the Green-Lagrange strain component

$$E_{11} = -\frac{\sigma_1^{pret}}{E} \quad (7.67)$$

Strains below that magnitude will not be allowed, entailing wrinkling behaviour. As a consequence, stress and constitutive tensors are zero. The energy functional can be showed as:

$$\widehat{w}_{int} = \frac{-\sigma_1^{pret^2}}{2E} \quad (7.68)$$

REMARK: If temperature effects are wanted to be considered, these can be taken into account by means of a modified Green-Lagrange strain tensor. That is, e_i and ξ_i should be changed by $(e_i - e_i^0)$ and$(\xi_i - \xi_i^0)$, respectively, where e_i^0 and ξ_i^0 should include the temperature effect.

Chapter 8

Topological meshing algorithms

8.1 Introduction.

The design of prestressed membranes is a complex process which involves several stages. The design stage can be highlighted as remarkable. Not in vane, it combines aesthetic interests -see Otto (1967), Hildebrandt and Tromba (1990), Ishii (1995) and Berger (1999)- with structural calculation challenges -see Lewis and Lewis (1996), Levy and Spillers (1998) and Canner and Hsu (1999).

The generation of an initial shape is a task that depends not only on the designer's criterion, that is, some other factors are also involved. The consideration of an arbitrary free form as initial configuration could derive in the appearance across the membrane of areas subjected to compressive or flexure strengths. This fact would promote instability phenomena. The initial shape must be adapted to the stress flux developed across the membrane. This procedure to generate the shape results in initial forms that verify the equilibrium equations.

Therefore, the form finding of a tensioned membrane consists of the determination of the equilibrium configuration corresponding to a prescribed stress distribution. Hence, the initial form adapts to the prestressing distribution by following a load-adaptive process, what reveals the non-linear nature of the problem -see Ramm (1992), Maurin and Motro (1997), Wakefield (1999) and Maurin and Motro (2001).

Numerous papers have been published on the shape finding problem of membranes and on the different techniques available to succeed it: Barnes (1988) and Ramm (1992). The description of the most important procedures may be found in Haber and Abel (1982a), Haber and Abel (1982b) and Wood (2002). The nonlinear methods based on incremental schemes by employing the Newton-Raphson algorithm have reached remarkable importance: Tabarrok and Qin (1992), Zhang and Tabarrok (1999) or Nouri-Baranger (2002). Recently, Bletzinger (1997) has introduced a new method whereby the initial configuration is updated progressively: Updated Reference Strategy (URS). This approach is also gathered in Bletzinger and Ramm (2001) and in Bonet and Mahaney (2001) is even improved.

All these nonlinear methods are nothing more than particular cases of the general problem consisting of the analysis of structural membranes subjected to external loads. Interesting references related to it are: Oden and Sato (1967), Grutmann and Taylor (1992), Souza et al. (1995), Gosling and Lewis (1996a), Gosling and Lewis (1996b), Wu et al. (1996), Bonet et al. (2000) and Taylor (2001).

8.1.1 Generalities about the Force Density Method (FDM).

The Force Density Method, firstly introduced by Linkwitz in 1971, was extensively revised in Linkwitz (1999). In this Reference interesting advantages of the technique may be found in detail. In Bletzinger (1997), this method is pointed out as a particular case of the formerly referred to as Updated Reference Strategy. Two-noded finite elements with linear shape functions are used as connectivity entities of the mesh's nodes. An assemblage of cable elements is then generated which will

enable to define the spatial geometry of the membrane by means of a simile cable network.

A brief introduction of this method is presented hereafter. The notation which will be used throughout this section is presented next:

I, J stand for nodes belonging to the structure's mesh.

n_I symbolizes the total number of nodes connected to node I.

k is an index to identify the k-th spatial direction. Thus $k = 1, 2, 3$.

T^{IJ} is the axial force along the element whose endpoints are I and J.

$\cos\theta_k^{IJ}$ stands for the k-th cartesian component of the unit vector which can be defined along the element that joins nodes I and J.

P_k^I represents the external nodal load acting on node I according to k-th cartesian direction.

L^{IJ} stands for the final stressed length of the element whose extreme nodes are I and J.

x_k^I is the k-th coordinate of the node I.

Every single point belonging to the analyzed domain must verify the local equilibrium equations, that is:

$$\forall I \Rightarrow \sum_{J=1, J\neq I}^{n_I} T^{IJ} \cos\theta_k^{IJ} = P_k^I \qquad k = 1, 2, 3 \tag{8.1}$$

where:

- The equality's left hand side gathers the internal elemental forces acting on node I according to their projections along the k-th direction.
- The right hand side symbolizes exterior acting forces projected along k-th direction.

The direction cosine can be computed as:

$$\cos\theta_k^{IJ} = \frac{x_k^I - x_k^J}{L^{IJ}} \tag{8.2}$$

By substituting equation (8.2) back into (8.1), it turns out to be::

$$\forall I \Rightarrow \sum_{J=1, J\neq I}^{n_I} T^{IJ} \frac{x_k^I - x_k^J}{L^{IJ}} = P_k^I \qquad k = 1, 2, 3 \tag{8.3}$$

The elements' lengths are easily obtained from their endpoints' coordinates as:

$$L^{IJ} = \sqrt{(x_1^I - x_1^J)^2 + (x_2^I - x_2^J)^2 + (x_3^I - x_3^J)^2} \tag{8.4}$$

If it is considered that exterior forces do not act on this first structural stage, that is, only pretressed loading is present, then equation (8.3) could be reformulated according to the following way:

$$\forall I \Rightarrow \sum_{J=1, J\neq I}^{n_I} T^{IJ} \frac{x_k^I - x_k^J}{L^{IJ}} = 0 \qquad k = 1, 2, 3 \tag{8.5}$$

The shape finding problem involves the solution of the $3n$ equilibrium equations of the system (8.5). In addition, essential or kinematic boundary conditions must be accounted for. These boundary conditions correspond to known anchorage points. To achieve the solution of the system (8.5), the ratio between the tension force and the final length for every cable element is set up. This parameter is the so called *force density coefficient*, whose name is due to the fact that it distributes the axial force along the element's length[1]. Indeed:

$$g^{IJ} = \frac{T^{IJ}}{L^{IJ}} \tag{8.6}$$

The mentioned force density coefficients (8.6) can be placed in the system of equations (8.5), to result in:

$$\forall I \Rightarrow \sum_{J=1, J\neq I}^{n_I} g^{IJ}(x_k^I - x_k^J) = 0 \qquad k = 1, 2, 3 \tag{8.7}$$

In the wake of setting up the force density coefficients g^{IJ} for all the cable elements IJ comprising the simile cable network, a solvable linear system of equations emerges as a result of formula (8.7). Solution of this system of equations enables to compute the nodal coordinates x_k^I of the structure. Then elements' length may be deduced through the use of equation (8.4). Eventually, the axial force in every cable element is obtained after rearranging equation (8.6) as: $T^{IJ} = g^{IJ} L^{IJ}$.

An important property associated to the system of equations (8.7) pertains to its uncoupling for all three spatial directions in $\mathbf{R}^3$. This fact implies that the system can be decomposed in three systems of n equations. By solving each system separately, computational time is considerably reduced. Provided this, computational implementation into a code has been performed for obtaining the results which are shown later in the chapter. The stiffness matrix of the above equilibrium system (8.7) presents the following attributes:

i) It is a positive definite matrix.

ii) It is a diagonally dominant matrix.

[1] According to Linkwitz (1999), the ratio of the force density coefficient between perimeter cables (that represent the reinforcing cables) and interior cables (that represent the textile fabric) should be in the range of $[5, 10]$.

iii) The matrix is, out of the diagonal, made up of a regular and uniform distribution of numerical values 0 and $-g^{IJ}$.

iv) Along the diagonal, positive values are found. These are obtained by the addition of various force density coefficients corresponding to adjacent cable elements.

Due to the aforementioned characteristics of the system of equilibrium equations, and in the wake of following the indications pointed out by the Kahan and Ostrowski-Reich theorems, see attached appendix A for further details, an iterative method called successive over-relaxation, with parameter $\omega = 1.5$, has been selected to find out its solution.

8.2 Topological meshing algorithms.

8.2.1 From the graph to the spatial mesh.

The generation of grids for complex geometries is an issue which requires too much space to be dealt with in great detail here. We shall present only some basic ideas and the properties that a grid should have.

By looking at the set of equations (8.7), the FDM may be regarded as a transformation procedure from a topological structure -where only nodal connectivities are relevant- to a real physical structure with spatial coordinates completely defined. Indeed, this method depends entirely on three factors, namely, the connectivity of the mesh, the force density distribution and the location of the anchorage points. Hence, the system of equations (8.7) can be numerically solved to lead to the spatial location of the membrane's nodes. Therefore, an initial topological distribution of nodes is demanded by the technique. This topological structure is perfectly identified by means of a graph, see Gorini (2000) and Iványi and Topping (2002).

A graph is a pair (V, E), where V is a finite set whose elements are the vertices of the graph and E is a collection of pairs of vertices called the edges of the graph. This is a mathematical entity whose main properties are gathered in the attached appendix C.

It is feasible, therefore, to set up a parent domain topologically isomorphic to that the membrane will finally embrace. Then, discretize such a parent domain in order to define a connectivity pattern or graph. This graph along with an arbitrary definition of the force density coefficients (between pairs of nodes) and the essential boundary conditions are needed in order to solve the system of equations (8.7).

As a consequence, two wide group of properties related to cable nets or membrane structures may be anticipated. Those which depend only on the type of connectivity in the net and not on the spatial location of its nodes. These properties are called combinatorial. On the other hand, the remainder which depends absolutely on the spatial configuration. These are the so called geometric properties. The first of

the former ones, therefore, are shared by all structures with the same topological disposition, see Graver (2001).

Knowing the most important properties of a graph, makes it possible to understand the incidence that those could have on the resulting spatial structure's properties. Within the wide group of properties that graphs can exhibit, the interest will be focused on those of direct application in the scope of membranes and cable nets.

Let us point out that the equilibrium configuration, obtained as a result of the FDM, is nominally stressed along the cable elements due to the values adopted for the force density coefficients g^{IJ}, see equation (8.6). The absolute value of such a prestressed effect can be as small as desired by adjusting suitably the absolute magnitude of the coefficients[2] g^{IJ}. The smaller the latter are, the more negligible the prestressed loading can be regarded.

Once the initial equilibrium configuration has been deduced (after applying the FDM), it can then be used as a reference surface to proceed with the subsequent static analysis under the external acting loads. Among those loads, real prestressed effects could be included. Indeed, the real prestressed configuration is then determined computationally exactly as in practical applications, by stretching the cables or moving the supports. Therefore, the prestressed Cauchy stress tensor as a result of this realistic prestressed loading is the one used as a basis for subsequent analyses under in-service loads.

8.2.2 Remarks about the topological discretization criterion.

It does not seem convenient to choose a random criterion to set up the domain's connectivity, also named as graph. This could result in the appearance of spatial structures considerably irregular and distorted, as well as isolated zones within the final mesh. The latter could emerge if the employed graph is not connected[3].

Besides, the selected graphs should be planar in order to guarantee the feasible representation of the membrane by means of a polyhedral surface. A planar graph is mathematically represented as a triplet (V, E, F), where apart from the sets V and E, previously defined, F represents the set of faces of the graph. Finally, they should dispose of a high number of vertices to provide accuracy in the final representation of the mesh. The latter should be carefully analyzed in order to avoid unnecessary computational time.

Furthermore, a homogeneous and isotropic graph representation should be pursued. The first is accomplished when a similar valence[4] is reached at every node of

[2]Although reducing the absolute magnitude of the force density coefficients, the ratio of such a factor between perimeter and interior cables should be maintained in the range of $[5, 10]$ according to Linkwitz (1999).

[3]The formal definition of a connected graph can be found in appendix C.

[4]The definition of valence can be found in appendix C.

the mesh. The latter is fulfilled when the distribution of elements does not have any preference along a certain spatial direction. These two conditions can be justified just by looking at the system of equations (8.7). As a matter of fact, the stiffness matrix of this system depends exclusively on the connectivity and on the force density coefficients per element. Therefore, an inadequate distribution of nodes would imply a very distorted final prestressed membrane.

Eventually, in the case of tensile structures, the final prestressed membrane acquires the shape of an anticlastic surface, that is, it possesses a negative Gaussian curvature across the whole domain. This means the non-existence of coplanar nodes -those with null Gaussian curvature- across the structure. To ensure this, according to Graver (2001), it is advisable the valence of every vertex to be less than or equal to six.

In case that a real cable network is analyzed, the set of faces F can be neglected, that is, only nodes and edges are demanded for the subsequent static analysis under a realistic prestressing loading or live loading. On the other hand, if the structural model considered for analysis is a membrane, then such a set of faces establishes the connectivity of the finite elements comprising the textile fabric, namely, triangle, quadrilateral and so on. In the examples shown in forthcoming chapters, only graphs which generate triangular faces are accounted for.

8.2.3 Shape finding flowchart.

The architectural design stage of any tensile structure, demands primary from the designer the definition of a finite set of fixed points or anchorage points. Let n be the cardinal of this set which conforms the group of upper and lower anchorage points of the membrane. As it is well known for tensile structures, it is required the anchorage points not to be coplanar in order to maintain negative the Gaussian curvature across the domain.

The plan view of these anchorage points defines a mathematically closed and bounded domain. This domain can be graphically defined by a series of straight lines between pairs of adjacent boundary nodes to result in a polygonal closed boundary. In this way, an irregular planar n-side polygon is obtained, which can be regarded topologically isomorphic to any other simple closed and bounded planar domain. This domain can be selected as a parent configuration. Then, the main tasks that have to be undertaken in order to obtain the final equilibrium shape are summarized in figure 8.1. A more detailed flowchart of the preprocessor stage is depicted in figure 8.2.

It is also convenient to point out the distinction that must be made between perimeter and internal edges within the final mesh. In fact, the prestressed force is transmitted from the anchorage points to the internal fabric textile by means of the perimeter cables. Because of this reason, the rigidity of these cables is regarded as considerably superior to those which tend to represent the internal textile fabric. Therefore, as previously suggested, a ratio within the range of $[5, 10]$ between perime-

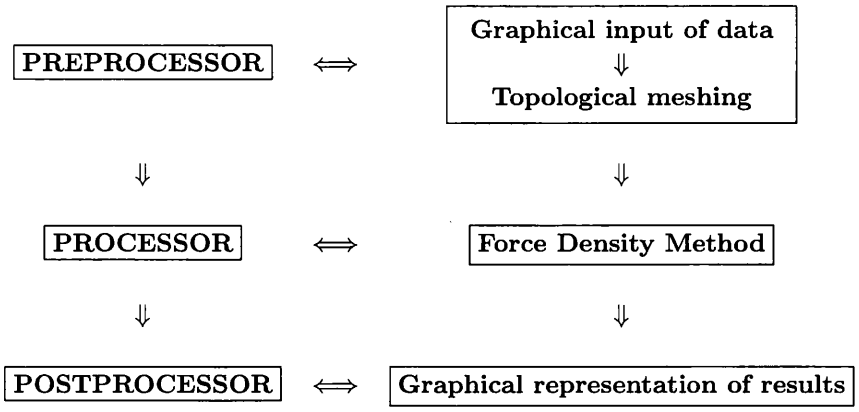

Figure 8.1: Shape finding flowchart.

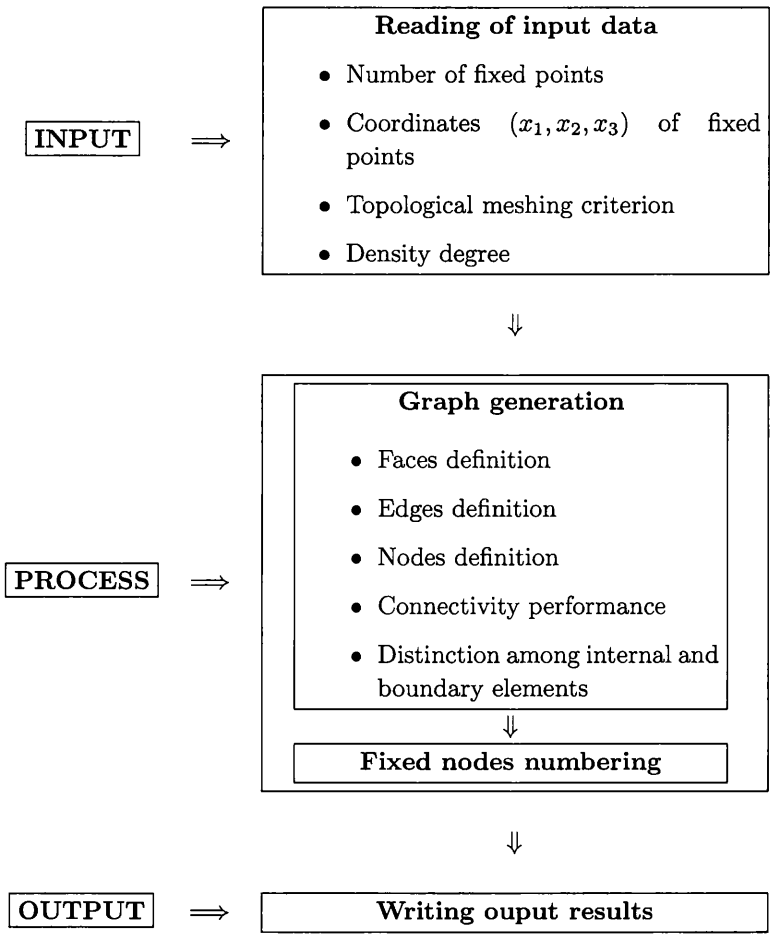

Figure 8.2: Shape finding preprocessor flowchart.

ter and interior cables, is frequently employed to account for this matter. Moreover, if it is desired to model the behaviour of rigid beams as boundary elements, it can be achieved by rising drastically their force density coefficient g^{IJ}.

Henceforth, several numerical examples[5] demonstrating the calculation of the equilibrium shape in tensile structures by means of the aforementioned technique are presented. Different algorithmic techniques for the generation of plane graphs are briefly detailed.

Algorithm for radial planar graphs.

Consider the plan view of the domain shown in figure 8.3, delimiting a given membrane. It clearly presents an image rather axisymmetric with respect to an interior point of its compact domain. It is then feasible to consider the circle as the most adequate topologically isomorphic domain to establish an internal graph.

Indeed, a planar graph can be set up within such a parent domain by a series of radii (n_r stands for the number of radii that are considered) and concentric circles (n_c symbolizes the number of concentric circles that are considered). Thus, a series of nodes $\{1, \ldots n_r(n_c + 1)\}$ and edges $\{1, \ldots 2^{n_c} n_r\}$ are obtained as the result of a simple recurrence formula. Figure 8.4 displays the general numbering of nodes and edges.

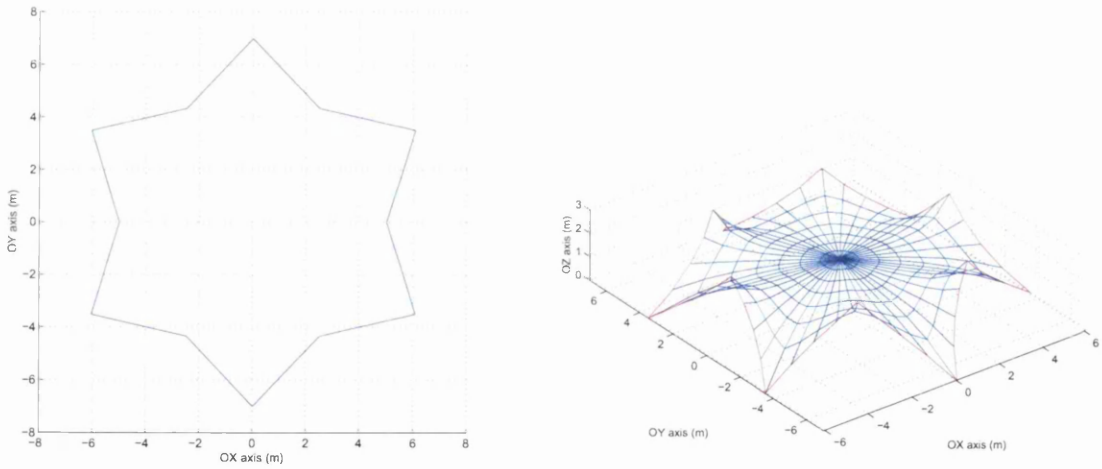

Figure 8.3: Roof with radial meshing.

Figure 8.3 shows the isometric view of the membrane, once the shape finding method has been employed according to the mesh criterion described. As it can deduced, the topological structure obtained from figure 8.4 has been transformed into a real spatial structure. For the generation of the topological mesh, numerical values such as $n_r = 48$ and $n_c = 6$ have been introduced into the calculations.

To achieve the final equilibrium shape, the spatial location of the nodes that define the boundary of the membrane as well as the node located at the center, have been set up as kinematic boundary conditions.

[5] A selected ratio between perimeter and internal cables of value 10 was adopted to run all the analyses.

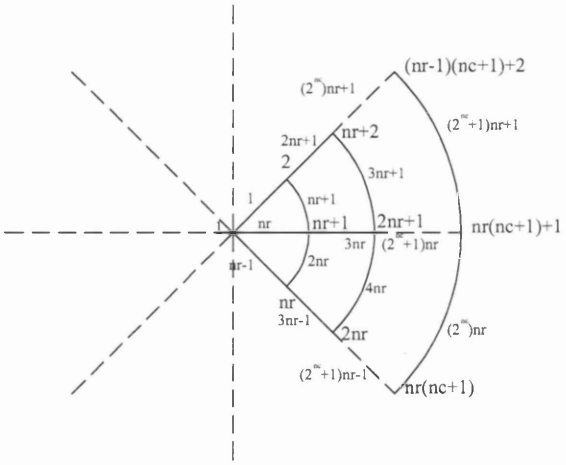

Figure 8.4: Meshing for a radial plane graph.

Algorithm for n-polygonal planar graphs.

When the plan view of the structure is completely irregular, a planar n-side polygon is advisable to be taken as the most adequate topologically isomorphic domain. As an example, figure 8.5 on the left shows the plan view of a real membrane domain starting from the anchorage points.

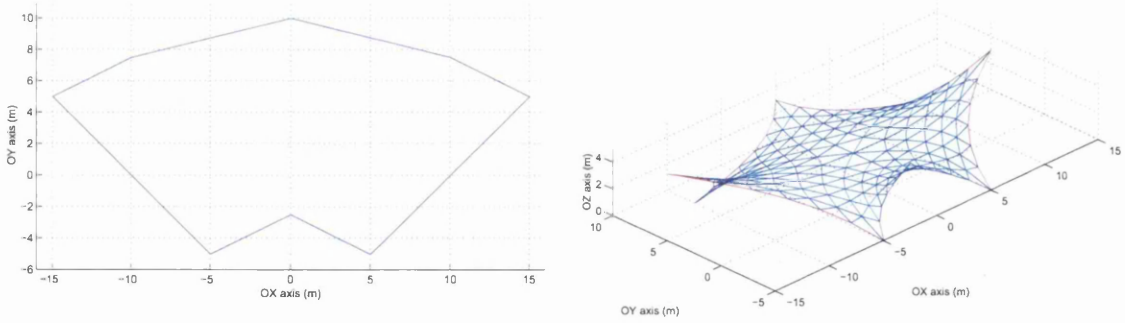

Figure 8.5: Roof with n-polygonal meshing.

The parent domain can be subdivided in n adjacent triangles by means of a series of straight lines drawn from an internal arbitrary node to the set of vertices comprising the perimeter of the polygon. Then, each one of those triangles can be meshed according to an arbitrary selected criterion. Thus, in case of using such a connectivity pattern, which is schematically sketched in figure 8.6, the resulting graph is defined by introducing two parameters: the number of polygon's sides n and the number of interior rings n_r. Development of simple recurrence formulae enable to enumerate the series of nodes, edges and faces.

Figure 8.5 on the right shows an isometric view of the final tensile membrane for

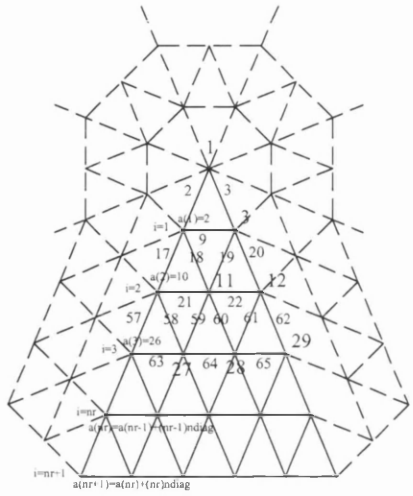

Figure 8.6: Meshing for an n-polygonal plane graph.

selected parameters $n = 8$ and $n_r = 5$. The nodes that determine the boundary of the membrane have been adopted as kinematic boundary conditions.

Algorithms for rectangular planar graphs.

When the plan view of the real membrane domain looks like a rectangle, i.e., four of its sides have a prevailing length over the remainder and opposite sides have similar lengths, the rectangle must be chosen as the most adequate topologically isomorphic domain to depict an internal graph. If the perimeter of the membrane has more than four sides, but it is feasible to split the boundary into four sides of similar length reached through the addition of adjacent sides, the described algorithm is valid as well. Figures 8.7 and 8.8 represent two possible internal graphs for a chosen rectangular reference domain, where vertices and edges appear enumerated.

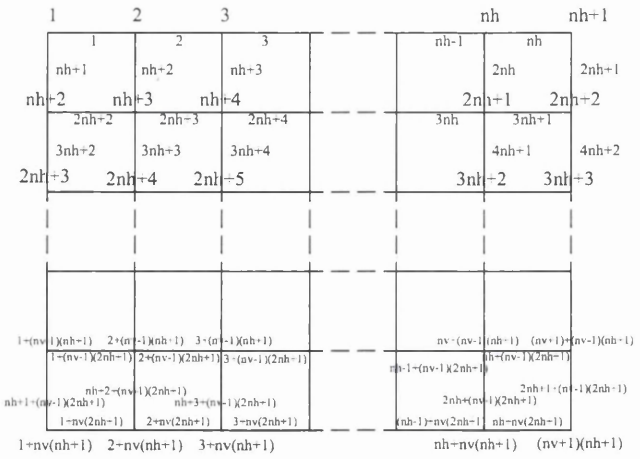

Figure 8.7: Meshing for a rectangular planar graph.

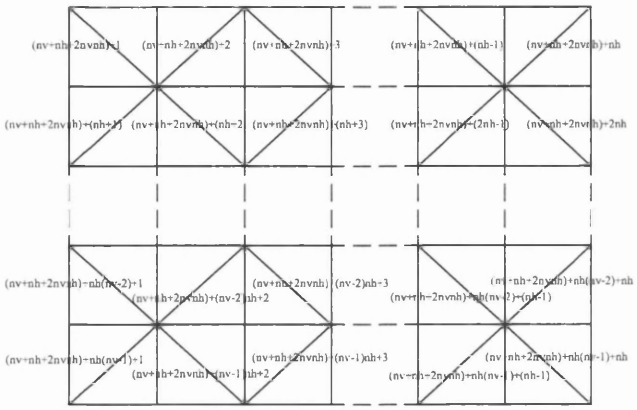

Figure 8.8: Meshing for a rectangular-diagonal planar graph.

In the second of the mentioned diagrams, diagonal edges are added with respect to the first diagram. Once again, new recurrence formulae were developed in order to enumerate the series of nodes, edges and faces. In both cases, the graph definition depends directly on the number of horizontal and vertical divisions, i.e., n_h and n_v, respectively. In both graphs, the number of nodes is $(n_v + 1)(n_h + 1)$. However, the inclusion of diagonal edges into the second graph increases its number of edges. In case of using the second of the above graphs, an even number of divisions in both orthogonal directions is recommended to be chosen in order to avoid spatial distortions.

To increase the number of edges on the final graph, it is possible either to select a large number of divisions n_h and n_v or to include the diagonals as new edges. Furthermore, let us point out that whereas the valence ρ of a face is 3 according to figure 8.8, $\rho = 4$ by looking at figure 8.7. Consequently, membrane finite elements of three or four nodes, respectively, should afterwards be employed for the static analysis .

The membrane with anchorage points according to the figure 8.9 on the left, has been calculated by means of a connectivity according to figure 8.7, with $n_h = 8$ and $n_v = 14$. The image 8.9 on the right gathers the isometric view of the final tensile structure. For the construction of this structural membrane, points that define the perimeter of the membrane and those that give form to the curved ridge beam crossing longitudinally, have been considered as fixed.

Analogously, for the membrane with anchorage points detailed according to figure 8.10 on the left, and by using a planar graph with the topological structure shown at figure 8.8, the calculation of the equilibrium shape of the membrane has been performed. To obtain the final results, parameters $n_h = 20$ and $n_v = 14$ have been selected, see figure 8.10 on the right. In this case, only the points that delimit the boundary of the membrane structure have been set up as fixed.

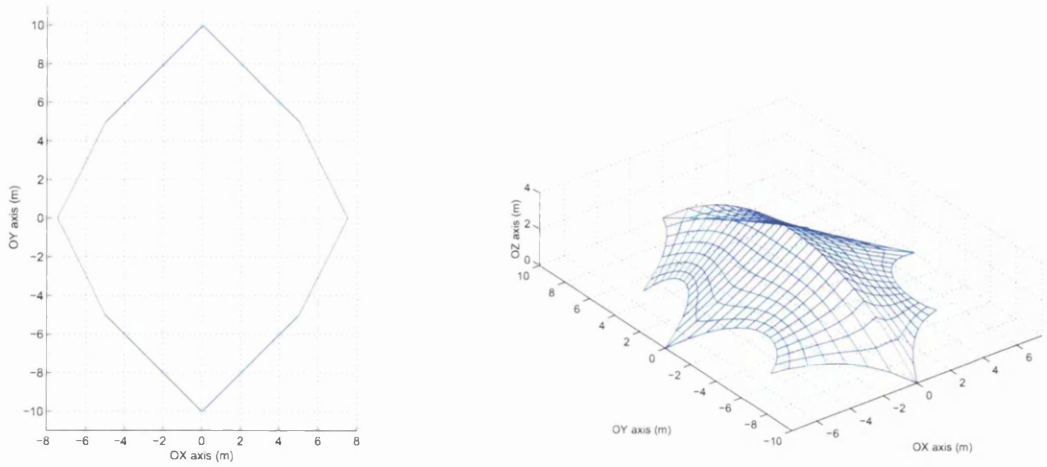

Figure 8.9: Roof with rectangular meshing.

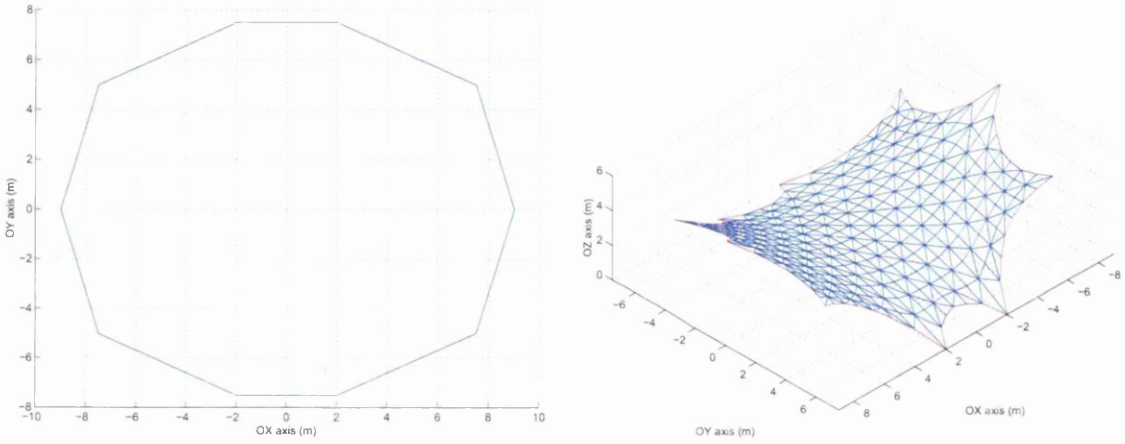

Figure 8.10: Roof with rectangular-diagonal meshing.

Algorithm for triangular planar graphs.

For the design of membrane structures when they are reinforced by means of perimeter cables, it is convenient sometimes to increase the number of membrane finite elements in proximity to the cables. Therefore, algorithmic techniques capable of refining the mesh as it approximates from the inner to the outer, become necessary. This section and the following one present two valid algorithms.

When the plan view of the real membrane domain presents similarities with respect to a triangle, because three of its sides or addition of adjacent sides have a similar and prevailing length over the rest, the triangle must be adopted as the most adequate topologicallly isomorphic domain to establish an internal plane graph.

Figure 8.11 on the left shows the plan view of the anchorage points belonging to the perimeter of a possible membrane. Figure 8.12 shows the graph for the generation of the internal connectivity. The numbering of faces, edges and vertices can be obtained by a developed recurrence formula. The degree of density of this graph is a function of the number of internal rings n_r considered within the triangle.

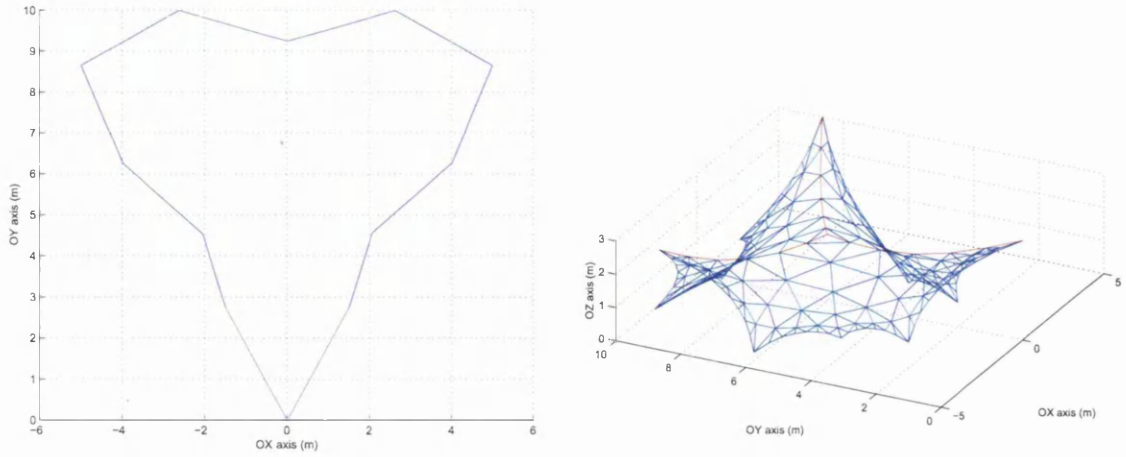

Figure 8.11: Roof with triangular meshing.

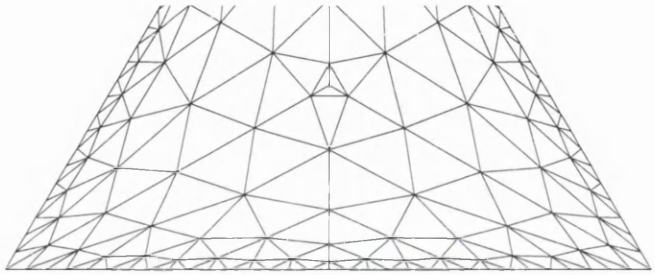

Figure 8.12: Meshing for a triangular planar graph.

Figure 8.11 shows isometric and plan views of the final tensile structure obtained from the chosen planar graph with a parameter $n_r = 5$. The points that define the boundary of the membrane as well as the central point of the plane graph have been considered fixed for the set of kinematic boundary conditions.

Algorithm for quadrangular planar graphs.

The graph that has been detailed in the former section can be extended to mesh a square: when the plan view of the structure presents four of its sides or addition of adjacent sides with length rather similar and prevailing over the rest of the perimeter's sides.

Figure 8.13 on the left shows the plan view of the membranes anchorage points and figure 8.14 displays the planar graph that has been employed for the creation of the internal connectivity. Again, the degree of density of the graph depends directly on the number of internal rings n_r.

Figure 8.13 on the right gathers the isometric view of the final tensile membrane. This is the result of the force density method applied on the topological structure described at figure 8.14 with $n_r = 5$. As kinematic boundary conditions, the spatial location of the nodes conforming the boundary of the membrane as well as an interior point of the planar graph have been considered fixed.

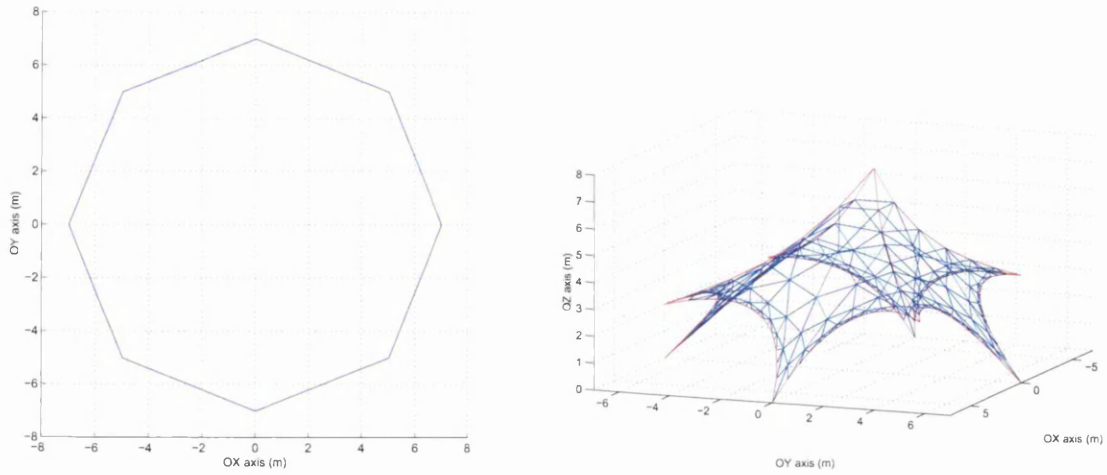

Figure 8.13: Roof with quadrangular meshing.

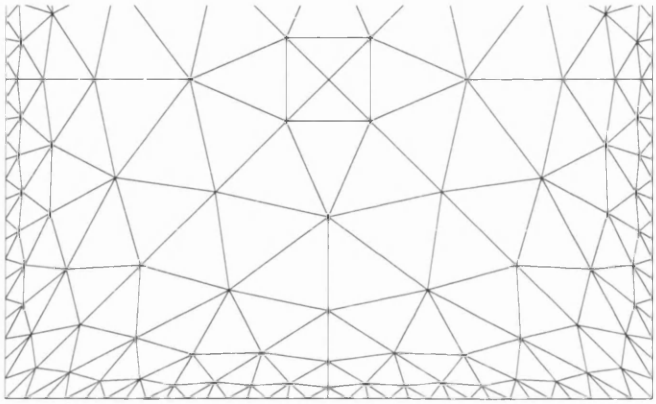

Figure 8.14: Meshing for a quadrangular planar graph.

8.3 Concluding remarks.

The FDM has been shown as an appropriate tool for the determination of an initial shape for tension structures (cable nets and fabric membranes). This equilibrium shape can be employed as an initial guess for the subsequent highly nonlinear problem that entails the structural analysis of the membrane under the actual presence of prestressing loading or external loading. The spatial distribution of the nodes as well as the existing connectivity among them (faces and/or edges), resulted from the method, are used as input data for the following structural calculation.

The FDM can be regarded as an instrument for the transformation of a topological structure (planar graph) into a real spatial structure. As a consequence, it results in a linear system of equations whose unknowns are the 3-D spatial coordinates of the nodes. The system is uncoupled for all the spatial directions. The algorithms to be employed for the generation of graphs should provide planar, isotropic and connected graphs. According to the 3-D spatial configuration of the membrane (axisymmetric, rectangular,...), a type of graph is selected (radial, rectangular,...).

Part III

Numerical methods

Chapter 9

Unconstrained optimization: numerical methods

9.1 Introduction.

In this chapter, we consider optimization problems of the form:

$$minimize\ f(\mathbf{x}) \quad subject\ to\ \mathbf{x} \in \Omega \tag{9.1}$$

where f is a real-valued function and Ω, the feasible set, is a subset of $\mathbf{R}^n$. If $\Omega \equiv \mathbf{R}^n$, the optimization problem is said to be *unconstrained.* Before presenting different nonlinear algorithms to solve these kinds of problems, a revision of some important definitions and theorems is shown.

Definition 1 (Local minimum point) *A point $\mathbf{x}^* \in \Omega$ is said to be a local minimum point of a function f over Ω if:*

$$\exists\, \epsilon > 0 \ / \ f(\mathbf{x}) \geq f(\mathbf{x}^*) \ \ \forall\, \mathbf{x} \in \Omega, \ \ \|\mathbf{x} - \mathbf{x}^*\| < \epsilon$$

Furthermore, a point $\mathbf{x}^* \in \Omega$ is said to be a strict local minimum of a function f over Ω if:

$$\exists\, \epsilon > 0 \ / \ f(\mathbf{x}) > f(\mathbf{x}^*) \ \ \forall\, \mathbf{x} \in \Omega, \ \ \|\mathbf{x} - \mathbf{x}^*\| < \epsilon$$

Definition 2 *A point $\mathbf{x}^* \in \Omega$ is said to be a global minimum point of a function f over Ω if:*

$$f(\mathbf{x}) \geq f(\mathbf{x}^*) \ \ \forall\, \mathbf{x} \in \Omega$$

Furthermore, it is said to be a strict global minimum if:

$$f(\mathbf{x}) > f(\mathbf{x}^*) \ \ \forall\, \mathbf{x} \in \Omega$$

The solution of the problem (9.1) entails, by definition, the search of a global minimum point on Ω. As a first approximation, necessary conditions are set up to guarantee the existence of local minimum points. By doing this, the search for a global minimum point will be replaced by the search for local minimum points. Among them, the former should be encountered. The existence of a global minimum point will be ensured by the imposition of some convexity conditions over the function f.

With the purpose of deriving necessary conditions for a point $\mathbf{x}^*$ to be a local minimum, we will start by introducing a concept related to the possible movement away from the point in some given direction. Along this *feasible direction* of movement, the function f, named *objective function* from now on, is transformed into a real-valued function of a single variable -the parameter defining movement in this direction-. This concept can be mathematically formulated as:

Definition 3 (Feasible direction) *Let $\mathbf{x} \in \Omega$ be a point, a vector $\mathbf{d}$ is said to be a feasible direction at $\mathbf{x}$ if:*

$$\exists\, \widehat{\alpha} > 0 \ / \ \mathbf{x} + \alpha \mathbf{d} \in \Omega \ \ \forall\, \alpha\ ,\ 0 \leq \alpha \leq \widehat{\alpha}$$

Once set up the previous concept and, by means of a Taylor series expansion of the single parameter function $g(\alpha) = f(\mathbf{x}^* + \alpha\mathbf{d})$, is possible to deduce the necessary conditions that must be satisfied for a minimum local point $\mathbf{x}^*$ of the function f to occur. These conditions can be allocated in two different categories: *first order* and *second order* conditions, according to the degree of derivative of the function f, namely, $f \in C^1$ or $f \in C^2$, respectively.

9.2 Local minimum point characterization.

Theorem 1 (First order necessary condition for local minima) *Let*[1] Ω *be a subset of* $\mathbf{R}^n$ *and let* f *be a* C^1 *function in* Ω. *If* $\mathbf{x}^*$ *is a local minimum point of* f *in* Ω, *then for all admissible directions* $\mathbf{d}$ *at* $\mathbf{x}^*$ *is verified that* $\nabla f(\mathbf{x}^*)^T \cdot \mathbf{d} \geq 0$. *This means that the directional derivative at the local minimum point is positive.*

As a consequence of the above theorem, an interesting corollary can be set up when the optimization problem is without restrictions, namely, $\Omega \equiv \mathbf{R}^n$ or, equivalently, when $\mathbf{x}^*$ is in the interior of Ω:

Corollary 1 *Let* Ω *be a subset of* $\mathbf{R}^n$, *let* f *be a* C^1 *function in* Ω. *If* $\mathbf{x}^*$ *is a local minimum point of* f *in* Ω *and if* $\mathbf{x}^*$ *is in the interior of* Ω, *then this implies that:* $\nabla f(\mathbf{x}^*) = 0$.

The former corollary yields the classical problem $\nabla f(\mathbf{x}^*) = 0$, that is, a non-linear n-dimensional system of equations.

Theorem 2 (Second order necessary condition for local minima) *Let*[2] Ω *be a subset of* $\mathbf{R}^n$ *and let* f *be a* C^2 *function in* Ω. *If* $\mathbf{x}^*$ *is a local minimum point* f *in* Ω, *then for all feasible directions* $\mathbf{d} \in \mathbf{R}^n$ *is verified:*

i) $\nabla f(\mathbf{x}^*)^T \cdot \mathbf{d} \geq 0$.

ii) if $\nabla f(\mathbf{x}^*)^T \cdot \mathbf{d} = 0$ *then* $\mathbf{d}^T \cdot \nabla^2 f(\mathbf{x}^*) \cdot \mathbf{d} \geq 0$.

Analogously, for unconstrained optimization problems, the following corollary arises:

Corollary 2 *Let* $\mathbf{x}^*$ *be a point which is the interior of* Ω, *and let* $\mathbf{x}^*$ *be a local minimum point in* Ω *of the function* $f \in C^2$. *Thus:*

i) $\nabla f(\mathbf{x}^*) = \mathbf{0}$.

[1] The demonstrations of this and the next theorems exposed in this chapter, can be found in Luenberger (1989) and Dennis Jr. and Schnabel (1996).

[2] With the expressions $\nabla f(\mathbf{x}^*)$ and $\nabla^2 f(\mathbf{x}^*)$ we denote the gradient and the Hessian of the function f evaluated at $\mathbf{x}^*$. The former is a vector of order n whereas the latter is a second order tensor of order $n \times n$.

ii) $\forall\, \mathbf{d},\ \mathbf{d}^T \cdot \nabla^2 f(\mathbf{x}^*) \cdot \mathbf{d} \geq 0.$

The second of the above conditions means that the Hessian of the function f at $\mathbf{x}^*$ is positive semidefinite.

Theorem 3 (Second order sufficient condition for local minima) *Let $f \in C^2$ be a function defined in a domain in such a way that $\mathbf{x}^*$ is in the interior of such a domain. Let us also suppose:*

i) $\nabla f(\mathbf{x}^*) = \mathbf{0}.$

ii) $\nabla^2 f(\mathbf{x}^*)$ *is positive definite.*

Then $\mathbf{x}^*$ is a strict local minimum point of f.

9.3 Convex and concave functions.

In order to develop a theory directed toward characterizing global, rather than local, minimum points, it is necessary to introduce some sort of convexity assumptions. This provides an interesting geometric interpretation of the second order sufficiency result derived above.

Definition 4 (Convex and concave functions) *A function f defined in a convex domain[3] Ω is said to be convex if $\forall\ \mathbf{x}_1$ and $\mathbf{x}_2\ \in \Omega$ and $\forall\ \alpha,\ 0 \leq \alpha \leq 1$, it is verified:*

$$f(\alpha \mathbf{x}_1 + (1-\alpha)\mathbf{x}_2) \leq \alpha f(\mathbf{x}_1) + (1-\alpha) f(\mathbf{x}_2)$$

Furthermore, if $\forall\ \alpha,\ 0 \leq \alpha \leq 1$ and $\mathbf{x}_1 \neq \mathbf{x}_2$,

$$f(\alpha \mathbf{x}_1 + (1-\alpha)\mathbf{x}_2) < \alpha f(\mathbf{x}_1) + (1-\alpha) f(\mathbf{x}_2)$$

then the function is named as strictly convex.

In case the function f is differentiable, then there exits an alternative characterization of convexity[4].

Proposition 1 *Let $f \in C^1$. Then f is convex over a convex set Ω if and only if:*

$$f(\mathbf{y}) \geq f(\mathbf{x}) + \nabla f(\mathbf{x}) \cdot (\mathbf{y} - \mathbf{x}) \quad \forall\, \mathbf{x},\ \mathbf{y}\ \in \Omega$$

For twice continuously differentiable functions, there is another characterization of convexity:

Proposition 2 *Let $f \in C^2$. Then f is convex over a convex set Ω if and only if the Hessian matrix of f is positive semidefinite throughout Ω.*

As a consequence of the above definition, we sometimes refer to a function as being locally convex if its Hessian matrix is positive semidefinite in a small region, and locally strictly convex if the Hessian is positive definite in the region.

[3] A domain $\Omega \in \mathbf{R}^n$ is said to be convex if $\forall\ \mathbf{x}_1,\ \mathbf{x}_2\ \in \Omega$ and $\forall\ \alpha,\ 0 < \alpha < 1$, the point $\alpha \mathbf{x}_1 + (1-\alpha)\mathbf{x}_2\ \in \Omega$. This means that given two points belonging to the domain, all the points located in the straight line which join them, belong as well as to the domain.

[4] Analogously, a function f is said to be *concave* if the function $-f$ verifies to be *convex*.

9.4 Minimization and maximization of convex functions.

When dealing with concave functions over convex sets, interesting properties can be implied to characterize the minima (maxima) that the functions can achieve. Some theorems are exposed right below:

Theorem 4 *Let f be a convex function defined on the convex set Ω. Then the set Γ where f achieves its minimum is convex, and any relative minimum of f is a global minimum.*

Theorem 5 *Let $f \in C^1$ be a convex function defined on the convex set Ω. If $\exists\, \mathbf{x}^* \in \Omega \;/\; \forall\, \mathbf{y} \in \Omega,\ \nabla f(\mathbf{x}^*)^T \cdot (\mathbf{y} - \mathbf{x}^*) \geq 0$, then $\mathbf{x}^*$ is a global minimum of the function f in the set Ω.*

As a summary, the above theorems offer sufficient conditions which enable to guarantee the existence of global minima in concave functions over convex sets.

9.5 Numerical methods.

We turn now to a description of the basic techniques used for iteratively solving unconstrained minimization problems. These techniques are, of course, important for their practical applications since they often offer the simplest, most direct alternative to achieve the solutions. Recall that an unconstrained optimization problem is settled in the following manner:

$$\textit{minimize } f(\mathbf{x}) \quad \textit{subject to } \mathbf{x} \in \Omega \textit{ with } \Omega \equiv \mathbf{R}^n \tag{9.2}$$

There are available numerous techniques to tackle the resolution of the problem (9.2). While some of them are simple, however, others can be really complex. The use of the former or the latter depends basically on the following issues:

- Sort of problem to be solved, that is, sort of objective function to be dealt with.
- Degree of convergence which is desired to accomplish throughout the process.
- Computational time, which defines how cheap or expensive the method is.

There is a fundamental underlying structure for almost all the descent algorithms we discuss. One starts at an *initial* point $\mathbf{x}^0$; determines, according to a fixed rule, a direction of movement (*feasible direction*) and a absolute distance (*step*); and then moves in that direction and with that step to a *relative minimum* of the *objective function* along that line. At the new point, $\mathbf{x}^1 = \mathbf{x}^0 + \alpha \mathbf{d}^0$, a new direction is determined and the process is repeated, namely:

$$\mathbf{x}^{k+1} = \mathbf{x}^k + \alpha \mathbf{d}^k, \quad k = 0, 1, 2, \ldots, n \tag{9.3}$$

The primary differences between algorithms rest with rule by which successive feasible directions are selected. Once the selection is made, all algorithms call for the movement to the minimum point on the corresponding line. This last process is called *parametric line search.* For general nonlinear functions that cannot be minimized analytically, this process is actually accomplished by searching, in an intelligent manner, along the line for the minimum point.

In Haftka and Gürdal (1992), a detailed summary is presented to classify the whole range of numerical algorithms into different categories, namely:

1. Zero order methods, which only use the value of the objective function f.
2. First order methods, which use the value of the objective function f as well as its gradient ∇f.
3. Second order methods, where the objective function f itself and its gradient ∇f and Hessian $\nabla^2 f$ are employed to carry out the minimization procedure.

Next sections will be devoted to a description and analysis of the basic descent algorithms for unconstrained problems.

9.6 The method of steepest descent.

This method[5] -also known as **gradient method-** is the easiest technique to be formulated but, at the same time, the most important for the sake of its consequences to the rest of the developed numerical schemes. More advance algorithms are often motivated by an attempt to modify this basic technique in such a way that the new algorithm will have superior convergence properties. This is, according to the above classification, a first order method.

Let $f \in C^1$ be the objective function over $\mathbf{R}^n$. For any point $\mathbf{x}^k$, the gradient of the functions f is defined as:

$$\mathbf{g}(\mathbf{x}^k) = \nabla f(\mathbf{x}^k) \tag{9.4}$$

or per every single cartesian component:

$$g_i(\mathbf{x}^k) = \frac{\partial f(\mathbf{x}^k)}{\partial x_i^k} \tag{9.5}$$

The method of steepest descent is defined by an iterative algorithm:

$$\mathbf{x}^{k+1} = \mathbf{x}^k - \alpha^k \mathbf{g}(\mathbf{x}^k), \quad k = 0, 1, 2, \ldots, n \tag{9.6}$$

[5]The steepest descent method was first proposed by Cauchy in 1847, according to Quesada (1996).

Roughly speaking, from the point $\mathbf{x}^k$ we search along the direction of the negative gradient $-\mathbf{g}(\mathbf{x}^k)$ to a minimum point on this line. Thus, the minimum point is taken to be $\mathbf{x}^{k+1}$. As it was already mentioned, the scalar α^k is obtained by minimizing the single parameter function $f(\mathbf{x}^k - \alpha^k \mathbf{g}(\mathbf{x}^k))$.

In Einstein's notation and by applying the chain rule, we can write:

$$\frac{df}{d\alpha^k} = \frac{\partial f}{\partial x_i^{k+1}} \frac{dx_i^{k+1}}{d\alpha^k} = 0 \quad \textit{to minimize } f \tag{9.7}$$

The above equation (9.7) can be rewritten in vector notation as follows:

$$\mathbf{g}(\mathbf{x}^{k+1})^T \cdot \mathbf{g}(\mathbf{x}^k) = 0 \tag{9.8}$$

which implies that two consecutive gradient vectors are orthogonal, that is, the scalar product between them yields null. By means of a Taylor series expansion of the function f and by assuming that this function could admit second order derivative, we get:

$$\mathbf{g}(\mathbf{x}^{k+1}) = \mathbf{g}(\mathbf{x}^k) + \nabla^2 f(\mathbf{x}^k) \cdot \mathbf{s}^k = \mathbf{g}(\mathbf{x}^k) - \nabla^2 f(\mathbf{x}^k) \cdot \alpha^k \mathbf{g}(\mathbf{x}^k) \tag{9.9}$$

Combining equations (9.8) and (9.9), it turns out to be:

$$\alpha^k = \frac{\mathbf{g}(\mathbf{x}^k)^T \cdot \mathbf{g}(\mathbf{x}^k)}{\mathbf{g}(\mathbf{x}^k)^T \cdot \nabla^2 f(\mathbf{x}^k) \cdot \mathbf{g}(\mathbf{x}^k)} \tag{9.10}$$

According to the above formula, the parametric line search is made analytically. As a matter of fact, in equation (9.10), the calculation of the parameter α^k requires to know in advance analytical expressions for the gradient and Hessian of the function[6] f. The sort of problems that we will deal with in this research present that feature, that is, the analyzed objective functions will be at least C^2.

A very important property of this method is that it satisfies the *Global Convergence Theorem*[7] for the algorithmic sequence (9.6). Therefore, no matter which initial guess is used to start the solution process, the method always converges towards the actual solution.

Finally, it is remarkable to point out the rate of convergence that can be accomplished with this numerical scheme when minimizing objective functions. In case the Hessian matrix of the function f is positive definite everywhere, that is, all its eigenvalues are real positive, thus the convergence is linear[8] verifying that:

$$f(\mathbf{x}^{k+1}) - f(\mathbf{x}^*) \leq c[f(\mathbf{x}^k) - f(\mathbf{x}^*)]$$

with a constant c such that:

$$c = \left(\frac{\lambda_{max} - \lambda_{min}}{\lambda_{max} + \lambda_{min}}\right)^2 = \left(\frac{r-1}{r+1}\right)^2 \leq r^2 \leq K^2 \tag{9.11}$$

[6] In index notation, $\nabla f(\mathbf{x})_i = \frac{\partial f(\mathbf{x})}{\partial x_i}$ and $\nabla^2 f(\mathbf{x})_{ij} = \frac{\partial^2 f(\mathbf{x})}{\partial x_i \partial x_j}$

[7] See appendix B for a discussion about this theorem.

[8] For a survey of the different degrees of convergence, refer to appendix B.

where:

λ_{max} is the largest eigenvalue of the Hessian.

λ_{min} is the smallest eigenvalue of the Hessian.

r is the ratio between the largest and the smallest eigenvalues.

K is the condition number[9] of the Hessian.

Hence, we can conclude that for a objective function whose Hessian is a positive definite matrix, the steepest descent method has a linear degree of convergence. Moreover, the smaller the ratio r or, equivalently, the nearer the condition number K to the unity[10], the faster the speed of convergence will be.

9.7 Newton's method.

The idea behind Newton's method is that the function f being minimized can be locally approximated by a quadratic function, and this approximate function is minimized exactly. Thus, let f be a twice differentiable function; then the Newton's algorithm[11] is derived as follows. As any other iterative algorithm, the general expression is adopted:

$$\mathbf{x}^{k+1} = \mathbf{x}^k + \mathbf{d}^k$$

Then the function m_c is defined as:

$$m_c(\mathbf{x}^{k+1}) = m_c(\mathbf{x}^k + \mathbf{d}^k) = f(\mathbf{x}^k) + \nabla f(\mathbf{x}^k)^T \cdot \mathbf{d}^k \tag{9.12}$$

The local minimum of this new function must satisfy:

$$\nabla m_c(\mathbf{x}^{k+1}) = \mathbf{0} \implies \nabla f(\mathbf{x}^k) + \nabla^2 f(\mathbf{x}^k) \cdot \mathbf{d}^k = \mathbf{0} \tag{9.13}$$

Thus:

$$\mathbf{x}^{k+1} = \mathbf{x}^k - \nabla^{-2} f(\mathbf{x}^k) \cdot \nabla f(\mathbf{x}^k) \tag{9.14}$$

Equation (9.14) summarizes a general formula for the Newton's method, which is a well known second order method. In contrast to the study of the steepest descent method, where global convergence followed almost immediately, this property is not guaranteed here. In fact, the following theorem reflects this issue.

[9] See appendix A.

[10] These matrices are referred to be *well conditioned* -see appendix A-.

[11] This method is known as well as Newton-Raphson's method.

Theorem 6 (Newton's method's convergence) *Let $f \in C^2$ over $\mathbf{R}^n$, let $\mathbf{x}^*$ be a local minimum point of f and that the Hessian of f is a positive definite matrix when evaluated at $\mathbf{x}^*$. Then, if the initial guess $\mathbf{x}^0$ is near enough the final solution $\mathbf{x}^*$, the algorithmic sequence of the Newton's method converges under a quadratic degree of convergence.*

This theorem, of great importance, about the fundamental features of Newton's method, can be summarized in two main key-points:

i) The method is locally convergent, but not always globally.

ii) The degree of convergence is two.

Therefore, this method possesses an interesting advantageous feature with respect to the previously described steepest descent method: the fact of its quadratically convergence with respect to the linear convergence of the latter. Nevertheless, a notable drawback emerges, that is, the method is not convergent unless the initial guess is good enough. Therefore, despite Newton's method results very appealing to be used, its convergence's deficiency results in the necessity of introducing some variations into its original formulation. Among the wide range of possible modifications, a two-fold action was undertaken in this research:

1. Numerical perturbation of the Hessian to assure that its eigenvalues are always positive.

2. Use of a parametric line search with the purpose of improving the step along the feasible direction.

9.8 Parametric line search.

By observing the equation (9.14), which summarizes the Newton's method, the feasible direction of movement can be identified as $-\nabla^{-2} f(\mathbf{x}^k) \cdot \nabla f(\mathbf{x}^k)$. The method adopts as step along that direction the module of such a vector, that is, $\|\nabla^{-2} f(\mathbf{x}^k) \cdot \nabla f(\mathbf{x}^k)\|$.

Nevertheless, an improvement can be introduced to such a formula by multiplying that step by a parameter α^k, with $0 \leq \alpha^k \leq 1$. This parameter will be chosen according to a parametric line search, that is, by minimizing the objective function along the feasible direction.

Thus, the new formulation can be displayed as:

$$\mathbf{x}^{k+1} = \mathbf{x}^k - \alpha^k \nabla^{-2} f(\mathbf{x}^k) \cdot \nabla f(\mathbf{x}^k) \tag{9.15}$$

If we proceed, analytically, in an analogous manner as for the steepest descent method, see equations (9.7) to (9.10), this numerical factor α^k will be obtained to be the unity. However, according to Dennis Jr. and Schnabel (1996), until the sixties, it

was believed that the parameter α^k should be obtained from the analytical resolution of the single parameter minimization problem. However, a more exhaustive study led to a completely different conclusion. A numerical solution will make possible to obtain better results.

Therefore, next we will present different numerical methods to obtain the mentioned parameter α^k. Computationally, the search for a minimum in a nonlinear single variable function, results in a nonlinear algebraic equation. Iterative techniques to solve such an equation must be used cautiously, for the sake of round-off errors.

9.8.1 Numerical parametric line search.

In this research[12], three different numerical algorithms have been implemented, according to Crisfield (1991a), Dennis Jr. and Schnabel (1996) and Burden and Douglas (1998). All of the methods which will be introduced in this section, can be employed with any unconstrained optimization method, that is, not only with the Newton's method. The parametric line search, specially by a quadratic or mixed (quadratic and cubic) interpolation technique, increases considerably the convergence of every method in a decisive manner.

All of the implemented strategies are backtracking strategies, where α^k initially takes the unity value to be reduced successively within the interval $(0, 1)$ until the adequate value is achieved. Therefore, if the step provided by the optimization technique results to be optimum, α^k will turn out to be the unity. Otherwise, its value will be decreased in a systematic way, but no further than a certain threshold.

Dennis Jr. and Schnabel's criterion.

The general framework of the algorithm can be formulated as:

Given $\lambda \in (0, 1)$ and starting with $\alpha^k = 1$;

while:

$$f(\mathbf{x}^k + \alpha^k \mathbf{d}^k) > f(\mathbf{x}^k) + \lambda \alpha^k \boldsymbol{\nabla} f(\mathbf{x}^k)^T \cdot \mathbf{d}^k \tag{9.16}$$

compute:

$$\alpha^k = \zeta \alpha^k \quad with\ \zeta \in (0, 1)$$
$$\mathbf{x}^{k+1} = \mathbf{x}^k + \alpha^k \mathbf{d}^k$$

The scalar ζ is obtained according to an imposed interpolation polynomial in order to come out with the minimum of the, as yet undefined, single parameter function $\hat{f}$.

Indeed, once defined this function, namely:

[12]For an exhaustive study of the available parametric line search techniques, we recommend the References: Luenberger (1989), Dennis Jr. and Schnabel (1996) and Burden and Douglas (1998).

$$\widehat{f}(\alpha^k) = f(\mathbf{x}^k + \alpha^k \mathbf{d}^k) \tag{9.17}$$

the initial condition when $\alpha^k = 1$ can be reformulated in terms of the new function's evaluations:

$$\widehat{f}(0) = f(\mathbf{x}^k) \quad \widehat{f}(1) = f(\mathbf{x}^k + \mathbf{d}^k) \quad \widehat{f}'(0) = \nabla f(\mathbf{x}^k)^T \cdot \mathbf{d}^k$$

In fact, expression (9.16) can be reformulated for an initial $\alpha^k = 1$ as follows:

$$\widehat{f}(1) > \widehat{f}(0) + \lambda \widehat{f}'(0) \tag{9.18}$$

The rewritten formula (9.16) in (9.18) establishes somehow a criterion to stop the line search and sets up a superior bound for α^k. Indeed, this criterion is included in the well known:

- Armijo's rule.
- Goldstein's rule.
- Wolfe's test.

Thus, if equation (9.18) holds, then a quadratic spline for the for the $\hat{f}$ function is written as:

$$\widehat{m}_q(\alpha^k) = \left(\widehat{f}(1) - \widehat{f}(0) - \widehat{f}'(0)\right)\left(\alpha^k\right)^2 + \widehat{f}'(0)\alpha^k + \widehat{f}(0) \tag{9.19}$$

The minimum of this function is localized at:

$$\widehat{\alpha^k} = \frac{-\widehat{f}'(0)}{2\left(\widehat{f}(1) - \widehat{f}(0) - \widehat{f}'(0)\right)} \tag{9.20}$$

With this new value for α^k, equation (9.16) can be again studied. If verified, a new either quadratic interpolation or cubic interpolation can be set up to keep iterating in search of the minimum. In the case that a cubic interpolation is chosen:

$$\widehat{m}_{cu}(\alpha^k) = a\left(\alpha^k\right)^3 + b\left(\alpha^k\right)^2 + \widehat{f}'(0)\alpha^k + \widehat{f}(0) \tag{9.21}$$

Where constants a and b are obtained from:

$$\begin{bmatrix} a \\ b \end{bmatrix} = \frac{1}{\alpha_a^k - \alpha_{a2}^k} \cdot \begin{bmatrix} \frac{1}{(\alpha_a^k)^2} & -\frac{1}{(\alpha_{a2}^k)^2} \\ \frac{-\alpha_{a2}^k}{(\alpha_a^k)^2} & \frac{\alpha_a^k}{(\alpha_{a2}^k)^2} \end{bmatrix} \cdot \begin{bmatrix} \widehat{f}(\alpha_a^k) - \widehat{f}(0) - \widehat{f}'(0) \cdot \alpha_a^k \\ \widehat{f}(\alpha_{a2}^k) - \widehat{f}(0) - \widehat{f}'(0) \cdot \alpha_{a2}^k \end{bmatrix} \tag{9.22}$$

where:

α_a^k is the minimum location in the previous step.

α_{a2}^k corresponds to the minimum location two trials ago.

We just need to enforce the derivative of this polynomial to equal zero, in order to come out with the location of the next minimum. With this new parameter, we can study the fulfillment of condition (9.16) once again. Successive interpolations are carried out until the optimum coefficient is achieved. For the purpose of avoiding an infinite number of iterations, a minimum threshold for α^k is set up.

The degree of precision which is required for the parameter α^k depends also on the coefficient λ. The larger the latter is, the more restrictive the search is. For those methods which require a considerable computational time per iteration, typically second order methods, a demanding condition to obtain the search parameter is set up. Specifically, the following criteria has been discovered to be satisfactory:

- Newton's method: $\lambda = 0.90$.
- Steepest descent method: $\lambda = 0.25$.
- Conjugate gradient method: $\lambda = 0.50$.

Burden and Douglas's criterion.

This criterion is less restrictive and accurate than the former one. A quadratic interpolation technique was used along with a stop's criterion as follows:

$$f(\mathbf{x}^k + \alpha^k \mathbf{d}^k) \leq f(\mathbf{x}^k) \tag{9.23}$$

Crisfield's criterion.

The two above described techniques require the evaluation of the objective function. However, in this case, only its directional derivative is demanded. This makes the analysis more flexible[13]. The condition enforced is:

$$\left| \frac{\nabla f(\mathbf{x}^k + \alpha^k \mathbf{d}^k)^T \cdot \mathbf{d}^k}{\nabla f(\mathbf{x}^k)^T \cdot \mathbf{d}^k} \right| \leq \beta \tag{9.24}$$

A parameter $\beta = 0.80$ has been probed to be effective. If the above condition is not satisfied, then a backtracking strategy within $(0, 1)$ is adopted.

9.9 Quasi-Newton's methods.

This family of methods arises from the modification of the Hessian of the objective function f for the sake of the following reasons:

- Increase the degree of convergence, whenever possible.

[13]When the objective function cannot be obtained properly. This is very common if dealing with non-conservative problems.

- Increase the rate of convergence, whenever possible.
- Avoid the divergence of the algorithmic sequence.
- Save computational time.

Among the wide variety of techniques, a very classical is the one which consists of maintaining the Hessian constant throughout the whole iterative process, named *modified Newton method.* This method, even though saves computational time and storage, reduces considerably the convergence of the method.

Another possible technique results from the combination of the Newton's method and the steepest descent method. The iterative algorithm is formulated as follows:

$$\mathbf{x}^{k+1} = \mathbf{x}^k - \alpha^k \mathbf{M}^k \cdot \boldsymbol{\nabla} f(\mathbf{x}^k) \tag{9.25}$$

where:

$\mathbf{M}^k$ is a matrix of order nxn, which can be:

i) $\mathbf{I}_{nxn}$, identity matrix in the case of the steepest descent method.

ii) $\left[\boldsymbol{\nabla}^2 f(\mathbf{x})\right]^{-1}$, inverse of the Hessian in the case of the Newton's method.

iii) An intermediate solution could be $\left[\boldsymbol{\nabla}^2 f(\mathbf{x})\right]^{-1} + \epsilon^k \mathbf{I}$

In the latter of the above, $\epsilon^k \in \mathbf{R}$ is a scalar which has been chosen in such a way that the matrix $\mathbf{M}^k$ is positive definite or, equivalently, whose eigenvalues are all positive. The *Levenberg-Marquardt* method can be allocated in this category. In this method, a Cholesky decomposition is performed over the matrix $\left[\boldsymbol{\nabla}^2 f(\mathbf{x})\right]^{-1} + \epsilon^k \mathbf{I}$ to verify the positiveness of every single eigenvalue. Whether this is not satisfied, the coefficient ϵ^k is risen.

Other alternative techniques may be used to calculate computationally the Hessian of the function f. We can mention **BFGS** techniques, due to Broyden, Fletcher, Goldfarb and Shanno, and **DFP** techniques, due to Davidon, Fletcher and Powell[14]. Nevertheless, these techniques will not be used throughout this research.

9.9.1 Scaling.

With the purpose of obtaining a smooth convergence algorithm, we need to guarantee that the Hessian of the function f possesses all its eigenvalues around a certain magnitude, without much variation. To guarantee that, a scaling procedure can be developed.

In general, the unknowns variables x_i can be re-expressed in another dimensional space of variables $\widetilde{x}_j$, by means of an adequately chosen matrix H_{ij}. Indeed:

[14]See Zienkiewicz and Taylor (1995) for further details.

$$x_i = H_{ij}\widetilde{x}_j, \quad H_{ij} = \frac{\partial x_i}{\partial \widetilde{x}_j} \tag{9.26}$$

Thus, the gradient of the objective functional f can be obtained as:

$$g_i = \frac{\partial f}{\partial x_i} = \frac{\partial f}{\partial \widetilde{x}_j} \cdot \frac{\partial \widetilde{x}_j}{\partial x_i} = \widetilde{g}_j H_{ji}^{-1} \tag{9.27}$$

Analogously, the Hessian of the functional f can be calculated as:

$$G_{ij} = \frac{\partial^2 f}{\partial x_i \partial x_j} = \frac{\partial}{\partial x_j}(\widetilde{g}_k H_{ki}^{-1}) = \widetilde{G}_{kl} H_{lj}^{-1} H_{ki}^{-1} \tag{9.28}$$

In matrix notation, the Newton-Raphson method could then be summarized as:

$$\Delta \mathbf{x}^k = -\alpha^k \mathbf{G}^{k^{-1}} \cdot \mathbf{g}^k \implies \Delta \widetilde{\mathbf{x}}^k = -\alpha^k \widetilde{\mathbf{G}}^{k^{-1}} \cdot \widetilde{\mathbf{g}}^k \tag{9.29}$$

Hence, the matrix H_{ij} is a diagonal matrix built up to adjust suitably the magnitude of the different unknowns.

9.10 Conjugate direction methods.

Conjugate direction methods[15] can be regarded as being somewhat intermediate between the method of steepest descent and Newton's method. They are first order methods. They are motivated by the desire to:

- Accelerate the typically slow linear convergence associated with the steepest descent.
- Avoid the evaluation, storage and inversion of the Hessian as required by Newton's method.

Before proceeding to present the main features of these methods, some important definitions must be settled:

Definition 5 *Given a symmetric matrix* $\mathbf{Q}$*, two vectors* $\mathbf{v}^1$ *and* $\mathbf{v}^2$ *are said to be* $\mathbf{Q}$*-orthogonal or conjugate with respect to* $\mathbf{Q}$*, if:*

$$\mathbf{v}^{1^T} \cdot \mathbf{Q} \cdot \mathbf{v}^2 = 0$$

Corollary 3 *If* $\mathbf{Q} \equiv \mathbf{0}$ *then any two vectors are conjugate. If* $\mathbf{Q} \equiv \mathbf{I}$*, conjugacy is equivalent to the usual concept of orthogonality.*

Proposition 3 *If* $\mathbf{Q}$ *is a positive definite matrix and the set of nonzero vectors* $\mathbf{v}^0, \mathbf{v}^1, \ldots, \mathbf{v}^k$ *are* $\mathbf{Q}$*-orthogonal, then these vectors are linearly independent.*

[15] Initially proposed by Powell in 1964, according to Quesada (1996).

Before discussing the general conjugate direction algorithm, let us investigate the existing relationship between an unconstrained optimization problem and a non-linear algebraic system of equations. In general, the resolution of problem (9.2) entails to solve:

$$\textit{minimize } f(\mathbf{x}) \quad \textit{in } \mathbf{x} \in \mathbf{R}^n \implies \nabla f(\mathbf{x}) = \mathbf{0} \quad \textit{in } \mathbf{x} \in \mathbf{R}^n \tag{9.30}$$

In case f is a quadratic function, the following expression holds:

$$f(\mathbf{x}) = \frac{1}{2}\mathbf{x}^T \cdot \mathbf{Q} \cdot \mathbf{x} - \mathbf{b}^T \cdot \mathbf{x} \tag{9.31}$$

In this way, problem (9.2) can be re-expressed in an equivalent linear system of equations[16]:

$$\mathbf{Q} \cdot \mathbf{x} = \mathbf{b} \tag{9.32}$$

A set of important theorems are presented next:

Theorem 7 (Conjugate direction theorem) *Let $\{\mathbf{d}^i\}_{i=0}^{n-1}$ be a set of nonzero $\mathbf{Q}$-orthogonal vectors. For any $\mathbf{x}^0 \in \mathbf{R}^n$ the sequence $\{\mathbf{x}^k\}$ generated according to:*

$$\mathbf{x}^{k+1} = \mathbf{x}^k + \alpha^k \mathbf{d}^k, \quad k \geq 0 \tag{9.33}$$

with:

$$\alpha^k = -\frac{\mathbf{g}^{k^T} \cdot \mathbf{d}^k}{\mathbf{d}^{k^T} \cdot \mathbf{Q} \cdot \mathbf{d}^k} \tag{9.34}$$

and:

$$\mathbf{g}^k = \mathbf{Q} \cdot \mathbf{x}^k - \mathbf{b} \tag{9.35}$$

converges to the unique solution $\mathbf{x}^*$ such that $\mathbf{Q} \cdot \mathbf{x}^* = \mathbf{b}$ after n steps, that is, $\mathbf{x}^n = \mathbf{x}^*$.

Theorem 8 (Expanding Subspace Theorem) *Let $\{\mathbf{d}^i\}_{i=0}^{n-1}$ be a sequence of nonzero $\mathbf{Q}$-orthogonal vectors. Then for any $\mathbf{x}^0 \in E^n$ the sequence $\{\mathbf{x}^k\}$ generated according to:*

$$\mathbf{x}^{k+1} = \mathbf{x}^k + \alpha^k \mathbf{d}^k, \quad k \geq 0 \tag{9.36}$$

with:

$$\alpha^k = -\frac{\mathbf{g}^{k^T} \cdot \mathbf{d}^k}{\mathbf{d}^k \cdot \mathbf{Q} \cdot \mathbf{d}^k} \tag{9.37}$$

[16]Reciprocally, given an algebraic system of equations $\mathbf{Q}(\mathbf{x}) \cdot \mathbf{x} = \mathbf{b}(\mathbf{x})$, it is feasible to build up an objective function whose minimization returns the solution of the initial system, namely, $f(\mathbf{x}) = \frac{1}{2}\mathbf{x}^T \cdot \mathbf{Q}(\mathbf{x}) \cdot \mathbf{x} - \mathbf{b}(\mathbf{x})^T \cdot \mathbf{x}$

and:

$$\mathbf{g}^k = \mathbf{Q} \cdot \mathbf{x}^k - \mathbf{b} \tag{9.38}$$

has the property that that $\mathbf{x}^k$ *minimizes* $f(\mathbf{x}) = \frac{1}{2}\mathbf{x}^T \cdot \mathbf{Q} \cdot \mathbf{x} - \mathbf{b}^T \cdot \mathbf{x}$ *on the line* $\mathbf{x} = \mathbf{x}^{k-1} + \alpha \mathbf{d}^{k-1}$ *with* $-\infty < \alpha < \infty$, *as well as on the linear variety* $\mathbf{x}^0 + \mathcal{B}^k$, *where* $\mathcal{B}^k$ *is the subspace of* $\mathbf{R}^n$ *spanned by* $\{\mathbf{d}^0, \mathbf{d}^1, \ldots, \mathbf{d}^{k-1}\}$.

Corollary 4 (Gradient direction's orthogonality) *In the method of conjugate directions, the gradients* $\mathbf{g}^k$, *with* $k = 0, 1, \ldots, n$ *satisfy:*

$$\mathbf{g}^{k^T} \cdot \mathbf{d}^i = 0 \quad \forall\, i < k \tag{9.39}$$

In the wake of observing the theorems presented in this section, the only difference that can be established between the different methods of this general family of techniques, lies in the selection of the conjugate directions. A classical way of doing it, is shown in the next section.

9.11 The conjugate gradient method.

The conjugate gradient method[17] is the conjugate direction method that is obtained by selecting the successive direction vectors as a conjugate version of the successive gradients obtained as the method progresses.Thus the directions are not specified beforehand, but rather are determined sequentially at each step of the iteration.

At step k, and to know the feasible direction, one evaluates the current negative gradient vector and adds to it a linear combination of the previous directions vectors to obtain a new conjugate direction vector along which to move. For a quadratic objective function f the algorithm can be summarized as follows:

$$f(\mathbf{x}) = \frac{1}{2}\mathbf{x}^T \cdot \mathbf{Q} \cdot \mathbf{x} - \mathbf{b}^T \cdot \mathbf{x}$$

Starting at any $\mathbf{x}^0 \in \mathbf{R}^n$ define $\mathbf{d}^0 = -\mathbf{g}^0$ and:

$$\mathbf{x}^{k+1} = \mathbf{x}^k + \alpha^k \mathbf{d}^k \tag{9.40}$$

$$\alpha^k = -\frac{\mathbf{g}^{k^T} \cdot \mathbf{d}^k}{\mathbf{d}^{k^T} \cdot \mathbf{Q} \cdot \mathbf{d}^k} \tag{9.41}$$

$$\mathbf{d}^{k+1} = -\mathbf{g}^{k+1} + \beta^k \mathbf{d}^k \tag{9.42}$$

$$\beta^k = \frac{\mathbf{g}^{k+1^T} \cdot \mathbf{Q} \cdot \mathbf{d}^k}{\mathbf{d}^{k^T} \cdot \mathbf{Q} \cdot \mathbf{d}^k} \tag{9.43}$$

[17]Originally presented by Hestenes and Stiefel in 1952.

It follows from the above equations that the first step is identical to a steepest descent method; each succeeding step moves in a direction that is a linear combination of the current gradient and the preceding direction vector. The attractive feature of the algorithm is the simplicity of the formula used for its implementation. The coefficient β^k is selected according to formula (9.43) in such a way that:

$$\mathbf{d}^{k^T} \cdot \mathbf{Q} \cdot \mathbf{d}^i = 0 \quad \forall\, i \leq k-1 \tag{9.44}$$

As a result of the above formulation, this method presents some very interesting aspects:

i) The gradient is always nonzero and linearly independent of all previous direction vectors. Indeed, the gradient $\mathbf{g}^k$ is orthogonal to the vector subspace $\mathcal{B}^k$ generated by the feasible directions $\{\mathbf{d}^0, \mathbf{d}^1, \ldots, \mathbf{d}^{k-1}\}$. If the solution is achieved before n steps, then the gradient vanishes.

ii) A very simple formula is used to determine the new direction vector.

iii) As the directions are based on the gradients, the process makes good uniform progress towards the solution at every step.

A collection of methods that are natural to consider at this point are those in which the conjugate gradient procedure is carried out for steps $m+1 < n$ and then, rather than continuing, the process is restarted from the current point and $m+1$ more conjugate gradient steps are taken.

As a consequence, three different generic families can be established according to that criterion:

i) If $m = 0$, the method is the so called *steepest descent method.*

ii) If $m = n-1$, we refer to the *complete conjugate gradient method.*

iii) If $m < n-1$, it represents the *partial conjugate gradient method.*

Throughout this research, only the second of the above methods is used. The algorithmic sequence developed in (9.40) to (9.43) is straightforwardly extrapolated for the case when the objective function results to be non-quadratic.

Starting at $\mathbf{x}^0 \in \mathbf{R}^n$ compute $\mathbf{d}^0 = -\mathbf{g}^0 = -\boldsymbol{\nabla} f(\mathbf{x}^0)$, then:

$$\mathbf{x}^{k+1} = \mathbf{x}^k + \alpha^k \cdot \mathbf{d}^k \tag{9.45}$$

$$\alpha^k = -\frac{\mathbf{g}^{k^T} \cdot \mathbf{d}^k}{\mathbf{d}^{k^T} \cdot \boldsymbol{\nabla}^2 f(\mathbf{x}^k) \cdot \mathbf{d}^k} \tag{9.46}$$

$$\mathbf{d}^{k+1} = -\mathbf{g}^{k+1} + \beta^k \cdot \mathbf{d}^k = -\boldsymbol{\nabla} f(\mathbf{x}^{k+1}) + \beta^k \cdot \mathbf{d}^k \tag{9.47}$$

$$\beta^k = \frac{\mathbf{g}^{k+1^T} \cdot \boldsymbol{\nabla}^2 f(\mathbf{x}^k) \cdot \mathbf{d}^k}{\mathbf{d}^{k^T} \cdot \boldsymbol{\nabla}^2 f(\mathbf{x}^k) \cdot \mathbf{d}^k} \tag{9.48}$$

9.12 Computational improvements to the conjugate gradient method.

Two important features can be pointed out from equations (9.45) to (9.48):

- The parameter α^k is obtained in an analytical manner by means of the formula (9.46).
- To obtain parameters α^k and β^k, the evaluation of the Hessian of the function f at $\mathbf{x}^k$ is required, in accordance with the formulae (9.46) and (9.48).

About the first of the above issues, we can prove that expression (9.46) is obtained from the minimization of the single parameter function f along the feasible direction defined by the conjugate gradient method, that is:

$$\widehat{f}(\alpha^k) = f(\mathbf{x}^k + \alpha^k \mathbf{d}^k) = f(\mathbf{x}^k + \alpha^k(-\nabla f(\mathbf{x}^k) + \beta^k \mathbf{d}^{k-1})) \tag{9.49}$$

$$\frac{d\widehat{f}}{d\alpha^k} = \nabla f(\mathbf{x}^{k+1})^T \cdot \mathbf{d}^k = 0 \tag{9.50}$$

Using a Taylor series expansion of the gradient of f at $\mathbf{x}^k$, yields:

$$\nabla f(\mathbf{x}^{k+1}) = \nabla f(\mathbf{x}^k) + \alpha^k \nabla^2 f(\mathbf{x}^k) \cdot \mathbf{d}^k \tag{9.51}$$

By combining equations (9.50) to (9.51), expression (9.46) is obtained. Therefore, the above analytical technique can be substituted by any numerical parametric line search, to come out with more accurate results. As regards the second aspect aforementioned, the evaluation and storage of the Hessian constitutes an important brake to the computational performance of the algorithm. For the sake of this reason, there are alternative approaches which enable to overcome such a difficulty. In this research, three of the wide variety of available techniques have been employed, namely:

- **Fletcher-Reeves** method: β_{FR}^k
- **Polak-Ribiere** method: β_{PR}^k
- **Modified Polak-Ribiere** method: β_{OP}^k

In all of the above numerical schemes, the parameter α^k is achieved in the same way, that is, by means of the polynomial interpolation technique already described. On the other hand, the second parameter β^k is calculated differently according to the next expressions:

$$\beta_{FR}^k = \frac{\nabla f(\mathbf{x}^{k+1})^T \cdot \nabla f(\mathbf{x}^{k+1})}{\nabla f(\mathbf{x}^k)^T \cdot \nabla f(\mathbf{x}^k)} \tag{9.52}$$

$$\beta_{PR}^{k} = \frac{[\nabla f(\mathbf{x}^{k+1}) - \nabla f(\mathbf{x}^{k})]^{T} \cdot \nabla f(\mathbf{x}^{k+1})}{\nabla f(\mathbf{x}^{k})^{T} \cdot \nabla f(\mathbf{x}^{k})} \tag{9.53}$$

The modified Polak-Ribiere, as gathered by Maurin and Motro (2001), and due to the contribution of Gilbert and Nocedal, in 1992, yields:

$$\beta_{OP+}^{k} = \min(\beta_{FR}^{k}, \beta_{PR+}^{k}) \quad \beta_{PR+}^{k} = \max(\beta_{PR}^{k}, 0) \tag{9.54}$$

Chapter 10

Computational implementation

10.1 Introduction.

As it has been already pointed out, the design of prestressed membranes is a very complex process comprised of distinct inter-related stages. A comprehensive design might entail, for instance, an initial architectural design, a shape finding problem and visualization of results with a CAD tool, a structural analysis under prestressing and in-service loading conditions and a final patterning generation, see Iványi (2002).

This research intends to deal with all of the above phases, except for the last one. Therefore, the main goal is the development of a computer program in order to model them successfully. Thus, this chapter will attempt to summarize the main capabilities of the computer code, explaining up to a certain extent the structural problems that can be handled.

The analysis process can be depicted by means of figure 10.1. Preprocessor and postprocessor programs were performed under the computer language named Matlab, see MathWorks (1996) and Pérez (1999), whereas the rest of the programs are based on the language Fortran 90-95, see Smith (1995), Nyhoff and Leestma (1997) and Chapman (1998).

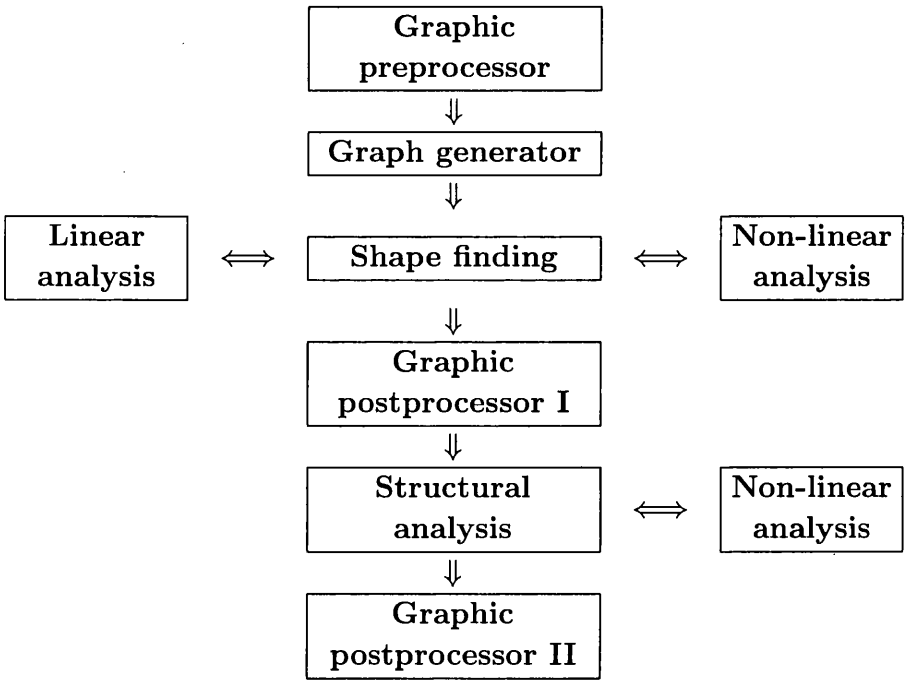

Figure 10.1: Structural analysis strategy

The program is built up on the concept of modular or structured programming, that is, there are several independent modules, with multiple subroutines in each one of those, which are properly interconnected[1].

[1]This programming technique accelerates considerably the errors' detection within the main code or any of its modules. Some other advantages about the use of this approach can be encountered in Gaylord and Gaylord (1990).

10.2 Shape finding.

Two shape finding schemes were included for the determination of an initial equilibrium shape: Force Density Method and Smoothing Method[2]. The use of any of these methods, requires beforehand the generation of an internal connectivity graph. Therefore:

1. Sub-program **MESHER.EXE** generates an internal connectivity graph.
2. Sub-program **FDMC.EXE** solves for the Force Density method -see figure 10.2-.
3. Sub-programs **NLCE.EXE** and **NLTE.EXE**, solve for the Smoothing method, namely, cables and membranes, respectively.

Figure 10.2 gathers the flowchart corresponding to sub-program **FDMC.EXE**. The implemented formulation, due to Linkwitz (1971), is detailed.

1. Loop over number of actions ***iaction***
   (a) Arbitrary definition of force density coefficients: g_i
   (b) Stiffness matrix assembling:
   $\boldsymbol{assembling} \longrightarrow \mathbf{K} \longleftarrow \mathbf{K}_i(g_i) \quad i = 1 \ldots nelem$
   (c) Loop over dimensions ***idime=1,2,3***
      i. Initialization of variables: $\mathbf{K}_{idime} = \mathbf{K}$, $\mathbf{f}_{ext_{idime}} = \mathbf{0}$
      ii. Boundary conditions: $\mathbf{f}_{ext_{idime}} \longleftarrow \mathbf{x}^{B.C.}_{idime}$
      iii. Linear system of equations solver:
      $\mathbf{K}_{idime} \cdot \mathbf{x}_{idime} = \mathbf{f}_{ext_{idime}} \longrightarrow \mathbf{x}_{idime}$
   (d) End loop over dimensions ***idime***
   (e) Calculation of cable geometry and cable stresses:
   $L_i,\ \sigma_i^{pret} = L_i g_i \quad i = 1 \ldots nelem$
   (f) Calculation of reactions: $\boldsymbol{reaction} \longrightarrow \mathbf{React}$
   (g) Verifying global equilibrium: $\sum_i \mathbf{f}_i^{ext} - \sum_j \mathbf{React}_j$
2. End loop over number of actions ***iaction***

Figure 10.2: Flowchart of the sub-program **FDMC.EXE**

[2]In this last method, see Levy and Spillers (1995), given an initial spatial shape, a nonlinear analysis can be used to smooth out the forces or stresses in order to obtain either a uniform stress pattern or a predefined stress pattern. This method has been reviewed in a novel approach named the Updated Reference Strategy, see Bletzinger and Ramm (2001) for further details.

10.2.1 Sub-program MESHER.EXE architecture.

The sub-program **MESHER.EXE** consists of a set of modules which enable to generate internal connectivity graphs as a function of a chosen criterion, namely:

1. **Intpoint** module enables to generate n-polygonal planar graphs.
2. **Rect** module enables to generate rectangular planar graphs.
3. **Diag1Rect** module enables to generate rectangular planar graphs with a diagonal direction included.
4. **Diag2Rect** module enables to generate rectangular planar graphs with both diagonal directions included.
5. **Graph3** module enables to generate triangular planar graphs
6. **Graph4** module enables to generate quadrangular planar graphs.
7. **Radial** module enables to generate radial planar graphs.

As it was formerly explained in previous chapters, these procedures enable to generate planar graphs whose edges can be assimilated to cable finite elements to perform the subsequent shape finding analysis. Nevertheless, some of these graphs generate triangular facets which can be regarded as prospective membrane finite elements.

10.3 Geometrically non-linear structural analysis.

Once established an initial equilibrium shape, the program carries out the static structural analysis: either prestressing loading conditions or in-service loading conditions can be studied. Both cable networks or prestressed membranes can be handled suitably by the developed code. In particular:

- **NLCE.EXE** enables to deal with cable network themselves.
- **NLTE.EXE** is designed to perform analysis of prestressed membranes or cable reinforced prestressed membranes.

The program was developed under a finite element discretization basis, by using isoparametric linear two-noded and three-noded finite elements. A TLF under a DCCF was employed. The code allows to tackle a broad set of external loads, characterized by the next features:

1. Point loads applied on the nodes of the Lagrangian mesh.
2. Longitudinal distributed loads along the reinforced cables, either per unit of real length -gravity loading- or per unit of projected length -snow loading-.

3. Superficial distributed loads across the fabric membrane, either per unit of real surface -gravity loading- or per unit of projected surface -snow loading-.
4. Pressure loading -wind loading-.
5. Thermal effects as a result of an increase or a decrease of temperature.
6. Sudden displacements of supports next to foundations.

Because the program has been designed to deal with tensioned membrane structures originally, a wrinkling algorithm was implemented to deal with the likelihood of wrinkles' appearance. Furthermore, different essential boundary conditions were regarded, namely:

1. Fixed supports, where $\mathbf{u}^{B.C.} = \mathbf{0}$ to model rigid foundations.
2. Mobile supports, where $\mathbf{u}^{B.C.} = \overline{\mathbf{u}}$, to model sudden displacements in foundations.
3. Elastic foundations, where $\mathbf{f}^{B.C.} = \mathbf{K}^{elast} \cdot \mathbf{u}^{B.C.}$.
4. Masts which are fixed or pinned to the surrounding medium.

To account for the last two boundary conditions, a new finite element was implemented into the code. These support finite elements will be two-noded with two possible configurations: pinned-pinned or fixed-pinned. According to that, their equivalent internal nodal forces vector and total tangent stiffness matrices can be deduced from: Cook, Malkus, and Plesha (1989), Kadlcak (1994), Oñate (1995), Bathe (1996) or Ghali and Neville (1997). In all theses cases, due to the enormous rigidity of these elements with respect to the rest of the membrane, a pure linear elastic approach was used in terms of the mechanical properties of the support. Thus, the global stiffness matrix $\mathbf{K}^g$, the global equivalent internal forces vector $\mathbf{f}^g_{int}$ and the strain energy functional W_{int} will be calculated as follows:

$$\begin{aligned} \mathbf{K}^g &= \mathbf{T} \cdot \mathbf{K} \cdot \mathbf{T}^T \\ \mathbf{f}^g_{int} &= \mathbf{T} \cdot \mathbf{f}_{int} = \mathbf{T} \cdot \mathbf{K} \cdot \mathbf{u} = \mathbf{T} \cdot \mathbf{K}^g \cdot \mathbf{u}^g \\ W_{int} &= \tfrac{1}{2} \mathbf{u}^{g^T} \cdot \mathbf{K}^g \cdot \mathbf{u}^g \end{aligned} \tag{10.1}$$

where $\mathbf{T}$ represents an element rotation matrix and $\mathbf{u}^g$ stand for the global nodal displacements.

10.4 Sub-program NLTE.EXE architecture.

The architecture of the program **NLTE.EXE** is displayed in figure 10.3. The flowchart of this sub-program follows the same pattern as the sub-program **NLCE.EXE**.

1. Loop over number of actions ***iaction***
   (a) Transforming distributed loads into equivalent nodal loads: ***distload***, ***longload***
   (b) Loop over number of increments ***iincrem***
      i. Initialization of variables: $\mathbf{S} = \boldsymbol{\sigma}^{pret}$
      ii. Incremental strategy: $\lambda_{iincrem} = \lambda_{iincrem-1} + \Delta\lambda_{iincrem-1}$
      iii. Incremental equivalent external nodal forces: $\mathbf{f}_{ext_{iincrem}} = \lambda_{iincrem}\mathbf{f}_{ext}^{tot}$
      iv. Loop over number number of iterations ***iter***
         - Iterative numerical scheme
      v. End loop over number number of iterations ***iter***
   (c) End loop over number of increments ***iincrem***
2. End loop over number of actions ***iaction***

Figure 10.3: Flowchart of the program **NLTE.EXE**

1. Initialization of incremental displacements: $\Delta\mathbf{u} = 0$
2. Incremental boundary conditions: $\Delta\mathbf{u}^{B.C.}_{iincrem} = \lambda_{iincrem}\Delta\mathbf{u}^{B.C.\mathbf{tot}}$
3. If ***iter=1***
   (a) Calculation of element geometric properties: ***elementprop***
   (b) Calculation of element mechanical properties: ***tension***
   (c) Stresses transformation from global to local coordinates:
   $\mathbf{S} = \mathbf{T}^T \cdot \mathbf{S}^g \cdot \mathbf{T} \quad \sigma^{pret} = \mathbf{T}^T \cdot \sigma^{pret^g} \cdot \mathbf{T}$
4. End if ***iter=1***
5. Nonlinear numerical method: ***nonlinmethod*** $\longrightarrow \Delta\mathbf{u}^{iter}_{iincrem}$
6. Linear parametric search: $\Delta\mathbf{u}^{iter}_{iincrem} = \alpha\Delta\mathbf{u}^{iter}_{iincrem}$
7. Updating nodal displacements: $\mathbf{u}^{iter}_{iincrem} = \mathbf{u}^{iter-1}_{iincrem} + \Delta\mathbf{u}^{iter}_{iincrem}$
8. Recalculating element geometric properties: ***elementprop***
9. Recalculating element geometric properties: ***tension***
10. Calculation of reactions: ***reaction*** $\longrightarrow \mathbf{React}^{iter}_{jiincrem}$
11. Checking global equilibrium: $\sum_i \mathbf{f}^{ext^{iter}}_{iiincrem} - \sum_j \mathbf{React}^{iter}_{jiincrem}$
12. Checking convergence of the scheme: ***converg***
13. If ***converg=TRUE***
   (a) Updating of stresses: $\sigma = J^{-1}\mathbf{F} \cdot \mathbf{S} \cdot \mathbf{F}^T$
   (b) Principal stresses and principal directions:
   $S_{xx}, S_{xy}, S_{yy} \longrightarrow S_I, S_{II} \quad \sigma_{xx}, \sigma_{xy}, \sigma_{yy} \longrightarrow \sigma_I, \sigma_{II}$
   (c) Maximum and minimum nodal displacements and element stresses
   (d) Stresses transformation from local to global coordinates:
   $\mathbf{S}^g = \mathbf{T} \cdot \mathbf{S} \cdot \mathbf{T}^T \quad \sigma^{pret^g} = \mathbf{T} \cdot \sigma^{pret} \cdot \mathbf{T}^T$
14. End if ***converg=TRUE***

Figure 10.4: Flowchart of the iterative numerical scheme

1. Loop over number of cable elements ***i=1,nelem***
   (a) Calculation of coordinates difference between cable nodal edges α and β: $\Delta x_l^i = x_l^{i^\beta} + u_l^{i^\beta} - x_l^{i^\alpha} - u_l^{i^\alpha} \qquad l = 1 \ldots 3$
   (b) Current cable length: $L^i = \sqrt{\sum_l (\Delta x_l^i)^2}$
   (c) Initial prestressed cable length: $L^{pret^i} \longleftarrow L^i$ (si ***iter=1***)
   (d) Director cosines of the cable element: $\theta_l^i = \frac{\Delta x_l^i}{L^{pret^i}}$
2. End loop over number of cable elements
3. Loop over number membrane elements ***i=1,ntelem***
   (a) If ***iter=1***
      i. Rotation matrix from local to global axes: $\mathbf{T}$
      ii. Nodal coordinates transformation from global to local axes: $\mathbf{x} = \mathbf{T}^T \cdot \mathbf{x}^g$
      iii. Zienkiewicz's coefficients: $\mathbf{b}$, $\mathbf{c}$
      iv. Membrane element's area: Γ^{pret}
      v. Displacements transformation from global to local axes: $\mathbf{u} = \mathbf{T}^T \cdot \mathbf{u}^g$
      vi. Deformation and displacement gradient tensors: $\mathbf{F}$, $\mathbf{G}$
      vii. Green-Lagrange strain tensor: $\mathbf{E}$
   (b) If ***iter≠1***
      i. Displacements transformation from global to local axes: $\mathbf{u} = \mathbf{T}^T \cdot \mathbf{u}^g$
      ii. Deformation and displacement gradient tensors: $\mathbf{F}$, $\mathbf{G}$
      iii. Green-Lagrange strain tensor: $\mathbf{E}$
4. End loop over number membrane elements
5. Loop over number of masts ***i=1,nsupport***
   (a) If ***iter=1***
      i. Rotation matrix from local to global axes: $\mathbf{T}$
   (b) End if ***iter=1***
6. End loop over number of masts

Figure 10.5: Flowchart of the subroutine ***elementprop***

1. Loop over number of cable elements ***i=1,nelem***
   (a) Shape finding (Updated Reference Strategy)
      i. $S_{11} = \sigma_{11}^{pret}$
   (b) Non-linear structural analysis
      i. Thermal effects: $E_{0_{11}} = \lambda_n^k \alpha \Delta T$
      ii. Young modulus: E
      iii. Second Piola Kirchhoff stress tensor: $S_{11} = \sigma_{11}^{pret} + E \cdot (E_{11} - E_{11_0})$
2. End loop over number of cable elements
3. Loop over number of membrane elements ***i=1,ntelem***
   (a) Shape finding (Updated Reference Strategy)
      i. $\{\mathbf{S}\} = \{\sigma^{pret}\}$
   (b) No-linear structural analysis
      i. Thermal effects: $\{\mathbf{E_0}\} = \lambda_n^k \alpha \Delta T \cdot (1\ 1\ 0)^T$
      ii. Constitutive tangent moduli tensor: $\mathcal{C} = \mathcal{C}(E, \nu)$
      iii. Second Piola Kirchhoff stress tensor: $\{\mathbf{S}\} = \{\sigma^{pret}\} + \mathbf{C} \cdot (\{\mathbf{E}\} - \{\mathbf{E_0}\})$
4. End loop over number of membrane elements
5. Loop over number of mast elements ***i=1,nsupport***
   (a) Element stiffness matrix:
      i. Pinned-pinned mast: $\mathbf{K} = \mathbf{K}(E, A, L)$
      ii. Fixed-pinned mast: $\mathbf{K} = \mathbf{K}(E, A, I_y, I_z, L)$
   (b) Equivalent internal nodal forces vector: $\mathbf{f}_{int}^g = \mathbf{T} \cdot \mathbf{K} \cdot \mathbf{T}^T \cdot \mathbf{u}^g$
6. End loop over number of mast elements

Figure 10.6: Flowchart of the subroutine ***tension***

1. Parameters calculation:
   (a) Residual force vector:
   unbforvec $\longrightarrow \mathbf{f}_{iincrem}^{unb^{iter}} = \mathbf{f}_{iincrem}^{int^{iter}} - \mathbf{f}_{iincrem}^{ext^{iter}}$
   (b) Total tangent stiffness matrix:
   assembling $\longrightarrow \mathbf{K}^{g} = \mathbf{K}^{geo^{g}} + \mathbf{K}^{mat^{g}} - \mathbf{K}^{ext^{g}}$
2. Nonlinear optimization numerical method:
   (a) **Steepest descent** method:
      i. $\Delta\mathbf{u}_{iincrem}^{iter} = \mathbf{f}_{iincrem}^{unb^{iter}}$
      ii. Applying boundary conditions: ***boundcon***
      $\Delta\mathbf{u}_{iincrem}^{iter} \longleftarrow \Delta\mathbf{u}_{iincrem}^{B.C.^{iter}}$
   (b) **Conjugate gradient** method:
      i. Omitting components of $\mathbf{f}_{iincrem}^{unb^{iter}}$ where **BCs** exist
      ii. Parameter calculation β: $\mathbf{g}^{iter} = \mathbf{f}_{iincrem}^{unb^{iter}}$
         A. **Fletcher-Reeves**: $\beta^{FR} = \frac{(\mathbf{g}^{iter} - \mathbf{g}^{iter-1})^{T} \cdot \mathbf{g}^{iter}}{\mathbf{g}^{iter-1^{T}} \cdot \mathbf{g}^{iter-1}}$
         B. **Polak-Ribiere**: $\beta^{PR} = \frac{\mathbf{g}^{iter^{T}} \cdot \mathbf{g}^{iter}}{\mathbf{g}^{iter-1^{T}} \cdot \mathbf{g}^{iter-1}}$
         C. **Modified Polak-Ribiere**:
         $\beta^{OP+} = \min(\beta^{FR}, \beta^{PR+})$, $\beta^{PR+} = \max(\beta^{PR}, 0)$
      iii. Updating incremental nodal displacements:
      $\Delta\mathbf{u}_{iincrem}^{iter} = \mathbf{g}^{iter} + \beta \cdot \Delta\mathbf{u}_{iincrem}^{iter-1}$
      iv. Applying boundary conditions: ***boundcon***
      $\Delta\mathbf{u}_{iincrem}^{iter} \longleftarrow \Delta\mathbf{u}_{iincrem}^{B.C.^{iter}}$
   (c) **Newton-Raphson** method:
      i. **Levenberg-Marquardt**: ***levmarglstma***
      ii. Scaling: ***scaling***
      iii. Applying boundary conditions: ***boundcon***
      $\Delta\mathbf{u}_{iincrem}^{iter} \longleftarrow \Delta\mathbf{u}_{iincrem}^{B.C.^{iter}}$
      iv. System of equations solver:
      $\Delta\mathbf{u}_{iincrem}^{iter} = -\mathbf{K}^{g^{-1}} \cdot \mathbf{f}_{iincrem}^{unb^{iter}}$

Figure 10.7: Flowchart of the subroutine ***nonlinmethod.***

10.4.1 Numerical schemes.

The final equilibrium solution of the static analysis will be obtained by *continuation*, which means through an incremental multiple-level process: actions, steps or increments and iterations. These *incremental*[3] procedures could be **pure incremental**,

[3]According to Felippa (2001), the incremental methods present numerous positive attributes: facilitate the convergence, eliminate the erroneous equilibrium solutions and enable a better un-

only a predictor phase, or **iterative**, that is, a predictor phase will be followed by several corrector phases. Each class has relative strengths and weaknesses compared to the other class.

A weakness in the iterative methods is that an initial trial solution is required in the neighborhood of the exact solution. If the initial guess is within the radius of convergence, the convergence itself will be very rapid. The strength of the iterative method is that the accuracy of the solution at a particular value of the external forces is not dependent on the accuracy obtained in any other value of the external forces.

In the purely incremental methods of solution, no initial guess is required. Instead, the solution at a certain increment of the external forces is considered as the solution at the previous increment plus the solution of the locally linearized equations of motion. A great drawback is the accumulated error that emerges as the analysis progresses.

To combine the strengths of both methodologies, a combined approach, named **mixed method** is used. In this approach, the incremental method is used to obtain an initial trial solution, which is then iterated upon to converge within a prescribed error bound of the exact solution. The initial trial should be sufficiently closed to the exact solution that few iterations would be required.

10.4.2 Incremental strategy.

In Crisfield (1991a) and Felippa (2001), some of the most known incremental strategies are reported. In this case, the external load will be employed as a parameter to control the incremental increase. The discretized equilibrium equations at each step can be formulated as:

$$\mathbf{f}_{ext}(\mathbf{u}_n + \Delta\mathbf{u}_n) - \mathbf{f}_{int}(\mathbf{u}_n + \Delta\mathbf{u}_n) = \mathbf{0} \qquad \mathbf{u}_{n+1} - \mathbf{u}_n = \Delta\mathbf{u}_n \tag{10.2}$$

where for the n-th load step:

$$\mathbf{f}_{ext}(\mathbf{u}_n + \Delta\mathbf{u}_n) = \Delta\lambda_n \mathbf{f}_{ext}^{tot}(\mathbf{u}_n + \Delta\mathbf{u}_n) \qquad \lambda_{n+1} - \lambda_n = \Delta\lambda_n \tag{10.3}$$

Any feasible heuristic procedure could have been implemented to modify successively the parameter $\Delta\lambda_n$. Two different schemes were used as follows:

1. Constant linear increment:

$$\lambda_n = \frac{n}{N} \qquad n = 1 \ldots N \tag{10.4}$$

derstanding of the structural behaviour by following the so called *load path.*

2. Decreasing increment, which according to Crisfield (1991a) is formulated as follows:

$$\Delta\lambda_1 = 0.5 \quad \Delta\lambda_{n+1} = \Delta\lambda_n \frac{I_{fix}}{I_n} \tag{10.5}$$

where I_n stands for the number of iterations required to reach convergence at the previous increment, whereas I_{fix} is a fixed parameter which is usually fixed as 3.

10.4.3 Unconstrained optimization methods.

Three different families of methods have been implemented into the computer code, as follows:

1. Newton-Raphson's method with a Levenberg-Marquardt correction whether required.

2. Steepest descent method.

3. Conjugate gradient method:

   (a) Polak-Ribiere method.

   (b) Fletcher-Reeves method.

   (c) Modified Polak-Ribiere method.

10.4.4 Parametric line search.

Line search increases the effectiveness of every unconstrained optimization method when convergence is slow due to substantial deviation of the residual from the underlying linearized model and roughness of the residual. The line search can be carried out by means of any one of the following procedures:

1. Exact minimization of the Total Potential Energy functional.

2. Purely quadratic interpolation of the Total Potential Energy functional, according to Burden and Douglas.

3. Quadratic and then cubic interpolation of the Total Potential Energy functional, according to Dennis Jr. and Schnabel.

4. By using the directional derivative of the functional, according to Crisfield.

10.4.5 Convergence criteria.

To terminate the iterative procedure, different convergence criteria have been implemented into the computer code. All of them will be based on norms pertaining to the incremental displacement vector or the residual vector. For the sake of that reason, it is recommended to consult appendix A about vector and matrix norms.

The solution at the n-th increment and k-th iteration can be considered to have converged, according to any of the following criteria:

1. Euclidean norm on the incremental displacement vector:

$$\frac{\|\Delta \mathbf{u}_n^k\|_2}{\|\mathbf{u}_n^k\|_2} \leq TOL \tag{10.6}$$

2. Infinity norm on the incremental displacement vector:

$$\frac{\|\Delta \mathbf{u}_n^k\|_\infty}{\|\mathbf{u}_n^k\|_\infty} \leq TOL \tag{10.7}$$

3. Euclidean norm on the residual force vector:

$$\frac{\|\Delta \mathbf{f}_n^{unb^k}\|_2}{\|\mathbf{f}_n^{unb^k}\|_2} \leq TOL \tag{10.8}$$

4. Infinity norm on the residual force vector:

$$\frac{\|\Delta \mathbf{f}_n^{unb^k}\|_\infty}{\|\mathbf{f}_n^{unb^k}\|_\infty} \leq TOL \tag{10.9}$$

5. Energy error criterion:

$$\frac{|\Delta \mathbf{u}_n^{k^T} \cdot \mathbf{f}^{unb_n^k}|}{\Pi} \leq TOL \tag{10.10}$$

6. Infinity norm on the residual vector between the external loads and the support reactions:

$$\frac{\|\sum_i \mathbf{f}_{i_n}^{ext^k} - \sum_j \mathbf{React}_{j_n}^k\|_\infty}{\|\sum_i \mathbf{f}_{i_n}^{ext^1} - \sum_j \mathbf{React}_{j_n}^1\|_\infty} \leq TOL \tag{10.11}$$

The error tolerance TOL determines the precision with which the displacements are calculated before terminating the iterative procedure. Therefore, it determines the speed and the accuracy of the final solution. If the criterion is too coarse, the solution may be quite inaccurate. On the other hand, a criterion which is too tight could entail unnecessary calculations. Infinity norms are more restrictive that Euclidean norms. Finally, any norm acting on the residual vector is preferred rather than any other one acting on the incremental displacements vector.

Part IV

Numerical examples

Chapter 11

Robustness

11.1 Introduction.

To illustrate and validate the developed solution process for cable and membrane finite elements, different numerical examples will be analyzed in detail. In all instances, numerical results will be checked with the ones reported in the existing literature to conclude the validity and quality of the methods used herein.

Cable networks and prestressed membranes will be subjected to different sorts of loadings. Wrinkling considerations as well as follower loads will be regarded in some of the applications. An attempt will be made to prove the quadratic convergence of the Newton-Raphson scheme.

11.2 Cable networks.

11.2.1 Numerical example 1.

This first example has been extracted from Leonard (1988). Originally, the same problem was analyzed by Baron and Vendatesan (1971). It is a 2D cable network structure comprised of three cables joined consecutively, whose internal nodes are free to move whereas external nodes are fixed, see figure 11.1. All cables dispose of the same cross sectional area $A = 0.227\ in^2$ and of an initial length of 1200 in. The initial prestressed loading is achieved by applying two downward point dead loads on nodes 2 and 3 of identical value 4 kip. The unique Young modulus adopted for the whole structure is $E = 12000\ Ksi$.

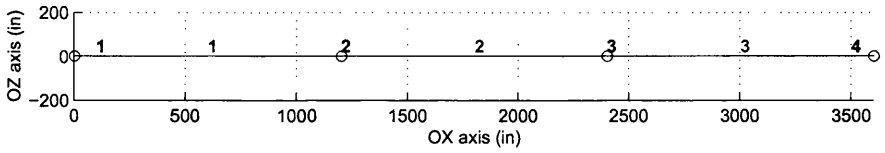

Figure 11.1: Leonard: discretization.

After the prestressed loading, the structure is subjected to an upward point live load of value 3 kip acting only on node 3. For the resolution of the problem, the Newton-Raphson method for a single load increment was employed.

Figure 11.2 gathers prestressed and in-service configurations in different colours, blue and red, respectively. At the same time, tables 11.1 and 11.2 display nodal displacements -u and w, for horizontal and vertical displacements, respectively-, as well as element Cauchy stresses. Comparison of results accomplished in this research and in aforementioned references is depicted.

To check the goodness of the numerical technique, convergence curves are displayed in figure 11.3. The left hand side graph represents the Total Potential Energy of the system with respect to the number of iterations. The right hand side graph shows the evolution of the infinity norm taken on the residual force vector through the iterative process. The expected quadratic descent of the latter is observed.

	Baron		Leonard		Present work	
Node	u	w	u	w	u	w
2	26.28	52.08	26.00	52.36	26.31	52.02
3	23.40	-48.48	23.80	-49.11	23.44	-48.46

Table 11.1: Leonard: Displacements (in).

Element	Baron	Leonard	Present work
1	53.32	52.96	53.15
2	48.91	48.52	48.70
3	55.52	55.18	55.40

Table 11.2: Leonard: Cauchy stresses (Ksi).

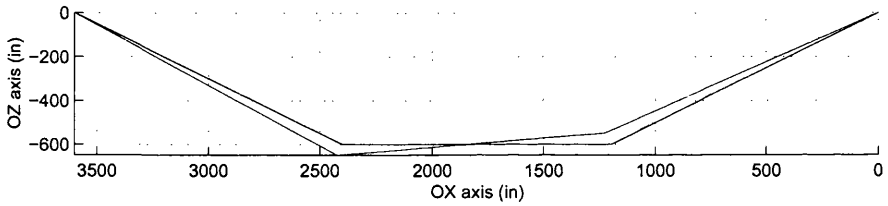

Figure 11.2: Leonard: prestressed and in-service configurations.

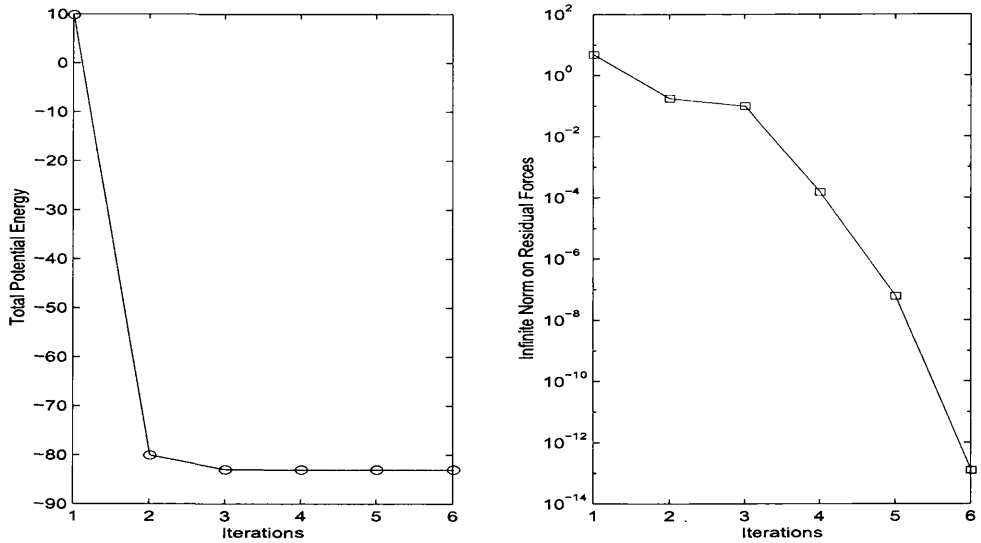

Figure 11.3: Convergence curves.

11.2.2 Numerical example 2.

This example, extracted from Broughton and Ndumbaro (1994), represents a squared hyperbolic paraboloid with a 12 *foot* horizontal side. The difference between the highest and lowest points is measured as 1.5 *feet*. The sides of the structural model are composed of rigid beams which prevent any displacement.

The structure is modeled by means of a cable network depicted at figure 11.4, where a representation of nodes and elements can be observed. The external nodes are fixed and the only allowed displacement is for the inner nodes.

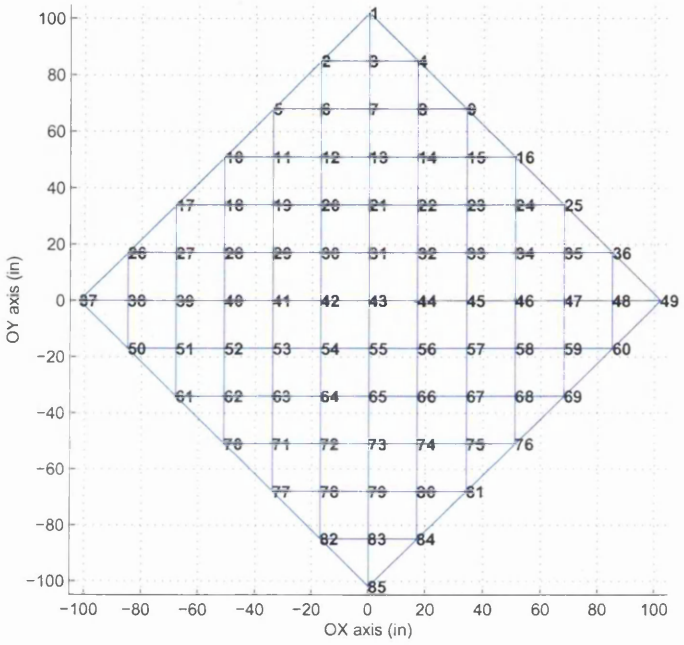

Figure 11.4: Broughton: cable discretization.

All the cables are subjected to a previous prestressed state of 1.2 Kip. In addition to that, the cables will be represented by a unique material of $0.618e3$ Kip for the mechanical factor EA.

Under service conditions the structural model undergoes a downward point load of value 0.22 Kip applied at node 79, see figure 11.4. The analysis has been solved by using a Newton-Raphson numerical scheme in one incremental step.

Figures 11.5 and 11.6 represent both original and displaced shapes. Analogously, table 11.3 reflects a survey of displacements according to the different spatial directions for some remarkable internal nodes. Results according to reference Broughton and Ndumbaro (1994) and present work are displayed.

Figure 11.7 gathers the convergence curves for the numerical method which has been employed. Eventually, a representation of the Cauchy axial forces is shown in figure 11.8.

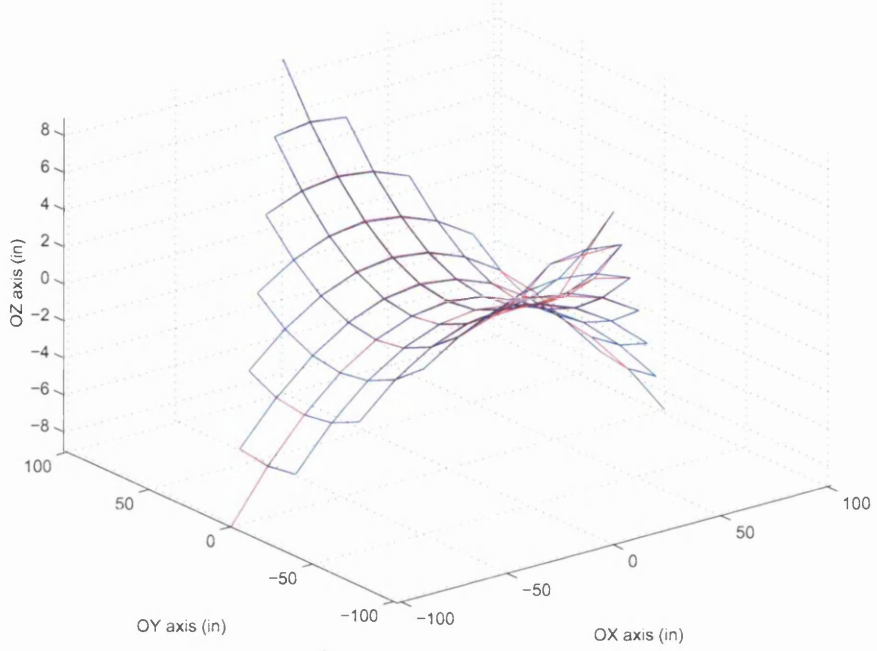

Figure 11.5: Structural model: cable isometric view.

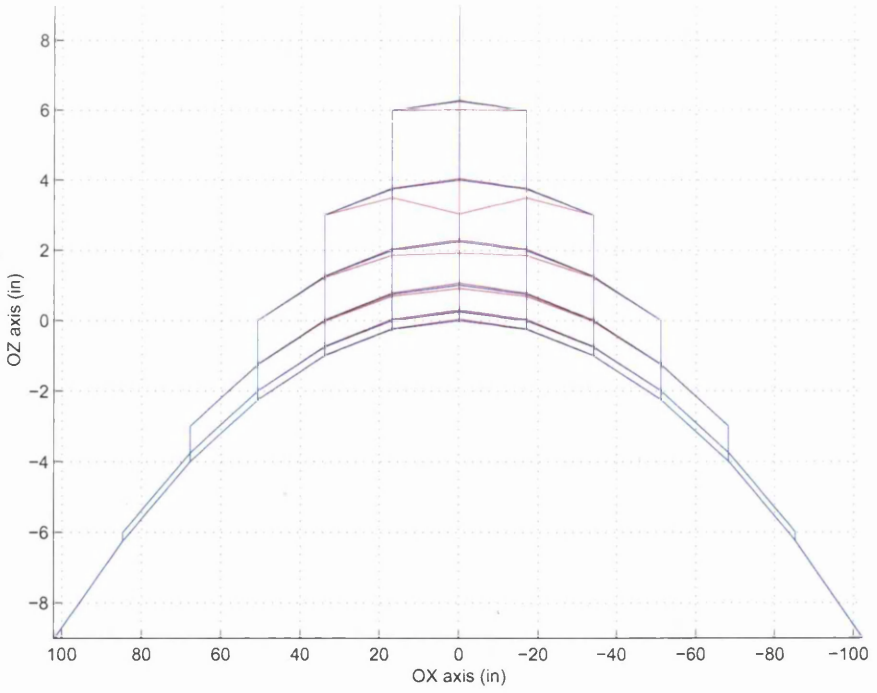

Figure 11.6: Structural model: cable lateral view.

	Broughton			Present work		
Node	u	v	w	u	v	w
83	0.0000	-0.0334	-0.2410	0.0000	-0.0340	-0.2415
79	0.0000	-0.1390	-0.9650	0.0000	-0.1388	-0.9667
43	0.0000	-0.0410	0.0510	0.0000	-0.0414	0.0516
23	0.0000	-0.0020	0.0160	-0.0002	-0.0016	0.0155

Table 11.3: Displacements (in).

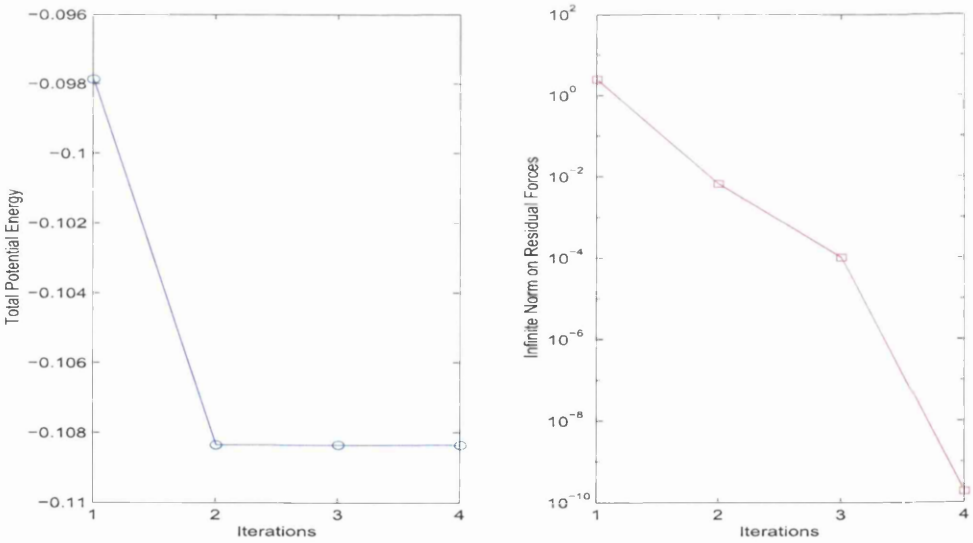

Figure 11.7: Convergence curves.

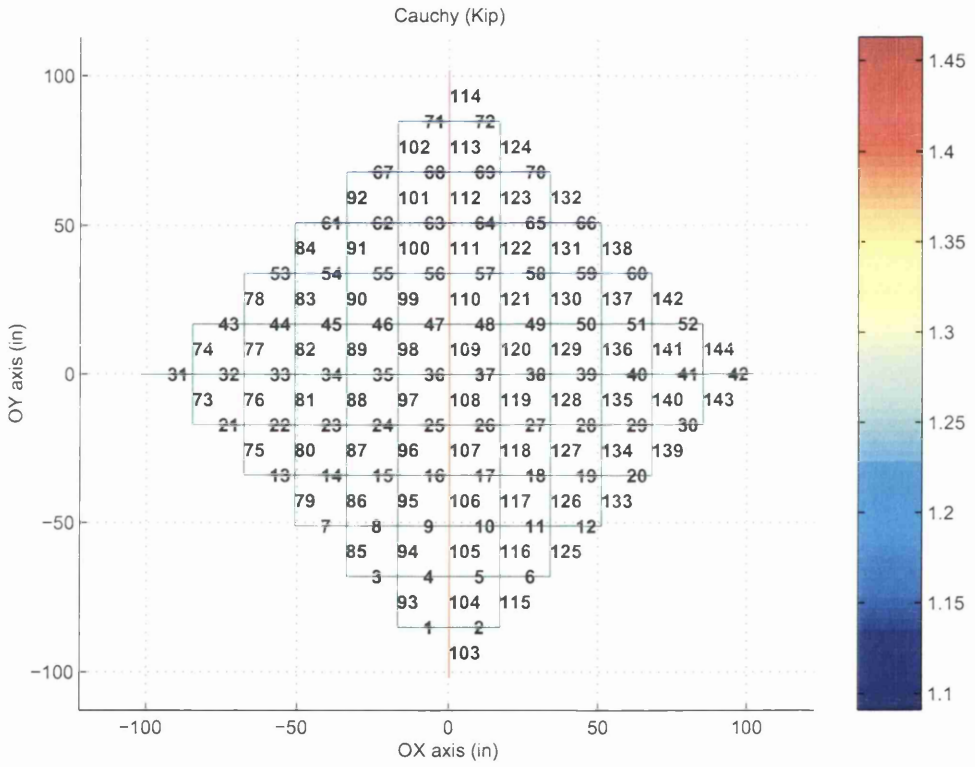

Figure 11.8: Axial forces(Kip).

11.3 Structural membranes.

11.3.1 Numerical example 3.

This example is gathered at Levy and Spillers (1995). It represents a 2D beam with a considerable ratio between its depth and its length. In fact, a length of 30 in and a depth of 28 in are set up. The beam is fixed in one of its edges but free in the rest of its domain. To describe the mechanical behaviour of the structure, a unique Young modulus of $29.0e3$ Ksi together with a Poisson ratio of value 0.2, are considered. Only one downward point load of value $1.0e-3$ Kip acting on the free edge will be included in the analysis.

For the resolution of the problem, the same spatial discretization as in Levy and Spillers (1995) was assumed. Figure 11.9 shows the distribution of the 24 isoparametric linear triangular elements adopted.

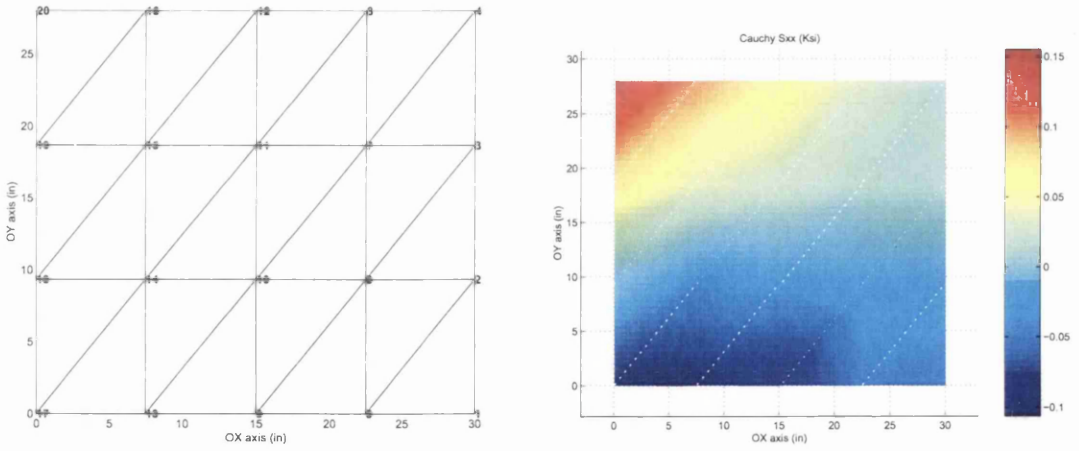

Figure 11.9: Levy & Spillers, 111: Discretization and Cauchy stress σ_{xx}.

The problem was solved by means of a Newton-Raphson numerical scheme in just two iterations. Results for the Cauchy stress component σ_{xx} can be seen also in figure 11.9. In this particular case, it is worthwhile to point out that a pure membrane theory was used -wrinkling considerations were not included into the numerical analysis-. That is the reason why compressive triangular elements can be observed in such a picture.

Finally, table 11.4 shows displacements u (horizontal) and v (vertical) for some of the Lagrangian nodes employed in the mesh[1].

[1] Although the formulation gathered in Levy and Spillers (1995) is not as robust as the one presented in this research, numerical results show perfect agreement. This fact is because of the smallness of the strains reached in the loading process.

	Levy & Spillers, 111		Present work	
Nodo	u	v	u	v
1	-.125e-6	-.296e-6	-.125e-6	-.296e-6
5	-.965e-7	-.169e-6	-.965e-7	-.169e-6
9	-.727e-7	-.950e-7	-.727e-7	-.950e-7
13	-.419e-7	-.408e-7	-.419e-7	-.408e-7

Table 11.4: Levy & Spillers, 111: Displacements(in).

11.3.2 Numerical example 4.

This example is considered in Levy and Spillers (1995). It is a squared plane membrane initially prestressed. The edges of the membrane are completely fixed. The side's length is 240 *in* and the thickness is measured as 0.004167 *in*. Mechanical properties for the material have the following values: $30,000$ Ksi for the Young modulus and 0.3 for the Poisson ratio. The prestressing effect is considered to be $80,000$ *psi* isotropically distributed. The mesh adopted is the same as the one employed in the original reference for the sake of comparison purposes. More accurate results would have been achieved with a finer mesh.

In-service loading conditions are taken to be a point transverse load applied in the center of the membrane. The load, which takes a value of 10 Kip, is taken downwards. According to the figure 11.10, the Lagrangian mesh is comprised of 32 isoparametric three-node linear elements and 25 nodes.

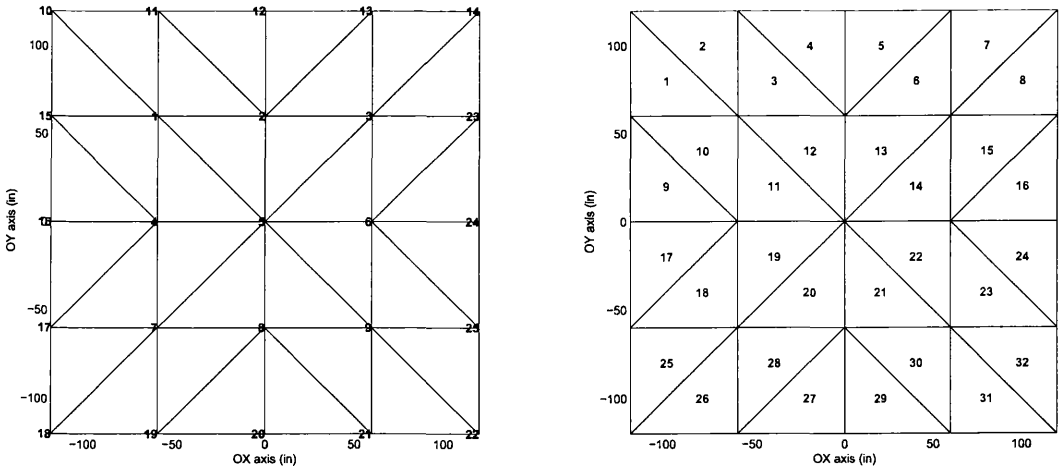

Figure 11.10: Numerical example 4: Discretization.

To accomplish the final solution, the method which was employed was the Newton-Raphson method for a single load increment. Two convergence curves are gathered in figure 11.11. The first of the curves shows the evolution of the Total Potential Energy along the iterations' path, whilst the second curve represents the infinity norm over the residual forces vector with respect to the number of iterations as well. The second curve shows perfectly the required quadratic convergence of the

Newton-Raphson algorithm.

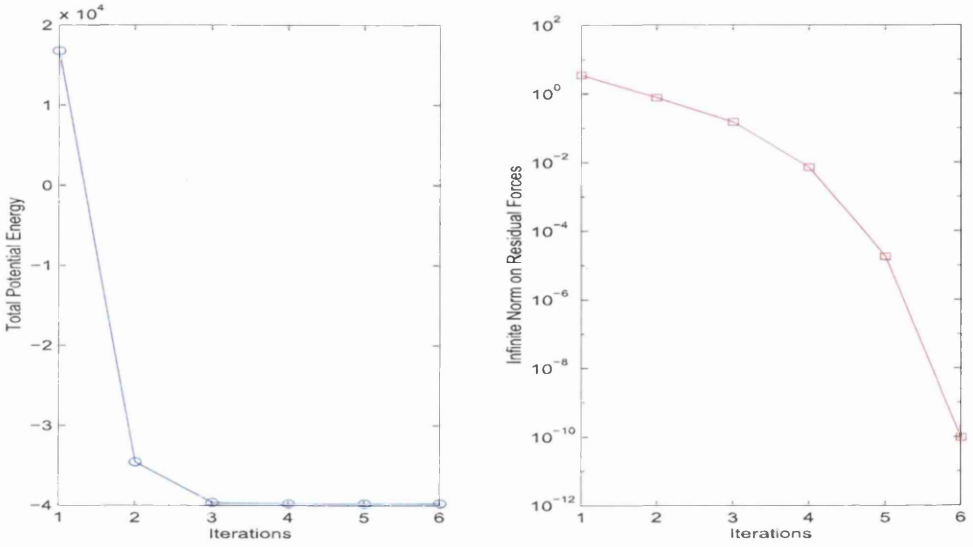

Figure 11.11: Numerical example 4: Convergence curves.

Figure 11.12 shows the displacement field along the cartesian axis OX and OZ, respectively. Both representations reveal in a clear manner the axisymmetry of the membrane. Table 11.5 details the displacement values for three different nodes of the mesh. The accuracy of the numerical example can be observed by checking the results with those obtained in Levy and Spillers (1995).

	Levy & Spillers			**Present work**		
Node	u	v	w	u	v	w
1	0.015	-0.015	-1.431	0.014	-0.014	-1.423
2	0.000	-0.017	-2.605	0.000	-0.017	-2.600
5	0.000	0.000	-6.642	0.000	0.000	-6.626

Table 11.5: Numerical example 4: Displacements (in).

Analogously, principal Cauchy stresses σ_I and σ_{II} can be viewed in figure 11.13. Table 11.6 presents the numerical values for three different elements of the membrane as well as its comparison with those of Levy and Spillers (1995). Perfect agreement can be deduced.

	Levy & Spillers			**Present work**		
Element	σ_{xx}	σ_{yy}	σ_{xy}	σ_{xx}	σ_{yy}	σ_{xy}
1	97377.6	85212.4	-2801.5	97300.1	85163.9	-2796.7
3	83510.2	96859.1	-8657.1	83501.5	96830.3	-8630.7
11	144691.0	97830.7	-15615.6	144470.8	97849.2	-15582.4

Table 11.6: Numerical example 4: Cauchy stresses (Psi).

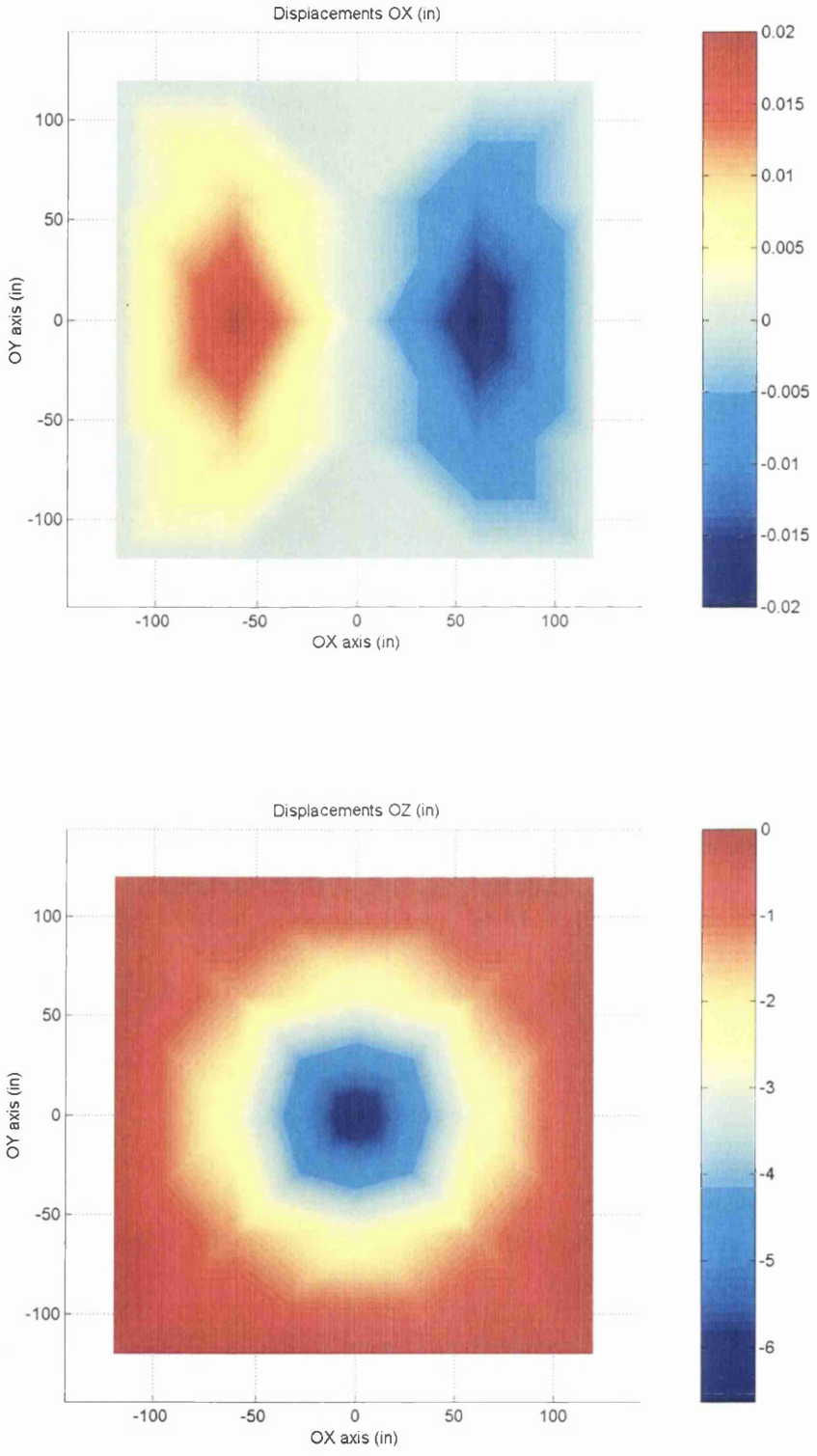

Figure 11.12: Numerical example 4: Displacements OX & OZ.

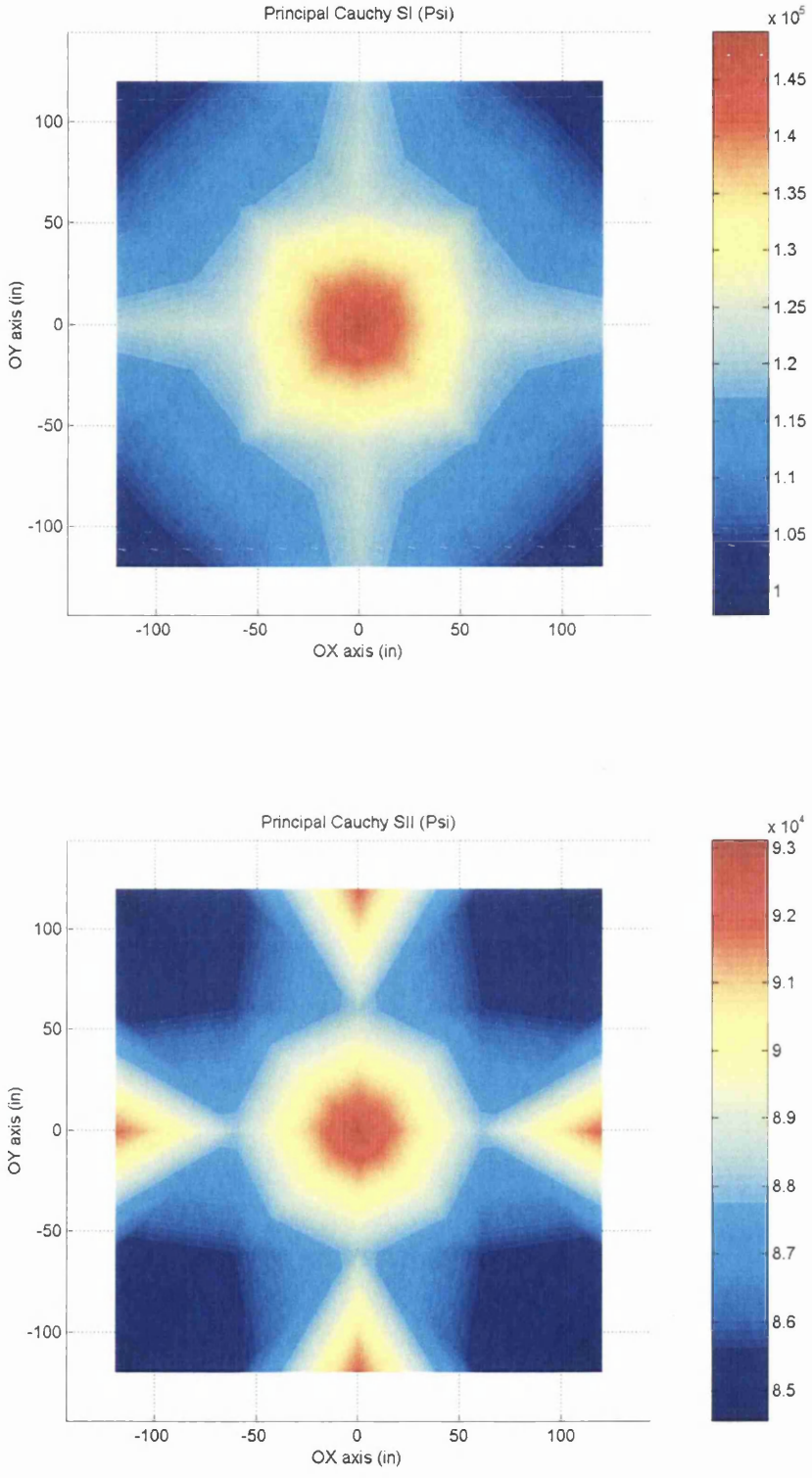

Figure 11.13: Numerical example 4: Cauchy stresses σ_I & σ_{II}.

11.4 Follower loads and wrinkling analysis.

11.4.1 Numerical example 5.

This numerical example has been taken from Kang and Im (1999), although the same problem has been analyzed by previous authors in the past. This example allows to compare numerical results provided by the algorithm suggested in this paper with those already reported in the literature. It consists of an initially squared airbag under static loading. The loading process will be achieved through an internal increase of pressure until a desired final configuration is reached -see Simo et al. (1991) and Rumpel and Schweizerhof (2004) for implementation purposes-. This model will be studied within the wrinkling membrane framework developed in previous chapters.

The material will be considered isotropic and its mechanical properties are adopted to be Young modulus of 588.0 MPa and a Poisson's ratio of 0.4. From the geometrical standpoint, the membrane displays a thickness of 1 mm and an initial diagonal measured as 1.2 m. Due to the implicit symmetry of the structural model with respect to three cartesian planes, namely, OXY, OXZ and OYZ, only one quarter needs to be computationally modelled. Moreover, appropriate boundary conditions need to be regarded. The internal pressure is raised linearly until a final threshold magnitude of 5.0 Kpa is attained. As boundary conditions, those nodes located on the boundary of the structure are considered to remain always in the plane OXY.

For the numerical solution of the problem, the Newton-Raphson method was employed. The load was applied in ten equal incremental steps. To avoid divergence problems within the first increment, due to high instability, the Levenberg-Marquardt method was taken into consideration to modify appropriately the total tangent stiffness matrix -see Dennis Jr. and Schnabel (1996) and Luenberger (1989). This mathematical modification of the energy functional's Hessian is, roughly speaking, nothing else than a fictitious prestressed state.

After the corresponding calculation, the convergence curves for the last incremental step are displayed in figure 11.14, where the quadratic convergence is clearly verified.

Figures 11.15 and 11.16 represent initial and final shapes for the airbag, both in plan and isometric view.

The displacements of some of the most remarkable structural nodes, according to the mesh shown in figure 11.15, are displayed in table 11.7. In table 11.7, w_1 is the deflection at the center point of the airbag, u_{121} stands for the displacement along the OX axis at the corner and u_{11} symbolizes the displacement along the OX axis at the center of the airbag. Results agree adequately with previous work.

Finally, the principal components σ_1 and σ_2 of the Cauchy stress tensor are represented in figure 11.17. It is worthwhile to point out the numerous amount of elements in wrinkling state.

The same structure was analyzed when different prestressed loadings were ap-

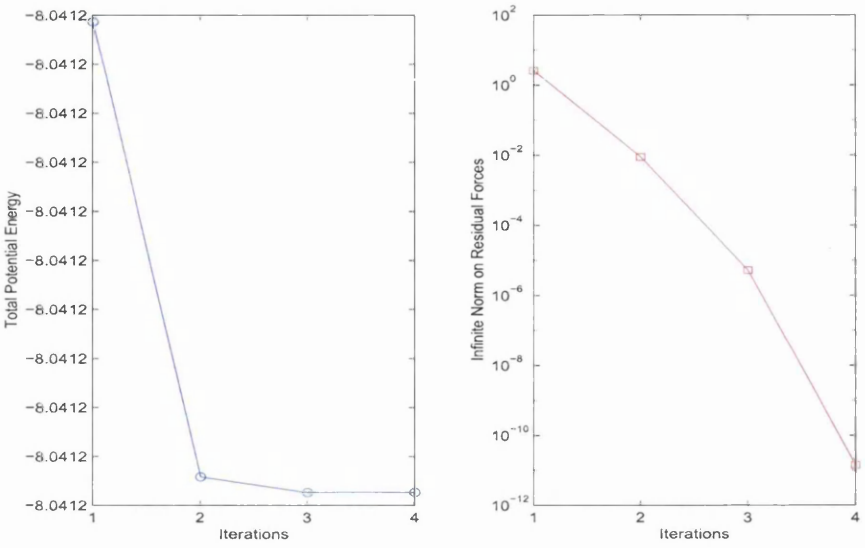

Figure 11.14: Convergence curves.

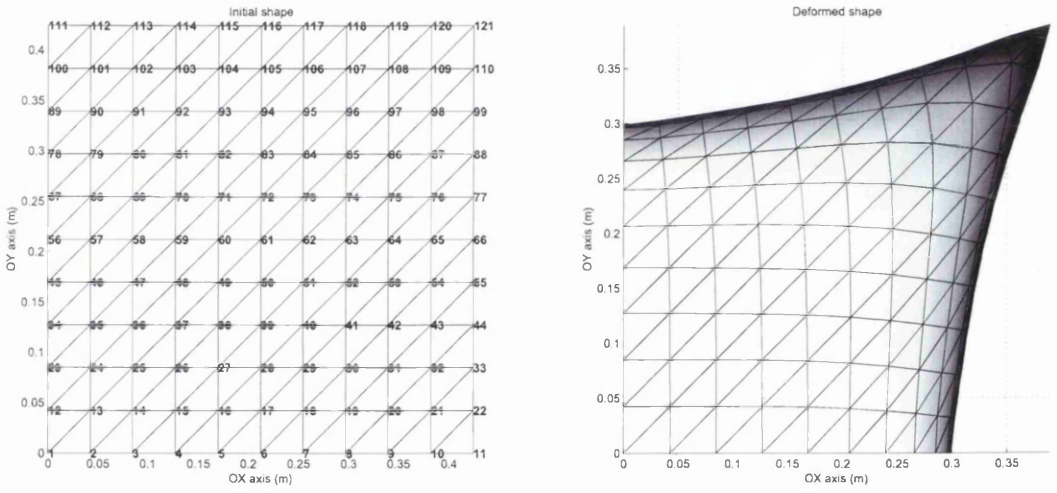

Figure 11.15: Kang & Im (1999). Initial and deformed airbag. Plan view.

plied on the membrane prior to the consideration of the internal pressure. An initial isotropically distributed prestressing was regarded acting within the plane OXY, which contains the undeformed membrane. Thus, the resulting prestressed membrane was subsequently subjected to the internal pressure process. The displacements in some notable nodes were again monitored and its values are displayed in table 11.8 for a set of different prestressing magnitudes. Figures 11.18 and 11.19 show the evolution of the principal Cauchy stress σ_{II} contour diagram in a series of images. As it can be noticed, the presence of finite elements in a wrinkling state increases as the prestressed loading magnitude is risen.

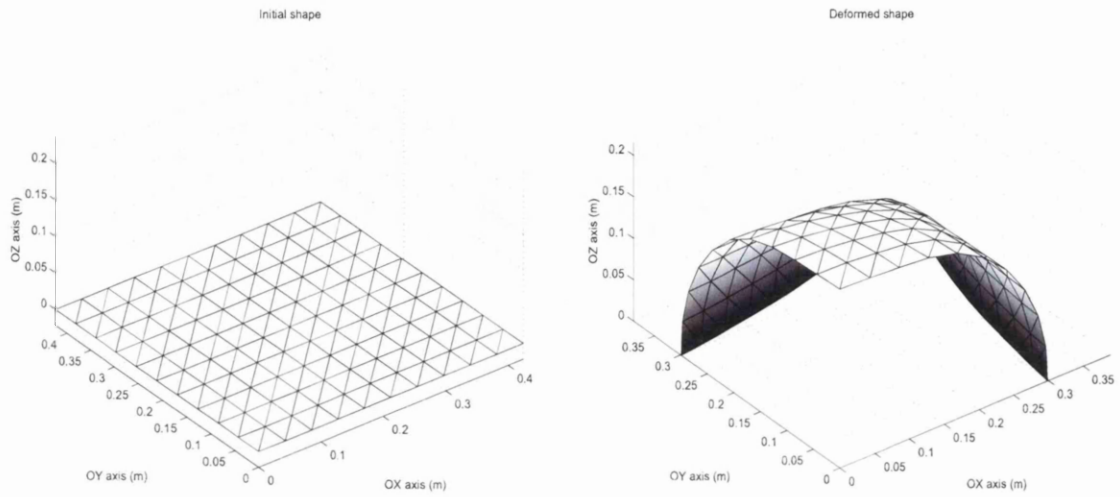

Figure 11.16: Kang & Im (1999). Initial and deformed airbag. Isometric view.

	Bauer	Conti & Schrefler	Kang & Im (1999)	Present study
Node		25 elem (4 nodes)	25 elem (9 nodes)	200 elem (3 nodes)
w_1	20.5	21.7	21.5	21.6
u_{121}	-3.3	-4.5	-3.7	-3.5
u_{11}	-13.0	-11.0	-12.0	-12.5

Table 11.7: Kang & Im (1999). Displacements(cm).

$\sigma^{pret}(\times 1000\ \mathrm{KN/m^2})$	2.5	12.5	18.75	25.0
w_1	16.32	7.54	5.77	4.74
u_{121}	-6.17	-0.89	-0.35	-0.11
u_{11}	-1.88	-0.19	0.00	0.11

Table 11.8: Kang & Im (1999). Evolution of displacements (cm).

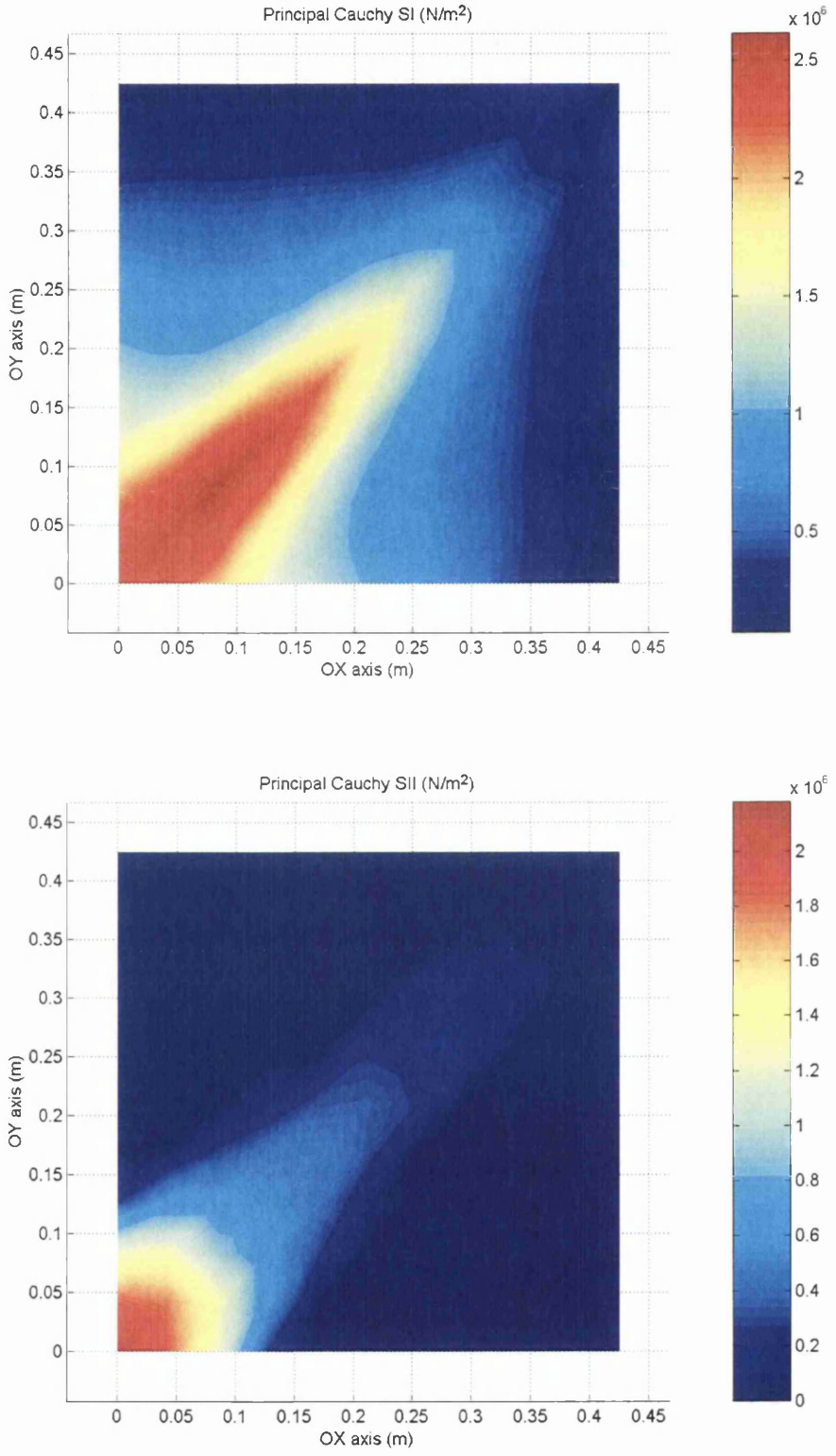

Figure 11.17: Kang & Im (1999). Principal Cauchy stresses: σ_I and σ_{II}.

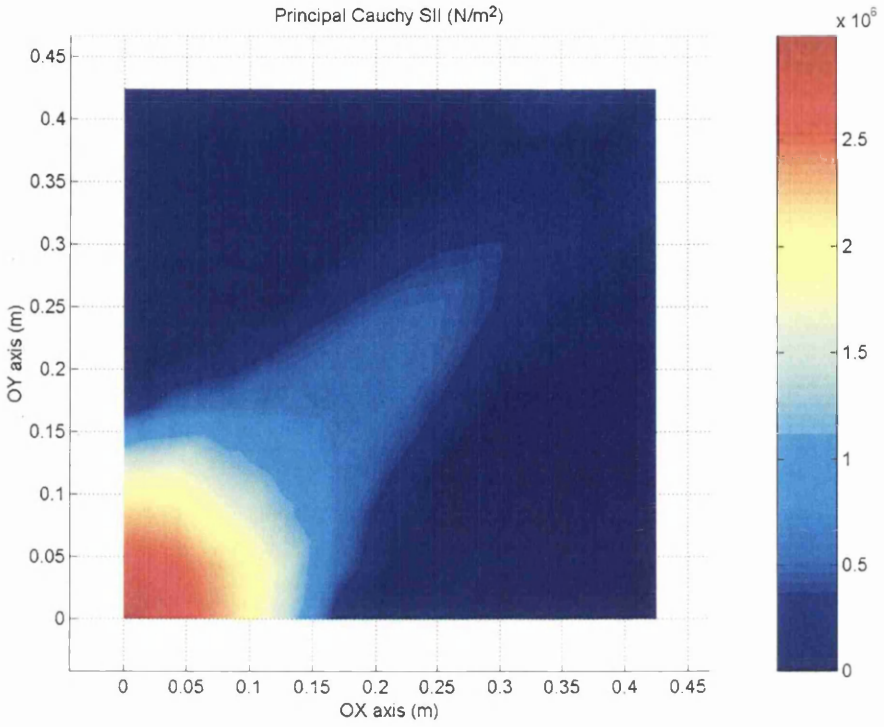

$$\sigma^{pret} = 2.5\ KN/m^2$$

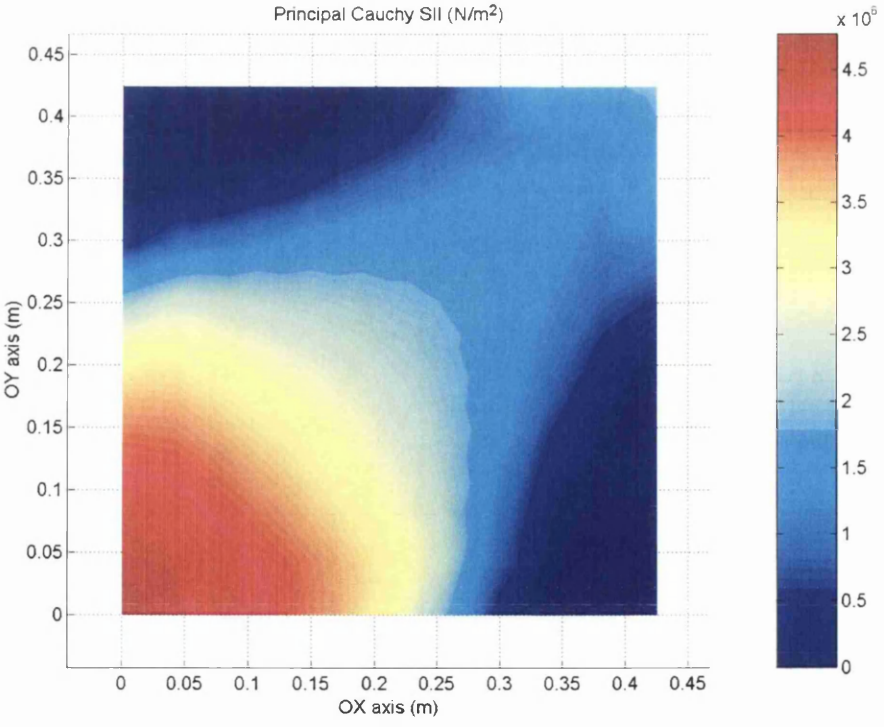

$$\sigma^{pret} = 12.5\ KN/m^2$$

Figure 11.18: Kang & Im (1999). Evolution of the minimum principal Cauchy stress (I).

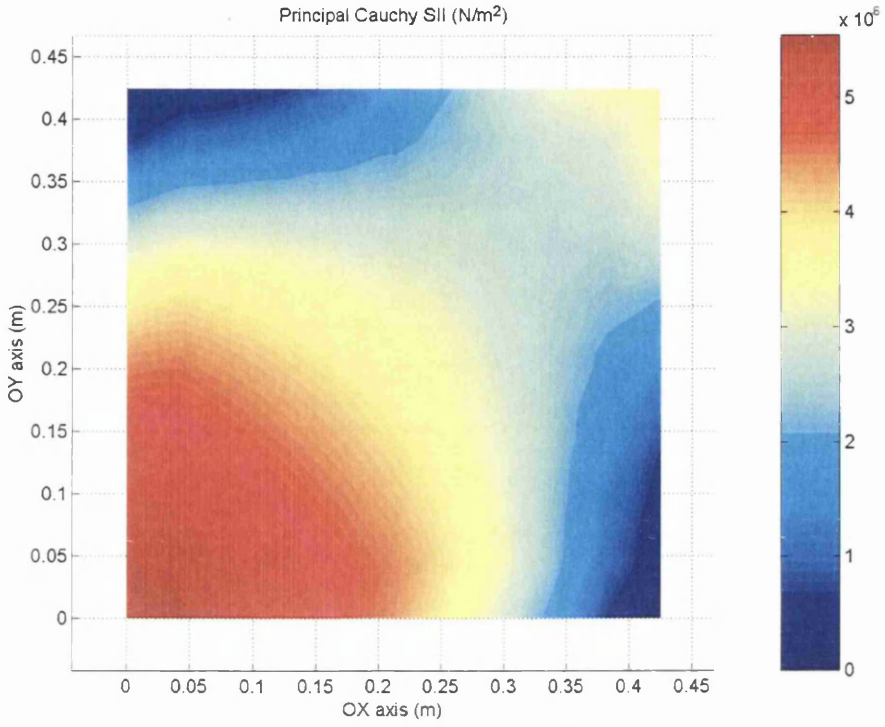

$\sigma^{pret} = 18.75\ KN/m^2$

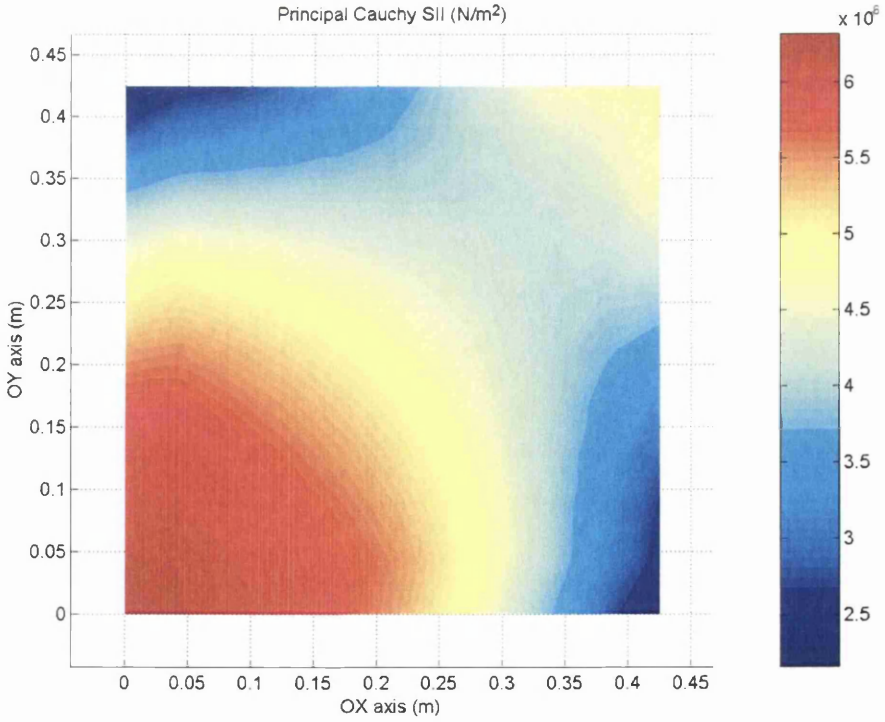

$\sigma^{pret} = 25.0\ KN/m^2$

Figure 11.19: Kang & Im (1999). Evolution of the minimum principal Cauchy stress (II).

11.4.2 Numerical example 6.

This sample has been extracted from Kang and Im (1997). Consider an inflatable circular airbag that initially consists of two flat circular pieces of fabric sewed together along the edge. The considered problem will be analyzed by means of the classical membrane theory allowing for compressive stresses, as well as according to the wrinkling theory developed earlier in the thesis. Results provided by both formulations will be compared.

The material will be adopted to be isotropic with Young modulus 6.0 Mpa and a Poisson's ratio of 0.3. The thickness arises to be 0.4 mm and the diameter of the initial flat membrane takes the value 0.7 m. Analogously to what it was established in the previous example, just one quarter of the structure has to be modelized for computational reasons. The airbag will be loaded with an increasing internal pressure up to a magnitude of 10.0 Kpa. Figure 11.20 represents the initial configuration of the analyzed membrane, as well as the adopted discretization.

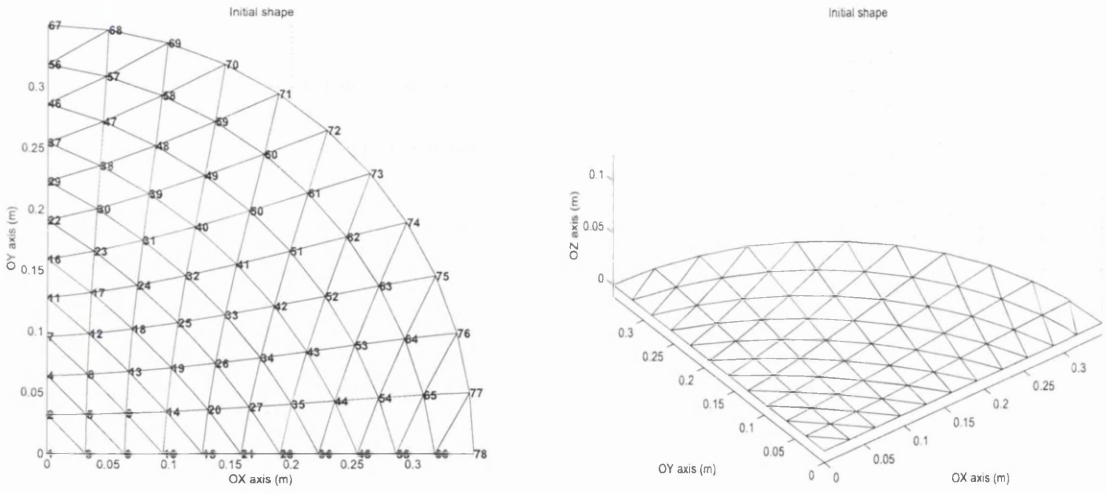

Figure 11.20: Kang & Im (1997). Initial airbag: plan and isometric views.

The load was applied in ten equal incremental steps. To avoid divergence problems within the first increment, this has been split into ten sub-increments in its turn. For the numerical solution of the problem, the Polak-Ribiere numerical method was employed for the first increments. After that, a change to the Newton-Raphson method is performed.

The final configuration of the membrane according to the wrinkling theory is showed in figure 11.21. The convergence curves for the last increment are gathered in 11.22 and 11.23 for both formulations. Quadratic convergence is observed.

For the problem accounting for wrinkling, the principal Cauchy stress components are shown in figure 11.24. Figure 11.25 displays the final configuration of the whole upper half of the airbag.

Figure 11.26 shows the vertical displacement of the center point and the radial contraction of a point of the circumference; both of them with respect to the increase

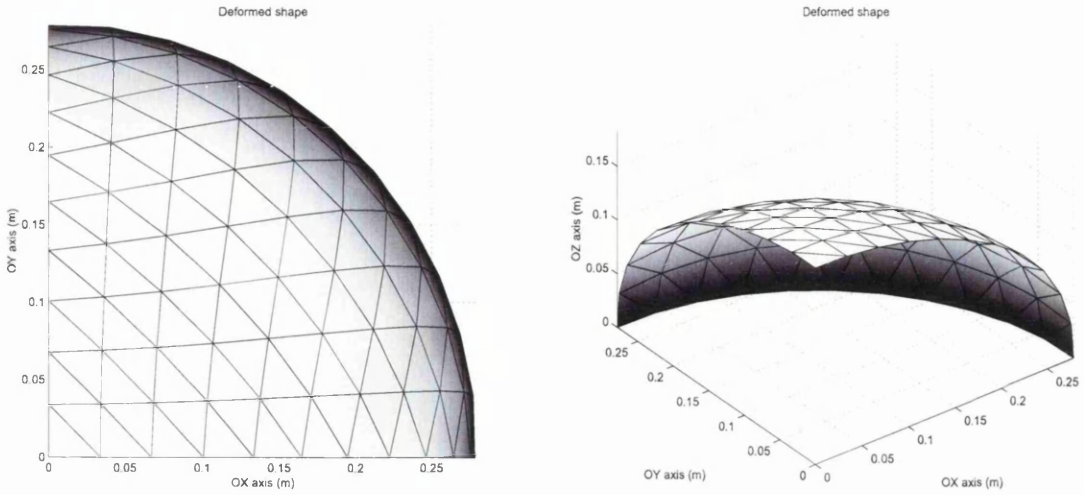

Figure 11.21: Kang & Im (1997). Deformed airbag: plan and isometric views.

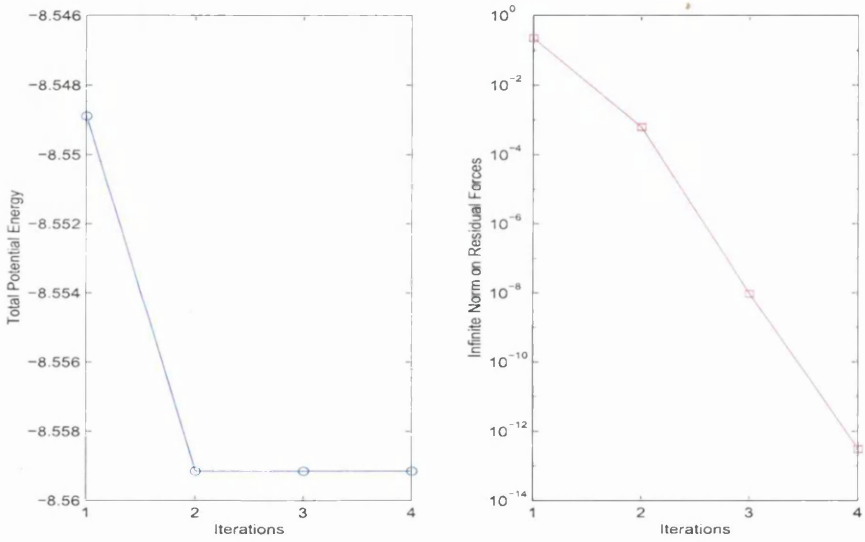

Figure 11.22: Convergence curves: membrane theory.

in the internal pressure. Two different circumstances were analyzed; one obtained with wrinkling being taken into account and the other one obtained from pure membrane theory with no wrinkling being taken into consideration. The difference between both cases is highest in the low pressure region. As the pressure gets higher values, the displacement difference is smaller since the wrinkled region decreases.

The results from the present study seems to agree with those gathered in Kang and Im (1997). Just only small differences are detected for the case when wrinkling is not accounted for. This is due to local bucking effects around the perimeter of the airbag. These effects distort the numerical algorithm by offering not very reliable results. A suitable way to account for the bending effect should be included if accurate results want to be obtained according to the pure membrane theory.

The same circular airbag was studied under the effect of different prestressed

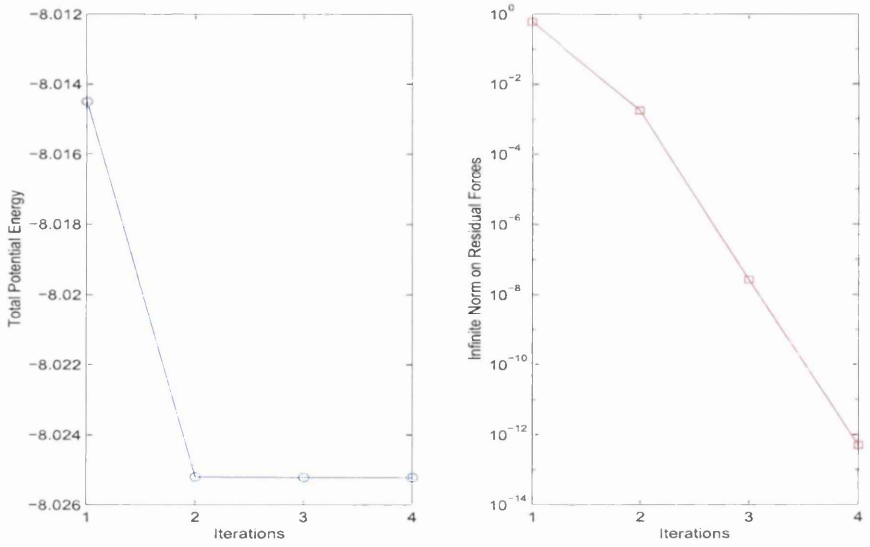

Figure 11.23: Convergence curves: wrinkling theory.

loadings. An initial isotropically distributed prestressing was considered acting within the plane OXY which contains the undeformed membrane. Once the airbag is deformed in order to reach the prestressed state, the internal pressure is then raised linearly. The maximum vertical deflection of the airbag, represented by the vertical displacement w of node 1, as well as its radial contraction, symbolized by the displacement u along the OX axis of node 78, are displayed in table 11.9 for different prestressed loadings. Analogously, a series of contour diagrams depicting the minimum principal Cauchy stress σ_{II}, is shown in figures 11.27 and 11.28 .

$\sigma^{pret}(\times 1000\ \mathbf{KN/m^2})$	**0.25**	**2.5**	**12.5**	**18.75**	**25.0**
w_1	16.98	10.74	4.71	3.90	3.47
u_{78}	-5.00	1.24	8.96	12.13	14.83

Table 11.9: Kang & Im (1997). Evolution of displacements (cm).

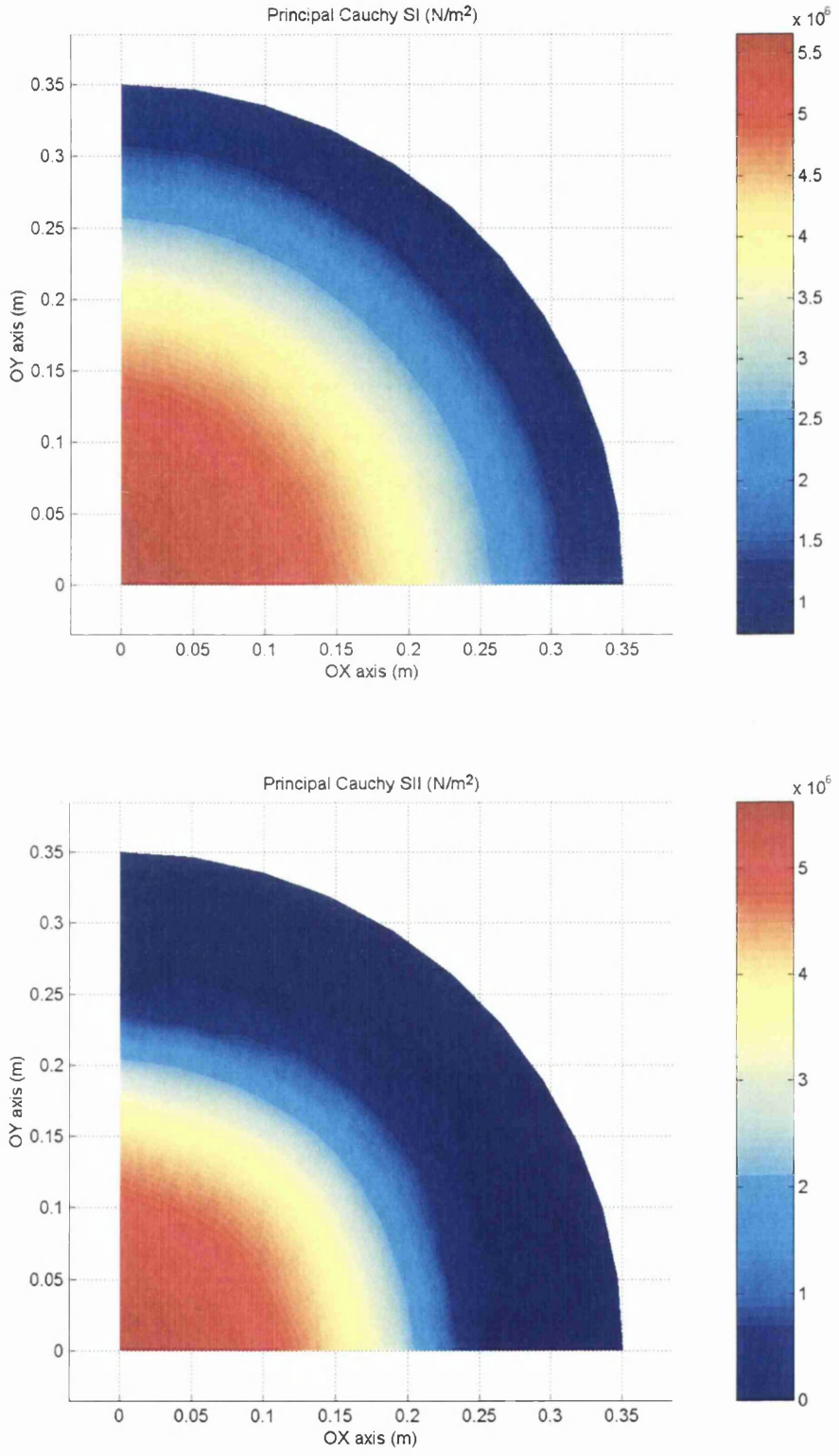

Figure 11.24: Kang & Im (1997). Principal Cauchy stresses: σ_I and σ_{II}.

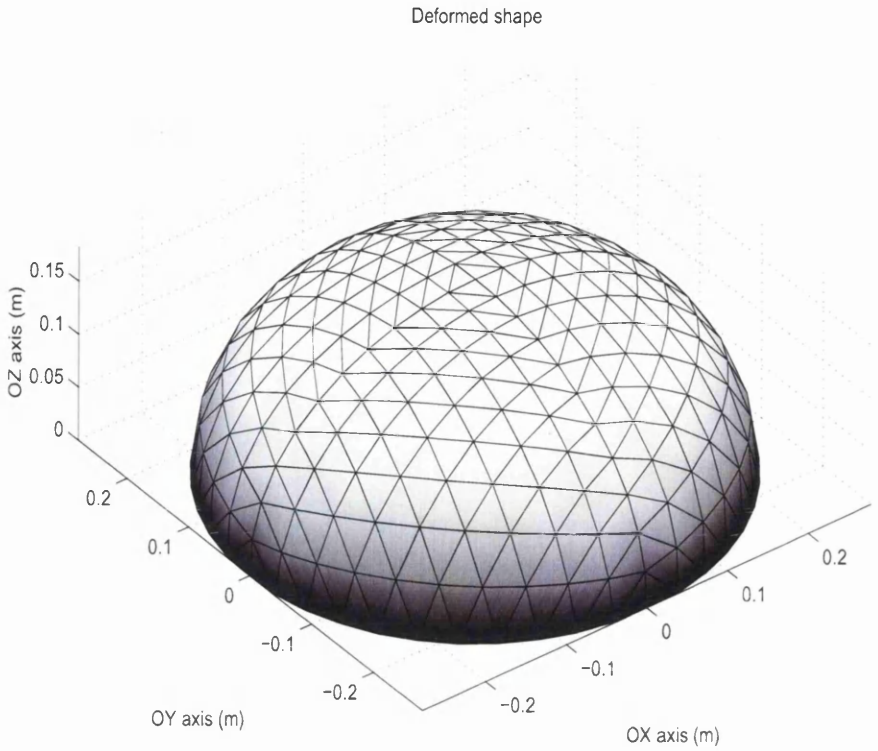

Figure 11.25: Kang & Im (1999). Deformed airbag

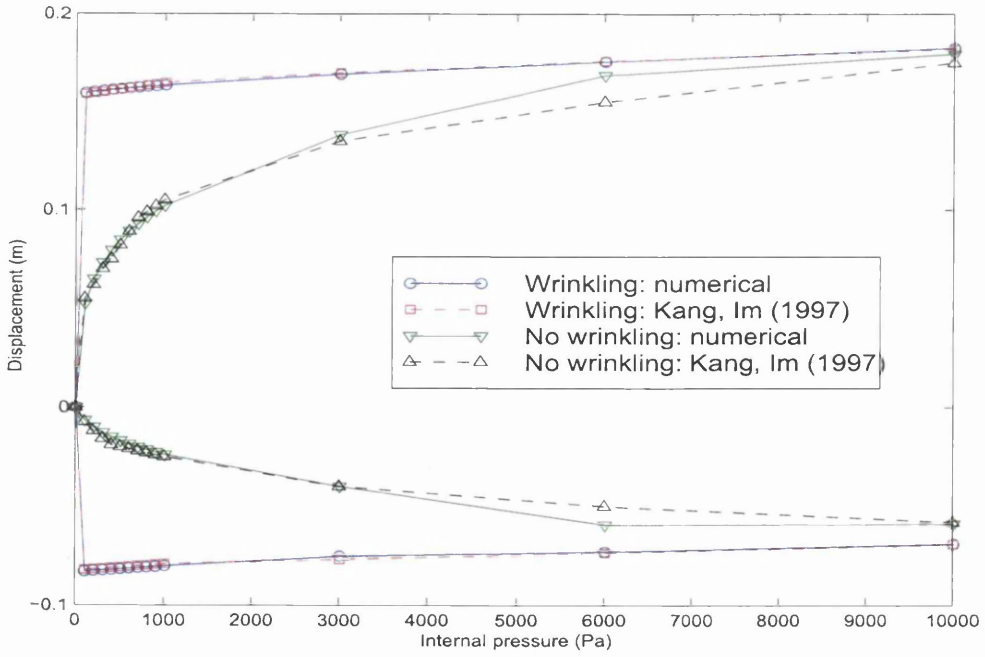

Figure 11.26: Kang & Im (1997). Vertical displacement and radial contraction.

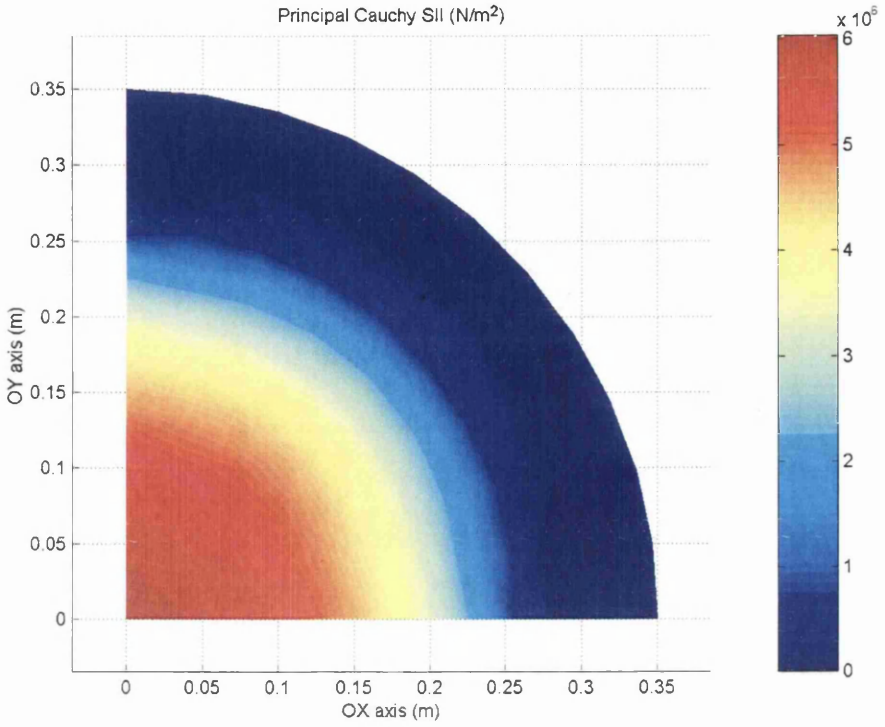

$$\sigma^{pret} = 0.25\ KN/m^2$$

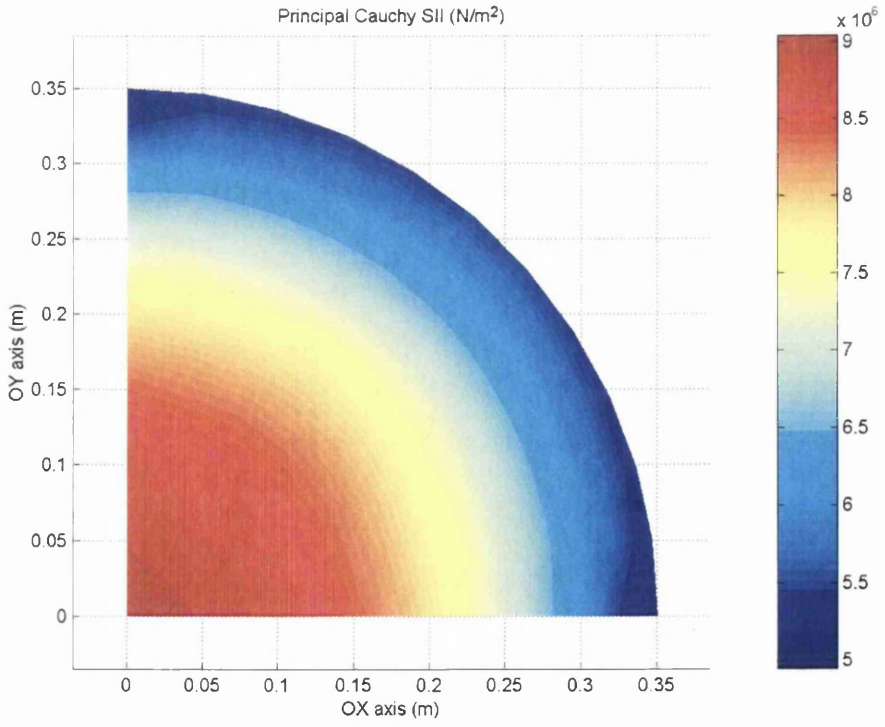

$$\sigma^{pret} = 2.5\ KN/m^2$$

Figure 11.27: Kang & Im (1997). Evolution of the principal Cauchy stress σ_{II} (I).

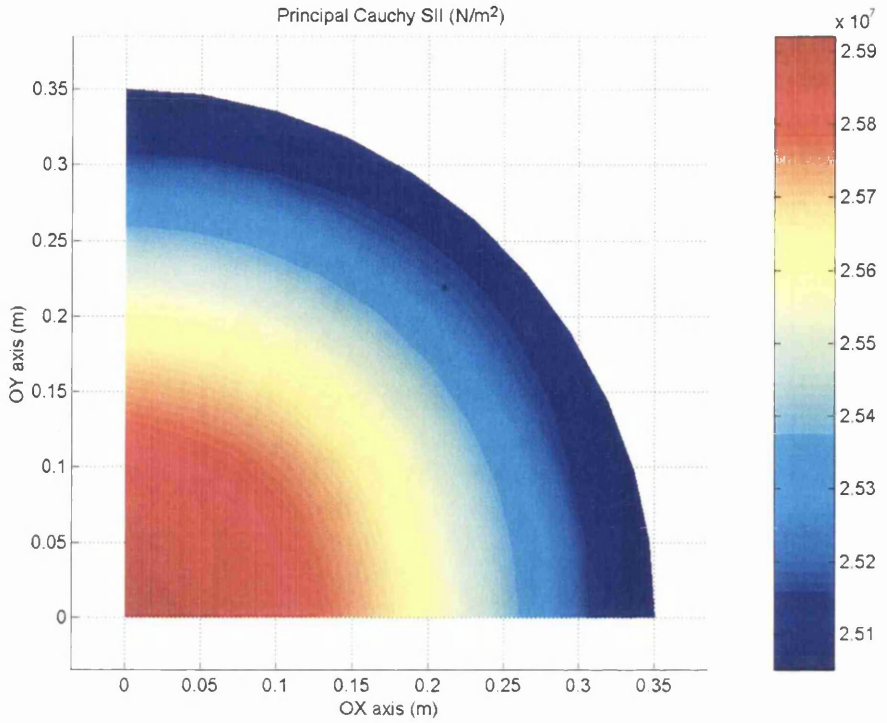

$$\sigma^{pret} = 12.5\ KN/m^2$$

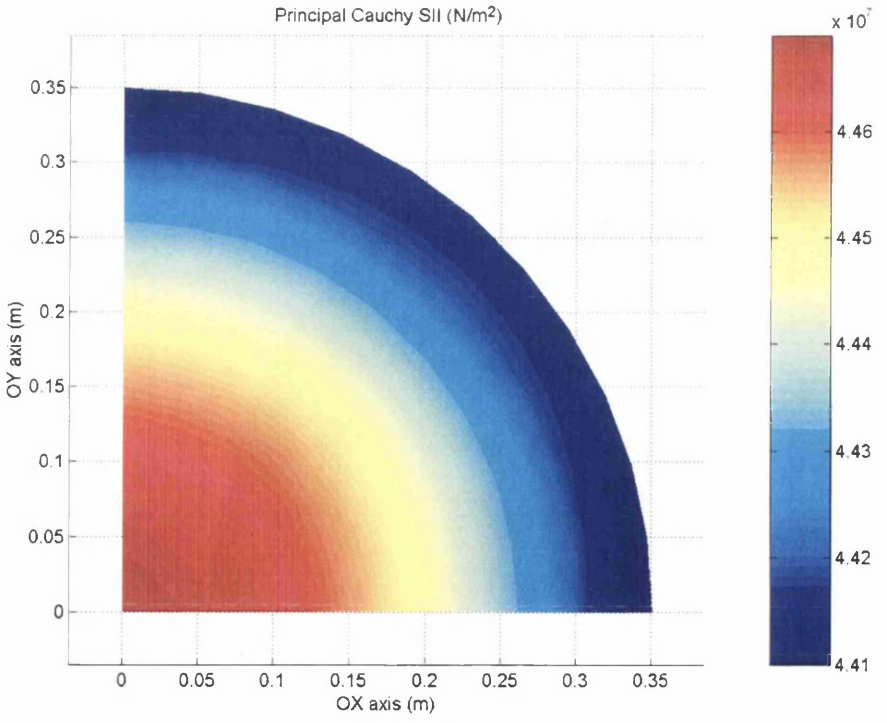

$$\sigma^{pret} = 25.0\ KN/m^2$$

Figure 11.28: Kang & Im (1997). Evolution of the principal Cauchy stress σ_{II} (II).

11.4.3 Numerical example 7.

This numerical example has been reviewed several times in the existing literature -see Miller et al. (1985) and Lu et al. (2001)-. It is a 2D beam, which can be considered as a 2D rectangular membrane, isotropically prestressed according to the principal directions OX and OY with a constant stress σ_0. The membrane presents a cross sectional area of depth h and of thickness t, in such a way, that the total axial longitudinal prestressed load acting along the direction OX turns out to be:

$$P = \sigma_0 t h \tag{11.1}$$

Once the initial prestressed loading is applied on the structure, an external bending moment M is applied acting on one of the edges of the structure, whereas the other edge is fully fixed. As the magnitude of such a bending moment increases its value, a compression state starts to be generated in part of the membrane domain, so wrinkling must be taken into consideration in order to accomplish an accurate result for such a structural problem. The compression domain can be represented by a lower horizontal strip of depth b.

Analytically, the ratio between both depths b and h, can be formulated as:

$$\frac{b}{h} = \begin{cases} 0, & \frac{M}{Ph} < \frac{1}{6} \\ \frac{3M}{Ph} - \frac{1}{2}, & \frac{1}{6} \leq \frac{M}{Ph} < \frac{1}{2} \end{cases} \tag{11.2}$$

The components σ_x, σ_y and τ_{xy} of the Cauchy stress tensor can also be obtained according to the following expressions:

$$\frac{\sigma_x}{\sigma_0} = \begin{cases} 2\left(\frac{y}{h} - \frac{b}{h}\right) / \left(1 - \frac{b}{h}\right)^2, & \frac{b}{h} < \frac{y}{h} \leq 1 \\ 0, & 0 \leq \frac{y}{h} \leq \frac{b}{h} \end{cases} \tag{11.3}$$

$$\frac{\sigma_y}{\sigma_0} = 1 \tag{11.4}$$

$$\tau_{xy} = 0 \tag{11.5}$$

Eventually, if we denote as κ the curvature, the relationship between the latter and the applied bending moment can be written as:

$$\frac{2M}{Ph} = \begin{cases} \frac{1}{3}\frac{Eth^2}{2P}\kappa, & \frac{Eth^2}{2P}\kappa \leq 1 \\ 1 - \frac{2}{3}\sqrt{\frac{2P}{Eth^2\kappa}}, & \frac{Eth^2}{2P}\kappa > 1 \end{cases} \tag{11.6}$$

where E represents the Young modulus of the material. For the resolution of the problem, the membrane was discretized into a Lagrangian mesh comprised of 1024 isoparametric linear triangular elements distributed uniformly. Left hand side

nodes are immobilized along the OX axis, being also fixed along the OY axis the node located at the center of the section. Discretization is showed in figure 11.29.

The prestressed loading σ_0 along the OY axis has been accomplished by means of nodal loads acting on membrane's upper and lower lawyers.

With the purpose of defining in the most accurate manner the external bending moment, a rigid thin beam attached to the main membrane by means of short connectors was introduced into the analysis. This rigid beam was modelized through membrane elements with Young modulus one hundred times larger than the one of the actual analyzed membrane. Pure membrane theory without wrinkling effects was used to represent its mechanical behaviour. The connectors were generated as extremely short but stiff cables.

Both the external bending moment and the horizontal prestressed loading were achieved by means of two horizontal point loads acting on the upper and lower nodes of the right edge of the rigid beam. The so called connectors enable the transmission of the bending moment as well as the horizontal prestressed loading from the rigid beam to the membrane without introducing any fictitious shear stresses but only axial stresses (recall figure 11.29).

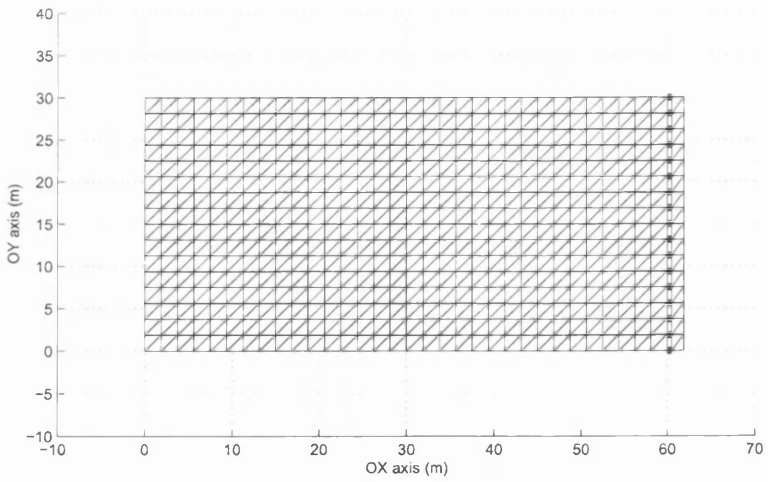

Figure 11.29: Discretization

For the sake of assimilating the analyzed structural model with the classical Euler beam model, a null Poisson ratio was considered. The curvature of the structure as the loading process progresses is calculated by interpolating a parabolic or quadratic spline along the horizontal center fiber of the membrane. In accordance with the Saint Venant principle, localized buckling effects can be omitted.

For the resolution of the problem, a Newton-Raphson method for a single load increment was employed. The figure 11.30 represents the Cauchy stress σ_{xx} which is reached when a loading status of ratio $\frac{2M}{Ph} = 0.5$ is undergone by the structure. The depth of the compressive strip agrees perfectly with the result of formula (11.2).

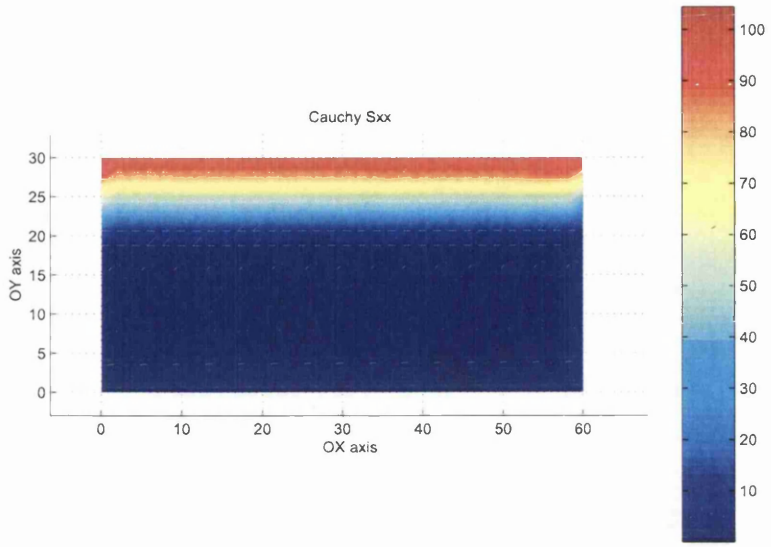

Figure 11.30: Cauchy stress component σ_{xx} for $\frac{2M}{Ph} = 0.5$

Figure 11.31 represents the bending moment evolution with respect to the curvature. Figure 11.32 represents the Cauchy stress plotted as a function of the depth. Both numerical and analytical results seem to agree.

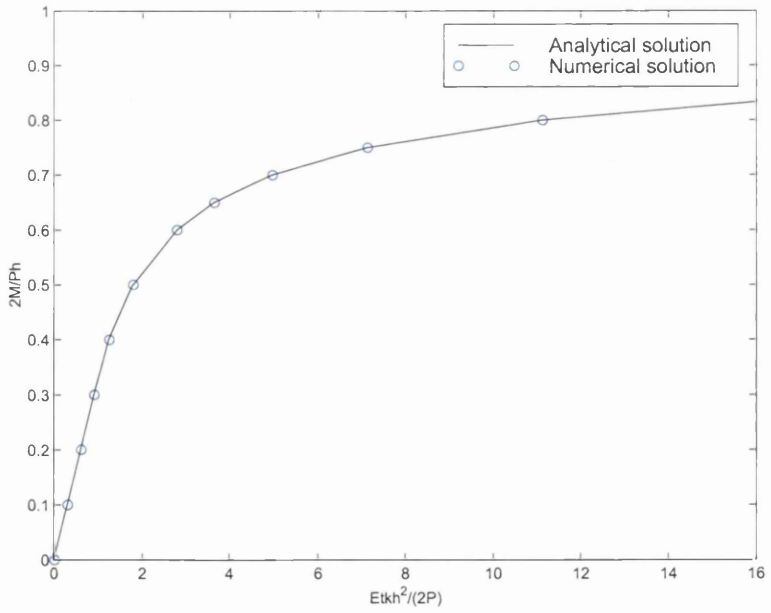

Figure 11.31: Bending moment vs curvature.

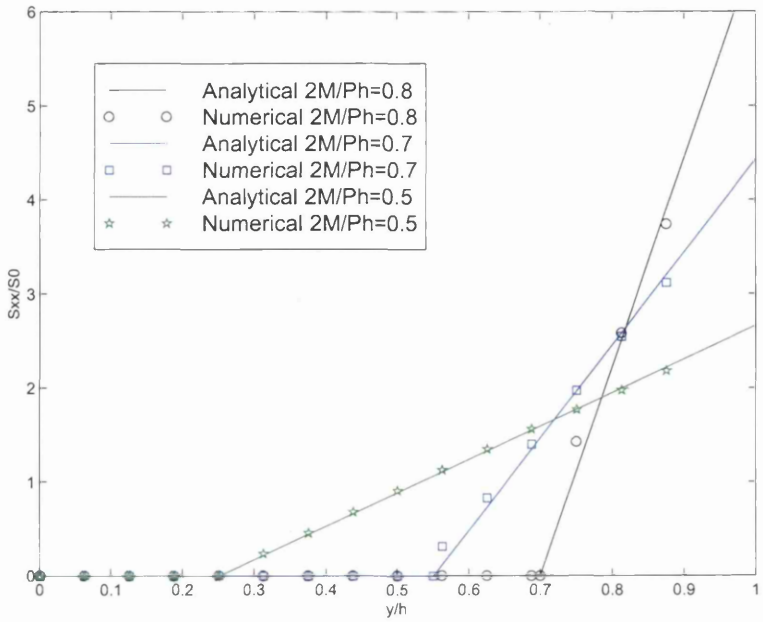

Figure 11.32: Cauchy stress σ_{xx} vs depth.

11.5 Cable reinforced prestressed membranes.

11.5.1 Numerical example 8.

It results rather difficult to find experimental analyses for prestressed membranes. Nevertheless, in Magara and Okamura (1986) some interesting examples may be found, whose results will be compared with the numerical method developed in this research. Two structures will be studied, one here and another one in the next section.

It is convenient to point out in advance that some important issues are not sufficiently explained in such a reference, specially those pertaining to how the loads were applied and how the resulting displacements or stresses were measured. Therefore, it is fundamental to be cautious when comparing numerical and experimental results. Nonetheless, it seems appealing to cope with these examples at least from a qualitative point of view.

This first example deals with a membrane bounded by rigid members and subjected to a successive process of prestressed loading and in-service loading. The in-service loading consists in snow uniformly distributed across the membrane's domain. The structure itself, whose plan and isometric views are shown in figure 11.33, presents as initial configuration a hyperbolic paraboloid described by the equation:

$$z = -\frac{x^2}{400} + \frac{y^2}{400} \tag{11.7}$$

with plan dimensions $160 \times 160\ cm^2$ and with a difference of height between highest and lowest nodes of $32\ cm$.

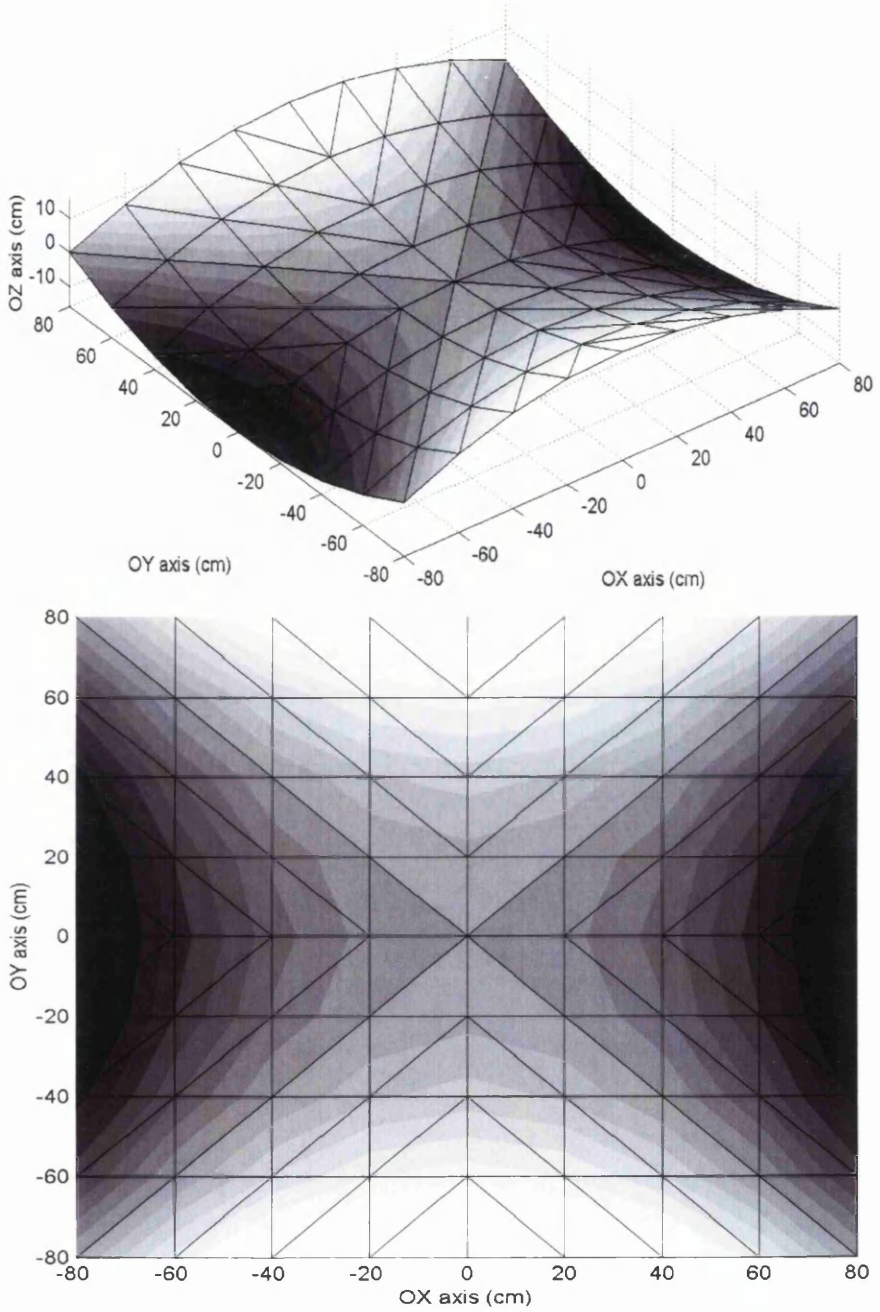

Figure 11.33: Numerical example 8: isometric and plan views.

The structural process will be split into two stages. During the first stage, an isotropic prestressed loading of value 2.0 $\frac{Kp}{cm}$ is applied on the structure. The resulting membrane shape is accomplished as a form finding problem. Throughout the second stage, a total snow load of 2080 Kp is exerted[2]. The mechanical char-

[2]In Magara and Okamura (1986), because of typographic error, a total snow load of 520 kp is written down.

acteristics of the material are: $Et = 2.47e2\ \frac{Kp}{cm}$ and[3] $\nu = 0.39$. For the sake of the structural symmetry, only a quarter of the whole membrane will be analyzed.

For any point contained in the membrane's domain, the direction parallel to the OX axis presents negative Gaussian curvature (bracing direction), whereas along the direction parallel to the OY axis, the Gaussian curvature results to be positive (hanging direction).

Figure 11.34 represents the equilibrium profile of the membrane after prestressing it along both bracing and hanging directions. Numerical and experimental results are included.

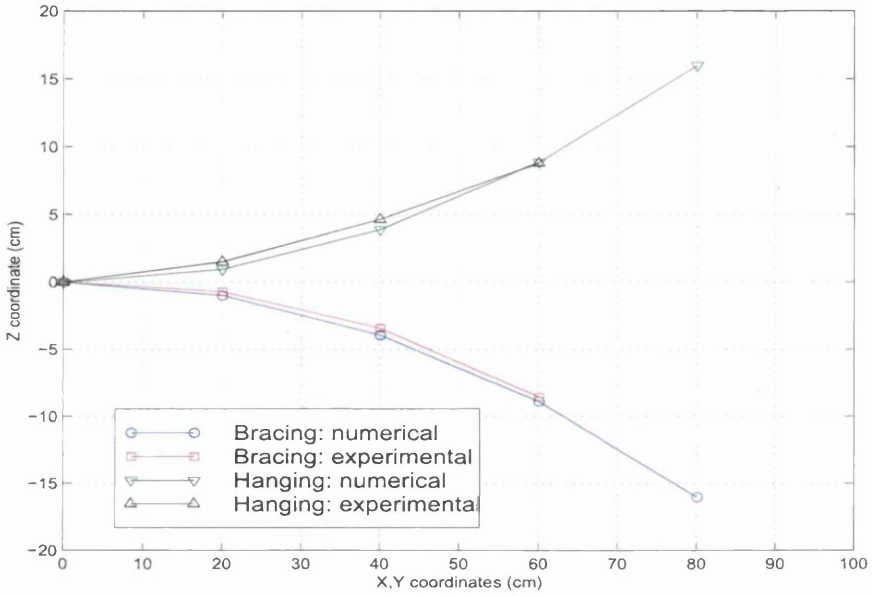

Figure 11.34: Numerical example 8: equilibrium profile curves.

Then, snow in-service loading is left acting on the structure. All the numerical analysis were performed by means of the Newton-Raphson's method in thirteen load increments. Figure 11.35 displays the absolute vertical displacement located at the center of the membrane's configuration. The displacement was plotted through the whole in-service loading process divided into thirteen equal increments.

Analogously, same figure's right hand side represents on the one hand, the Cauchy stress component σ_{xx} in the membrane's upper right quadrant's lower right point -bracing direction- and, on the other hand, the Cauchy stress component σ_{yy} in the membrane's upper right quadrant's upper left point -hanging direction-.

Numerical and experimental results seem to agree considerably, although some discrepancies can be observed in the stress component along the hanging direction. However, qualitatively, the numerical method can be regarded as adequate.

[3] Et represents the product of the Young modulus and the membrane's thickness.

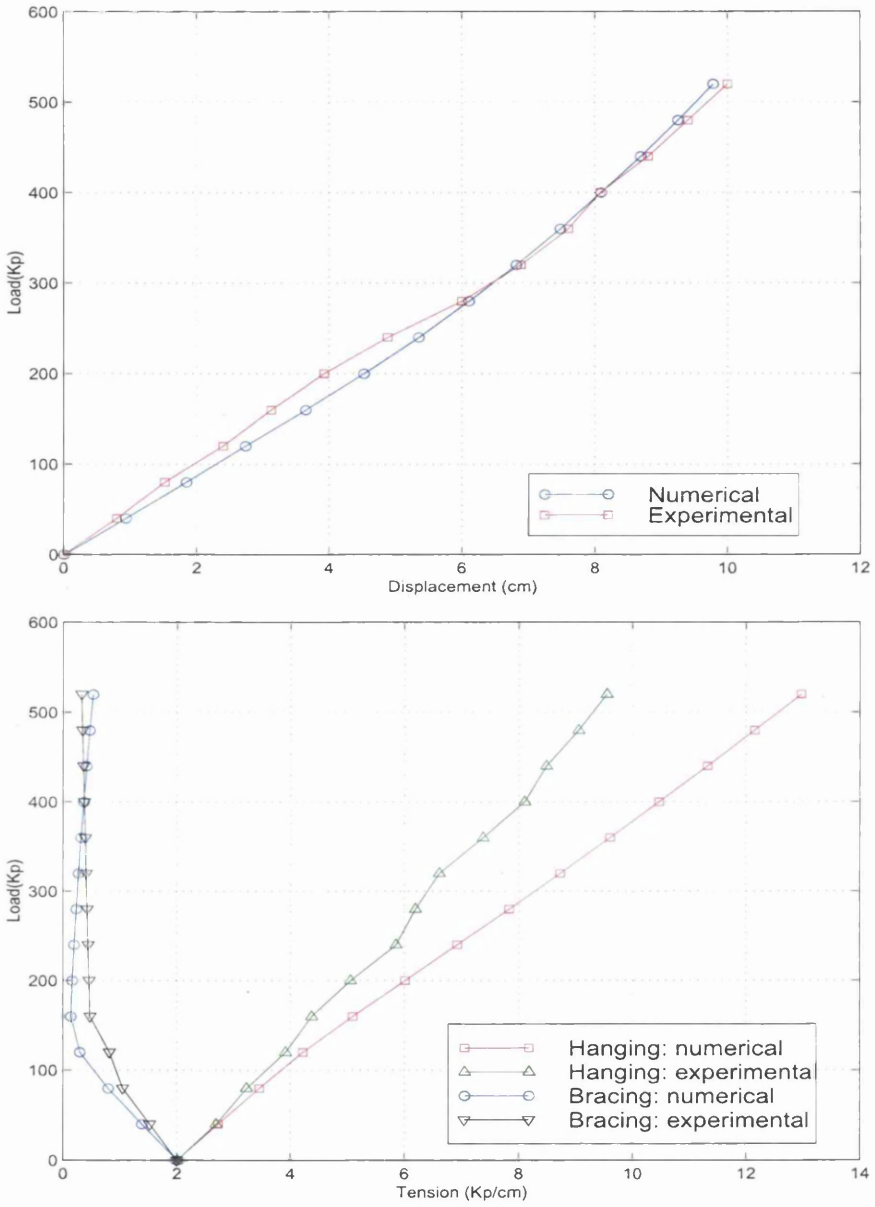

Figure 11.35: Numerical example 8: Displacement and stress vs loading.

11.5.2 Numerical example 9.

The second example, also extracted from Magara and Okamura (1986), is a prestressed membrane bounded by reinforcing cables. As in the former example, prestressed loading and snow in-service loading will be undergone by the structure. The initial membrane, whose plan and isometric views can be observed in figure 11.36, is described by a hyperbolic paraboloid of equation:

$$z = -\frac{x^2}{600} + \frac{y^2}{600} \tag{11.8}$$

with plan dimensions 240×240 cm^2 and with a difference of height between

highest and lowest nodes of 48 cm.

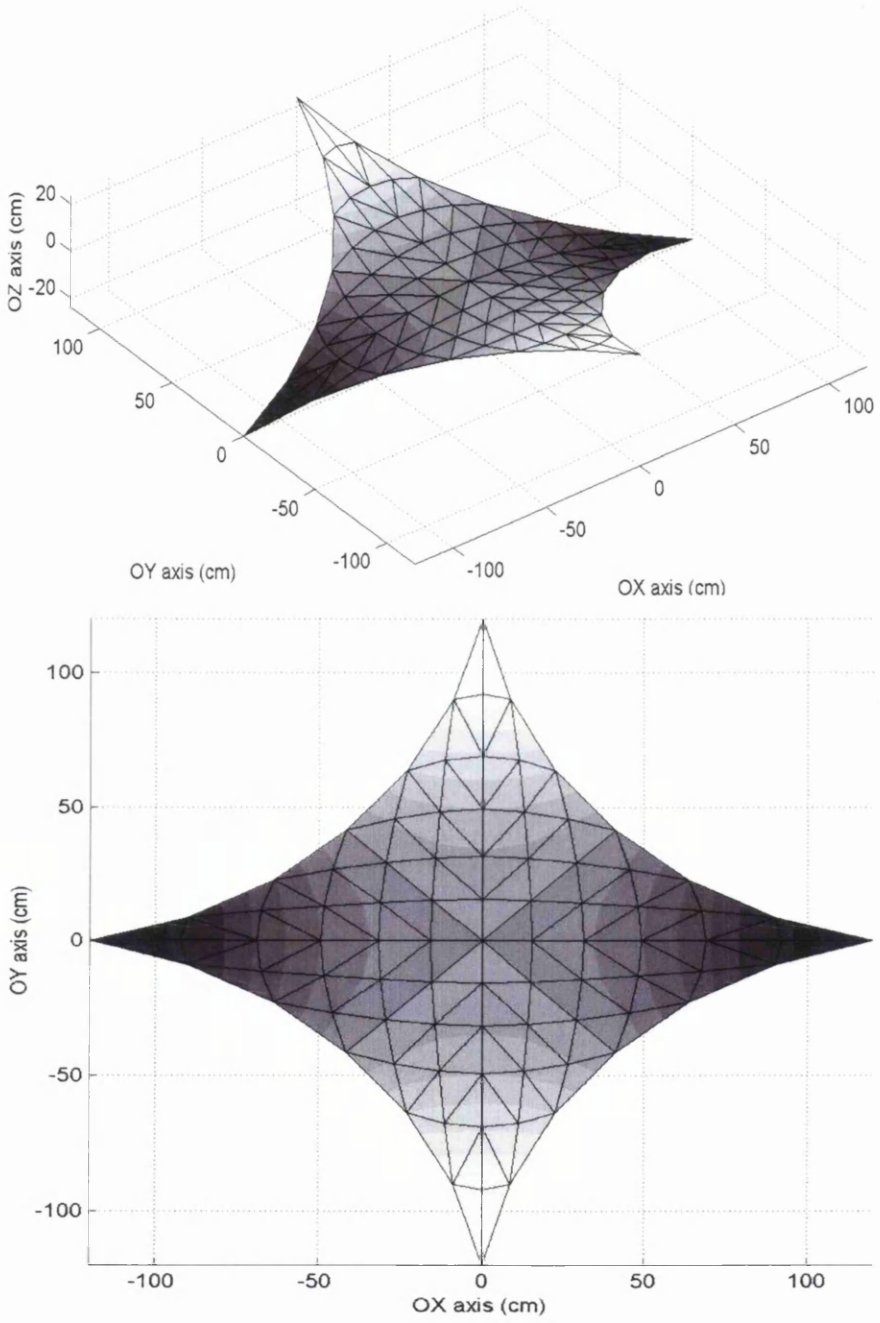

Figure 11.36: Numerical example 9: isometric and plan views.

The structural process will be split into two stages. During the first stage, an isotropic prestressed loading of value 0.57 $\frac{Kp}{cm}$ is applied on the membrane. Reinforcing perimeter cables will be subjected to 90 Kp. The resulting membrane shape is accomplished as a consequence of a form finding problem. Throughout the second stage, a total snow load of 300 Kp is exerted. The mechanical characteristics of the material are: $Et = 2.47e2\ \frac{Kp}{cm}$ and $\nu = 0.39$ for the membrane and $EA = 2.18e4Kp$

for the reinforcing cables[4]. For the sake of the structural symmetry, only a quarter of the whole membrane will be analyzed.

For any point contained in the membrane's domain, the direction parallel to the OX presents negative Gaussian curvature (bracing direction), whereas along the direction parallel to the OY axis, the Gaussian curvature results to be positive (hanging direction).

Figure 11.37 represents the equilibrium profile of the membrane after prestressing it along both bracing and hanging directions. Numerical and experimental results are included.

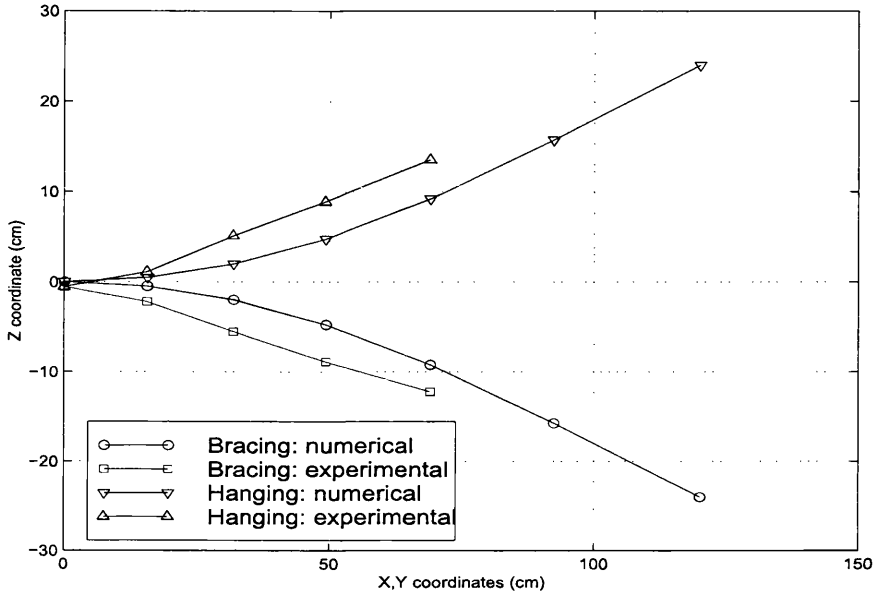

Figure 11.37: Numerical example 9: equilibrium profile curves.

Then, snow in-service loading is left acting on the structure. All the numerical analyses were performed by means of the Newton-Raphson in six load increments. Figure 11.38 displays the absolute vertical displacement located at the center of the membrane, plotted along a thirteen increment loading process.

Analogously, same figure's right hand side represents on the one hand, the Cauchy stress component σ_{xx} in the membrane's upper right quadrant's lower right point -bracing direction- and, on the other hand, the Cauchy stress component σ_{yy} in the membrane's upper right quadrant's upper left point -hanging direction-.

Numerical and experimental results seem to agree considerably, although some discrepancies can be observed. However, qualitatively, the numerical method can be regarded as adequate. A reason to explain such discrepancies is based on the fact that the initial prestressed equilibrium profile does not match perfectly numerically and experimentally. This introduces some disagreement that reflects in the final in-service loading results.

[4] EA represents the product of the cable's Young modulus with the cable's cross sectional area.

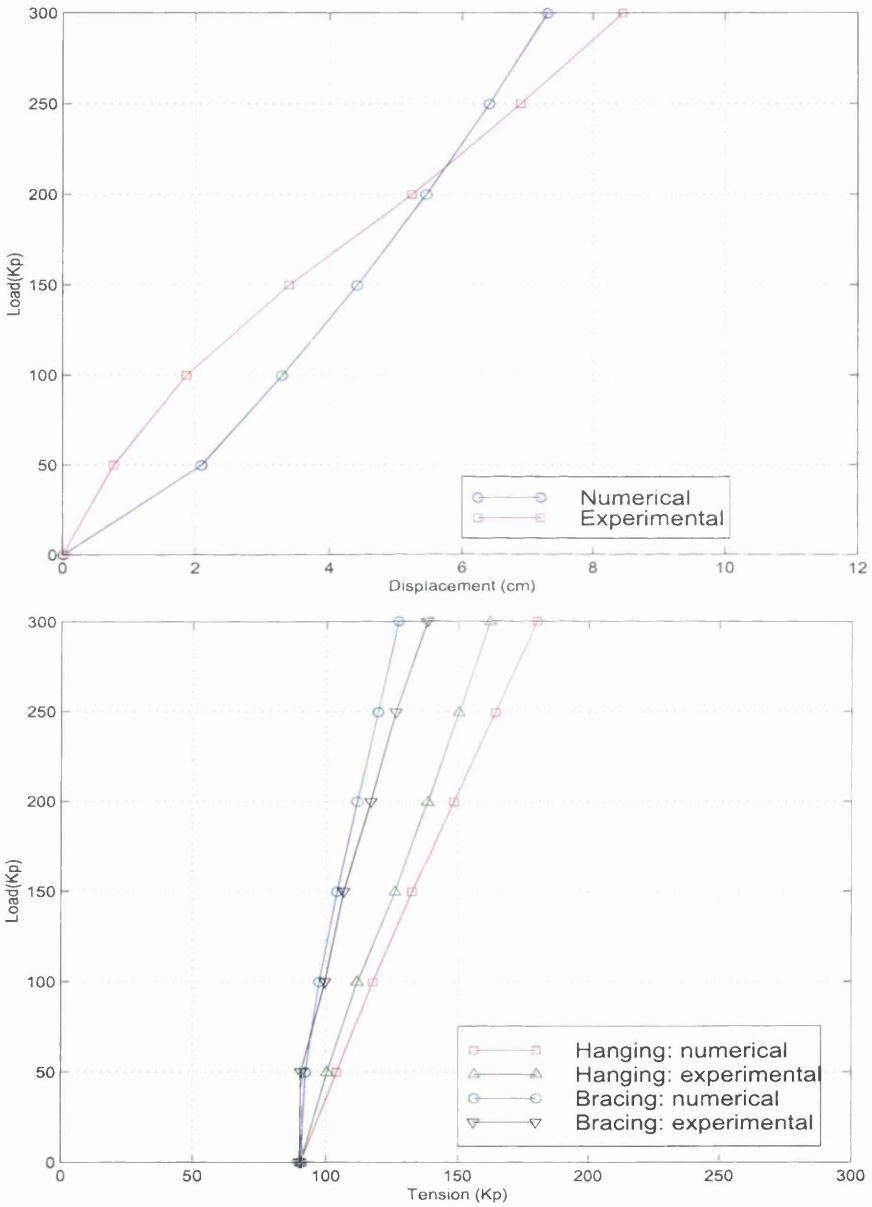

Figure 11.38: Numerical example 9: Displacement and stress vs loading.

Chapter 12

Structural applications

12.1 Introduction.

To reveal the capabilities and robustness of the procedure, this chapter presents two complete structures using the design computer program which incorporates the numerical techniques described in the previous chapters. Both structural models are comprised of fabric textile, reinforced cables and compressive members or rigid supports. Pseudo-static analysis will be run for snow and wind conditions according to Spanish standards NBE-AE88.

For the overall analysis, the process will be developed in three successive stages: form finding problem, prestressing loading application and in-service loading application. The numerical simulations were carried out by means of the Newton's method according to an incremental-iterative scheme.

12.2 Structure 1: E1.

The numerical example presented in what follows is a shade pavilion structure composed of a fabric textile. To provide a better performance of the overall structure, reinforcing cables have been added in the interior and in the perimeter of the membrane. The necessary anchorage has been achieved by means of pinned masts. Different perspectives of the structure are displayed in figure 12.1. As it can be observed from them, the membrane presents symmetry with respect to the OY axis, so hereafter half of the model is to be studied in detail provided that suitable boundary conditions are set up.

To define the initial equilibrium shape, the Force Density Method -see Linkwitz (1999)- was employed for the sake of its appealing simplicity to the detriment of other available techniques, namely, Dynamic Relaxation -see Brew and Brotton (1971)- or Updated Reference Strategy -see Bletzinger and Ramm (2001). For both internal and perimeter cables, the considered force density factor was ten times higher than the one for the interior domain. The kinematic boundary conditions for nodes along the membrane's perimeter are depicted in table 12.1. Figure 12.2 shows a plan view of the initial configuration, where the nodes' numbering of the selected Lagrangian mesh can be observed.

Node	x	y	z
1	5.0	0.0	10.0
98	6.0	-3.0	0.0
110	6.0	3.0	0.0
104	9.0	0.0	0.0
OY	0.0	-	-

Table 12.1: E1: Boundary conditions (m).

As a consequence of this shape finding analysis, it is feasible to come up with an initial equilibrium shape under a controllable prestress loading. This control is

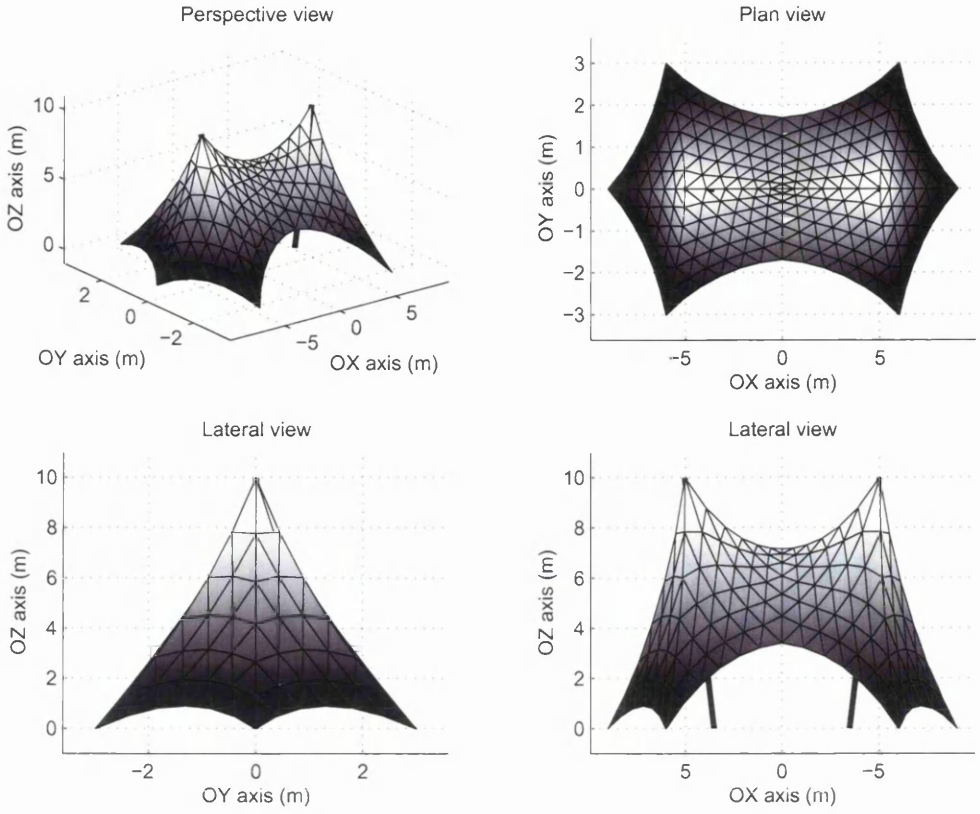

Figure 12.1: E1: initial configuration.

established in terms of the relative values for the force density coefficient among the different components of the membrane. Roughly speaking, the uniquely obtained equilibrium shape is not dependent on the absolute values of the prestress but on its relative ones, so this allows to reduce the former as much as desired. Figure 12.3 shows the isometric view of the structure, where cable and membrane elements can be easily distinguished.

12.2.1 Prestress loading

Once an initial referential shape has been set up, an adequate and realistic prestress can be applied to the membrane. First of all, masts are added to the structural model. This consideration permits tension membrane, reinforcing cables and masts behave in an interactive manner rather than analyzing the compressive members separated from the membrane-cable assemblage. This approach is strongly supported in Li and Siu-Lai (2004). Therefore, the masts will be designed leant with a horizontal projected length of 1.5 m along the OX axis, in such a way that the computationally modelled structure will have the appearance drawn in figure 12.4.

The reinforcing cables are adopted to have $EA = 1.2e4\ KN$, where E stands for the Young modulus and A symbolizes the cross sectional area. The mast pinned at their respective foundations are considered to have $EA = 2.0e5\ KN$. The fabric

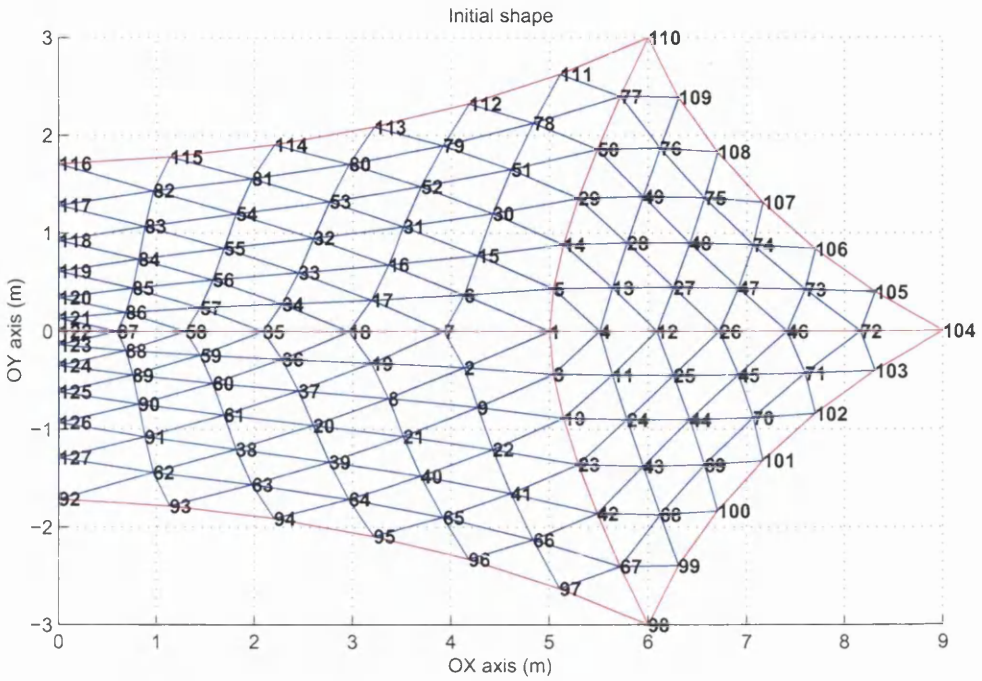

Figure 12.2: E1: initial configuration: plan view.

textile is assumed isotropic with $Et = 3.0e2\ \frac{KN}{m}$, where in this case t is for the membrane thickness. Therefore, the materials' mechanical properties end up completely defined.

The prestress process is carried out by means of an imposed displacement on nodes 110, 104 and 98, see figure 12.2, which are anchorage points for the interior reinforcing cables. As a results of this, the upper node 1, located at the top of the mast, see figure 12.2, is displaced outward and in so doing the overall membrane acquires the desired prestress effect. Table 12.2 summarizes the applied displacements u, v and w along the corresponding space directions OX, OY and OZ, respectively.

Node	u	v	w
98	1.0	-1.0	-1.0
110	1.0	1.0	-1.0
104	1.0	0.0	-1.0

Table 12.2: E1: Boundary conditions (cm).

12.2.2 In-service loading

Once the structure is completely prestressed and stabilized, different loads have been applied on it with the purpose of representing properly in-service conditions. Among the wide variety of possibilities, snow and wind loading have been adopted as the

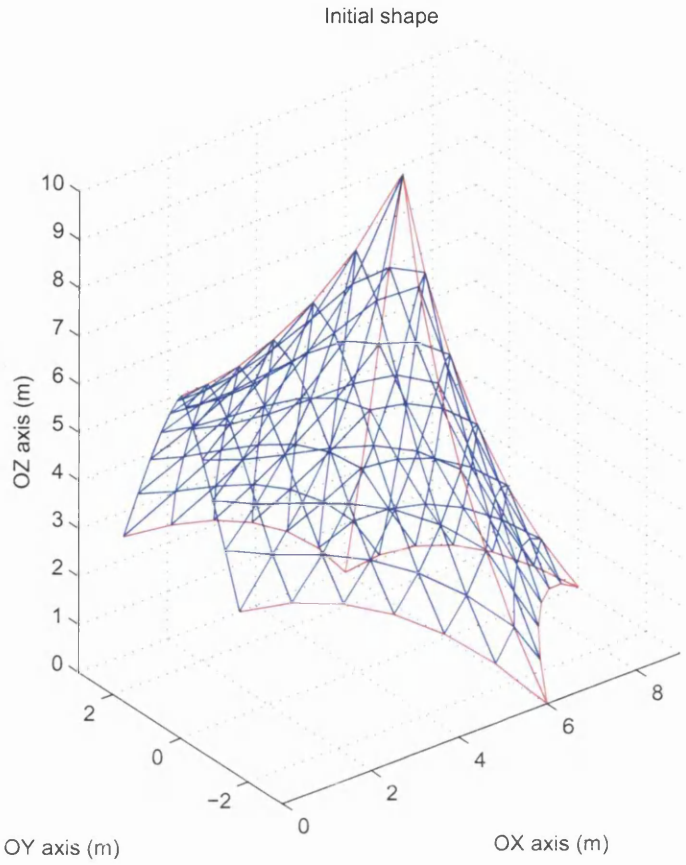

Figure 12.3: E1: initial configuration: isometric view.

most prominent ones. As a result of this, these two different cases will be studied in detail.

The snow load applied on the structural membrane will consist of 1.0 $\frac{KN}{m^2}$ distributed across a central region of the membrane which extends up to 6.0 m^2. This whole surface is accounted for according to its projection on a plan view according to standards.

For the wind load calculation, the Spanish wind loading standard NBE-AE88 will be used as a valid one. This standard establishes two possible limit hypotheses, namely, I and II, that require to be checked independently. The applied normal pressure which is considered to be undergone by any membrane's material point is the result of two factors. On the one hand, a dynamic pressure coefficient which accounts for the wind velocity as well as for the height of the considered location. On the other hand, a numerical factor whose magnitude is set up according to the angle between the wind direction and the spatial unit normal at the particular position of the membrane. Finally, pressure or suction is characterized according to the magnitude of the former angle.

Extreme conditions based upon a wind up to 125 $\frac{Km}{h}$ are considered. The wind direction is set up along the OY axis, where the largest exposure surface can be

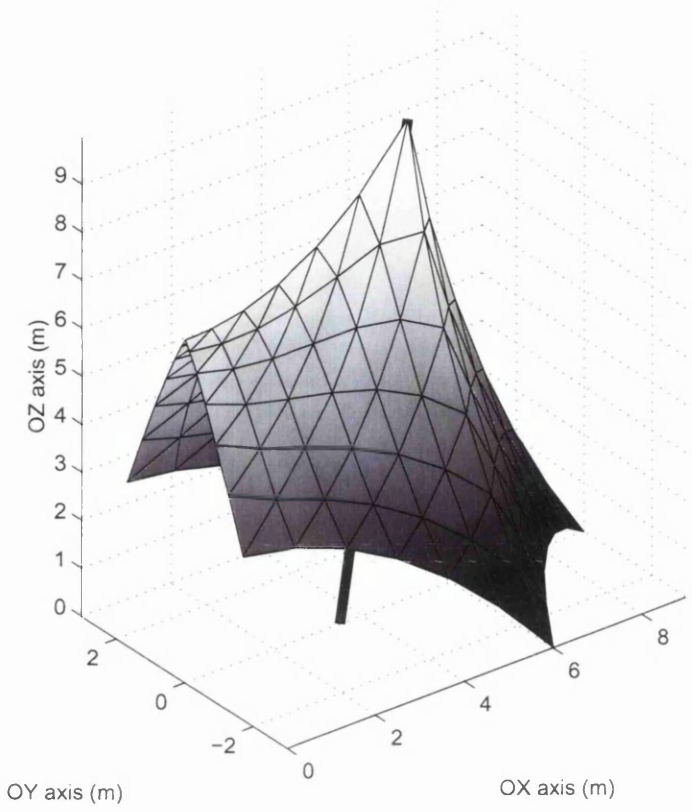

Figure 12.4: E1: initial configuration.

quantified, which results in the most critical situation. Figures 12.5 to 12.10 show the displacements contour diagrams for the different loading conditions. Figure 12.11 shows a comparison of the displaced shape for two different loading conditions. Interesting conclusions can be addressed at this point.

The interior and perimeter cables act as stabilizing members for the overall performance of the membrane and, in so doing, they reduce notably the displacements as a result of the different applied loads. As it can be observed, high values for the displacements are obtained as a consequence of the wind load application, specially along the wind direction. These results highlight the importance of a complete fluid-structure analysis with the objective of accounting for accurately the interaction between them. From the strain point of view, it is important to emphasize that a maximum value less than $9.0e-3$ was attained in the case of snow load whilst a figure around $3.0e-2$ was achieved for the wind case. This fact fulfills the moderate strain requirement for the justifiable application of the Saint Venant-Kirchhoff hyperelastic model.

Analogously, figures 12.12 and 12.15 displays the contour diagrams for the principal Cauchy stresses σ_I and σ_{II}. It transpires that at the prestressing stage, the whole membrane is under pure tension, given the second principal Cauchy stress σ_{II} always presents positive values. At the same time, it is remarkable to point out that

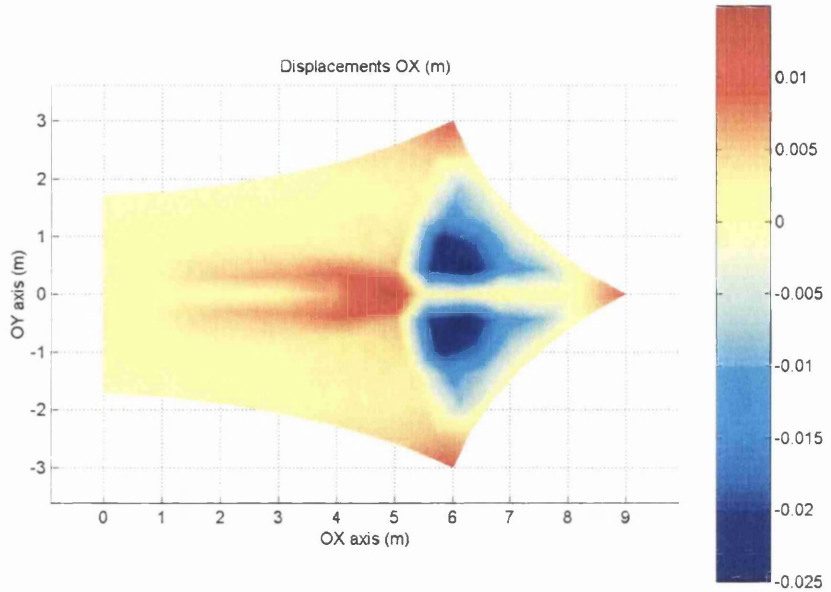

(a)

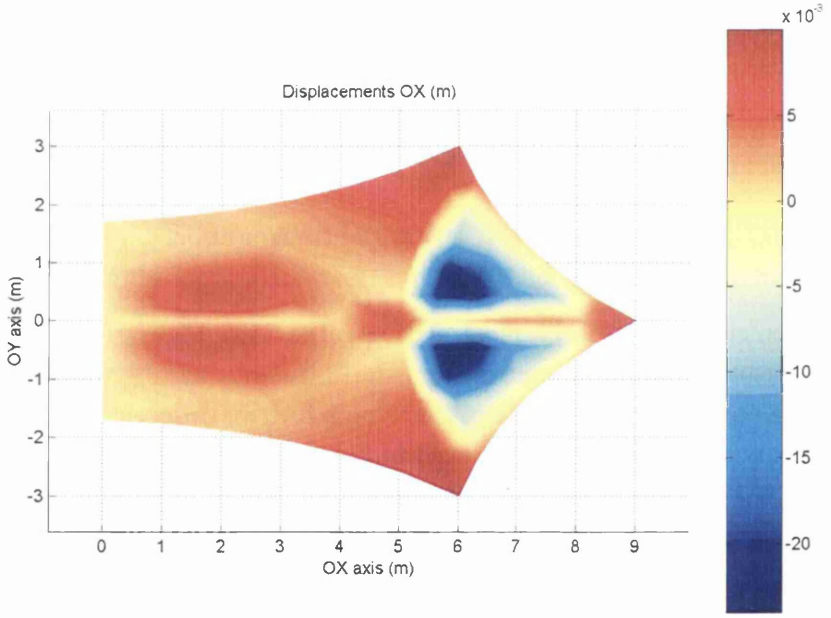

(b)

Figure 12.5: E1: OX displacements. (a) Prestress load. (b) Snow load.

the maximum stress values are attained across the central region of the membrane. This fact is due to the prestressed effect imposed along the longitudinal interior cable which is suitably conveyed to the fabric.

Moreover, the images reflect clearly the importance of including a wrinkling algorithm to account appropriately for localized buckling regions. In all of in-service situations, a wide zone of the membrane is affected by this phenomenon, so an adequate treatment should be used to deal with it. Furthermore, the maximum accom-

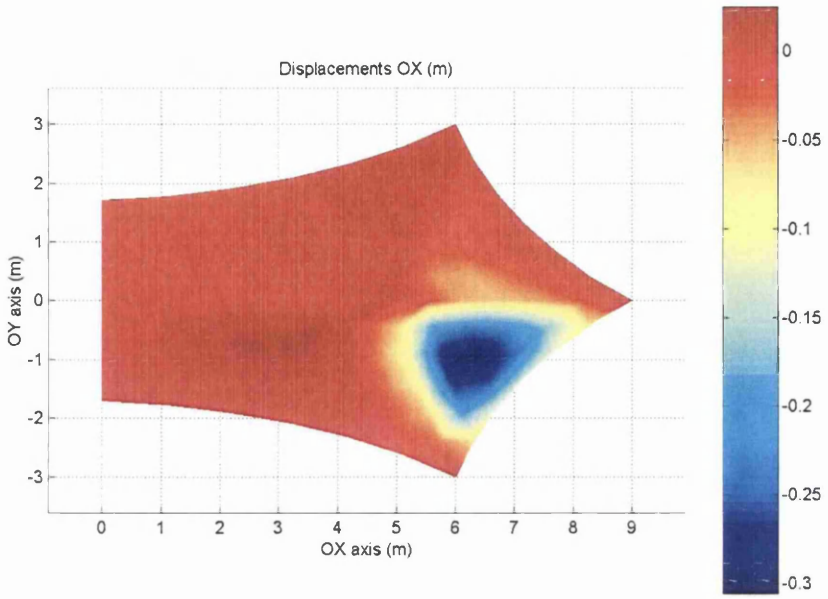

(a)

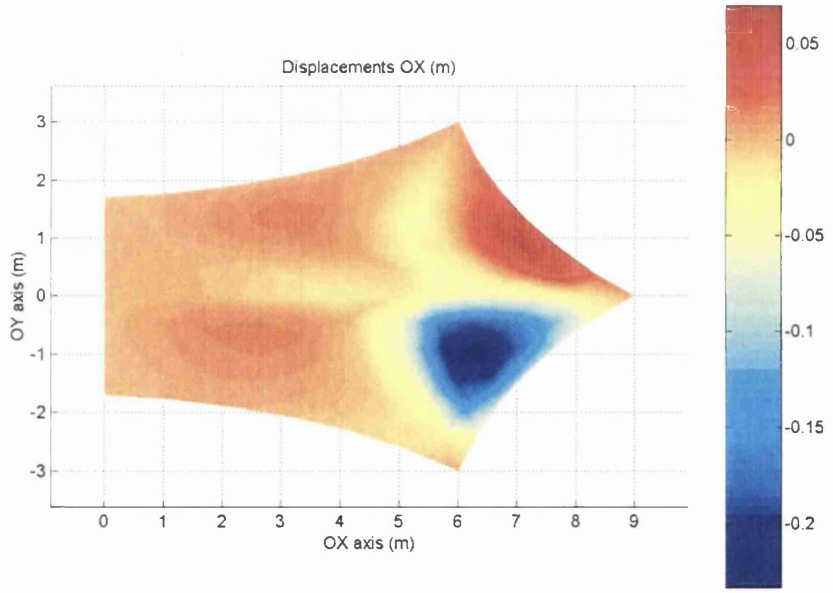

(b)

Figure 12.6: E1: OX displacements. (a) Wind load, hyp. I. (b) Wind load, hyp. II.

plished stress will supply useful information about possible required reinforcement and prevent unexpected tearing of the fabric. Results agreed to what it could be expected in advance.

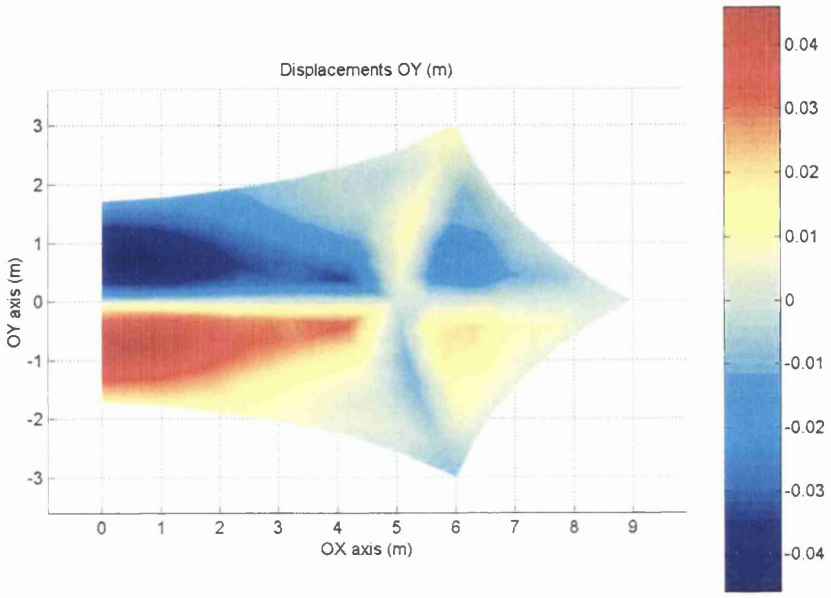

(a)

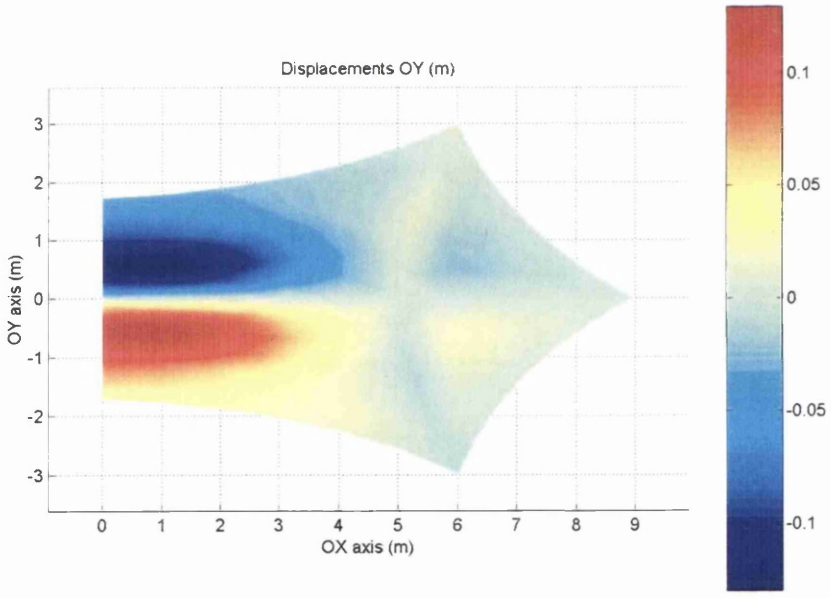

(b)

Figure 12.7: E1: OY displacements. (a) Prestress load. (b) Snow load.

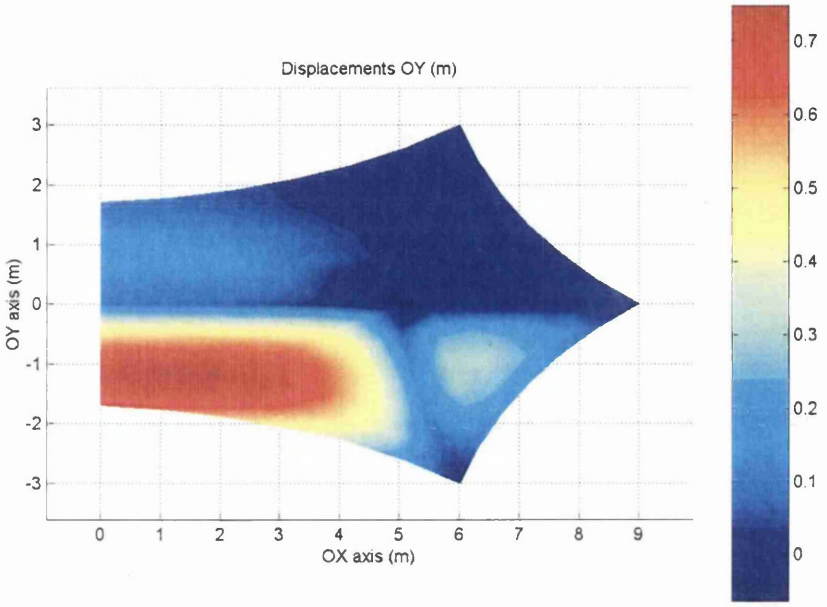

(a)

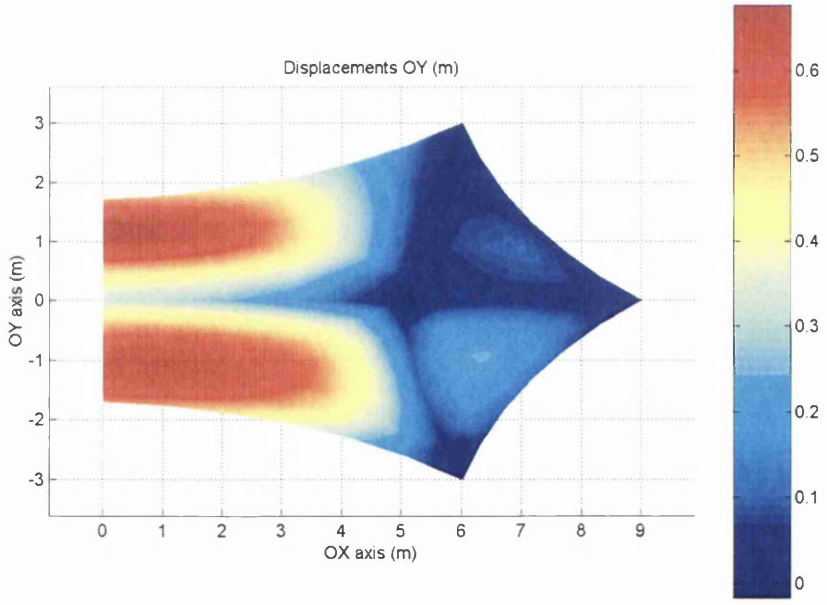

(b)

Figure 12.8: E1: OY displacements. (a) Wind load, hyp. I. (b) Wind load, hyp. II.

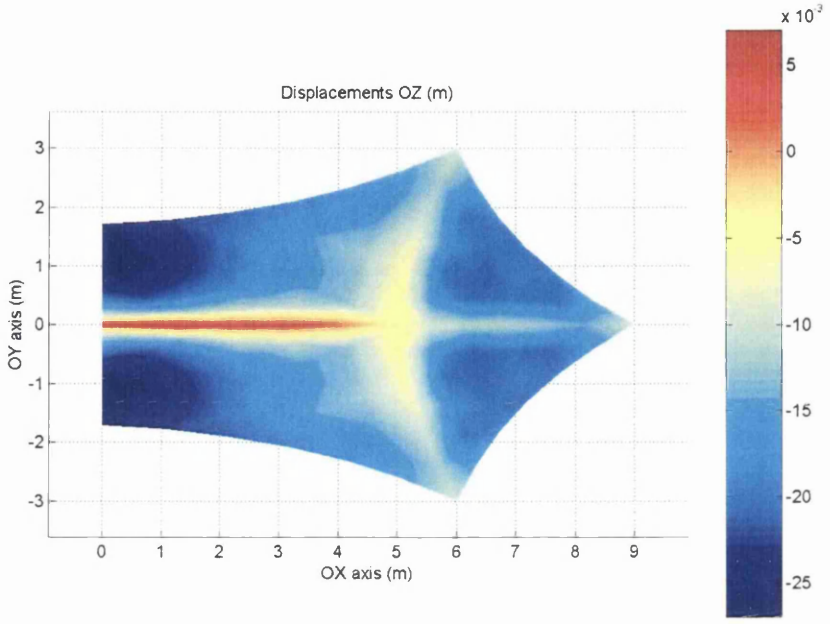

(a)

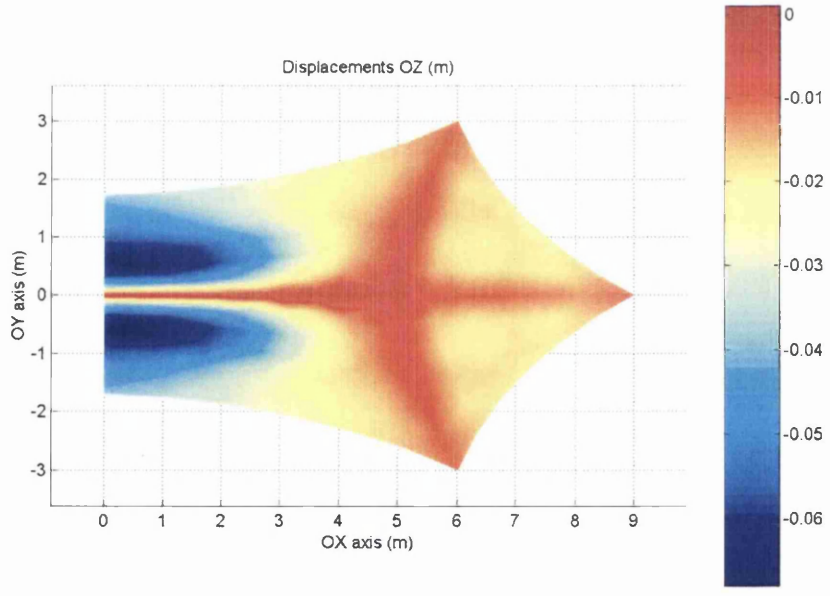

(b)

Figure 12.9: E1: OZ displacements. (a) Prestress load. (b) Snow load.

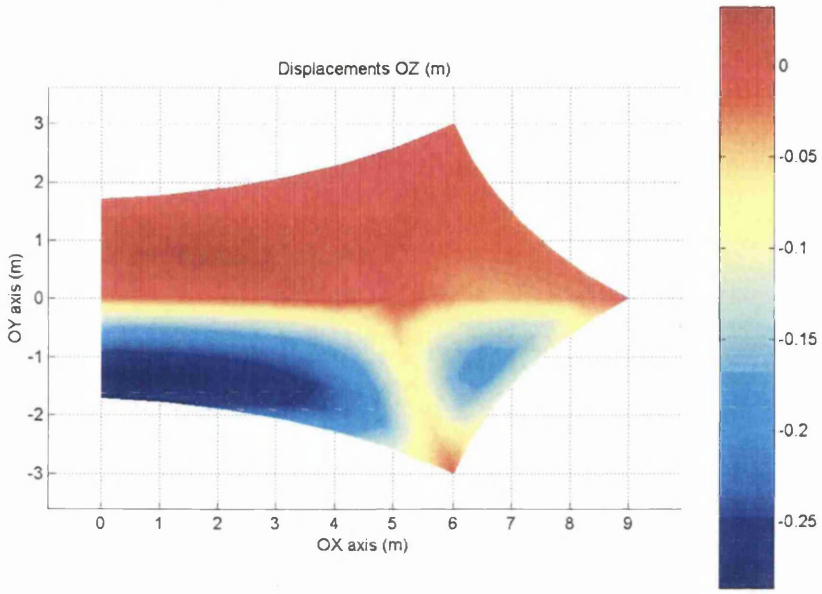

(a)

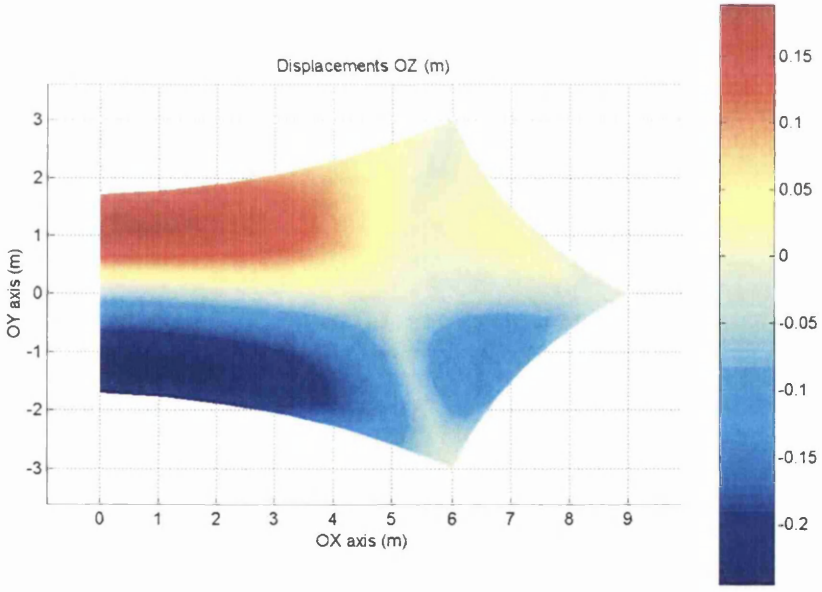

(b)

Figure 12.10: E1: OZ displacements. (a) Wind load, hyp. I. (b) Wind load, hyp. II.

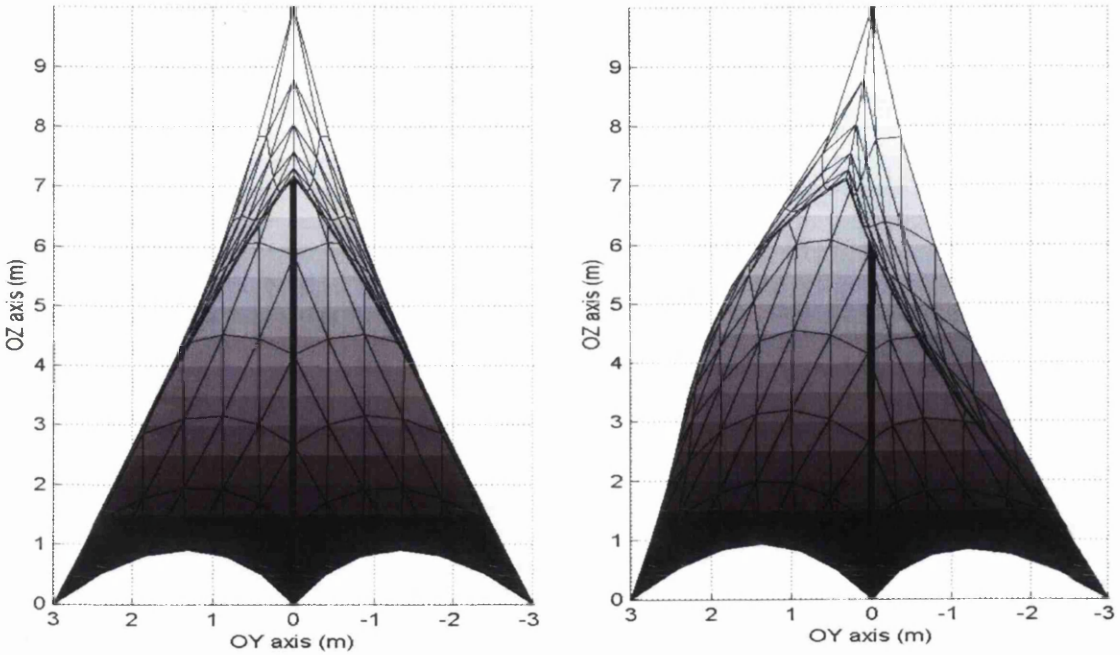

(a) (b)

Figure 12.11: E1: Shape. (a) Prestressed load. (b) Wind load, hyp II.

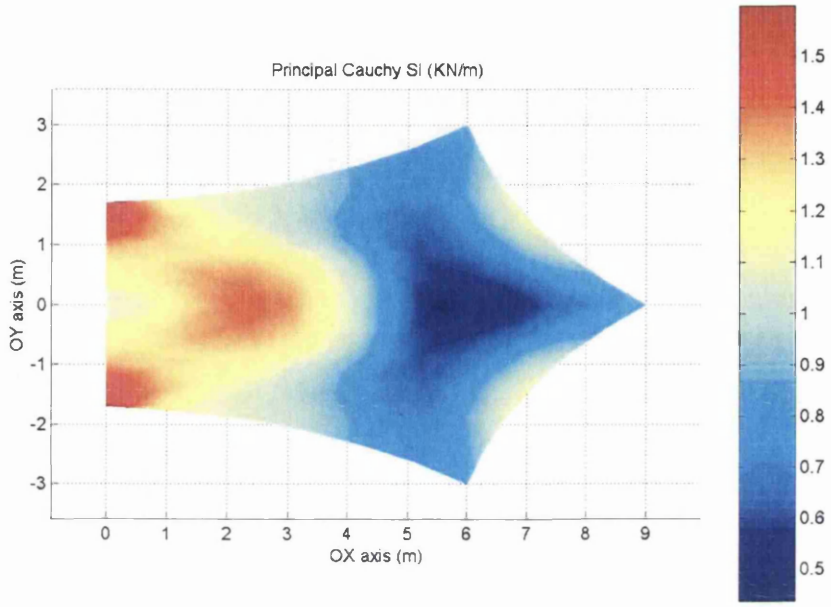

(a)

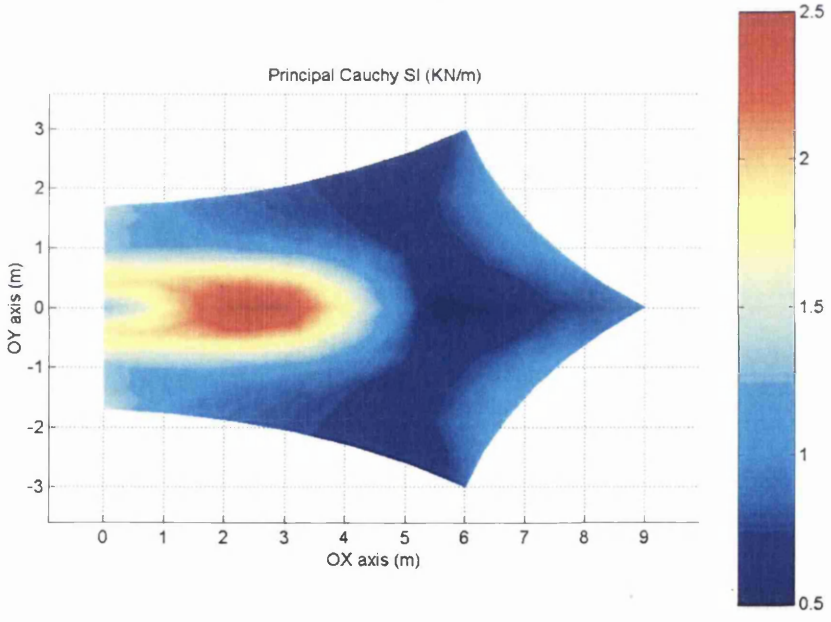

(b)

Figure 12.12: E1: Cauchy stress σ_I. (a) Prestress load. (b) Snow load.

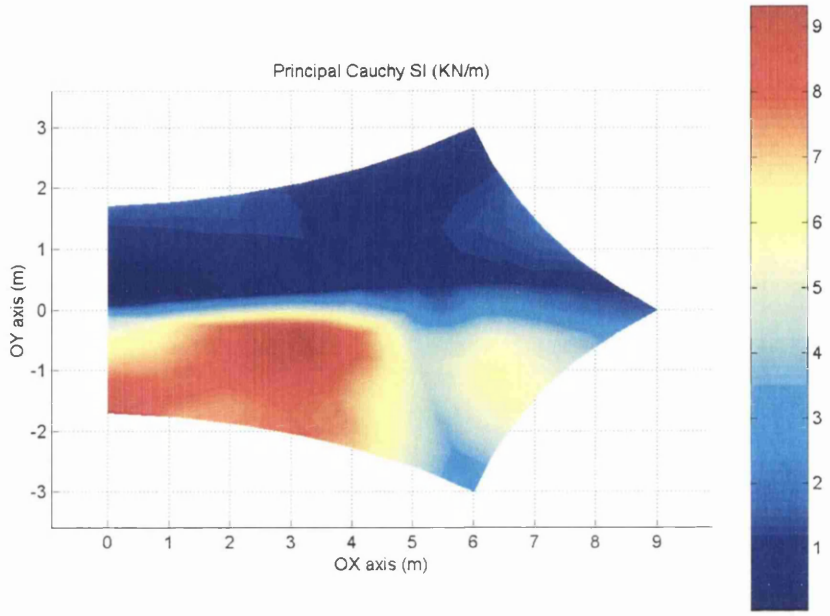

(a)

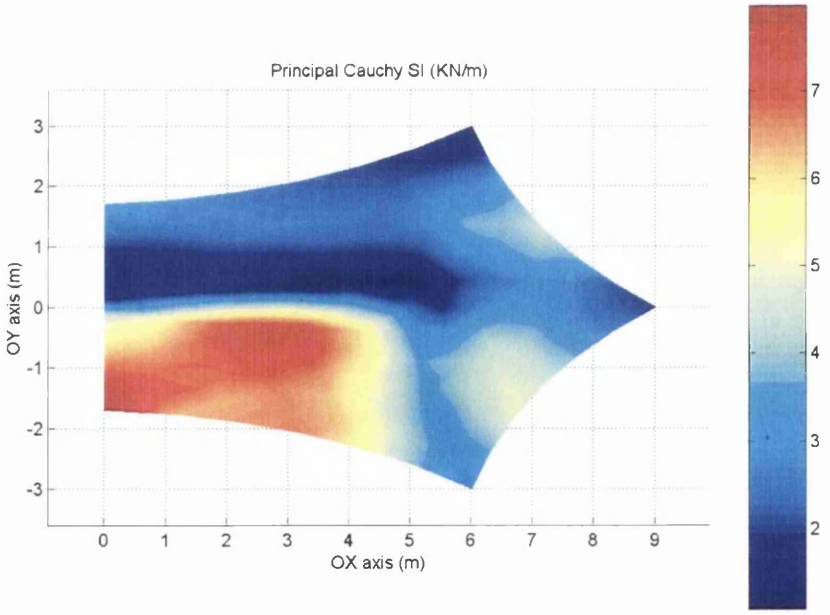

(b)

Figure 12.13: E1: Cauchy stress σ_I. (a) Wind load, hyp. I. (b) Wind load, hyp. II.

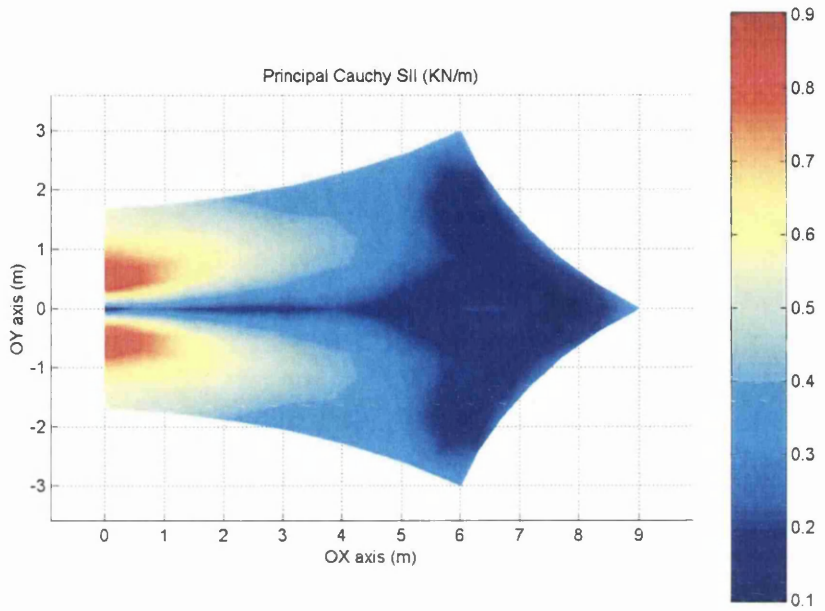

(a)

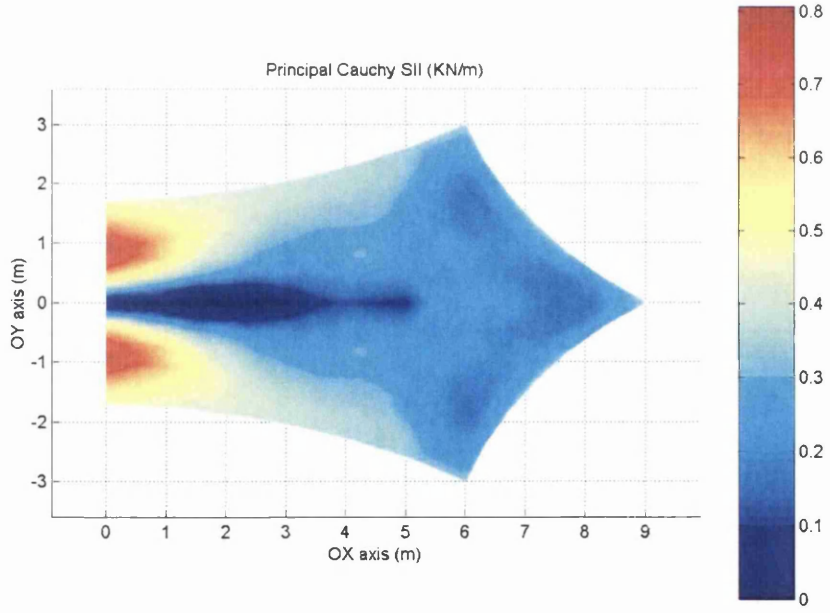

(b)

Figure 12.14: E1: Cauchy stress σ_{II}. (a) Prestress load. (b) Snow load.

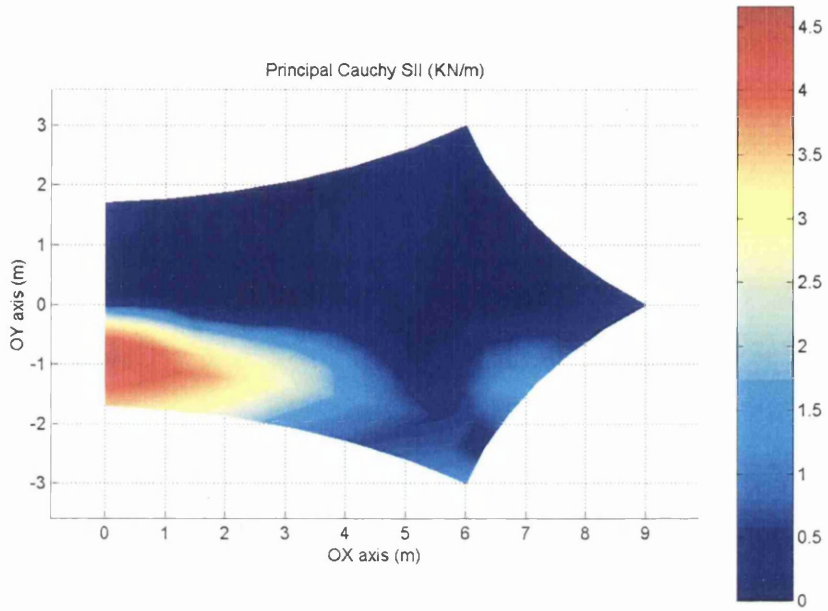

(a)

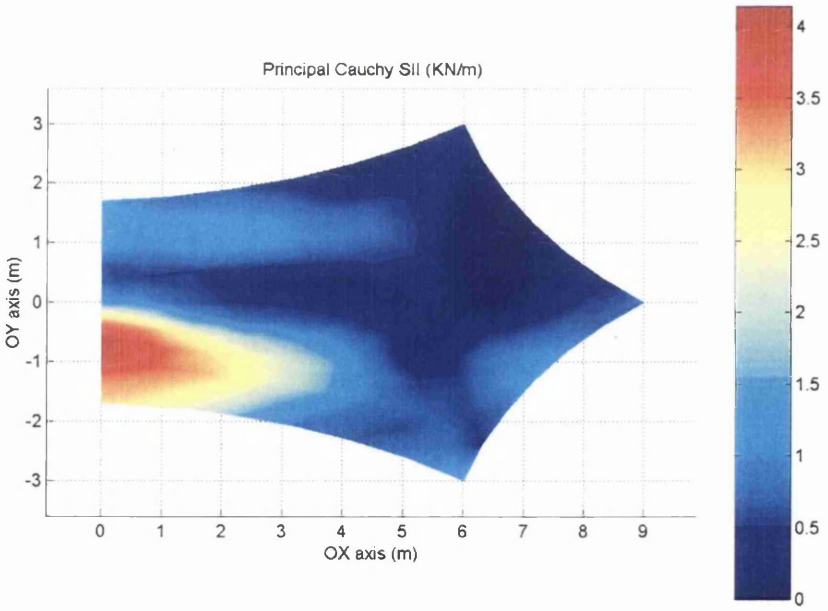

(b)

Figure 12.15: E1: Cauchy stress σ_{II}. (a) Wind load, hyp. I. (b) Wind load, hyp. II.

12.3 Structure 2: E2.

This example relates to another shade pavilion composed of a fabric textile reinforced by means of cables in the interior and in the perimeter of the prestressed membrane. The necessary anchorage has been achieved by means of pinned masts. Isometric perspective of the structure is displayed in figure 12.16 and a plan view is shown in figure 12.17. As it can be observed, the membrane as a whole presents symmetry with respect to the OY axis, so hereafter only half of the model is to be studied with suitable boundary conditions.

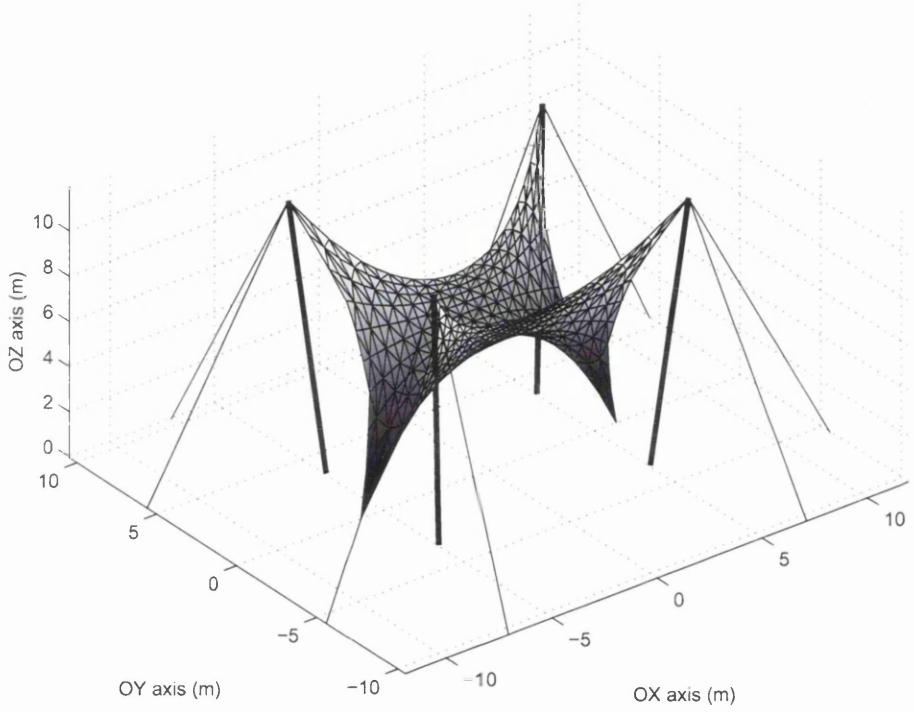

Figure 12.16: E2: initial configuration, isometric view.

To define the initial equilibrium shape, once again the force density method was used. For both internal and perimeter cables, the considered force density factor was ten times higher than the one for the interior domain. The kinematic boundary conditions for nodes along the membrane's perimeter are displayed in table 12.3. Figure 12.2 shows a plan view of the initial configuration, where the nodes' numbering of the selected Lagrangian mesh can be observed.

Figure 12.19 shows the isometric view of the structure after form finding analysis has taken place, where cable and membrane elements can be easily distinguished.

12.3.1 Prestressing loading.

Once the initial equilibrium shape is obtained, the prestressing loading is applied on the structure. Firstly, and as it was dome in the previous example as well, masts are

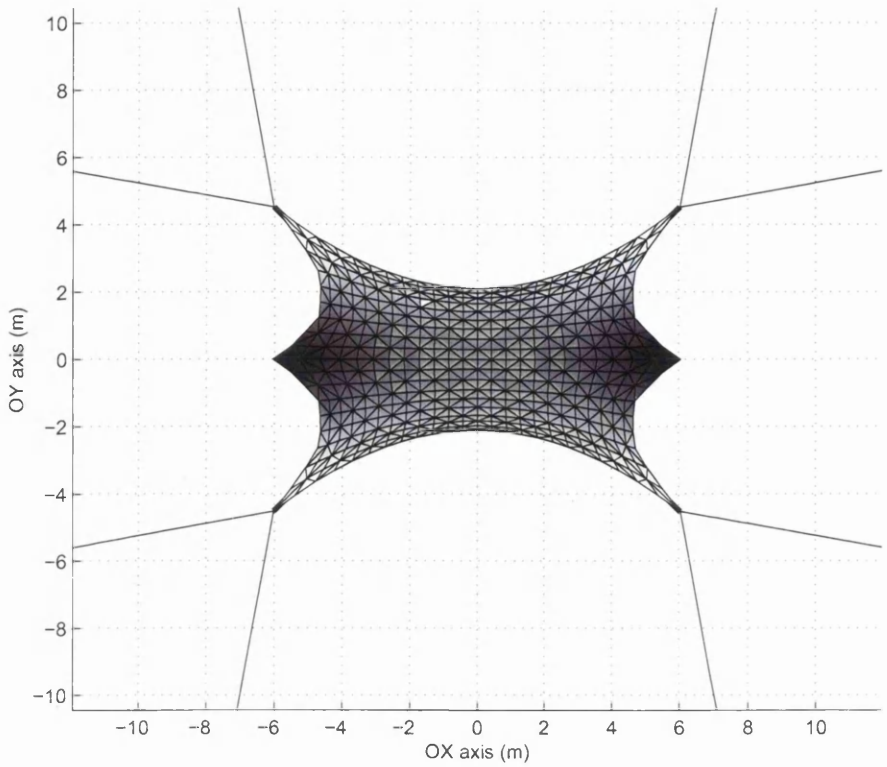

Figure 12.17: E2: initial configuration, plan view.

Node	x	y	z
13	6.0	-4.5	12.0
130	6.0	0.0	0.0
247	6.0	4.5	12.0
OY axis	0.0	-	-

Table 12.3: E2: Boundary conditions (m).

added to the structural model. This allows the tensioned membrane, the reinforcing cables and the masts to behave in an interactive manner rather than analyzing the compressive members separate from the membrane-cable assemblage.

Figure 12.20 represents all the masts and reinforced cables added up to the analysis. Spatial coordinates for the masts' extreme nodes are displayed in table 12.4, see also figure 12.20.

The reinforcing cables are taken with $EA = 1.2e4KN$, where E stands for the Young modulus and A symbolizes the cross sectional area. The masts pinned at their respective foundations are considered to have $EA = 2.0e5KN$. The textile fabric is assumed to behave isotropically with $Et = 5.0e2\frac{KN}{m}$ and $\nu = 0.3.$, where in this case t denotes the membrane thickness.

The prestress process is carried out by means of an imposed displacement on nodes plotted in figure 12.20. Table 12.5 summarizes the applied displacements u,

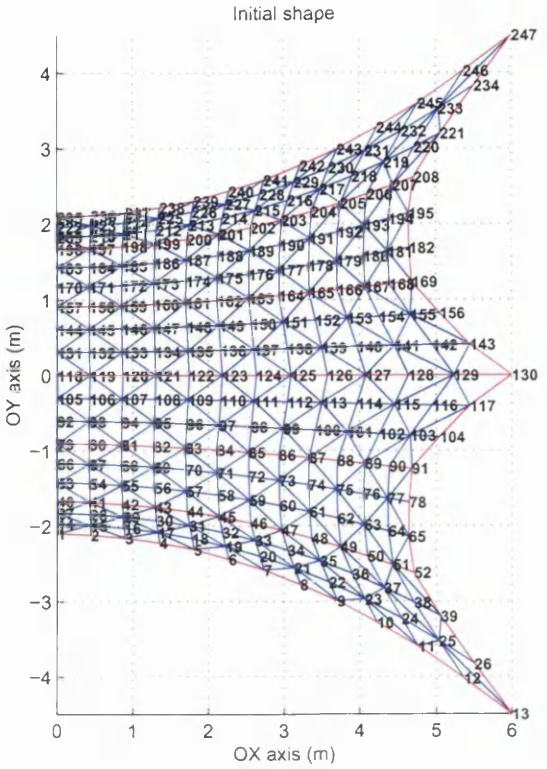

Figure 12.18: E2: initial configuration, plan view.

Node	x	y	z
248	5.000	3.500	.0000
249	5.000	-3.500	.0000
250	7.042	10.41	.0000
251	11.91	5.542	.0000
252	11.91	-5.542	.0000
253	7.042	-10.41	.0000
130	5.0	0.0	-5.0

Table 12.4: E2: Spatial coordinates (m).

v and w along the corresponding space directions OX, OY and OZ, respectively.

12.3.2 In-service loading.

Once the structure is prestressed and stabilized, different loads were considered, namely, snow and wind loading. The snow load applied on the structural membrane will consist of 1.0 $\frac{KN}{m^2}$ distributed across a central region of the membrane which extends up to 6.0 m^2. This whole surface is accounted for according to its projection on a plan view. For the wind load calculation, the Spanish wind loading standard NBE-AE88 will be used. Again, two possible limit hypotheses, namely, I and II, required to be checked independently.

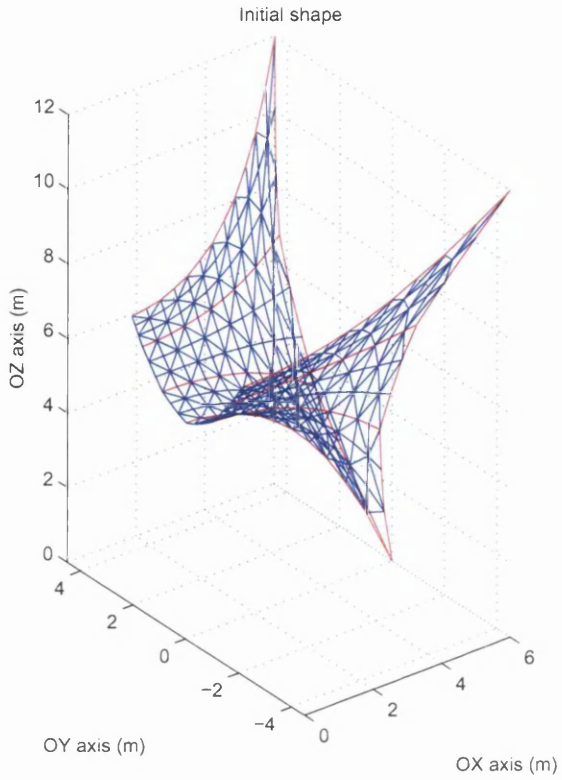

Figure 12.19: E2: initial configuration, isometric view.

Node	u	v	w
250	5.0	5.0	-5.0
251	5.0	5.0	-5.0
252	5.0	-5.0	-5.0
253	5.0	-5.0	-5.0
130	5.0	0.0	-5.0
248	0.0	0.0	0.0
249	0.0	0.0	0.0
OY axis	0.0	-	-

Table 12.5: E2: Boundary conditions (cm).

Extreme conditions based upon a wind up to 102 $\frac{Km}{h}$ are considered. The wind direction is established along the OY axis, where the largest exposure surface can be quantified, which ends up in the most critical situation. Figures 12.21 to 12.26 show the displacements contour diagrams for the different loading conditions. Figure 12.27 shows a comparison of the displaced shape for two different loading conditions.

Again, the interior and perimeter cables act as stabilizing members for the overall performance of the membrane and therefore, they reduce the displacements that result from the different applied loads. As it can be observed, high values for the displacements are obtained as a consequence of the wind load application, specially

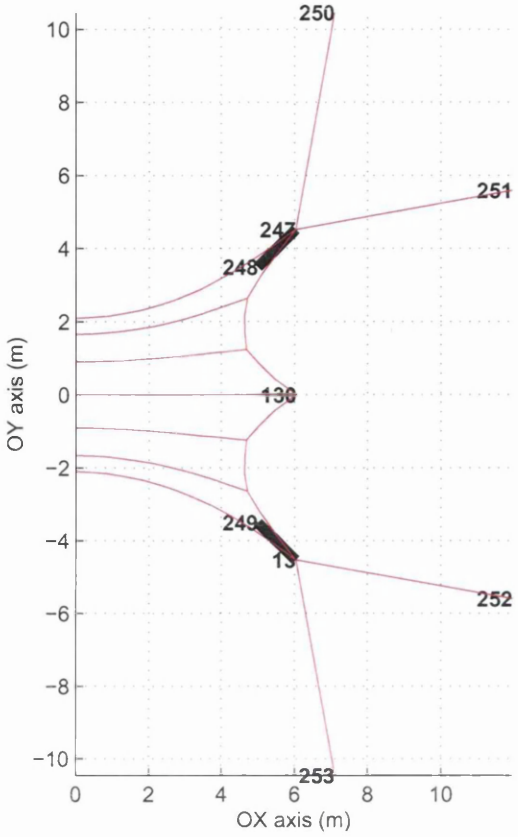

Figure 12.20: E1: Reinforced cables and masts configuration.

along the wind direction. From the strain point of view, a maximum value less than $1.0e-2$ was achieved. This fact agrees with the moderate strain requirement to justify the application of the Saint Venant-Kirchhoff hyperelastic model.

Figures 12.28 and 12.31 display the contour diagrams for the principal Cauchy stresses σ_I and σ_{II}, respectively. As it can be noticed, at the prestress stage the whole membrane is under pure tension. Again, images reflect neatly the importance of including a wrinkling algorithm to account appropriately for localized buckling regions.

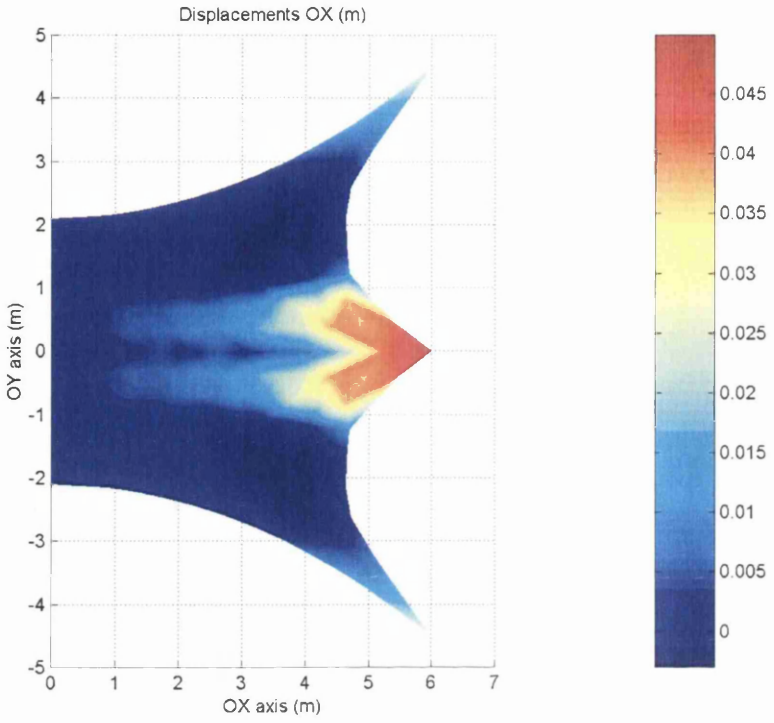

(a)

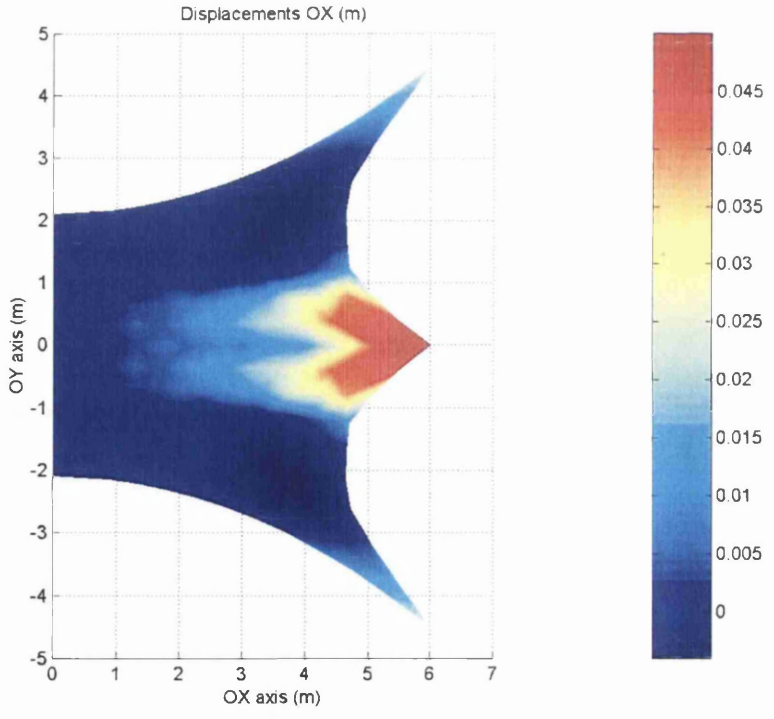

(b)

Figure 12.21: E2: OX displacements. (a) Prestress load. (b) Snow load.

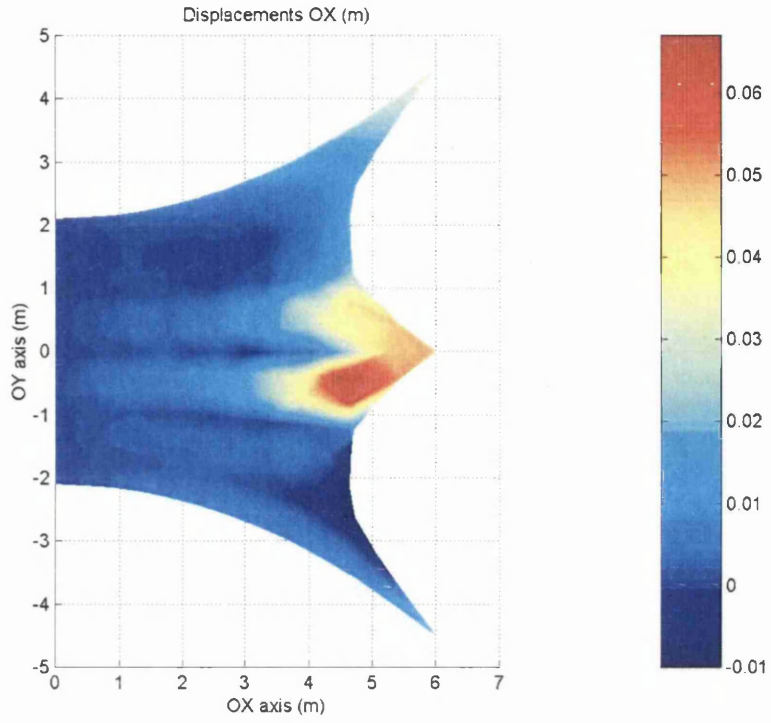

(a)

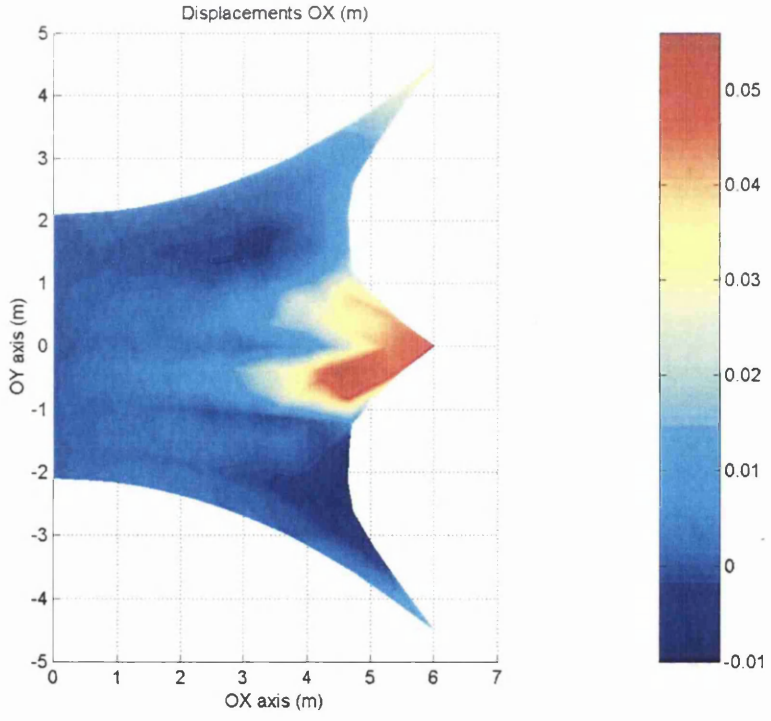

(b)

Figure 12.22: E2: OX displacements. (a) Wind load, hyp. I. (b) Wind load, hyp. II.

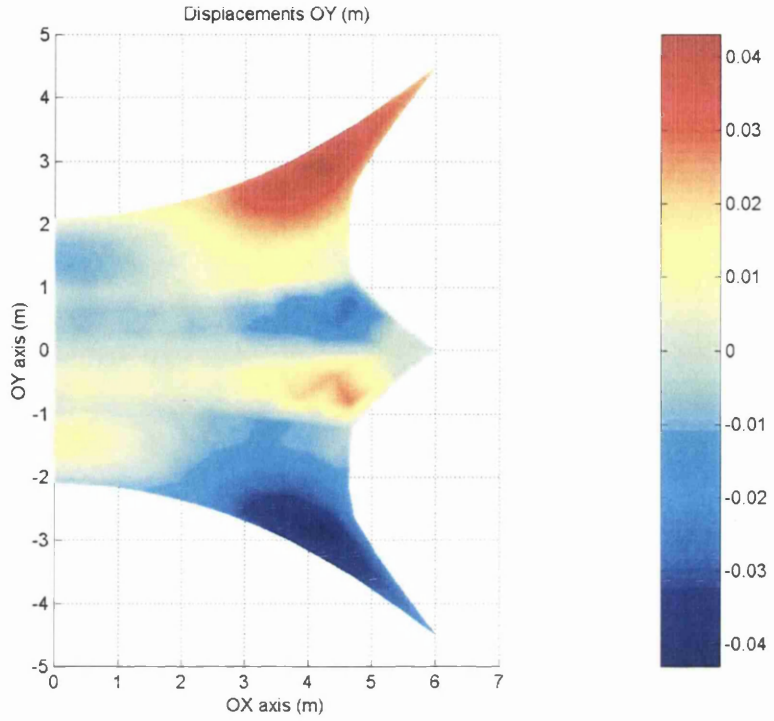

(a)

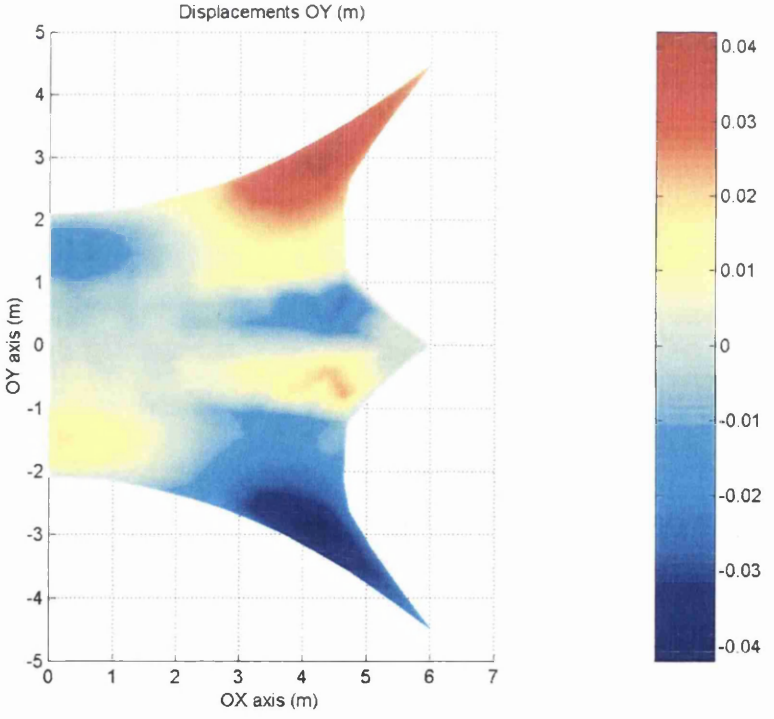

(b)

Figure 12.23: E2: OY displacements. (a) Prestress load. (b) Snow load.

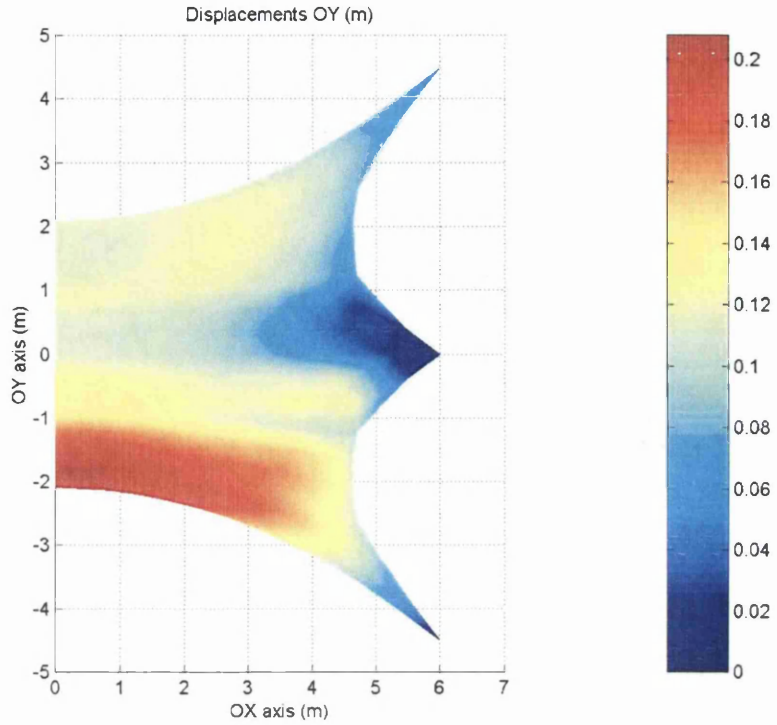

(a)

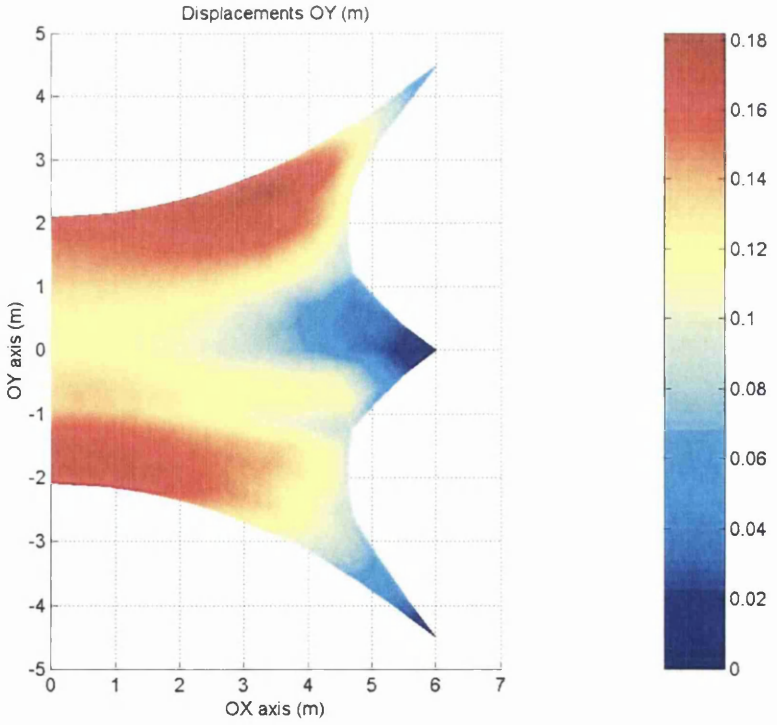

(b)

Figure 12.24: E2: OY displacements. (a) Wind load, hyp. I. (b) Wind load, hyp. II.

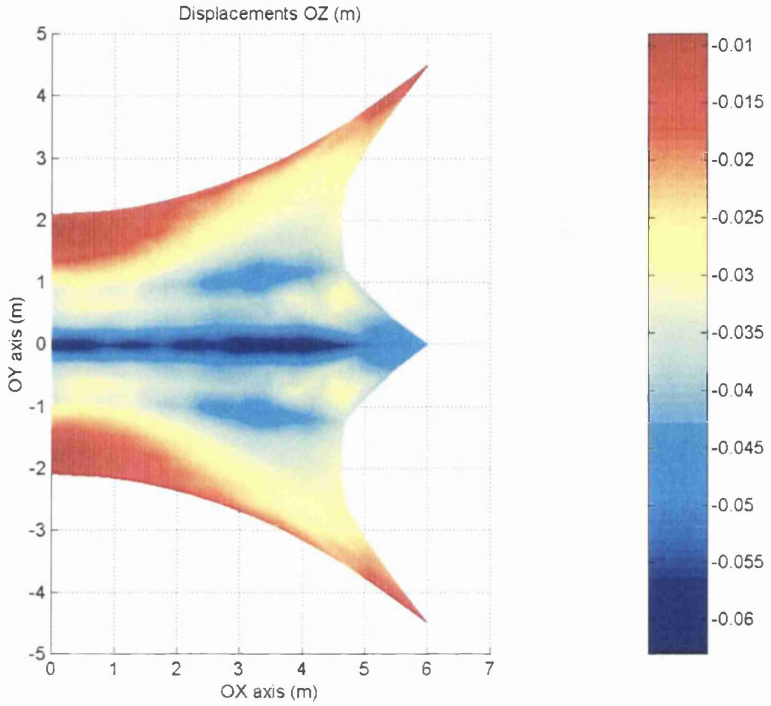

(a)

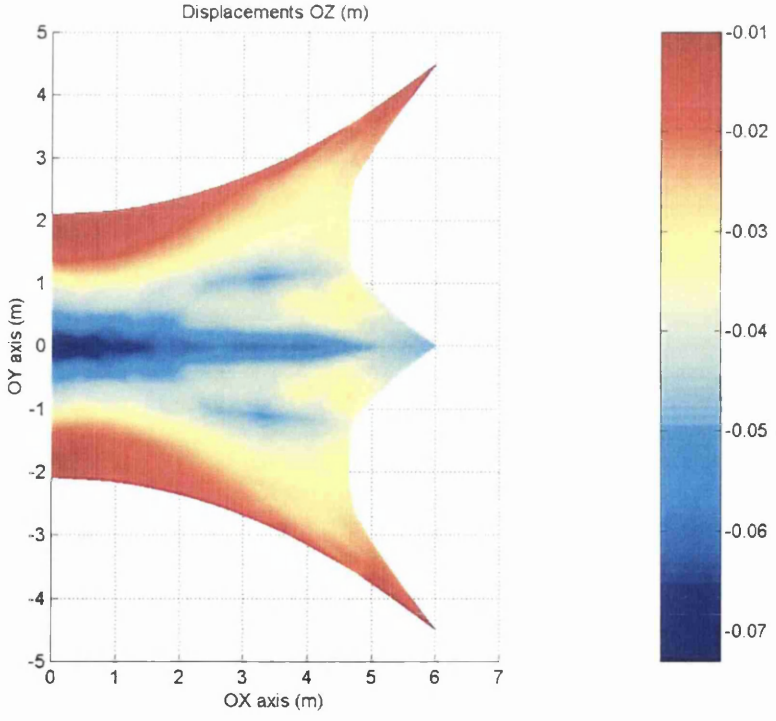

(b)

Figure 12.25: E2: OZ displacements. (a) Prestress load. (b) Snow load.

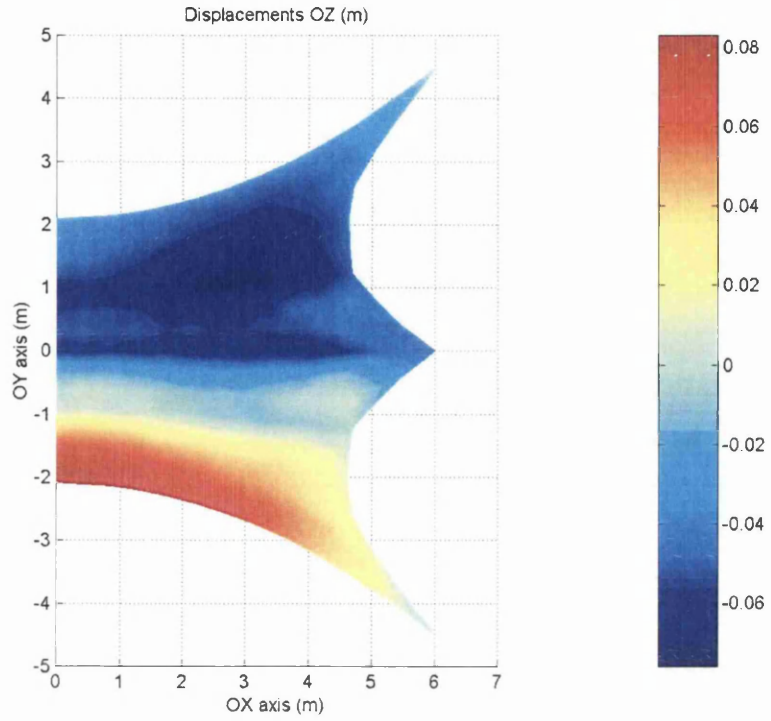

(a)

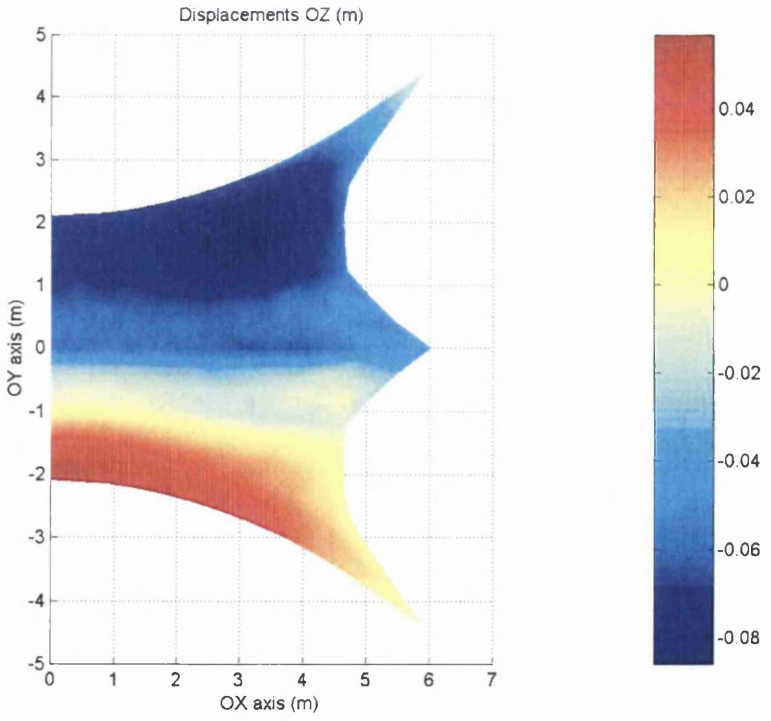

(b)

Figure 12.26: E2: OZ displacements. (a) Wind load, hyp. I. (b) Wind load, hyp. II.

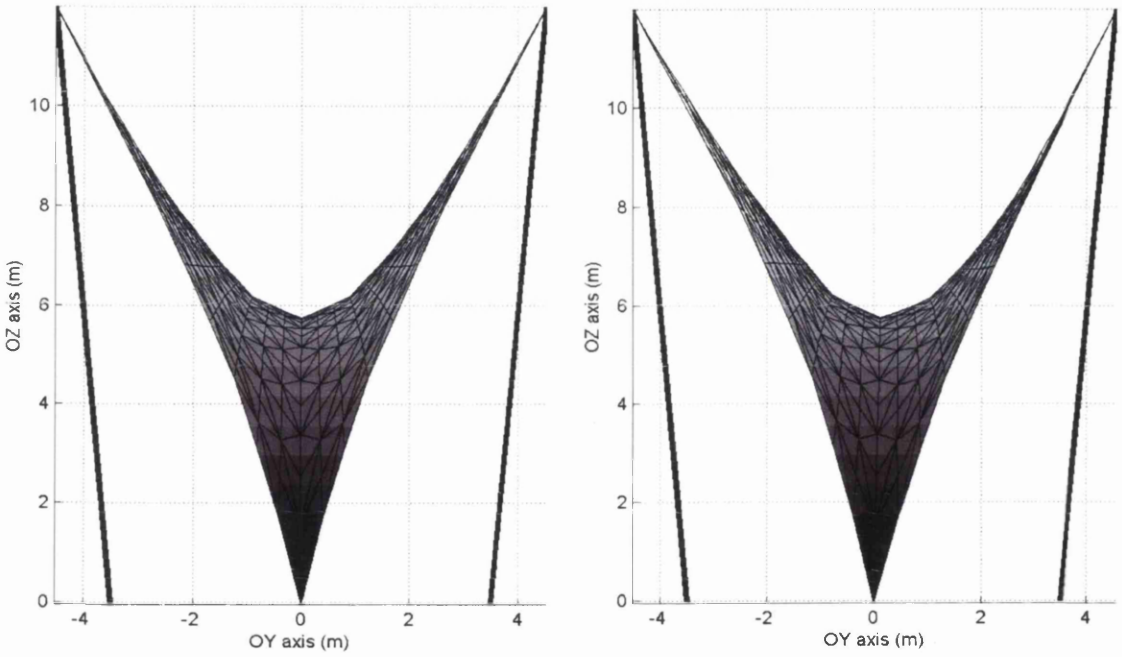

(a) (b)

Figure 12.27: E2: Shape. (a) Prestressed load. (b) Wind load, hyp II.

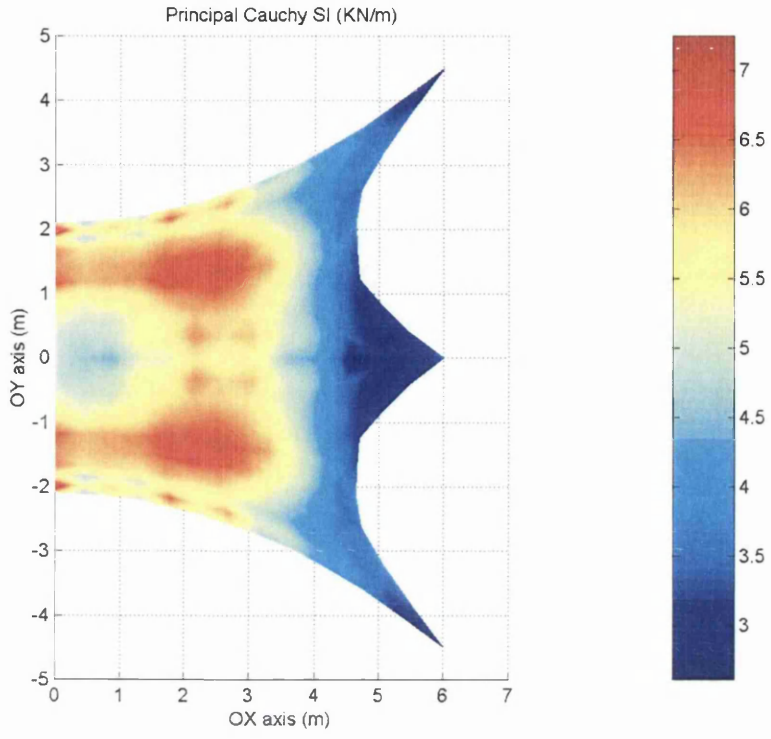

(a)

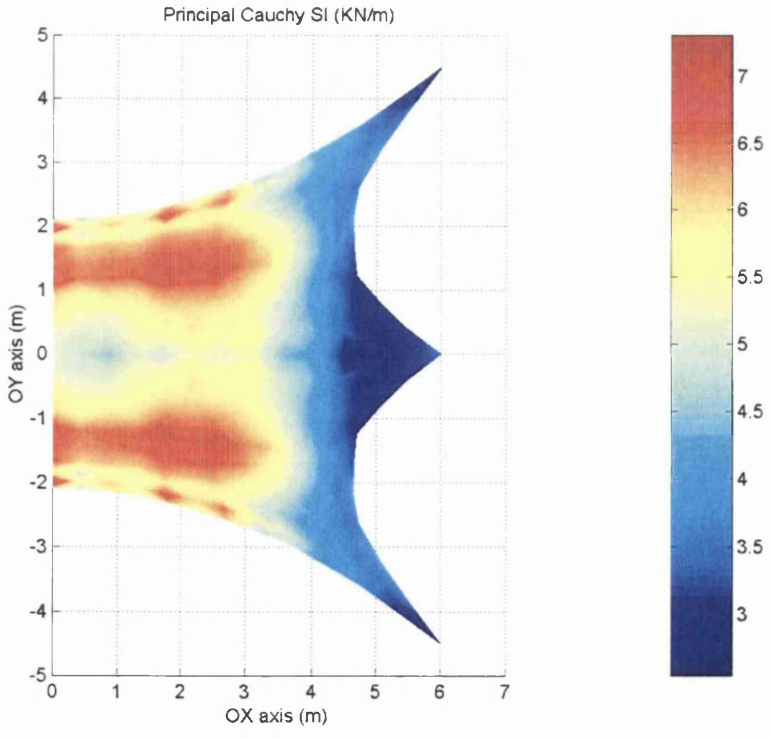

(b)

Figure 12.28: E2: Cauchy stress σ_I. (a) Prestress load. (b) Snow load.

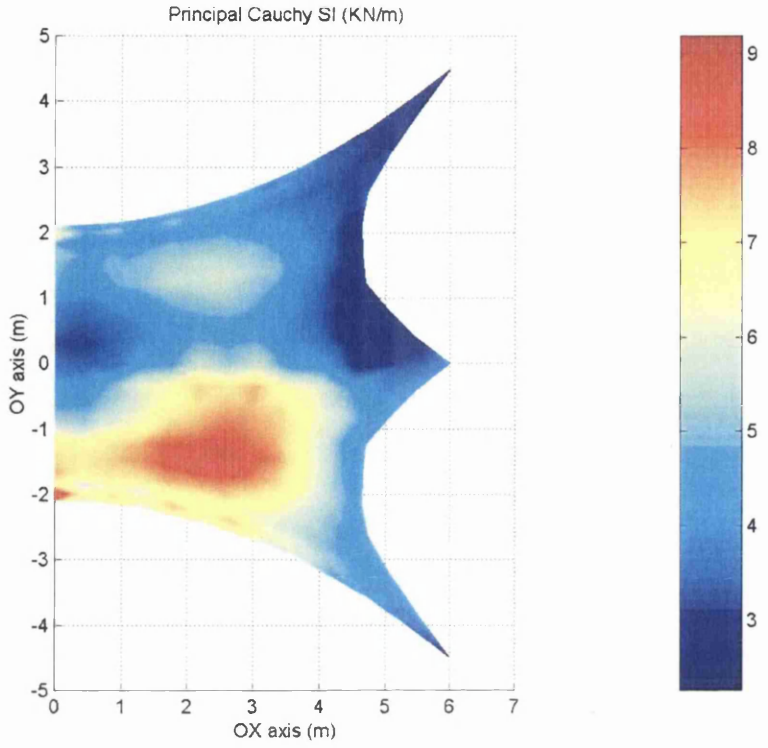

(a)

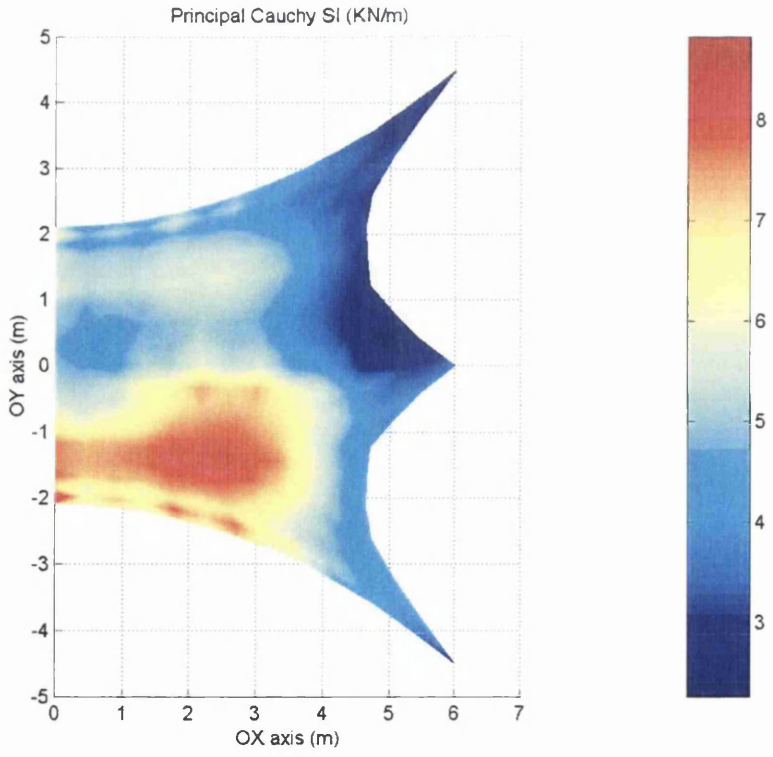

(b)

Figure 12.29: E2: Cauchy stress σ_I. (a) Wind load, hyp. I. (b) Wind load, hyp. II.

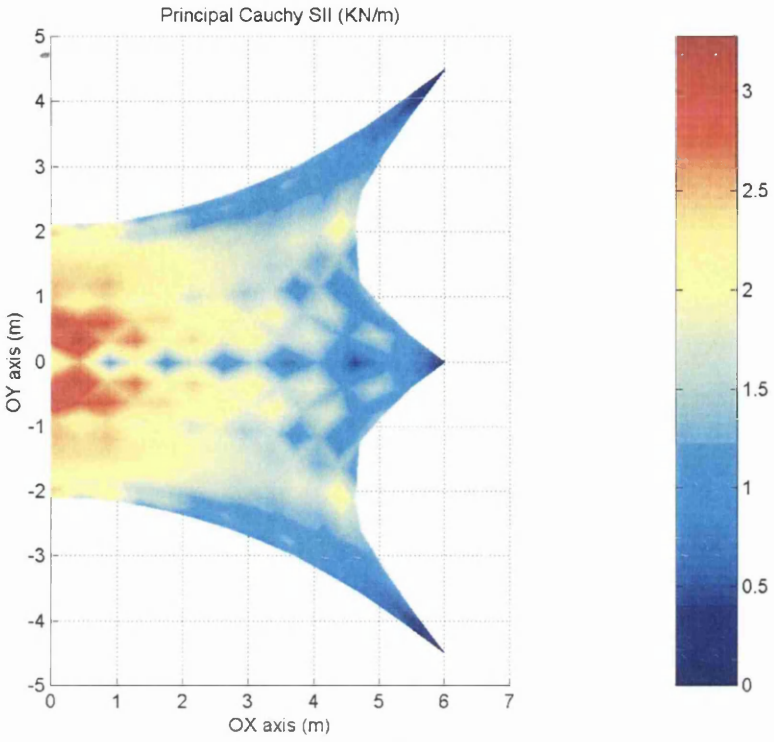

(a)

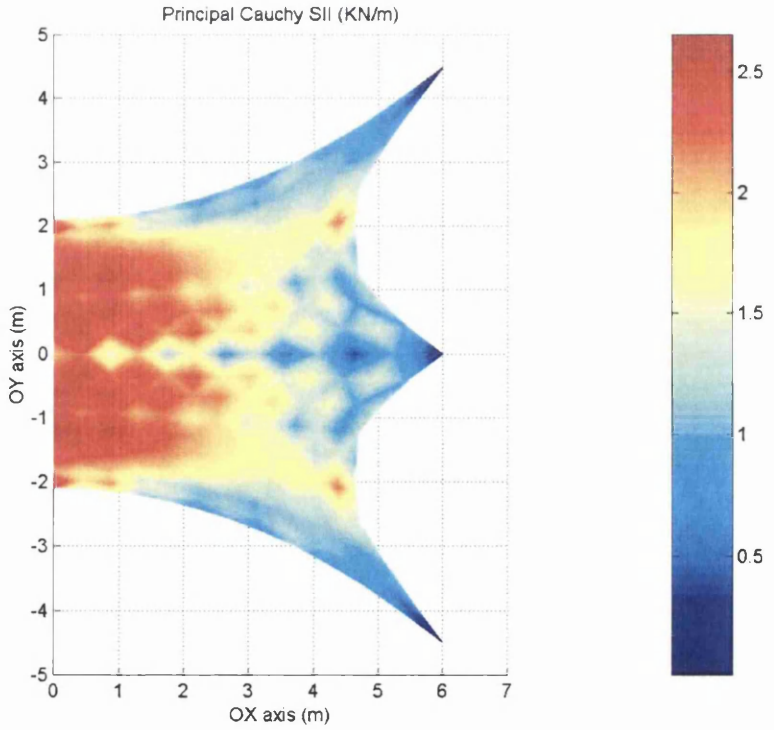

(b)

Figure 12.30: E2: Cauchy stress σ_{II}. (a) Prestress load. (b) Snow load.

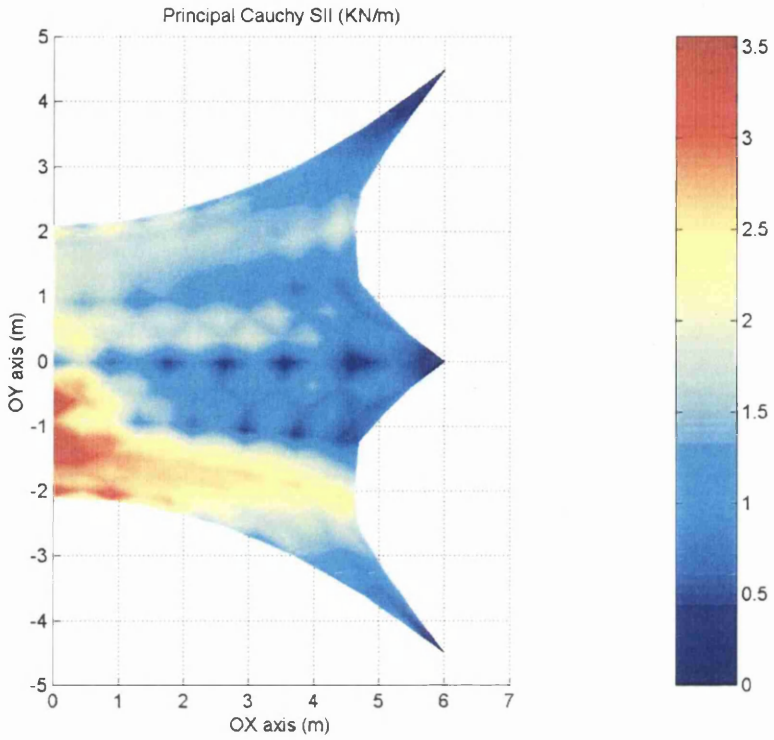

(a)

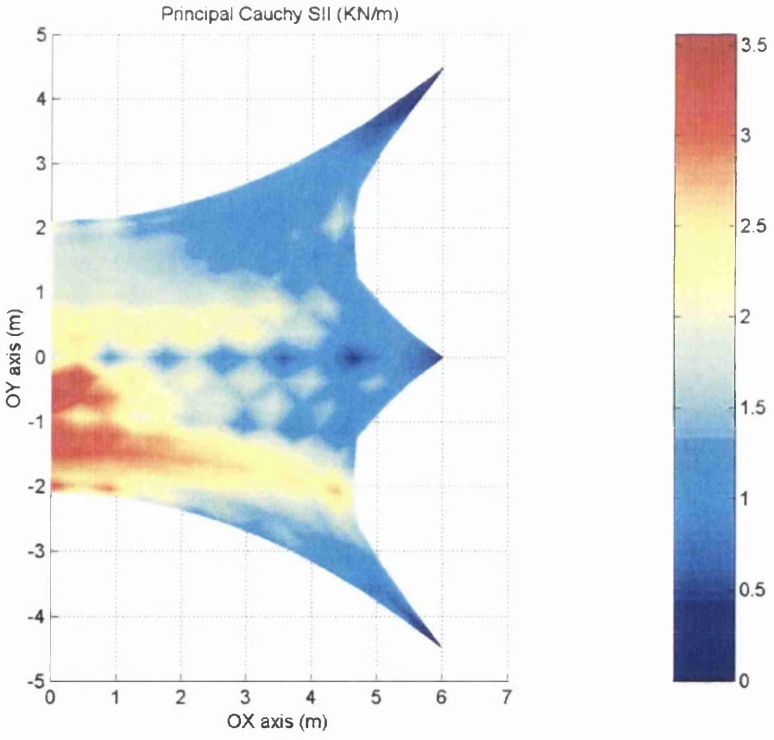

(b)

Figure 12.31: E2: Cauchy stress σ_{II}. (a) Wind load, hyp. I. (b) Wind load, hyp. II.

12.4 Conclusions.

The structural models presented in this chapter correspond to realistic examples of cable reinforced prestressed membranes. These structures were studied under the hypothesis of large displacements but moderate strains. Due to this issue, a Saint Venant-Kirchhoff hyperelastic model was regarded as the most appropriate to model the constitutive behaviour of the fabric textile. Indeed, strains no further than $1.0e-2$ were encountered, which demonstrate the accuracy of the assumed hypotheses.

The prestressing loading was applied on a constructive manner by means of pulling the supports or stretching the perimeter cables. Because of this, these prestressing loading can be reproduced efficiently in situ. Eventually, in-service loads can be applied. A larger nonlinearity is observed in the first loading stage than in the latter. This can be easily observed in figure 12.32, where convergence curves are plotted for the different loading hypotheses adopted over structure $E2$.

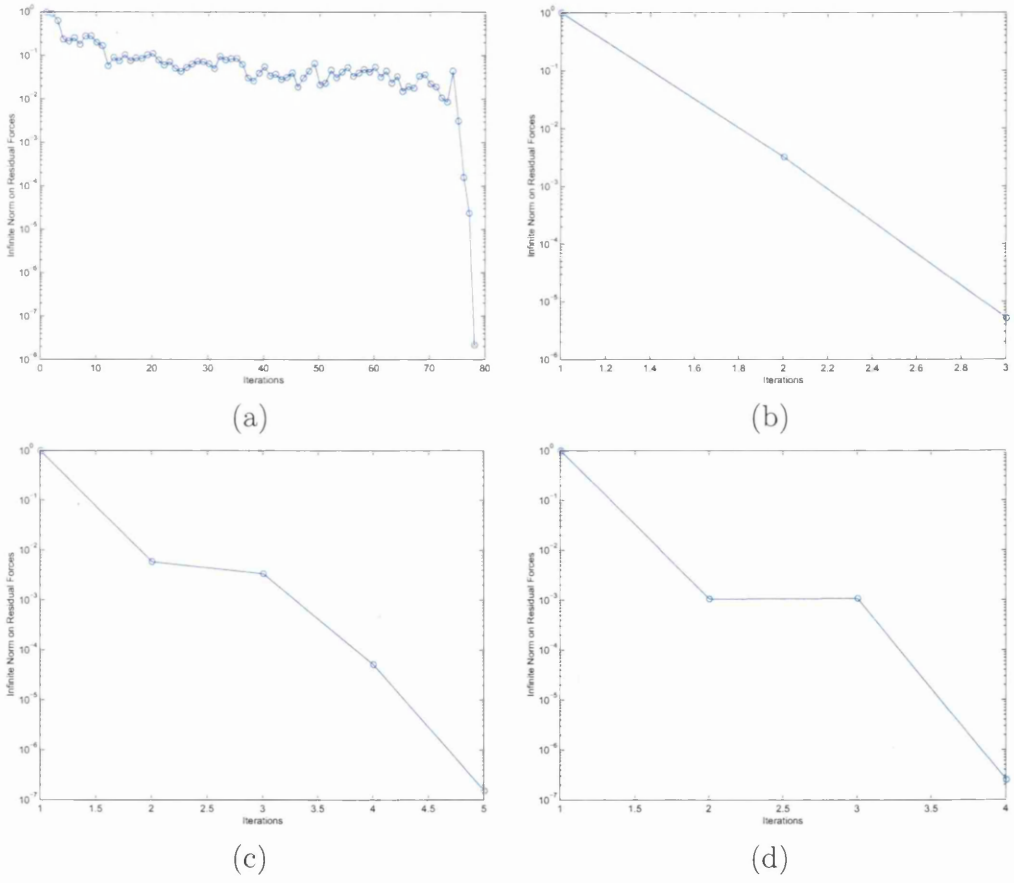

Figure 12.32: E2: convergence curves. (a) Prestress load. (b) Snow load. (c) Wind load, hyp. I. (c) Wind load, hyp. II.

Part V

Conclusions

Chapter 13

Concluding remarks

13.1 General considerations.

The preceding chapters have presented the numerical techniques required to develop a finite element program capable of coping with cable reinforced prestressed membranes.

These structures, comprised of cables and membranes, with broad application in Civil Engineering and Architecture, are subjected to large displacements and deformations, yet moderate strains. This fact implies that nonlinear continuum principles, under a finite deformations framework, must be accounted for. Hence, the physical formulation of the continuum is set up in terms of stress Lagrangian entities such as the first and second Piola-Kirchhoff stress tensors and, as a function of strain tensors like the Green-Lagrange strain tensor.

As the initial configuration of the problem cannot be established beforehand using only architectural criteria, the so called *shape finding problem* emerges in order to provide an initial equilibrium configuration under the imposition of certain boundary conditions and a predefined internal prestressing distribution. Amid all the available techniques, the *force density method* has emerged as the simplest and most useful.

Once an initial equilibrium configuration with a nominal stress distribution has been obtained using the previous shape finding procedure, realistic prestressed conditions can be applied on the structure by means of displacing fixed supports or stretching interior or perimeter cables. This prestressed configuration is used as the basis for the subsequent in-service loading analysis. For this reason, the finite deformations theory under prestressed bodies was developed as the foundation over which to build up the whole formulation.

The constitutive model employed to model the material's behaviour was the so called Saint Venant-Kirchhoff hyperelastic model, namely, a linear tensorial relationship between the second Piola-Kirchhoff stress tensor and the Green-Lagrange strain tensor. The finite element method (FEM) was established using a Total Lagrangian formulation (TLF), which was implemented for two-noded and three-noded isoparametric finite elements in a Direct Core Congruential format (DCCF).

The final problem comprising the balance equations at the nodal level, is presented by means of two different variational formulations. On the one hand, the Principle of Virtual Work is employed whereas, on the other hand, another approach based on the minimization of the Total Potential Energy functional is introduced.

The admissible loading was very versatile, consisting of thermal effects, snow loading, wind loading and non conservative forces among others. The resulting geometrically nonlinear problem, which involves the minimization of the total potential energy system functional, was solved by using unconstrained optimization techniques through a wide group of first and second order algorithms, specifically developed for it. These were improved by a parametric line search algorithm according to a polynomial interpolation.

The set of equilibrium equations presented a geometrically nonlinear feature, so

an iterative solution scheme was required. Among all the available methods, the second-order Newton-Raphson technique accomplished the best convergence properties. The total tangent stiffness matrix required to be calculated by this method was obtained by linearizing the global equilibrium equations.

13.2 Conclusions.

13.2.1 About the proposal of the method.

Even though the physical response of prestressed membranes was perfectly defined and set up in early works by Otto (1967), special needs are still requested within the field of the numerical simulation. An attempt to accomplish some of the goals in this direction has been made in this research.

The physical models, despite of being interesting to foresee the mechanical behaviour of the membrane -see Otto (1962) and Hildebrandt and Tromba (1990)-, they only provide a qualitative insight on the real response of such structures. In order to facilitate the design process, it is necessary to use numerical methods that are efficient and stable. These structures, which undergo large displacements and moderate strains, are very sensible to sudden changes in geometry, because of the geometrically nonlinearity of its own nature. All of these issues, make the numerical simulation a valuable tool to envisage the response when multiple and different sets of input loads want to be taken into consideration. The computational cost, namely, time, is the only one to face.

For years, the computational analysis of prestressed membranes has been performed by using cable networks as a valid model of its behaviour. However, although computationally efficient, this analogy has been proven to be only approximate -see Magara and Okamura (1986) and Levy and Spillers (1998)- to represent exactly real strains and stresses of the continuum.

On the other hand, a fully nonlinear approach in a Lagrangian format has not been reported so far in the existing literature. At most, the classical linear elasticity material stiffness matrix along with a modified geometric stiffness matrix to account for some geometrically nonlinear effects, are added up to form the final total tangent stiffness matrix. References such as Buchholdt (1985), Leonard (1988), Broughton and Ndumbaro (1994) or Levy and Spillers (1995) are based on this framework.

By combining a suitable representation of the continuum through three-noded finite elements and the fundamentals of the nonlinear continuum mechanics, a more robust, comprehensive and accurate approach was developed. References such as Oden and Sato (1967), Grutmann and Taylor (1992) and Souza et al. (1995) follow the same trend. At the same time, the inclusion of two-noded finite elements enabled to represent appropriately which could be likely assembled in the overall structure.

For real applications in the fields of Architecture or Civil Engineering, a mod-

erate strain-finite deformation continuum theory[1] -see Crisfield (1991b), Bonet and Wood (1997) and Belytschko et al. (2000)- was shown as adequate to formulate the problem. Furthermore, by realizing that the initial equilibrium shape is usually under the existence of an acting prestressing load pattern, a strong formulation based on initially prestressed bodies was developed -see Iésan (1989)- for membrane structures.

Numerical examples for two realistic structures were deeply described in an exclusive chapter. Both cases attempted to underline the importance of applying the prestressing load in a feasible manner: either moving locally certain nodes of the mesh or controlling the prestressed strength in reinforced cables, among other methods. The definition of initial shapes according to any form finding method, however appealing from a mathematical standpoint[2], it does not result achievable for practical engineering purposes.

Eventually, with the purpose of accelerating the design process, a modular software architecture was implemented with different capabilities: graphical preprocessor, form finding solver, shape graphical postprocessor, structural analysis solver and stresses graphical postprocessor. A friendly user interface was designed for it.

13.2.2 About the convergence of the numerical algorithms.

Some key conclusions has been discovered when dealing with the simulation of the different numerical examples:

- The Newton method has been proven as the most powerful method given its quadratic convergence. As a matter of fact, this method should be preferred, whether possible, over other techniques, such as dynamic relaxation, steepest descent or so on.

- When analyzing 2D membranes under in-plane loading conditions, the final solution is obtained in an incredibly fast rate. Nevertheless, if transverse loads are acting on the membrane, the convergence towards the solution is slowed down considerably. Indeed, the problem becomes extremely non-linear.

- Computationally, distributed loads are preferred rather than point loads, whenever possible. Another interesting remark already pointed out by Oden and Sato (1967), is the fact that in the analysis of membranes which undergo large out-of-plane deformations due to external loading, rates of convergence can be significantly increased by first analyzing a coarse mesh. Thus, an initial coarse mesh could be used initially and then, by a mesh refinement technique, new elements could be introduced into the finite element analysis.

[1] For Biomechanics applications, large strains constitutive laws must be regarded as more appropriate.

[2] The search of optimum shapes, also named minimum shapes, is well registered in Hildebrandt and Tromba (1990), Do Carmo (1995) or Castellano (1995).

- The presence of membrane elements in a wrinkling state slows down the convergence of the method, with respect to the convergence rate when fully traction is present in the whole domain.

- The initial steps for a prestressing loading analysis are very unstable, specially when dealing with nearly plane initial membranes. The inclusion of a fictitious prestress or, equivalently, the modification of the Hessian of the Total Potential Energy functional by the Levenberg-Marquardt method can be considered very useful.

- Another appealing way to overcome such difficulties throughout the first increments of the analysis is to combine first and second order methods in an efficient manner. To avoid initial divergences of the calculation, a more robust first order method is employed and only when local convergence is presumed, a second order algorithmic technique is used.

- The inclusion of a parametric line search scheme has been shown as fundamental to reach convergence in the majority of the analyses which have been carried out.

- When masts are included into the global analysis of the structure, the overall stiffness matrix could end up ill-conditioned, because of the considerable difference of stiffness between fabric textile and masts themselves. Scaling techniques are efficient to cope with these situations.

- The prestressing loading stage has been proven to be much more no-linear than the subsequent in-service loading stage. Due to this fact, a two-step analysis has been seen as very effective computationally.

13.3 Recommendations for further research.

According to Lewis (1998), pp. 181, *"... despite an upward trend in popularity of lightweight tension structures, factors such as cost and durability can render these exciting structural forms uncompetitive against conventional designs. This situation can be attributed to the lack of appropriate computational tools ... "*.

These words make clear that there are still many open fronts within the prestressed membranes's numerical analysis. Even though this thesis can be regarded as a forward step towards the proper computational treatment of this kind of structures, future research lines should be pointed out to cover the demanded needs of engineers and designers. Some of them are:

- **Incorporation of new constitutive models.** The consideration of the orthotropic model of Saint Venant-Kirchhoff, as well as some other materials' laws should be included within the computer code's library. This will permit to account for materials whose strains can be regarded as larger than moderate.

- **Fluid-structure interaction**. The structural models analyzed in this research, when subjected to follower loads such as wind loading, resulted into notable displacements outcomes. This could likely entail a drastic variation of the pressure coefficients acting on the membrane. Not just its magnitude, but its sign, can be altered, making the pseudo-static approach inefficient and inadequate.

- **Development of experimental examples**. It is believed that with the purpose of validating more exactly the computer program upshots, feasible experimental examples should be designed. A proper measure of strains and stresses, specially in terms of prestressing, should be incorporated in order to register variations of behaviour of the prestressed membrane, throughout the whole structural process. More accurate constitutive laws could be derived for further implementation into the computer code.

- **Creeping deformation analysis**. It is necessary to derive constitutive models to account for this phenomenon, so the stability of the prestressed membrane could be followed throughout its life.

In view of what has been exposed throughout this research, it is believed that even at the present state the numerical simulation of prestressed membranes provides the design engineer with valuable quantitative information. Nevertheless, much effort is still needed for the purpose of improving the accuracy of the analysis and including more complexities into the calculations.

Part VI

Apendices

Appendix A

Vector and tensor Algebra

A.1 Introduction.

The use of vectors, matrices and tensors is of fundamental importance in engineering analysis because it is only with the use of these quantities that the complete solution process can be expressed in a compact and elegant manner. The objective of this appendix is to present the fundamentals of matrices and vectors, with emphasis on those aspects that are important in finite element analysis.

Multiple definitions, theorems and corollaries are gathered in this appendix. The great majority of the demonstrations are omitted because they overcome the scope of this brief discussion. Therefore, although a rather limited presentation of matrices and vectors is given here, we hope that the focused practical treatment will provide enough basis for understanding of the thesis' main body. Nevertheless, for a further and detailed study, some references of contrasted interest are mentioned: Dahlquist et al. (1969), Krasnov et al. (1994), Burden and Douglas (1998) and Quesada (1996).

A.2 Introduction to matrices.

In this section, some basic definitions and properties about fundamentals of matrix analysis are detailed. Theses concepts will be referred to in some chapters of this thesis.

Definition 6 *A nxn matrix* $\mathbf{A} = a_{ij}$ *is said to be* **diagonally dominant** *when:*

$$|a_{ii}| \geq \sum_{j=1, j\neq i}^{n} |a_{ij}| \quad \forall\, i = 1, 2, \ldots, n \tag{A.1}$$

Analogously, the same nxn matrix $\mathbf{A}$ *is said to be* **strictly diagonally dominant** *when:*

$$|a_{ii}| > \sum_{j=1, j\neq i}^{n} |a_{ij}| \quad \forall\, i = 1, 2, \ldots, n \tag{A.2}$$

Theorem 9 *A strictly diagonally dominant matrix is not singular.*

Furthermore, in this case, the Gaussian elimination can be employed for any linear system of equations $\mathbf{A} \cdot \mathbf{x} = \mathbf{b}$ *to come out with its unique solution without swapping neither columns nor rows, and the calculations are stable with respect to round-off errors.*

Definition 7 *A squared matrix* $\mathbf{A}$ *is said to be* **positive definite** *if* $\mathbf{x}^{\mathbf{T}} \cdot \mathbf{A} \cdot \mathbf{x} > 0$, $\forall\, \mathbf{x} \neq \mathbf{0}$, *where* $\mathbf{x}$ *is a n-dimensional vector.*

Definition 8 *A squared matrix* $\mathbf{A}$ *is said to be* **positive semidefinite** *if* $\mathbf{x}^{\mathbf{T}} \cdot \mathbf{A} \cdot \mathbf{x} \geq 0$, $\forall\, \mathbf{x}$, *where* $\mathbf{x}$ *is a n-dimensional vector.*

Theorem 10 *Let* $\mathbf{A}$ *be a squared positive definite matrix, then all the following statements are satisfied:*

- $\mathbf{A}$ *is no singular.*
- $a_{ii} > 0 \quad i = 1, 2, \ldots, n.$
- $\max_{1 \leq k,j \leq n} |a_{kj}| \leq \max_{1 \leq i \leq n} |a_{ii}|.$
- $(a_{ij})^2 < a_{ii} a_{jj} \quad \forall i \neq j.$

Theorem 11 (Silvester's criterion) *A symmetric matrix* $\mathbf{A}$ *is positive definite if and only if its first principal submatrices have positive determinant.*

A.3 Vector and matrix norms.

If we deal with single numbers, we can identify a number as being large or small. Vectors and matrices are functions of many elements, but we also need to measure their size. A norm is a single number that depends on the magnitude of all elements in the vector or matrix.

Vector and matrix norms play an important role in error's theory and, as a consequence, in the definition of the accuracy and stability of the numerical methods employed for the resolution of problems with **ODE**[1] or **PDE**[2] and boundary or initial conditions.

Definition 9 *A* **vector norm** *in* $\mathbf{R}^n$ *is a function,* $\|\cdot\|$*, from* $\mathbf{R}^n$ *to* $\mathbf{R}$*, with the following properties:*

1. $\|\mathbf{x}\| \geq 0 \quad \forall\, \mathbf{x} \in \mathbf{R}^n.$
2. $\|\mathbf{x}\| = 0 \iff \mathbf{x} \equiv 0.$
3. $\|\alpha \mathbf{x}\| = |\alpha| \|\mathbf{x}\| \quad \forall\, \alpha \in \mathbf{R},\ \forall\, \mathbf{x} \in \mathbf{R}^n.$
4. $\|\mathbf{x} + \mathbf{y}\| \leq \|\mathbf{x}\| + \|\mathbf{y}\| \quad \forall\, \mathbf{x}, \mathbf{y} \in \mathbf{R}^n.$

Definition 10 (Euclidean vector norm) *The Euclidean vector norm,* l_2*, of a n-vector* $\mathbf{x}$ *is defined as follows:*

$$\|\mathbf{x}\|_2 = \sqrt{\sum_{i=1}^{n} x_i^2} \tag{A.3}$$

Definition 11 (Infinity vector norm) *The infinity vector norm,* l_∞*, of a n-vector* $\mathbf{x}$ *is defined as follows:*

$$\|\mathbf{x}\|_\infty = \max_{1 \leq i \leq n} | x_i | \tag{A.4}$$

[1] Ordinary Differential Equations.
[2] Partial Differential Equations.

The following relationship between the above norma can be obtained:

Theorem 12 *For all* $\mathbf{x} \in \mathbf{R}^n$,

$$\|\mathbf{x}\|_\infty \leq \|\mathbf{x}\|_2 \leq \sqrt{n}\|\mathbf{x}\|_\infty \tag{A.5}$$

Let x_j *be the* j^{th}*-coordinate of the vector* $\mathbf{x}$ *such that:* $\|\mathbf{x}\|_\infty = \max_{1\leq i\leq n} |x_i| = |x_j|$. *Thus, it is verified that:*

$$\|\mathbf{x}\|_\infty^2 = |x_j|^2 = x_j^2 \leq \sum_{i=1}^{n} x_i^2 \leq \sum_{i=1}^{n} x_j^2 = nx_j^2 = n\|\mathbf{x}\|_\infty^2 \tag{A.6}$$

Therefore, it is fulfilled:

$$\|\mathbf{x}\|_\infty \leq \sqrt{\sum_{i=1}^{n} x_i^2} = \|\mathbf{x}\|_2 \leq \sqrt{n}\|\mathbf{x}\|_\infty \quad (q.e.d.) \tag{A.7}$$

Definition 12 *The* **norm** *of a matrix of order nxn, written as* $\|\cdot\|$, *is a real valued function from* $\mathbf{R}^{2n}$ *to* $\mathbf{R}$, *which satisfies for any pair of matrices* $\mathbf{A}$ *and* $\mathbf{B}$ *and for any scalar* α, *the following requirements:*

(i) $\|\mathbf{A}\| \geq 0$.

(ii) $\|\mathbf{A}\| = 0 \iff \mathbf{A} \equiv 0$.

(iii) $\|\alpha\mathbf{A}\| = |\alpha|\|\mathbf{A}\|$.

(iv) $\|\mathbf{A} + \mathbf{B}\| \leq \|\mathbf{A}\| + \|\mathbf{B}\|$.

(v) $\|\mathbf{A} \cdot \mathbf{B}\| \leq \|\mathbf{A}\|\|\mathbf{B}\|$.

In order to obtain useful results, we need to employ only specific vector norms with specific matrix norms. Here and in what follows, only natural or induced matrix norms will be used. These norms are defined as follows:

Theorem 13 *Let* $\|\cdot\|$ *be a vector norm in* $\mathbf{R}^n$, *then:*

$$\|\mathbf{A}\| = \max_{\|\mathbf{x}\|=1} \|\mathbf{A} \cdot \mathbf{x}\| \tag{A.8}$$

is a matrix norm. This norm is named as **natural or induced matrix norm** *associated with the vector norm.*

Corollary 5 *For any vector* $\mathbf{x}$, *any matrix* $\mathbf{A}$ *and any natural or induced matrix norm* $\|\cdot\|$, *the following condition is satisfied:*

$$\|\mathbf{A} \cdot \mathbf{x}\| \leq \|\mathbf{A}\|\|\mathbf{x}\| \tag{A.9}$$

Definition 13 *The natural or induced infinity and Euclidean matrix norms of a matrix* $\mathbf{A}$ *of order nxn are defined as:*

$$\|\mathbf{A}\|_\infty = \max_{\|\mathbf{x}\|=1} \|\mathbf{A}\cdot\mathbf{x}\|_\infty \qquad \|\mathbf{A}\|_2 = \max_{\|\mathbf{x}\|=1} \|\mathbf{A}\cdot\mathbf{x}\|_2 \tag{A.10}$$

Theorem 14 *If* $\mathbf{A} = a_{ij}$ *is a nxn matrix, then:*

$$\|\mathbf{A}\|_\infty = \max_{1\le i\le n} \sum_{j=1}^{n} |a_{ij}| \tag{A.11}$$

Definition 14 *The* **spectral radius** $\rho(\mathbf{A})$ *of a matrix* $\mathbf{A}$ *of order nxn is defined as:*

$$\rho(\mathbf{A}) = \max_{i=1,n} |\lambda_i| \quad \textit{where } \lambda_i \textit{ is an eigenvalue of } \mathbf{A}$$

Definition 15 *If* $\mathbf{A}$ *is a matrix of order nxn, then:*

(i) $\|\mathbf{A}\|_2 = \sqrt{\rho(\mathbf{A}^\mathbf{T}\cdot\mathbf{A})}$.

(ii) $\rho(\mathbf{A}) \le \|\mathbf{A}\|, \forall\ \|\mathbf{A}\|$.

where all the matrix norms are considered to be natural or induced.

For the demonstration of the above second condition, let λ *be an eigenvalue of the matrix* $\mathbf{A}$ *with its associated eigenvector* $\mathbf{x}$ *such that* $\|\mathbf{x}\| = 1$. *In this case, we can prove that:*

$$|\lambda| = |\lambda|\|\mathbf{x}\| = \|\lambda\mathbf{x}\| = \|\mathbf{A}\mathbf{x}\| \le \|\mathbf{A}\|\|\mathbf{x}\| = \|\mathbf{A}\| \tag{A.12}$$

As the spectral radius is equal to the maximum absolute value of the eigenvalues, the condition results to be demonstrated.

Definition 16 *A matrix* $\mathbf{A} = a_{ij}$ *of order nxn is said to be convergent if:*

$$\lim_{k\longrightarrow\infty} (a_{ij})^k = 0 \quad i = 1,2,\ldots,n \quad j = 1,2,\ldots,n. \tag{A.13}$$

Theorem 15 *The following statements are equivalent:*

(i) $\mathbf{A}$ *is a convergent matrix.*

(ii) $\lim_{n\longrightarrow\infty} \|\mathbf{A}^n\| = 0$, *for any natural norm.*

(iii) $\lim_{n\longrightarrow\infty} \|\mathbf{A}^n\| = 0$, *for all natural norms.*

(iv) $\rho(\mathbf{A}) < 1$.

(v) $\lim_{n\longrightarrow\infty} \mathbf{A}^n\cdot\mathbf{x} = 0 \quad \forall\, \mathbf{x}\in\mathbf{R}^n$.

A.4 Iterative methods for the solution of linear system of equations.

The result of the discretization process in structural mechanics problems, is a system of algebraic equations, which are linear or non-linear according to the nature of the **PDE**. Matrices derived from partial differential equations are always sparse, i.e. most of their elements are zero. Efficient methods for the resolution of systems $\mathbf{A} \cdot \mathbf{x} = \mathbf{b}$ are strongly demanded.

Although any system of equations can be solved by Gauss elimination or LU decomposition, unfortunately, these direct techniques entail a high computational cost along with somehow less accurate results, which stem from the presence of considerable round-off errors. This leaves an opening for iterative schemes.

The aim is to solve the system $\mathbf{A} \cdot \mathbf{x} = \mathbf{b}$, for which an initial approximate guess $\mathbf{x}^{(0)}$ is set up. Then, a series of vector solutions of the way $\{\mathbf{x}^{(k)}\}_{k=0}^{\infty}$ is generated in an iterative manner to converge to $\mathbf{x}$. If each iteration is cheap and the number of iterations is small, an iterative solver may cost less than a direct method.

By means of an iterative method, the problem $\mathbf{A} \cdot \mathbf{x} = \mathbf{b}$ is transformed into one of the form $\mathbf{x} = \mathbf{T} \cdot \mathbf{x} + \mathbf{c}$, for any matrix $\mathbf{T}$ and a vector $\mathbf{c}$. Hence, the solution of the system of equations is accomplished according to the following iterative formula:

$$\mathbf{x}^{(k)} = \mathbf{T} \cdot \mathbf{x}^{(k-1)} + \mathbf{c} \quad k = 1, 2, 3, \ldots \tag{A.14}$$

As a conclusion, direct methods[3] are preferred rather than iterative methods when dealing with small order system of equations, on account of its shorter computational time to achieve the solution. Nevertheless, large dimensional system of equations with a wide range of zeros among their matrices' components, should be preferably solved in an iterative manner[4]. These iterative schemes behave efficiently in terms of both computational time and storage capacity.

Theorem 16 *For all* $\mathbf{x}^{(0)} \in \mathbf{R}^n$, *the series* $\{\mathbf{x}^{(k)}\}_{k=0}^{\infty}$ *set up as:*

$$\mathbf{x}^{(k)} = \mathbf{T} \cdot \mathbf{x}^{(k-1)} + \mathbf{c} \quad \forall\, k \geq 1 \tag{A.15}$$

converges towards the unique solution of $\mathbf{x} = \mathbf{T} \cdot \mathbf{x} + \mathbf{c}$ *if and only if* $\rho(\mathbf{T}) < 1$.

A.4.1 Jacobi method.

This method, regarded as the simplest iterative technique, consists of solving the i-th equation of the system $\mathbf{A} \cdot \mathbf{x} = \mathbf{b}$ with the purpose of obtaining x_i –the following

[3] Among these methods, *Gauss* method, *Gauss-Jordan* method and matrix factorization schemes such as *Dootlittle* scheme, *Crout* scheme or *Cholesky* scheme, must be highlighted as the most common in use.

[4] These systems of equations usually emerge from computational techniques such as finite differences, finite elements or finite volumes, among others, when employed to solve **PDE** with boundary conditions of any type, that is, essential or *Dirichlet*, natural or *Neumann* and mixed boundary conditions.

condition must be fulfilled: $a_{ii} \neq 0$. The method is formulated as follows:

$$x_i^{(k)} = \frac{\sum_{j=1,j\neq i}^{n}(-a_{ij}x_j^{(k-1)}) + b_i}{a_{ii}} \quad i = 1, 2, \ldots, n. \tag{A.16}$$

A.4.2 Gauss-Seidel method.

A possible improvement of the former algorithm can be achieved if the following alternative formulation is employed:

$$x_i^{(k)} = \frac{-\sum_{j=1}^{i-1}(a_{ij}x_j^{(k)}) - \sum_{j=i+1}^{n}(a_{ij}x_j^{(k-1)}) + b_i}{a_{ii}} \quad i = 1, 2, \ldots, n. \tag{A.17}$$

where in order to calculate the i-th component of the solution vector $\mathbf{x}^{(k)}$, the components $x_j^{(k-1)}$ with $j = i+1, \ldots, n$ and $x_j^{(k)}$ with $j = 1, \ldots, i-1$ are used.

Theorem 17 *If the matrix* $\mathbf{A}$ *is strictly diagonally dominant, then for any initial guess* $\mathbf{x}^{(0)}$*, both* Jacobi *method and* Gauss-Seidel *method, generate a series of vectors which converge towards the solution of the system* $\mathbf{A} \cdot \mathbf{x} = \mathbf{b}$.

Theorem 18 (Stein-Rosenberg) *If the following condition is verified, that is,* $a_{ij} \leq 0$ $i \neq j$*, and if* $a_{ii} > 0$ $\forall$ $i = 1, \ldots, n$*, then one and only one of the following statements will be verified:*

(i) $0 \leq \rho(\mathbf{T_g}) < \rho(\mathbf{T_j}) < 1$.

(ii) $1 < \rho(\mathbf{T_j}) < \rho(\mathbf{T_g})$.

(iii) $\rho(\mathbf{T_g}) = \rho(\mathbf{T_j}) = 0$.

(iv) $\rho(\mathbf{T_g}) = \rho(\mathbf{T_j}) = 1$.

where:

- $\mathbf{T_g}$ *represents the* $\mathbf{T}$ *matrix obtained by means of the* Gauss-Seidel *iterative scheme.*
- $\mathbf{T_j}$ *represents the* $\mathbf{T}$ *matrix obtained by means of the* Jacobi *iterative scheme.*

Definition 17 *Let* $\widetilde{\mathbf{x}} \in \mathbf{R}^n$ *be an approximation to the solution of the system of equations* $\mathbf{A} \cdot \mathbf{x} = \mathbf{b}$. *The residual vector of* $\widetilde{\mathbf{x}}$ *with respect to this system is defined as* $\mathbf{r} = \mathbf{b} - \mathbf{A}\widetilde{\mathbf{x}}$.

By accounting for this definition, the Gauss-Seidel *iterative scheme can be reformulated as follows:*

$$x_i^{(k)} = x_i^{(k-1)} + \frac{r_{ii}^{(k)}}{a_{ii}} \tag{A.18}$$

The above formula can be slightly modified to yield:

$$x_i^{(k)} = x_i^{(k-1)} + \omega \cdot \frac{r_{ii}^{(k)}}{a_{ii}} \tag{A.19}$$

where for certain values of the positive scalar ω, a faster convergence can be accomplished.

Definition 18 *The iterative methods which may be summarized by means of the aforementioned equation (A.19), are named* ***relaxation methods****. Those with the parameter ω satisfying $0 < \omega < 1$ are specifically named* sub-relaxation methods, *and enable the convergence of those systems of equations which do not converge under the* Gauss-Seidel *method. On the other hand, those methods where $\omega > 1$ are referred to as* over-relaxation methods *and enable to speed up the convergence of those systems of equations which already converge under the* Gauss-Seidel *method*[5].

The equation (A.19) can be rewritten in an alternative manner for the sake of computational implementation, that is:

$$x_i^{(k)} = (1-\omega)x_i^{(k-1)} + \frac{\omega}{a_{ii}}[b_i - \sum_{j=1}^{i-1} a_{ij}x_j^{(k)} - \sum_{j=i+1}^{n} a_{ij}x_j^{(k-1)}] \tag{A.20}$$

Theorem 19 (Kahan) *If $a_{ii} \neq 0 \; \forall \, i = 1, 2, \ldots, n$, then $\rho(\mathbf{T}_\omega) \geq |\omega - 1|$. This fact implies that the* **relaxation** *method converges if and only if $0 < \omega < 2$.*

Theorem 20 (Ostrowski-Reich) *If $\mathbf{A}$ is a positive definite matrix and if $0 < \omega < 2$, then the* **relaxation** *method converges for all possible guesses of the initial solution vector $\mathbf{x}^{(0)}$.*

A.4.3 On the convergence of the method.

When using iterative solvers, it is important to know when to quit. The most common procedure is based upon te difference between two successive iterates; the procedure is stopped when this difference, measured by some norm, is less than a pre-selected value. Unfortunately, this difference may be small when the error is not small and a proper normalization is essential.

At first, it seems logical to think that if $\widetilde{\mathbf{x}}$ is an approximation to the solution $\mathbf{x}$ of the system of equations $\mathbf{A} \cdot \mathbf{x} = \mathbf{b}$, and if the residual vector $\mathbf{r} = \mathbf{b} - \mathbf{A} \cdot \widetilde{\mathbf{x}}$ has got the attribute of having a small norm $\|\mathbf{r}\|$, then the following norm $\|\mathbf{x} - \widetilde{\mathbf{x}}\|$ will be small as well. Nonetheless, there are certain systems of equations where this reasoning is not verified.

Theorem 21 *If $\widetilde{\mathbf{x}}$ is an approximation to the solution $\mathbf{x}$, $\mathbf{A}$ is a non-singular matrix and $\mathbf{r}$ is the residual vector of $\widetilde{\mathbf{x}}$, then for all natural or induced matrix norms, the following condition is fulfilled :*

[5]These methods are abbreviated by means of the following acronym: **SOR** (***Succesive Over Relaxation***).

$$\|\mathbf{x} - \widetilde{\mathbf{x}}\| \leq \|\mathbf{A}^{-1}\|\|\mathbf{r}\| \tag{A.21}$$

Or rewritten in an alternative manner:

$$\frac{\|\mathbf{x} - \widetilde{\mathbf{x}}\|}{\|\mathbf{x}\|} \leq \|\mathbf{A}\|\|\mathbf{A}^{-1}\|\frac{\|\mathbf{r}\|}{\|\mathbf{b}\|} \quad \textit{such that } \mathbf{x} \neq \mathbf{0}, \ \ \mathbf{b} \neq \mathbf{0} \tag{A.22}$$

Definition 19 *The* ***condition number*** *of a non-singular matrix* $\mathbf{A}$*, that is,* $K(\mathbf{A})$*, related to the norm* $\|\cdot\|$ *is defined as:*

$$K(\mathbf{A}) = \|\mathbf{A}\|\|\mathbf{A}^{-1}\| \tag{A.23}$$

In accordance with this definition, the above formuale (A.21) and (A.22) can be rewritten as follows:

$$\|\mathbf{x} - \widetilde{\mathbf{x}}\| \leq K(\mathbf{A})\frac{\|\mathbf{r}\|}{\|\mathbf{A}\|} \tag{A.24}$$

$$\frac{\|\mathbf{x} - \widetilde{\mathbf{x}}\|}{\|\mathbf{x}\|} \leq K(\mathbf{A})\frac{\|\mathbf{r}\|}{\|\mathbf{b}\|} \tag{A.25}$$

Theorem 22 *For all non-singular matrices* $\mathbf{A}$ *and under any natural or induced matrix norm* $\|\cdot\|$*, it is verified that the condition number is always greater or equal to one. Indeed, this is easily proved as follows:*

$$1 = \|\mathbf{I}\| = \|\mathbf{A} \cdot \mathbf{A}^{-1}\| \leq \|\mathbf{A}\|\|\mathbf{A}^{-1}\| = K(\mathbf{A}) \tag{A.26}$$

Corollary 6 *A matrix* $\mathbf{A}$ *is* ***well conditioned*** *if* $K(\mathbf{A})$ *approaches 1 and it is* ***ill conditioned*** *if* $K(\mathbf{A})$ *is significantly larger than 1.*

Corollary 7 *If the matrix* $\mathbf{A}$ *is not ill conditioned, then a small residual vector will imply an accurate approximation to the exact solution of the system of equations. On the contrary, if the matrix* $\mathbf{A}$ *may be regarded as ill conditioned because of its large condition number, then a small residual vector will not guarantee an accurate iterate next to the final exact solution of the system.*

Theorem 23 *For all positive definite matrices* $\mathbf{A}$ *and under the existence of a natural or induced matriz norm* $\|\cdot\|$*, it is verified that the ratio between the largest and the smallest of their eigenvalues is less or equal to the condition number:*

$$K(\mathbf{A}) = \|\mathbf{A}\|\|\mathbf{A}^{-1}\|; \quad \rho(\mathbf{A}) \leq \|\mathbf{A}\|; \quad \rho(\mathbf{A}^{-1}) = \frac{1}{\lambda_{min}(\mathbf{A})} \leq \|\mathbf{A}^{-1}\|$$

Therefore:

$$r(\mathbf{A}) = \frac{\rho(\mathbf{A})}{\lambda_{min}(\mathbf{A})} \leq \|\mathbf{A}\|\|\mathbf{A}^{-1}\| = K(\mathbf{A})$$

where:

$\lambda_{min}(\mathbf{A})$ *is the smallest eigenvalue of the matrix* $\mathbf{A}$.

$\rho(\mathbf{A})$ *is the spectral radius or equivalently, the largest eigenvalue of the matrx* $\mathbf{A}$.

$r(\mathbf{A})$ *is the ratio between both eigenvalues of the matrix* $\mathbf{A}$.

As a consequence, if the matrix $\mathbf{A}$ *is well conditioned, then the ratio between the largest and the smallest of its eigenvalues is very near the unity.*

Appendix B

Nonlinear programming

B.1 Introduction.

The concept of optimization is now well-rooted as a principle underlying the solution of numerous structural problems. Most of these problems end up in unconstrained optimization[1] problems or, equivalently, nonlinear system of equations.

Although multiple algorithms may be established to solve these kinds of problems, all of the algorithms exposed in this research will present the following attributes:

1. Iterative, that is, an iterative sequence will be generated in such a way that every solution is generated based on a previous one.

2. Descent, as the iterative process progresses, the value of a certain function decreases.

3. Convergent, and in the best of the cases, globally convergent.

In this appendix, some definitions and theorems of interest will be detailed.

Definition 20 *An algorithm A is a mapping defined on a vector space χ that assigns to every point $\mathbf{x} \in \chi$ a subset of χ.*

Operated iteratively, the algorithm A initiated at $\mathbf{x}^0$ in χ would generate the sequence defined as:

$$\mathbf{x}^{k+1} = A(\mathbf{x}^k)$$

In general, χ will be a vector space which dispose of an Euclidean norm -see appendix A-. As the algorithm A is not a point-to-point mapping, the sequence generated by the algorithm A cannot, in general, be predicted solely from the knowledge of the initial point $\mathbf{x}^0$. This is to reflect the uncertainty that we may have in practice as to specific details of an algorithm.

Definition 21 (Descent function) *Let $\Gamma \subset \chi$ be a given solution set and let A be an algorithm on χ. A continuous real-valued function Z on χ is said to be a descent function for Γ and χ if it satisfies:*

(i) if $\mathbf{x} \notin \Gamma$ *and* $\mathbf{y} \in A(\mathbf{x}) \implies Z(\mathbf{y}) < Z(\mathbf{x})$

(ii) if $\mathbf{x} \in \Gamma$ *and* $\mathbf{y} \in A(\mathbf{x}) \implies Z(\mathbf{y}) \leq Z(\mathbf{x})$

The basic idea of a descent function, is that for points outside the solution set, a single step of the algorithm yields a decrease in the value of the descent function.

Definition 22 (Closed mapping) *A point-to-set mapping A from χ to γ is said to be closed at $\mathbf{x} \in \chi$ if the assumptions:*

[1] See Dennis Jr. and Schnabel (1996) and Luenberger (1989) for an extensive revision about the subject.

(i) $\mathbf{x}^k \longrightarrow \mathbf{x}$, $\mathbf{x}^k \in \chi$

(ii) $\mathbf{y}^k \longrightarrow \mathbf{y}$, $\mathbf{y}^k \in A(\mathbf{x}^k)$

imply:

(iii) $\mathbf{y} \in A(\mathbf{x})$

Corollary 8 *The point-to-set mapping A is said to be closed on χ if it is closed at each point of χ.*

Theorem 24 (Global Convergence Theorem) *Let* $\mathbf{A}$ *be an algorithm on χ, and suppose that given $\mathbf{x}^0$, the sequence $\{\mathbf{x}^k\}_{k=0}^{\infty}$ is generated satisfying:*

$$\mathbf{x}^{k+1} \in \mathbf{A}(\mathbf{x}^k)$$

Let a solution set $\Gamma \subset X$ be given, and suppose:

i) all points $\mathbf{x}^k$ are contained in a compact set $S \subset \chi$.

ii) there is a continuous descent function Z on χ.

iii) the mapping A is closed at points outside Γ.

Then the limit of any convergent subsequence of $\{x^k\}$ is a solution.

Corollary 9 *If under the assumptions of the Global Convergence Theorem, Γ is represented uniquely by the point $\overline{\mathbf{x}}$, then the sequence $\{\mathbf{x}^k\}$ converges to $\overline{\mathbf{x}}$.*

Definition 23 (Degree of convergence on series) *Let $\mathbf{x}^* \in R^n$, $\mathbf{x}^k \in R^n$, $k = 0, 1, 2, \ldots$. The sequence $\{\mathbf{x}^k\} = \{\mathbf{x}^0, \mathbf{x}^1, \mathbf{x}^2, \ldots\}$ is said to converge to $\mathbf{x}^*$ if it satisfies:*

$$\lim_{k \longrightarrow \infty} \|\mathbf{x}^k - \mathbf{x}^*\| = 0$$

If there exits a constant $c \in [0, 1)$ and an integer $\widehat{k} \geq 0$ such that for all $k \geq \widehat{k}$,

$$\|\mathbf{x}^{k+1} - \mathbf{x}^*\| \leq c\|\mathbf{x}^k - \mathbf{x}^*\|$$

then $\{\mathbf{x}^k\}$ is said to converge linearly to $\mathbf{x}^*$.

If for a sequence $\{c_k\}$ which tends to 0,

$$\|\mathbf{x}^{k+1} - \mathbf{x}^*\| \leq c_k\|\mathbf{x}^k - \mathbf{x}^*\|$$

then $\{\mathbf{x}^k\}$ is said to converge super-linearly to $\mathbf{x}^*$.

If there exit constants $p > 1$, $c \geq 0$ and $\widehat{k} \geq 0$ such that $\{\mathbf{x}^k\}$ converges to $\mathbf{x}^*$, and for all $k \geq \widehat{k}$,

$$\|\mathbf{x}^{k+1} - \mathbf{x}^*\| \leq c\|\mathbf{x}^k - \mathbf{x}^*\|^p$$

then $\{\mathbf{x}^k\}$ is said to converge to $\mathbf{x}^*$ with order p.

If $p = 2$ or $p = 3$, the sequence is said to be quadratically or cubically convergent, respectively.

Corollary 10 *The greater the order of convergence, for an initial point $\mathbf{x}^0$, the faster the speed of convergence towards the solution.*

Appendix C

Graphs theory: fundamentals

C.1 Introduction.

The discrete locations at which the variables are to be calculated are defined by the numerical grid which is essentially a discrete representation of the geometric domain on which the problem is to be solved. It divides the solution domain into a finite number of subdomains.

The generation of grids for complex geometries is an issue which requires too much space to be dealt with in great detail here. However, we shall present some basic ideas about graphs theory, because of its interest for the development of grids in membrane structures, as it can be read in a specific chapter of this thesis.

C.2 Fundamentals of Graphs theory.

Definition 24 *A graph is a pair (V, E), where V is a finite set whose elements are the vertices of the graph and E is a collection of pairs of vertices called the edges of the graph. Therefore, $(e = \{a, b\} \in E; a, b \in V)$, where a and b are adjacent vertices and extremes of the edge e.*

An m-dimensional cable net, mathematically represented by (V, E, p), can be obtained starting from the so called mathematical entity graph (V, E) and a function $\mathbf{p}$, so that:

$$\begin{aligned} \mathbf{p} : V &\rightarrow \mathbf{R}^m \\ a &\mapsto \mathbf{p}(a) \end{aligned} \tag{C.1}$$

$$\mathbf{p}(a_i) = \mathbf{p_i} = (x_i, y_i, z_i) \in \mathbf{R}^3 \quad \text{with} \quad a_i \in V \quad \text{(structure's node)} \tag{C.2}$$

$$\overline{\mathbf{p}(a_i)\mathbf{p}(a_j)} \quad \text{with} \quad a_i, a_j \in V \quad \text{(structure's cable)} \tag{C.3}$$

Consequently, (V, E) is called the *structure graph* of the cable net, and $\mathbf{p}$ is a function that transforms the topological structure into a spatial one.

Those properties of a cable network which strictly depend on the connectivity among their nodes and not on the spatial distribution of them, are named *combinatorial properties.* These properties are common attributes for all the cable networks sharing the same connectivity. Nonetheless, those aspects which are related to the spatial configuration of the structure are named *geometric properties.*

Definition 25 *A graph (V, E) is said to be disconnected if the vertex set V can de partitioned into two nonempty and disjointed sets, so that no edge belonging to the set E has its endpoints in each one of the sets simultaneously. Otherwise, the graph is said to be connected.*

Definition 26 *The number of edges of the graph with the vertex a as an endpoint is called the valence or degree of a and it is formulated as $\rho(a)$. In this way, it is implied:*

$$\Sigma_{a \in V} \rho(a) = 2 \cdot \mid E \mid$$
$$\overline{\rho} = \frac{2 \cdot |E|}{|V|} \tag{C.4}$$

where:

1. $\mid E \mid$ *represents the cardinal of* E.
2. $\overline{\rho}$ *is the average valence of a vertex.*

Definition 27 *A graph (U, D) comprised of some vertices and edges belonging to the graph (V, E), in such a way that $U \subseteq V, D \subseteq E$, is referred to as subgraph of (V, E).*

Definition 28 *Let (V, E) be a graph. If exists a series of vertices $a = a_0, a_1 \ldots a_n = b$, in such a way that every pair of consecutive vertices are interconnected by an edge, then it is said that the vertices a and b are connected by a path which belongs to the graph.*

Lemma 1 *A graph (V, E) is said to be connected if and only if every pair of vertices of the graph is connected by a path of the graph.*

Definition 29 *A graph (V, E) is said to be planar if it can be drawn in the plane without its edges crossing. Starting from that one, a plane graph can be defined as a graph which is planar along with a specific drawing in the plane.*

Once the graph can be drawn in a plane, we will name *faces* as those regions of the plane which are bounded by edges of the graph. A remarkable structural application of this sort of graphs which must be pointed out, is the covering of open spaces by means of roofing structures. For the sake of this reason, a planar graph (V, E, F) is introduced where F represents the set of faces of the graph.

Definition 30 *Given a plane graph, the valence of a face can be thought of as the number of edges surrounding the face and it is represented by $\rho(f)$, with $f \in F$.*

Theorem 25 (Theorem of Euler) *Let (V, E, F) be a connected plane graph. Then we have that:*

$$|V| - |E| + |F| = 2 \tag{C.5}$$

where:

1. $|V|$ *is the number of vertices.*
2. $|E|$ *is the number of edges.*

3. $|F|$ *is the number of faces.*

Lemma 2 *Let* (V, E, F) *be a plane graph. Then* $|E| <= 3 \cdot |V| - 6$ *with equality if and only if all the faces are triangular.*

In order to guarantee an adequate discrete representation of a domain by means of a planar graph, a sufficiently enough number of nodes, edges and faces must be accounted for. Coarser or finer meshes will depend on the selection of the cardinal of these sets. According to Graver (2001), in the case of anticlastic surfaces -shape shown by prestressed membranes-, it is helpful to ensure that the valence of every vertex is less or equal to six, in order to avoid coplanar nodes.

Appendix D

Nonlinear continuum mechanics: fundamentals

D.1 Introduction.

Nonlinear continuum mechanics is a fundamental instrument for the correct study of structures undergoing large deformations. As it is well known, two sources of nonlinearity exist in the analysis of solids, namely, material and geometric nonlinearity. The latter is the one of major concern throughout this thesis. Practical stress analysis of complex solids and structures requires to be solved by non-classical structural techniques. Numerical analysis such as the Finite Element Method have acquired a stunning acceptance among the scientist community.

In Reference Bathe (1996), a rigorous classification is presented for the different nonlinear structural mechanics problems that can be encountered. In actual analysis, it is necessary to decide in advance whether a problem falls into one or another category of nonlinear problem. This fact will impose the use of a specific formulation rather than another one.

This appendix intends to present briefly the basic kinetic and kinematic tools in nonlinear continuum mechanics. Strain and stress tensors will arise in a natural manner. Basic definitions and relations among them will be developed for the sake of completeness. Nevertheless, for an extensive revision of these concepts, a wide bibliography can be encountered. According to the author's criterion, some of the most remarkable References are: Timoshenko and Goodier (1968), Green and Zerna (1968), Malvern (1969), Díaz del Valle (1989), Truesdell and Noll (1992), Bonet and Wood (1997), Chadwick (1999), Holzapfel (2000) and Belytschko et al. (2000).

Finally, let us remark the importance of disposing of a sufficient knowledge of tensor analysis. This topic will be assumed to be known by the reader, although some comprehensive studies are mentioned, namely: Lichnerowicz (1962), Santaló (1969), González de Posada (1983) and Sokolnikoff (1987).

D.2 An introduction to kinematics.

Let $\mathcal{B}$ a deformable solid, also named material body, which satisfies the requirements to be regarded as a continuum[1], that is, we disregard the molecular structure of matter and picture it as being without gaps or empty spaces. Under the presence of a displacements field[2], the movement of the material body can be tracked as a series of configurations throughout the time domain. Furthermore, it is feasible to define a mapping between the initial undeformed configuration $\mathbf{B}_0$ at time $t = 0$ and any other configuration $\mathbf{B}_t$ at time t, which is given as:

$$\mathcal{F} : \mathbf{B}_0 \longrightarrow \mathbf{B}_t$$

$$\mathbf{x} = (x_1, x_2, x_3) = \mathcal{F}(\mathbf{X_0}, t) = \mathcal{F}(X_1^0, X_2^0, X_3^0, t)$$

[1] In this particular investigation, the solid $\mathcal{B}$ could be either a structural membrane or a cable.

[2] Tensor (T_{ij}) and matrix $(\mathbf{T})$ notations will be employed throughout this appendix indistinctly, unless otherwise stated.

where $\mathbf{x}$ stands for the current or spatial coordinates whereas $\mathbf{X_0}$ represents the coordinates of the material particle itself. In Malvern (1969), four distinct classical nonrelativistic descriptions of a continuum are cited, namely:

1. **Material description** where the independent variables are the instant t and the material particle itself $\mathbf{X_0}$.

2. **Referential description**[3] whose independent variables are the instant t and the coordinates of a material particle $\mathbf{X_0}$ in an arbitrarily chosen referential configuration $\mathbf{B}_{ref}$, formulated as $\mathbf{X}$. This description is frequently referred to as the **Lagrangian description**[4].

3. **Spatial or Eulerian description**[5] where the independent variables are the instant t and the current position of the particle $\mathbf{X_0}$, namely, $\mathbf{x}$.

4. **Relative description** where the independent variables are the current coordinates $\mathbf{x}$ of a material particle $\mathbf{X_0}$ and a time variable τ, which corresponds to the instant in which the particle occupies certain location $\mathbf{z}$ different to the current $\mathbf{x}$.

As a consequence of the previous classification, here and in what follows a Lagrangian, referential or material description will be regarded as the most suitable. Therefore, any dependent magnitude of the continuum will be described by means of two independent variables: on the one hand, the current time t when the particle $\mathbf{X_0}$ occupies the location $\mathbf{x}$ and, on the other hand, the Lagrangian, referential or material coordinates $\mathbf{X}$ of the particle $\mathbf{X_0}$ when it belongs to the configuration $\mathbf{B}_{ref}$. This can be displayed as follows:

$$\mathcal{H} : \mathbf{B}_{ref} \longrightarrow \mathbf{B}_t$$

$$\mathbf{x} = (x_1, x_2, x_3) = \mathcal{H}(\mathbf{X}, t) = \mathcal{H}(X_1, X_2, X_3, t)$$

In accordance with this formulation, two second order tensors arise naturally to describe the kinematic of the process, namely:

Definition 31 (Deformation gradient tensor) *The deformation gradient tensor* $\mathbf{F}$ *is defined as the gradient of the current position vector* $\mathbf{x}$ *of a material particle, with respect to its position in the referential configuration* $\mathbf{B}_{ref}$*, that is*[6]*:*

[3]This description was introduced by Euler in 1762 according to Truesdell and Noll (1992).

[4]Some authors also employ the term *material description* when referring to it, although it should not be confused with the previous one. In this case, coordinates $\mathbf{X_0}$ are replaced by $\mathbf{X}$ as independent variables.

[5]This description was introduced by d'Alembert in 1752 according to Truesdell and Noll (1992).

[6]For the development of the forthcoming formulation, only cartesian coordinates in an Euclidean vector space will be taken into consideration, that is, $\{\widehat{i}, \widehat{j}, \widehat{k}\} \in \mathbf{R}^3$ will be adopted as the usual orthonormal triad. Hence and for the sake of simplicity, no distinction between covariant and contravariant coordinates has to be introduced.

$$F_{ij} = \frac{\partial x_i}{\partial X_j} \qquad \mathbf{F} = \boldsymbol{\nabla}_{ref}\mathbf{x} \tag{D.1}$$

Alternatively:

$$dx_i = \frac{\partial x_i}{\partial X_j} dX_j = F_{ij} dX_j \qquad d\mathbf{x} = \mathbf{F} \cdot d\mathbf{X} \tag{D.2}$$

The current coordinates $\mathbf{x}$ can be expressed in terms of the referential coordinates $\mathbf{X}$ by means of the displacement field $\mathbf{u}$ as follows:

$$\mathbf{x} = (x_1, x_2, x_3) = (X_1 + u_1, X_2 + u_2, X_3 + u_3) = \mathbf{X} + \mathbf{u} \tag{D.3}$$

Definition 32 (Displacement gradient tensor) *Combination of equations (D.1) and (D.3) enables to define the displacement gradient tensor* $\mathbf{G}$ *as follows:*

$$F_{ij} = \frac{\partial (X_i + u_i)}{\partial X_j} = \delta_{ij} + \frac{\partial u_i}{\partial X_j} = \delta_{ij} + G_{ij} \qquad \mathbf{F} = \mathbf{I} + \mathbf{G} \tag{D.4}$$

where δ_{ij} *and* $\mathbf{I}$ *stand for the well known Kronecker delta tensor and second order identity matrix, respectively.*

D.3 Strain numerical measures.

In contrast to linear elasticity, many different measures of strain may be used in nonlinear continuum mechanics. Provided that moderate strains are expected to emerge, finite deformation definitions are preferred rather than infinitesimal deformation ones. In this section, two important concepts are presented with the purpose of describing in an adequate manner the moderate strain undergone by a deformable body. We are referring to the so called *Green-Lagrange strain tensor* and the *strain rate tensor*. These two measures must satisfy a simple requirement, this is, their values must be null when representing a rigid body motion, either translation or rotation. Mathematically, a rigid body motion is recalled as follows:

$$\mathbf{x}(\mathbf{X}, t) = \mathbf{R}(t) \cdot \mathbf{X} + \mathbf{x_T}(t) \tag{D.5}$$

where the matrix $\mathbf{R}(t)$ is an orthogonal matrix describing a rotation[7] whereas $\mathbf{x_T}(t)$ can be identified as a translation vector.

As a starting point, firstly we introduce:

Definition 33 (Right Cauchy-Green deformation tensor) *This deformation tensor is formulated by means of the deformation gradient tensor as:*

$$C_{ij} = F_{ki} F_{kj} \qquad \mathbf{C} = \mathbf{F}^T \cdot \mathbf{F} \tag{D.6}$$

[7]Recall that a rotating matrix represents a change between orthogonal bases or, equivalently, an isometric transformation and, hence, it verifies: $\mathbf{R} \cdot \mathbf{R^T} = \mathbf{I}$.

As a result of the above definition, a valid[8] measure of the deformation can be defined as follows:

Definition 34 (Green-Lagrange strain tensor) *This tensor, closely related to the right Cauchy-Green deformation tensor, is defined by means of the following formulation:*

$$E_{ij} = \frac{1}{2}(C_{ij} - \delta_{ij}) = \frac{1}{2}(F_{ki}F_{kj} - \delta_{ij}) = \frac{1}{2}(G_{ij} + G_{ji}) + \frac{1}{2}G_{ki}G_{kj} \tag{D.7}$$

or in matrix notation:

$$\mathbf{E} = \frac{1}{2}(\mathbf{C} - \mathbf{I}) = \frac{1}{2}(\mathbf{F}^T \cdot \mathbf{F} - \mathbf{I}) = \frac{1}{2}(\mathbf{G} + \mathbf{G}^T) + \frac{1}{2}(\mathbf{G}^T \cdot \mathbf{G}) \tag{D.8}$$

In expressions (D.7) and (D.8), the term $\frac{1}{2}(G_{ij} + G_{ji})$ stands for the linearized strain tensor, commonly used in linear elasticity, whereas $\frac{1}{2}G_{ki}G_{kj}$ represents a non-linear source for the deformation. When dealing with large deformations, this non-linear term must not be neglected. As a matter of fact, the only way to represent accurately rigid body motions is by accounting for it. References Crisfield (1991a) and Belytschko et al. (2000) show a detailed demonstration of this issue.

Another useful measure of the strain is the so called *strain rate tensor.* To develop its definition, a previous concept should be introduced, which is the *spatial gradient of the velocity.*

Definition 35 (Spatial gradient of the velocity) *This tensor is formulated as follows:*

$$L_{ij} = \frac{\partial v_i}{\partial x_j} \qquad \mathbf{L} = \boldsymbol{\nabla}\mathbf{v} \tag{D.9}$$

This spatial gradient tensor[9] can be split into the summation of a symmetric tensor and a skew-symmetric tensor, that is, $\mathbf{L} = \mathbf{D} + \mathbf{W}$. Each component of the right hand side of the previous equation is defined as:

Definition 36 (Strain rate tensor or rate of deformation tensor) *This tensor presented as the symmetric component of the spatial gradient of the velocity yields:*

$$D_{ij} = \frac{1}{2}(L_{ij} + L_{ji}) \qquad \mathbf{D} = \frac{1}{2}(\mathbf{L} + \mathbf{L}^T) \tag{D.10}$$

[8]The Green-Lagrange strain tensor constitutes a valid measure for the deformation because as it was previously mentioned, in the case of a rigid body motion, $\mathbf{R} = \mathbf{F}$, and this entails that $\mathbf{C} = \mathbf{I}$. Eventually, $\mathbf{E} = \mathbf{0}$.

[9]Note the slight but notable difference between the Lagrangian operator $\boldsymbol{\nabla}_{ref} = \frac{\partial(.)}{\partial \mathbf{X}}$, formerly used for the definition of the deformation gradient tensor $\mathbf{F}$, and the Eulerian operator $\boldsymbol{\nabla} = \frac{\partial(.)}{\partial \mathbf{x}}$.

Definition 37 (Spin or vorticity tensor) *The skew-symmetric component is, analogously, formulated as follows:*

$$W_{ij} = \frac{1}{2}(L_{ij} - L_{ji}) \qquad \mathbf{W} = \frac{1}{2}(\mathbf{L} - \mathbf{L}^T) \tag{D.11}$$

Finally and as a way to conclude this section, some mathematical relationships can be set up between some of the kinematic magnitudes mentioned so far, namely[10]:

$$\dot{J} = J\boldsymbol{\nabla} \cdot \mathbf{v} = J\text{div}(\mathbf{v}) \tag{D.12}$$

$$\mathbf{L} = \dot{\mathbf{F}} \cdot \mathbf{F}^{-1} \tag{D.13}$$

$$\mathbf{D} = \mathbf{F}^{-T} \cdot \dot{\mathbf{E}} \cdot \mathbf{F}^{-1} \tag{D.14}$$

Demonstrations of the above relationships may be found in any of the References mentioned at the outset of this appendix.

D.4 Stress numerical measures.

When dealing with geometrically nonlinear problems, different measures of the stress state must conveniently be introduced for the sake of completeness. When we define strain as a function of the material coordinate $\mathbf{X}$ in a reference state $\mathbf{B}_{ref}$ other than the current configuration $\mathbf{B}_t$, we need also to express the stress as a function of the material coordinate $\mathbf{X}$ and derive equations of motion in such a reference state. The two Piola-Kirchhoff stress tensors[11], along with the Cauchy stress tensor, are the common alternative ways to define the stress state. These tensors will be symbolically represented as follows:

- $\boldsymbol{\sigma}$ represents the real or Cauchy stress tensor.
- $\mathbf{P}$ is known as the nominal stress tensor, also known as the transpose of the first Piola-Kirchhoff stress tensor, abbreviated as PK1.
- $\mathbf{S}$ symbolizes the second Piola-Kirchhoff stress tensor, abbreviated as PK2.

The basic ideas of the definition of the two Piola-Kirchhoff stress tensors can be indicated by means of the formulas detailed right below in matrix notation:

$$\mathbf{n}^T \cdot \boldsymbol{\sigma} d\Gamma = \mathbf{t}^T d\Gamma = d\mathbf{f}^T \tag{D.15}$$

$$\mathbf{n}_{ref}^T \cdot \mathbf{P} d\Gamma_{ref} = \mathbf{t}_{ref}^T d\Gamma_{ref} = d\mathbf{f}^T \tag{D.16}$$

[10]The dot above any magnitude stands for its derivative with respect to time.

[11]Due to Piola in 1833 and Kirchhoff in 1852.

$$\mathbf{n}_{ref}^T \cdot \mathbf{S} \cdot d\Gamma_{ref} = d\mathbf{f}_{ref}^T = d\mathbf{f}^T \cdot \mathbf{F}^{-T} \tag{D.17}$$

where:

- $\mathbf{n}$ and $\mathbf{n}_{ref}$ represent the normal unit vectors in both current $\mathbf{B}_t$ and reference configuration $\mathbf{B}_{ref}$.
- $\mathbf{t}$ and $\mathbf{t}_{ref}$ symbolize the stress vector in $\mathbf{B}_t$ and $\mathbf{B}_{ref}$, respectively.
- $\mathbf{df}$ and $\mathbf{df}_{ref}$ are the force vectors in both configurations.
- $d\Gamma$ and $d\Gamma_{ref}$ are the surface differentials in both configurations.

Nanson's rule -see Chadwick (1999) and Belytschko et al. (2000)- enables to establish a formal relationship between the unit normal vectors $\mathbf{n}$ and $\mathbf{n}_{ref}$, which turns out to be:

$$\mathbf{n}^T d\Gamma = J\mathbf{n}_{ref}^T \cdot \mathbf{F}^{-1} d\Gamma_{ref} \tag{D.18}$$

The above equations (D.15) to (D.18) can be combined in a simple manner to come out, by means of the deformation gradient tensor $\mathbf{F}$ and its determinant J, with the following relationships among the different stress tensors, namely[12]:

$$\sigma_{ij} = J^{-1} F_{ik} P_{kj} \qquad \boldsymbol{\sigma} = J^{-1} \mathbf{F} \cdot \mathbf{P} \tag{D.19}$$

$$P_{ij} = S_{ik} F_{jk} \qquad \mathbf{P} = \mathbf{S} \cdot \mathbf{F}^T \tag{D.20}$$

$$\sigma_{ij} = J^{-1} F_{ik} S_{kl} F_{jl} \qquad \boldsymbol{\sigma} = J^{-1} \mathbf{F} \cdot \mathbf{S} \cdot \mathbf{F}^T \tag{D.21}$$

The above equations gather the concept of *push forward* and *pull back* operations, extensively described in the literature about the subject -see Bonet and Wood (1997) and Holzapfel (2000)-.

[12]These relationships along with the fulfillment of the angular momentum balance law, make the first Piola-Kirchhoff to be a non-symmetric tensor, unlike the second Piola-Kirchhoff stress tensor and the Cauchy stress tensor, which are fully symmetric.

Appendix E

Derivatives for the Saint Venant-Kirchhoff hyperelastic model

E.1 Introduction.

Let us define the Helmholtz's free energy functional w_{int} in terms of the invariants I_i of the Green-Lagrange strain tensor $\mathbf{E}$, as well as of its eigenvalues ξ_i. For the case of a prestressed hyperelastic Saint Venant-Kirchhoff material, the first two invariants and eigenvalues are just required. With the purpose of deriving adequate expressions for the second Piola-Kirchhoff stress tensor $\mathbf{S}$ and the fourth order tangent moduli tensor $\boldsymbol{\mathcal{C}}$, first and second order derivatives of w_{int} with respect to I_i are a necessary requisite. In this appendix, an elegant technique is presented by following the work of Mahaney (2002).

E.2 First derivatives.

The Helmholtz's free energy functional can be gathered as follows:

$$w_{int} = w_{int}(I_1, I_2) \tag{E.1}$$

$$I_1 = I_{\mathbf{E}} = E_{ii} \tag{E.2}$$

$$I_2 = II_{\mathbf{E}} = E_{ij}E_{ij} \tag{E.3}$$

The first order partial derivatives of w_{int} with respect to I_i can be expressed through ξ_i by means of the straightforward chain rule. This can be carried out to get:

$$\frac{\partial w_{int}}{\partial I_i} = \frac{\partial w_{int}}{\partial \xi_j}\frac{\partial \xi_j}{\partial I_i} = \frac{\partial w_{int}}{\partial \xi_j}\Omega_{ji} \tag{E.4}$$

By considering the mathematical definitions of the invariants I_1 and I_2, suitably displayed in formulae (E.2) and (E.3) respectively, the inverse of the matrix Ω_{ij} yields:

$$\Omega_{ij}^{-1} = \frac{\partial I_i}{\partial \xi_j} = \begin{bmatrix} 1 & 1 \\ 2\xi_1 & 2\xi_2 \end{bmatrix} \tag{E.5}$$

The actual matrix Ω_{ij} is obtained simply by:

$$\Omega_{ij} = \frac{\partial \xi_i}{\partial I_j} = \frac{1}{2(\xi_2 - \xi_1)}\begin{bmatrix} 2\xi_2 & -1 \\ -2\xi_1 & 1 \end{bmatrix} \tag{E.6}$$

Therefore, the equation (E.4) can be detailed as follows:

$$\begin{bmatrix} \frac{\partial w_{int}}{\partial I_1} & \frac{\partial w_{int}}{\partial I_2} \end{bmatrix} = \frac{1}{2(\xi_2 - \xi_1)}\begin{bmatrix} \frac{\partial w_{int}}{\partial \xi_1} & \frac{\partial w_{int}}{\partial \xi_2} \end{bmatrix}\begin{bmatrix} 2\xi_2 & -1 \\ -2\xi_1 & 1 \end{bmatrix} \tag{E.7}$$

E.2.1 Second derivatives.

By taking heed of the equation (E.4), the calculation of the second order partial derivatives of w_{int} with respect to I_i can be carried out, namely:

$$\frac{\partial^2 w_{int}}{\partial I_i \partial I_j} = \frac{\partial}{\partial I_j}\left(\frac{\partial w_{int}}{\partial \xi_k}\Omega_{ki}\right) \tag{E.8}$$

By means of the chain rule:

$$\frac{\partial^2 w_{int}}{\partial I_i \partial I_j} = \frac{\partial^2 w_{int}}{\partial \xi_l \xi_k}\Omega_{lj}\Omega_{ki} + \frac{\partial w_{int}}{\partial \xi_k}\frac{\partial \Omega_{ki}}{\partial \xi_l}\Omega_{lj} \tag{E.9}$$

The second term of the right hand side of equation (E.9) can be deduced by realizing that:

$$\frac{\partial(\Omega_{kn}\Omega^{-1}_{nm})}{\partial \xi_l} = \frac{\partial \delta_{km}}{\partial \xi_l} = \frac{\partial \Omega_{kn}}{\partial \xi_l}\Omega^{-1}_{nm} + \Omega_{kn}\frac{\partial \Omega^{-1}_{nm}}{\partial \xi_l} \tag{E.10}$$

By expanding the above formula:

$$\frac{\partial \Omega_{ki}}{\partial \xi_l} = -\Omega_{kn}\Omega_{mi}\frac{\partial \Omega^{-1}_{nm}}{\partial \xi_l} \tag{E.11}$$

By substituting (E.11) back into (E.9) and applying Schwartz's lemma:

$$\frac{\partial^2 w_{int}}{\partial I_i \partial I_j} = \Omega_{ki}\frac{\partial^2 w_{int}}{\partial \xi_k \xi_l}\Omega_{lj} - \Omega_{mi}\frac{\partial w_{int}}{\partial \xi_k}\Omega_{kn}\frac{\partial \Omega^{-1}_{nm}}{\partial \xi_l}\Omega_{lj} \tag{E.12}$$

Hence, by redefining dummy indices, the following formula can be concluded:

$$\frac{\partial^2 w_{int}}{\partial I_i \partial I_j} = \Omega_{ki}\left(\frac{\partial^2 w_{int}}{\partial \xi_k \xi_l} - \frac{\partial w_{int}}{\partial \xi_m}\Omega_{mn}\frac{\partial \Omega^{-1}_{nk}}{\partial \xi_l}\right)\Omega_{lj} \tag{E.13}$$

If detailing some of the above terms, namely:

$$\frac{\partial \Omega^{-1}_{1k}}{\partial \xi_l} = \begin{bmatrix} 0 & 0 \\ 0 & 0 \end{bmatrix} \quad \frac{\partial \Omega^{-1}_{2k}}{\partial \xi_l} = \begin{bmatrix} 2 & 0 \\ 0 & 2 \end{bmatrix} \tag{E.14}$$

The final expression for the second order partial derivatives can be summarized as follows:

$$\left[\frac{\partial^2 w_{int}}{\partial I_i \partial I_j}\right] = \mathbf{\Omega}^T \cdot \begin{bmatrix} \frac{\partial^2 w_{int}}{\partial \xi_1 \partial \xi_1} - 2\frac{\partial w_{int}}{\partial I_2} & \frac{\partial^2 w_{int}}{\partial \xi_1 \partial \xi_2} \\ \frac{\partial^2 w_{int}}{\partial \xi_2 \partial \xi_1} & \frac{\partial^2 w_{int}}{\partial \xi_2 \partial \xi_2} - 2\frac{\partial w_{int}}{\partial I_2} \end{bmatrix} \cdot \mathbf{\Omega} \tag{E.15}$$

Part VII

References

References

Ando, K., A. Ishii, T. Suzuki, K. Masuda, and Y. Saito (1999). Design and construction of a double membrane air-supported structure. *Engineering Structures 21*, 786–794.

Ando, K., J. Mitsugi, and Y. Senbokuya (2000). Analyses of cable-membrane structure combined with deployable truss. *Computers and structures 74*, 21–39.

Arcaro, V. F. (2001a). A simple procedure for analysis of cable network structures. *UNICAMP Report*, 1–10.

Arcaro, V. F. (2001b). A simple procedure for shape finding and analysis of fabric structures. *UNICAMP Report*, 1–16.

Argyris, J. H. and D. W. Scharpf (1972). Large deflection analysis of prestressed networks. *Journal of the Structural Division 98*(ST3), 633–654.

Ashmawy, M. A., H. A. Buchholdt, and G. D. Stefanou (1997). A numerical method for the nonlinear static analysis of space cable skeletal structures. *Journal of the IASS 38*(123), 3–18.

Barnes, M. R. (1988). Form finding and analysis of prestressed nets and membranes. *Computers and Structures 30*(3), 685–695.

Baron, F. and M. S. Vendatesan (1971). Nonlinear analysis of cable and truss structures. *Journal of the Structural Division, ASCE 97*(ST2).

Bathe, K. (1996). *Finite element procedures.* New Jersey: Prentice-Hall, Inc.

Belytschko, T., W. K. Liu, and B. Moran (2000). *Nonlinear finite elements for continua and structures.* John Wiley and Sons.

Bergan, P. G. (1980). Solution algorithms for nonlinear structural problems. *Computers and Structures 12*, 497–509.

Berger, H. (1996). *Light Structures. Structures of light.* Birkhuser.

Berger, H. (1999). Form and function of tensile structures for permanent buildings. *Engineering Structures 21*, 669–679.

Bletzinger, K.-U. (1997). Form finding of membrane structures and minimal surfaces by numerical continuation. In *Colloqium Structural Morphology: towards a new millennium, Nottingham.* IASS.

Bletzinger, K.-U. and E. Ramm (2001). Structural optimization and form finding of light weight structures. *Computers and Structures 79*(22-25), 2053–2062.

Bonet, J. and J. Mahaney (2001). Form finding of membrane structures by the updated reference method with minimum mesh distortion. *International Journal of Solids and Structures 38*, 5469–5480.

Bonet, J. and R. D. Wood (1997). *Nonlinear continuum mechanics for finite element analysis.* Cambridge University Press.

Bonet, J., R. D. Wood, J. Mahaney, and P. Heywood (2000). Finite element analysis of air supported membrane structures. *Computer methods in applied mechanics and engineering 190*, 579–595.

Brew, J. S. and D. M. Brotton (1971). Non-linear structural analysis by dynamic relaxation. *International journal for numerical methods in Engineering 3*, 463–483.

Broughton, P. and P. Ndumbaro (1994). *The analysis of cable and catenary structures.* London: Thomas Teldford.

Buchholdt, H. A. (1985). *Introduction to cable roof structures.* Cambridge University Press.

Burden, R. L. and J. Douglas (1998). *Análisis numérico.* International Thomson Editores.

Candela, F. (1994). Estructuras laminares parabólico-hiperbólicas. *Informes de la Construcción* (76).

Canner, A. and R. Hsu (1999). Tensioned fabric shape-finding. *Journal of Structural Engineering 125*(9), 1065–1071.

Castellano, J. (1995). *Métodos matemáticos de las técnicas.* Proyecto Sur.

Castillo, E. and et al. (2002). *Formulación y resolución de modelos de programación matemática en Ingeniería y Ciencia.* Universidad de Castilla-La Mancha.

Chadwick, P. (1999). *Continuum Mechanics: Concise theory and problems.* New York: Dover Publications, Inc.

Chapman, S. J. (1998). *Fortran 90/95 for Scientists and Engineers.* McGraw Hill.

Contri, P. and B. A. Schrefler (1988). A geometrically nonlinear finite element analysis of wrinkled membrane surfaces by a no-compression material model. *Communications in Applied Numerical Methods 4*, 5–15.

Cook, R. D., D. S. Malkus, and M. E. Plesha (1989). *Concepts and applications of finite element analysis* (Third ed.). John Wiley and Sons.

Cortell, R. (1984). Formas, tensiones y deformaciones en estructuras laminares con puntos singulares. *Informes de la Construcción 36*(364).

Courbon, J. (1981). *Estructuras laminares.* Barcelona: Editores técnicos asociados, S. A.

Coyette, J. P. and P. Guisset (1988). Cable network analysis by a nonlinear programming technique. *Engineering Structures 10*, 41–46.

Crisfield, M. A. (1991a). *Non-linear finite element analysis of solids and structures*, Volume 1: Essentials. John Wiley and Sons.

Crisfield, M. A. (1991b). *Non-linear finite element analysis of solids and structures*, Volume 2: Advanced Topics. John Wiley and Sons.

Crivelli, L. A. and C. A. Felippa (1993). A three-dimensional non-linear timoshenko beam based on the core-congruential formulation. *Internationl Journal of Numerical Methods in Engineering 36*, 3647–3673.

Dahlquist, G., A. Bjrck, and N. Anderson (1969). *Numerical methods.* New Jersey: Prentice-Hall, Inc.

Dennis Jr., J. E. and R. B. Schnabel (1996). *Numerical Methods for Unconstrained Optimization and Nonlinear Equations*, Volume 16 of *Classics in Applied Mathematics.* Society for Industrial and Applied Mathematics.

Díaz del Valle, J. (1989). *Mecánica de los Medios Continuos.* Universidad de Cantabria.

Do Carmo, M. (1995). *Geometría diferencial de curvas y superficies.* Madrid: Alianza Universidad Textos.

Engel, H. (2001). *Sistemas de estructuras.* Gustavo Gili, S.A.

Farshad, M. (1992). *Design and analysis of shell structures.* Kluwer academic publishers.

Felippa, C. A. (2000). *A historical outline of matriz structural analysis: a play in three acts. Report No. CU-CAS-00-13.* University of Colorado: Center for Aerospace Structures.

Felippa, C. A. (2001). *Lecture notes in Nonlinear Finite Element Methods. Report No. CU-CSSC-96-16.* University of Colorado: Center for Aerospace Structures.

Felippa, C. A., L. A. Crivelli, and B. Haugen (1994). A survey of the core-congruential formulation for geometrically nonlinear tl finite elements. *Archives of Computational Methods in Engineering 1*, 1–48.

Gaylord, E. H. J. and C. N. Gaylord (1990). *Structural Engineering Handbook* (Third ed.). McGraw-Hill Publishing Company.

Ghali, A. and A. M. Neville (1997). *Structural analysis. A unified classical and matrix approach.* New York: E & FN Spon.

Gil, A. (2001). Métodos numéricos para el diseo de estructuras traccionadas: membranas y redes de cables. Technical report, Universidad de Granada.

Gil, A. (2003a). A comparision of prestressed membranes finite element analysis with membrane and cable elements. In *Textile composites and inflatable structures.* CIMNE: Oñate, E. and Kröplin, B.

Gil, A. (2003b). Finite element analysis of prestressed hyperelastic saint venant-kirchhoff membranes under large deformations. In *Textile composites and inflatable structures.* CIMNE: Oñate, E. and Kröplin, B.

Gil, A. and J. Bonet (2004). Wrinkling analysis of prestressed hyperelastic saint venant-kirchhoff membranes. In *Shell and Spatial Structures: from Models to Realization.* IASS: IASS.

González de Posada, F. (1983). *Estructuras algebraicas tensoriales.* Ed. Alhambra.

Gorini, C. A. (2000). *Geometry at Work.* The Mathematical Association of America.

Gosling, P. D. (1998). A discrete energy formulation for the definition of optimal tension structures. *Structural Optimization 16*, 76–80.

Gosling, P. D. and W. J. Lewis (1996a). Optimal structural membranes. part i: Formulation of a curved quadrilateral element for surface definition. *Computers and structures 61*(5), 871–883.

Gosling, P. D. and W. J. Lewis (1996b). Optimal structural membranes. part ii: Form-finding of prestressed membranes using a curved quadrilateral finite element for surface definition. *Computers and structures 61*(5), 885–895.

Graver, J. E. (2001). *Counting on frameworks.* The Mathematical Association of America.

Green, A. E. and W. Zerna (1968). *Theoretical Elasticity* (2nd ed.). Oxford University Press.

Gründig, L. and J. Bahndorf (1988). The design of wide-span roof structures using micro-computers. *Computers and Structures 30*(3), 495–501.

Grutmann, F. and R. L. Taylor (1992). Theory and finite element formulation of rubberlike membrane shells using principal stretches. *International Journal for Numerical Methods in Engineering 35*, 1111–1126.

Haber, R. B. and J. F. Abel (1982a). Initial equilibrium solution methods for cable reinforced membranes. part i: Formulation. *Computer methods in applied Mechanics and Engineering 30*(3), 263–284.

Haber, R. B. and J. F. Abel (1982b). Initial equilibrium solution methods for cable reinforced membranes. part ii: Implementation. *Computer methods in applied Mechanics and Engineering 30*(3), 285–306.

Haftka, R. T. and Z. Gürdal (1992). *Elements of structural optimization.* Kluwer Academic Publishers.

Hangai, Y. and M. Wu (1999). Analytical method of structural behaviours of a hybrid structure consisting of cables and rigid structures. *Engineering Structures 21*, 726–736.

Herzog, T. (1977). *Pneumatic structures.* Crosby Lockwood Staples.

Hildebrandt, S. and A. Tromba (1990). *Matemática y formas óptimas* (First ed.). Biblioteca Scientific American.

Holzapfel, G. A. (2000). *Nonlinear solid mechanics: a continuum approach for Engineering.* John Wiley and Sons.

Humphrey, J. D. (1998). Computer methods in membrane biomechanics. *Computer Methods in Biomechanics and Biomedical Engineering 1*, 171–210.

Iésan, P. (1989). *Prestressed bodies.* Longman Scientific & Technical.

Irvine, M. (1981). *Cable Structures.* New York: Dover publications Inc.

Ishii, K. (1995). *Membrane Structures in Japan.* Tokio: SPS Publishing Company.

Iványi, P. (2002). *Design of cable membrane structures.* http://www.sect.mce.hw.ac.uk/~peteri/work/.

Iványi, P. and B. H. V. Topping (2002). A new graph representation for cable-membrane structures. *Advances in Engineering Software 33*, 273–279.

Jayaraman, H. B. and W. C. Knudson (1981). A curved element for the analysis of cable structures. *Computers and structures 14*(3-4), 325–333.

Jiménez Montoya, P., A. García Meseguer, and F. Morán Cabré (1994). *Hormigón armado*, Volume I. Editorial Gustavo Gili, S. A.

Jufen, Z. and C. Wanji (1997). Geometric nonlinear analysis by using refined triangular thin plate element and free form membrane locking. *Computers and structures 63*(5), 999–1005.

Kadlcak, J. (1994). *Statics of suspension roofs.* A. A. Balkema Publishers.

Kang, S. and S. Im (1997). Finite element analysis of wrinkling membranes. *Journal of Applied Mechanics 64*, 263–269.

Kang, S. and S. Im (1999). Finite element analysis of dynamic response of wrinkling membranes. *Computer methods in applied Mechanics and Engineering 173*, 227–240.

Kebiche, K., M. N. Kazi-Aoual, and R. Motro (1999). Geometrical non-linear analysis of tensegrity systems. *Engineering Structures 21*, 864–876.

Kelley, C. T. (1995). *Iterative methods for linear and nonlinear equations.* Society for Industrial and Applied Mathematics.

Krasnov, M., A. Kiseliov, G. Makarenko, and E. Shikin (1994). *Curso de matemáticas superiores para ingenieros.* Madrid: Editorial MIR.

Kwan, A. S. K. (1998). A new approach to geometric nonlinearity of cable structures. *Computers and Structures 67*, 243–252.

Kwun, T. J., S. Y. Sur, and H. W. Cho (1994). A shape finding finite element analysis for an equally-stressed surface in membrane structures. In *Spatial, lattice and tension structures*. IASS-ASCE: Abel, J. and Leonard, J. and Penalba, C.

Leonard, J. W. (1988). *Tension structures*. New York: McGraw-Hill.

Leu, L. J. and Y. B. Yang (1990). Effects of rigid body and stretching on nonlinear analysis of trusses. *Journal of Structural Engineering 116*(10), 2582–2598.

Levy, R. and E. Gal (2001). Geometrically nonlinear three-noded flat triangular shell elements. *Computers and structures 79*, 2349–2355.

Levy, R. and W. Spillers (1995). *Analysis of geometrically nonlinear structures*. Chapman and Hall.

Levy, R. and W. R. Spillers (1998). Practical methods for shape finding for membrane and cable nets. *Journal of Structural Engineering 124*(4), 466–468.

Lewis, W. J. (1998). Lightweight tension membranes: an overview. *Civil Engineering 126*, 171–181.

Lewis, W. J. and M. S. Jones (1984). Dynamic relaxation analysis of the non-linear static response of pretensioned cable roofs. *Computers and structures 18*(6), 989–997.

Lewis, W. J. and T. S. Lewis (1996). Application of formian and dynamic relaxation to the form-finding of minimal surfaces. *Journal of the IASS 37*(122), 165–185.

Li, J.-J. and C. Siu-Lai (2004). An integrated analysis of membrane structures with flexible supporting frames. *Finite Elements in Analysis and Design 40*, 529–540.

Lichnerowicz, A. (1962). *Elementos de cálculo tensorial*. Ed. Aguilar.

Linkwitz, K. (1999). About form finding of double-curved structures. *Engineering Structures 21*, 709–718.

Liu, X., C. H. Jenkins, and W. W. Schur (2001). Large deflection analysis of pneumatic envelopes using a penalty parameter modified material model. *Finite Elements in Analysis and Design 37*, 233–251.

Lu, K., M. Accorsi, and J. Leonard (2001). Finite element analysis of membrane wrinkling. *International Journal for Numerical Methods in Engineering 50*, 1017–1038.

Luenberger, D. G. (1989). *Linear and Nonlinear Programming* (2nd ed.). USA: Addison-Wesley Publising Company.

Magara, H. and K. Okamura (1986). A study on modeling and structural behaviour of membrane structures. In *Shells, Membranes and Space Frames. Symposium Osaka*. IASS: Heki, K.

Mahaney, J. (2002). *Aspects of large strain membrane analysis using the finite element method.* Ph. D. thesis, University of Swansea.

Majowiecki, M. (1998). *Tensostrutture Progetto e Verifica.* Edizioni Crea.

Mallett, R. H. and P. V. Marcal (1968). Finite element analysis of nonlinear structures. *Journal of the Structural Division 94*(ST9), 2081–2105.

Malvern, L. E. (1969). *Introduction to the mechanics of a continuous medium.* New Jersey: Prentice Hall.

MathWorks (1996). *Matlab optimization toolbox users guide.* http://www.mathworks.com.

Maurin, B. and R. Motro (1997). Investigation of minimal forms with density methods. *Journal of the IASS 38*(125), 143–154.

Maurin, B. and R. Motro (1998). The surface stress density method as a form-finding tool for tensile membranes. *Engineering Structures 20*, 712–719.

Maurin, B. and R. Motro (2001). Investigation of minimal forms with conjugate gradient method. *International Journal of Solids and Structures 38*, 2387–2399.

Miller, R. K., J. M. Hedgepeth, V. I. Weingarten, and S. Das, P.and Kahyai (1985). Finite element analysis of partly wrinkled membranes. *Computers and Strcutures 20*(1-3), 631–639.

Monforton, G. R. and N. M. El Hakim (1980). Analysis of truss cable structures. *Computers and Structures 11*, 327–335.

Monjo, J. (1991). *Introducción a la arquitectura textil. Cubiertas colgadas.* Madrid: Servicio de publicaciones del Colegio oficial de Arquitectos de Madrid.

M.O.P.T.M.A. (1994). *Félix Candela, Arquitecto.* Madrid: M.O.P.T.M.A.

Motro, R., S. Belkacem, and N. Vassart (1994). Form finding numerical methods for tensegrity systems. In *Spatial, lattice and tension structures.* IASS-ASCE: Abel, J. and Leonard, J. and Penalba, C.

Murcia, J. (1990). Las estructuras a tracción y sus materiales. *Hormigón y Acero 174*, 121–133.

Nouri-Baranger, T. (2002). Form finding method of tensile fabric structures: revised geometric stiffness method. *Journal of the IASS 43*(138), 13–22.

Nyhoff, L. and S. Leestma (1997). *Fortran 90 for engineers and scientists.* Prentice-Hall.

Oñate, E. (1995). *Cálculo de estructuras por el método de los elementos finitos.* Barcelona: CIMNE.

Oden, J. T. (1967). Numerical formulation of nonlinear elasticity problems. *Journal of the Structural Division 93*(ST3), 235–255.

Oden, J. T. and S. W. Key (1973). Analysis of static nonlinear response by explicit time. *International journal for numerical methods in Engineering 7*, 225–240.

Oden, J. T. and E. A. Ripperger (1981). *Mechanics of elastic structures.* McGraw-Hill.

Oden, J. T. and T. Sato (1967). Finite strains and displacements of elastic membranes by the finite element method. *International Journal of Solids and Structures 3*, 471–488.

Otto, F. (1962). *Cubiertas colgantes.* Madrid: Editorial Labor, S.A.

Otto, F. (1967). *Tensile structures.* Cambridge: MIT Press.

París (1996). *Teoría de la Elasticidad.* GERM.

Pérez, C. (1999). *Análisis matemático y álgebra lineal con MATLAB.* Editorial RA-MA.

Peyrot, A. H. and A. M. Goulois (1979). Analysis of cable structures. *Computers and structures 10*, 805–813.

Pipkin, A. C. (1986). The relaxed energy density for isotropic elastic membranes. *IMA Journal of Applied Mathematics 36*, 85–99.

Quesada, J. J. (1996). *Ecuaciones Diferenciales, Análisis Numérico y Métodos Matemáticos.* Monachil (Granada): Ed. Santa Rita.

Quintas Ripoll, V. (1996). *Estructuras especiales en edificacin. Análisis y cálculo.* Madrid: Editorial Rueda.

Rade, L. and B. Westergren (1999). *Mathematics Handbook for Science and Engineering.* Springer.

Rajasekaran, S. and D. W. Murray (1973). Incremental finite elements matrices. *Journal of the Structural Division 99*(ST12), 2423–2438.

Ramaswamy, G. S. (1982). *Design and construction of concrete shell roofs.* Malabar (Florida): Robert E. Krieger publishing company.

Ramesh, G. and C. S. Krishnamoorthy (1995). Geometrically non-linear analysis of plates and shallow shells by dynamic relaxation. *Computational methods in applied mechanics and engineering 123*, 15–32.

Ramm, E. (1992). Shape finding methods of shells. *Bulletin of the IASS 33*(109), 89–99.

Recuero, A. y Gutiérrez, J. P. (1994). Análisis de estructuras con cables y telas. *Hormigón y acero* (191), 43–51.

Roddeman, D. G., J. Drukker, C. W. J. Oomens, and J. D. Janssen (1987a). The wrinkling of thin membranes: Part i-theory. *Journal of Applied Mechanics 54*, 884–887.

Roddeman, D. G., J. Drukker, C. W. J. Oomens, and J. D. Janssen (1987b). The wrinkling of thin membranes: Part ii-numerical analysis. *Journal of Applied Mechanics 54*, 888–892.

Rumpel, T. and K. Schweizerhof (2004). Hydrostatic fluid loading in nonlinear finite element analysis. *International Journal for Numerical Methods in Engineering 59*, 849–870.

Saitoh, M. and A. Okada (1999). The role of string in hybrid string structure. *Engineering Structures 21*, 756–769.

Saitoh, M. and A. Okada (2001). Tension and membrane structures. *Journal of the IASS 42*(135-136), 15–20.

Samartín, A. (1993). Numerical methods in nonlinear analysis of shell structures. *Bulletin of IASS 34*(112), 81–102.

Santaló, L. A. (1969). *Vectores y tensores con sus aplicaciones.* Ed. universitaria de Buenos Aires.

Sanz, L. J. (1999). El borde libre y félix candela. *Revista de Obras Públicas* (3383), 17–28.

Sastre, R. (1986). Aplicación del método de los elementos finitos al cálculo de membranas tensadas en arquitectura. In *II Simposium sobre aplicaciones del método de los elementos finitos en Ingeniería.* CIMNE: Oñate, E.

Schlaich, J. (2002). On some recent lightweight structures. *Journal of the IASS 43*(139), 69–79.

Schlaich, J., R. Bergermann, and W. Sobek (1990). Tensile membrane structures. *Bulletin of the IASS 31*(1-2), 19–32.

Schrefler, B., S. Odorizzi, and R. D. Wood (1983). A total lagrangian geometrically non-linear analysis of combined beam and cable structures. *Computers and Structures 17*(1), 115–127.

Shaeffer, R. E. (1996). *Tensioned fabric structures.* New York: American Society of Civil Engineers.

Simo, J. C., R. L. Taylor, and P. Wriggers (1991). A note on finite element implementation of pressure boundary loading. *Communications in Applied Numerical Methods 7*, 513–525.

Sindel, F., T. Nouri-Baranger, and P. Trompette (2001). Including optimization in the conception of fabric structures. *Computers and Structures 79*, 2451–2459.

Smith, I. M. (1995). *Programming in Fortran 90.* John Wiley and Sons.

Smith, I. M. and D. V. Griffiths (1998). *Programming the finite element method* (Third ed.). John Wiley and Sons.

Sokolnikoff, I. S. (1987). *Análisis tensorial. Teoría y aplicaciones a la geometría y mecánica de los medios continuos.* Ed. Limusa.

Souza, E. A., D. Peric, and D. R. J. Owen (1995). Finite elasticity in spatial description linearization aspects with 3-d membrane applications. *International Journal for Numerical Methods in Engineering 38*, 3365–3381.

Stanuszek, M. (2003). Finite element analysis of large deformations of membranes with wrinkling. *Finite elements in analysis and design 39*(7), 599–618.

Stefanou, G. D., E. Moossavi, and P. Bishop, S. Koliopoulos (1994). Conjugate gradients method for calculating the response of large cable nets to static loads. *Computers and structures 49*(5), 843–848.

Steigmann, D. J. and A. C. Pipkin (1989). Wrinkling of pressurized membranes. *Journal of Applied Mechanics 56*, 624–628.

Swaddiwudhipong, S., C. M. Wang, K. M. Liew, and S. L. Lee (1989). Optimal pretensioned forces for cable networks. *Computers and structures 33*(6), 1349–1354.

Tabarrok, B. and Z. Qin (1992). Nonlinear analysis of tension structures. *Computers and structures 45*(5-6), 973–984.

Talvik, I. (2001). Finite element modelling of cable networks with flexible supports. *Computers and structures 79*, 2443–2450.

Taylor, R. L. (2001). Finite element analysis of membrane structures. *Publication CIMNE 203*, 1–34.

Timoshenko, S. and S. Woinowsky-Krieger (1959). *Theory of plates and shells.* New York: McGraw-Hill.

Timoshenko, S. J. and J. N. Goodier (1968). *Teoría de la elasticidad.* Bilbao: Editorial Urmo.

Tonda, J. A. (1973). Bóvedas de cascarón para la planta bacardí en méxico. *Revista IMCYC 10*(60), 69–77.

Torroja, E. (1991). *Razón y Ser de los Tipos Estructurales.* Madrid: Instituto Eduardo Torroja de la construcción y del cemento.

Truesdell, C. and W. Noll (1992). *The non-linear field theories of mechanics* (2nd ed.). Springer-Verlag.

Turner, M. J., R. W. Clough, H. C. Martin, and L. J. Topp (1956). Stiffness and deflection analysis of complex structures. *Journal of the aeronautical sciences 23*(9), 805–824.

Turner, M. J., E. H. Dill, H. C. Martin, and R. J. Melosh (1960). Large deflections of structures subjected to heating and external loads. *Journal of the aerospace sciences 27*, 97–127.

Wakefield, D. S. (1999). Engineering analysis of tension structures: theory and practice. *Engineering Structures 21*, 680–690.

Wood, R. D. (2002). A simple technique for controlling element distortion in dynamic relaxation form-finding of tension membranes. *Computers and Structures 80*, 2115–2120.

Wood, R. D. and B. Schrefler (1978). Geometrically non-linear analysis - a correlation of finite element notations. *International Journal for Numerical Methods in Engineering 12*, 635–642.

Wu, B., X. Du, and H. Tan (1996). A three-dimensional finite element analysis of membranes. *Computers and Structures 59*(4), 601–605.

Zhang, Y. and B. Tabarrok (1999). Generation of surfaces of via equilibrium of forces. *Computers and Structures 70*, 599–613.

Zienkiewicz, O. C. (1982). *El método de los elementos finitos.* Barcelona: Editorial Reverté, S. A.

Zienkiewicz, O. C. and R. L. Taylor (1995). *El Método de los Elementos Finitos* (4th ed.), Volume 2: Mecánica de Sólidos y Fluidos. Dinámica y no Linealidad. Barcelona: CIMNE and McGraw-Hill.